TWO-PROTON INTENSITY INTERFEROMETRY IN INTERMEDIATE ENERGY HEAVY-ION COLLISIONS

By

Wen Guang Gong

AN ABSTRACT OF A DISSERTATION

Submitted to
Michigan State University
in partial fulfillment of the requirements
for the Degree of

DOCTOR OF PHILOSOPHY

Department of Physics and Astronomy

1991

Two-proton intensity interferometry has been studied both experimentally and theoretically in order to probe the space-time evolution of heavy-ion nuclear collisions at intermediate energy.

An approximate relation is derived which allows the calculation of the two-proton correlation function for any reaction model capable of predicting the single-particle phase-space distribution or the Wigner function in the exit channel. The sensitivity of two-proton correlation functions to source radii and lifetimes is illustrated by calculations with simple parametrizations. More realistic calculations are presented for two different regimes of emission time scales: slow particle evaporation from equilibrated compound nuclei, as predicted from the Weisskopf formula, and fast non-equilibrium particle emission in intermediate energy nucleus-nucleus collisions, as predicted from the Boltzmann-Uehling-Uhlenbeck transport equation.

Two-proton correlation functions have been measured at $\theta_{lab} \approx 25°$ for the "inverse kinematics" reaction $^{129}Xe + ^{27}Al$ at E/A = 31 MeV, and for the nearly symmetric reaction $^{129}Xe + ^{122}Sn$ at E/A = 31 MeV, for the "forward kinematics" reactions $^{14}N + ^{27}Al$ and $^{14}N + ^{197}Au$ at E/A = 75 MeV. For the reactions at 31 MeV per nucleon, the two-proton correlation functions do not exhibit maxima at q = 20 MeV/c, but only minima at q = 0 MeV/c. These correlations indicate emission on a slow time scale. They can be reproduced by calculations based on the Weisskopf formula for evaporative emission from fully equilibrated compound nuclei. For the reactions at 75 MeV per nucleon, the correlation functions exhibit pronounced maxima at relative momenta, q = 20 MeV/c, and minima at q = 0 MeV/c. These correlations indicate emission from fast, non-equilibrium processes. They are analyzed in terms of standard Gaussian source parametrizations and compared to microscopic simulations performed with the Boltzmann-Uehling-Uhlenbeck

equation. For all reactions, the measured longitudinal and transverse correlation functions are very similar, in agreement with theoretical predictions.

Two-proton correlation functions predicted by the BUU model for the reaction $^{14}N + ^{27}Al$ at $E/A = 75$ MeV reveal large sensitivity to the magnitude of the in-medium nucleon-nucleon cross sections and little sensitivity to the compressibility of nuclear matter. Moreover, they exhibit strong dependence on the total momenta of the emitted proton pairs when the collision impact parameter is selected.

TWO-PROTON INTENSITY INTERFEROMETRY IN INTERMEDIATE ENERGY HEAVY-ION COLLISIONS

By

Wen Guang Gong

A DISSERTATION

Submitted to

Michigan State University

in partial fulfillment of the requirements

for the Degree of

DOCTOR OF PHILOSOPHY

Department of Physics and Astronomy

1991

ABSTRACT

TWO-PROTON INTENSITY INTERFEROMETRY IN INTERMEDIATE ENERGY HEAVY-ION COLLISIONS

By

Wen Guang Gong

Two-proton intensity interferometry has been studied both experimentally and theoretically in order to probe the space-time evolution of heavy-ion nuclear collisions at intermediate energy.

An approximate relation is derived which allows the calculation of the two-proton correlation function for any reaction model capable of predicting the single-particle phase-space distribution or the Wigner function in the exit channel. The sensitivity of two-proton correlation functions to source radii and lifetimes is illustrated by calculations with simple parametrizations. More realistic calculations are presented for two different regimes of emission time scales: slow particle evaporation from equilibrated compound nuclei, as predicted from the Weisskopf formula, and fast non-equilibrium particle emission in intermediate energy nucleus-nucleus collisions, as predicted from the Boltzmann-Uehling-Uhlenbeck transport equation.

Two-proton correlation functions have been measured at $\theta_{lab} \approx 25°$ for the "inverse kinematics" reaction $^{129}Xe + ^{27}Al$ at $E/A = 31$ MeV, and for the nearly symmetric reaction $^{129}Xe + ^{122}Sn$ at $E/A = 31$ MeV, for the "forward kinematics" reactions $^{14}N + ^{27}Al$ and $^{14}N + ^{197}Au$ at $E/A = 75$ MeV. For the reactions at 31 MeV per nucleon, the two-proton correlation functions do not exhibit maxima at $q = 20$

MeV/c, but only minima at q = 0 MeV/c. These correlations indicate emission on a slow time scale. They can be reproduced by calculations based on the Weisskopf formula for evaporative emission from fully equilibrated compound nuclei. For the reactions at 75 MeV per nucleon, the correlation functions exhibit pronounced maxima at relative momenta, q = 20 MeV/c, and minima at q = 0 MeV/c. These correlations indicate emission from fast, non-equilibrium processes. They are analyzed in terms of standard Gaussian source parametrizations and compared to microscopic simulations performed with the Boltzmann-Uehling-Uhlenbeck equation. For all reactions, the measured longitudinal and transverse correlation functions are very similar, in agreement with theoretical predictions.

Two-proton correlation functions predicted by the BUU model for the reaction $^{14}N + ^{27}Al$ at E/A = 75 MeV reveal large sensitivity to the magnitude of the in-medium nucleon-nucleon cross sections and little sensitivity to the compressibility of nuclear matter. Moreover, they exhibit strong dependence on the total momenta of the emitted proton pairs when the collision impact parameter is selected.

TWO-PROTON INTENSITY INTERFEROMETRY IN INTERMEDIATE ENERGY HEAVY-ION COLLISIONS

By

Wen Guang Gong

A DISSERTATION

Submitted to

Michigan State University

in partial fulfillment of the requirements

for the Degree of

DOCTOR OF PHILOSOPHY

Department of Physics and Astronomy

1991

ABSTRACT

TWO-PROTON INTENSITY INTERFEROMETRY IN INTERMEDIATE ENERGY HEAVY-ION COLLISIONS

By

Wen Guang Gong

Two-proton intensity interferometry has been studied both experimentally and theoretically in order to probe the space-time evolution of heavy-ion nuclear collisions at intermediate energy.

An approximate relation is derived which allows the calculation of the two-proton correlation function for any reaction model capable of predicting the single-particle phase-space distribution or the Wigner function in the exit channel. The sensitivity of two-proton correlation functions to source radii and lifetimes is illustrated by calculations with simple parametrizations. More realistic calculations are presented for two different regimes of emission time scales: slow particle evaporation from equilibrated compound nuclei, as predicted from the Weisskopf formula, and fast non-equilibrium particle emission in intermediate energy nucleus-nucleus collisions, as predicted from the Boltzmann-Uehling-Uhlenbeck transport equation.

Two-proton correlation functions have been measured at $\theta_{lab} \approx 25°$ for the "inverse kinematics" reaction $^{129}Xe + ^{27}Al$ at $E/A = 31$ MeV, and for the nearly symmetric reaction $^{129}Xe + ^{122}Sn$ at $E/A = 31$ MeV, for the "forward kinematics" reactions $^{14}N + ^{27}Al$ and $^{14}N + ^{197}Au$ at $E/A = 75$ MeV. For the reactions at 31 MeV per nucleon, the two-proton correlation functions do not exhibit maxima at $q = 20$

MeV/c, but only minima at q = 0 MeV/c. These correlations indicate emission on a slow time scale. They can be reproduced by calculations based on the Weisskopf formula for evaporative emission from fully equilibrated compound nuclei. For the reactions at 75 MeV per nucleon, the correlation functions exhibit pronounced maxima at relative momenta, q = 20 MeV/c, and minima at q = 0 MeV/c. These correlations indicate emission from fast, non-equilibrium processes. They are analyzed in terms of standard Gaussian source parametrizations and compared to microscopic simulations performed with the Boltzmann-Uehling-Uhlenbeck equation. For all reactions, the measured longitudinal and transverse correlation functions are very similar, in agreement with theoretical predictions.

Two-proton correlation functions predicted by the BUU model for the reaction $^{14}N + ^{27}Al$ at E/A = 75 MeV reveal large sensitivity to the magnitude of the in-medium nucleon-nucleon cross sections and little sensitivity to the compressibility of nuclear matter. Moreover, they exhibit strong dependence on the total momenta of the emitted proton pairs when the collision impact parameter is selected.

To

my father, Yong-quan Gong,

and

my mother, Guo-fang Wen.

ACKNOWLEDGEMENTS

I would like to express my deepest gratitude to Dr. Claus-Konrad Gelbke, first of all. This thesis would be simply impossible without his supervision, encouragement and support. Over past years, he has taught me what experimental nuclear reaction physics is about and how to become a good researcher, I have enjoyed the most working with him. His enthusiasm for scientific research, his insight into a problem, his understanding of people, his efficiency of working are held in my greatest respect. His influence on my career will be long-lasting.

I should thank Dr. Wolfgang Bauer, Dr. George F. Bertsch, Dr. William G. Lynch, Dr. Bernard Pope, and Dr. Michael F. Thorpe for serving kindly on my degree committee and giving generously critical advice and helpful suggestions. Without their work and time, it would be impossible to get my degree. In particular, Dr. Lynch has given plenty of advice and ideas from which I benefitted a lot, he helped my thesis experiment to make it a success. Dr. Bauer generously accepted to be in my oral committe during Dr. Lynch's absence. Dr. Bauer was an essential collaborator to perform the BUU calculations. Dr. Bertsch kindly recommended me twice to attend the Summer School in Nuclear Physics at Gull Lake (1989) and at Santa Cruz (1990) where I learned a lot of important nuclear physics and made many new friends.

I greatly appreciate the essential contributions from all of my collaborators. Dr. Giacomo Poggi helped me develop the CsI(Tl) detector. It was fun working with him who is nice and humorous. I especially appreciated his invitation and

hospitality for a recent visit to the INFN in beautiful Florence. Dr. Betty Tsang helped greatly during the experiment and taught me a lot about SMAUG. Dr. Josef Pochodzalla generously sent me many FORTRAN codes which were useful for calibrating CsI(Tl) detectors. Extremely productive was the collaboration with Dr. Scott Pratt who formulated the theoretical basis for calculating two-proton correlation functions. It was very fruitful and enjoyable to work with Drs. Dave Sanderson, Tetsuya Murakami, Nelson Carlin, Remualdo de Souza, Hongming Xu, Ziping Chen, and Yeongduk Kim at Michigan State University and Drs. Kris Kwiatkowski, Vic Viola, Sherry Yennello, R. Planeta, and Doug Fields from Indiana University who had helped me at various stages.

I am very grateful to Prof. J.S. Kovacs for attracting me through the CUSPEA program to study in the Physics Department and work at the National Superconducting Cyclotron Laboratory. I sincerely thank all the fellow students, staff and faculty members of the Physics Department and the Cyclotron Laboratory for the quality education and the excellent support that I have received. Particularly, I acknowledge a number of individuals who provided me with useful assistance from time to time: Jerry Nolen, Peter Miller and the whole operator crew who provided the first 4 GeV $^{129}Xe^{23+}$ beam for my experiment; John Yurkon and Dennis Swan at the Detector Lab.; Michael Maier and Jim Vicent at the Electronics Shop; Richard Au, Ron Fox and Babara Pollack at the Computer Dept.; Len Morris, Phil Fighter, and Steve Hickson at the Mechanical Design and Machine Shop; Rilla McHarris, Jackie Bartlett and Stephanie Holland for graphics and paper works. I greatly appreciate the letter of recommendation from Director Sam Austin. Furthermore, I am indebted to the friendship with David Bowman, Ziping Chen, Yuming Chen, Yibing Fan, Mingzhuan Gong, Rich Harkewicz, Yeongduk Kim, Yongsheng Li, Mike Lisa, Tapan Nayak, Graham Peaslee, Larry Phair, Bo Pi, Hongming Xu, Fan Zhu during my stay at MSU.

The last but not the least thanks should go to my dear family: my father and mother, my brother, my sister and brother-in-law for their love, understanding and support throughout my life. It is they who always value my education at the highest priority and encourage me to go forward. I am fortunate enough to meet Ms. Yiwen Wang who becomes my dearest friend. Her understanding and love has given me new strength to move on. She deserves my heartfelt thanks.

TABLE OF CONTENTS

LIST OF TABLES

LIST OF FIGURES

CHAPTER 1. INTRODUCTION

1.1 Intensity Interferometry

Interferometric measurements are of great importance and wide application in physics and astronomy [Mich 03, Hari 85, Swen 87, Boal 90]. In the early 19th century, the interference study by Young's double-slit experiment contributed to the establishment of wave theory of light, which seemed to settle down the Newtonian-Huyghensian controversy over the ultimate nature of light (vibratory wave or corpuscular particle) [Swen 87]. Several decades later, Michelson perfected the technique of interferometry to perform the famous 'aether drift' experiment in 1881 [Mich 03, Mich 27]. The null results obtained by him led to the rejection of the 'aether' concept and laid the foundation for the special theory of relativity. Two of the very important applications of Michelson's interferometer (an amplitude interferometer) were to measure the length of the Pt-Ir bar (which was then the international standard of meter) in terms of the wavelength of light in 1896 [Mich 03] and to measure the diameters of Betelgeuse and six other stars in 1920 [Hari 85].

A conceptually different interferometer (an intensity interferometer) was proposed by Hanbury Brown and Twiss in 1954 [Hanb 54]. To measure the angular size of stars (on the order of 10^{-4} arc second), the use of an amplitude interferometer had two difficulties. One was mechanical stability associated with a long base-line, the other was atmospheric turbulence which introduced random phase variation in the light-path. However, the intensity interferometer

enabled Hanbury Brown to overcome those difficulties and measure angular sizes of 32 stars accurately [Hanb 74].

Figure 1.1 shows the schematics of two types of interferometers: the amplitude interferometer and the intensity interferometer [Boal 90]. In an amplitude interferometer, particles or waves from the source are split by double slits (or beam splitter in Michelson's interferometer) into two paths. They interfere constructively or destructively at the detector or on the screen to give rise to fringe patterns. The measurement of fringe visibility and slit seperation can provide information on the angular size of source. In an intensity interferometer, two particles emitted from the source are detected in coincidence by two detectors. A correlation function $C(\vec{p}_1,\vec{p}_2)$ or $R(\vec{p}_1,\vec{p}_2)$ is generated as follows:

$$C(\vec{p}_1,\vec{p}_2) = 1 + R(\vec{p}_1,\vec{p}_2) = \frac{< n_{12} >}{<n_1> <n_2>}. \qquad (1.1)$$

Here n_{12} is the number of counts where particles are detected in coincidence by both detectors and $n_i (i=1,2)$ are the numbers of counts where particles are detected individually by each detector. Information on the source size can therefore be extracted from such correlation functions in a two-particle coincidence experiment.

While amplitude interferometry involves the one-particle probability, intensity interferometry measures the two-particle joint probability. As photons are indistinguishable bosons, the symmetrization of the two-photon wave function results in the two-photon correlations [Paul 86]. After its original application in astronomy [Hanb 74], two-photon intensity interferometry has recently been used [Frib 85] to study the process of parametric down-conversion [Burn 70] in which pump photons incident on a non-linear dielectric fission into two highly

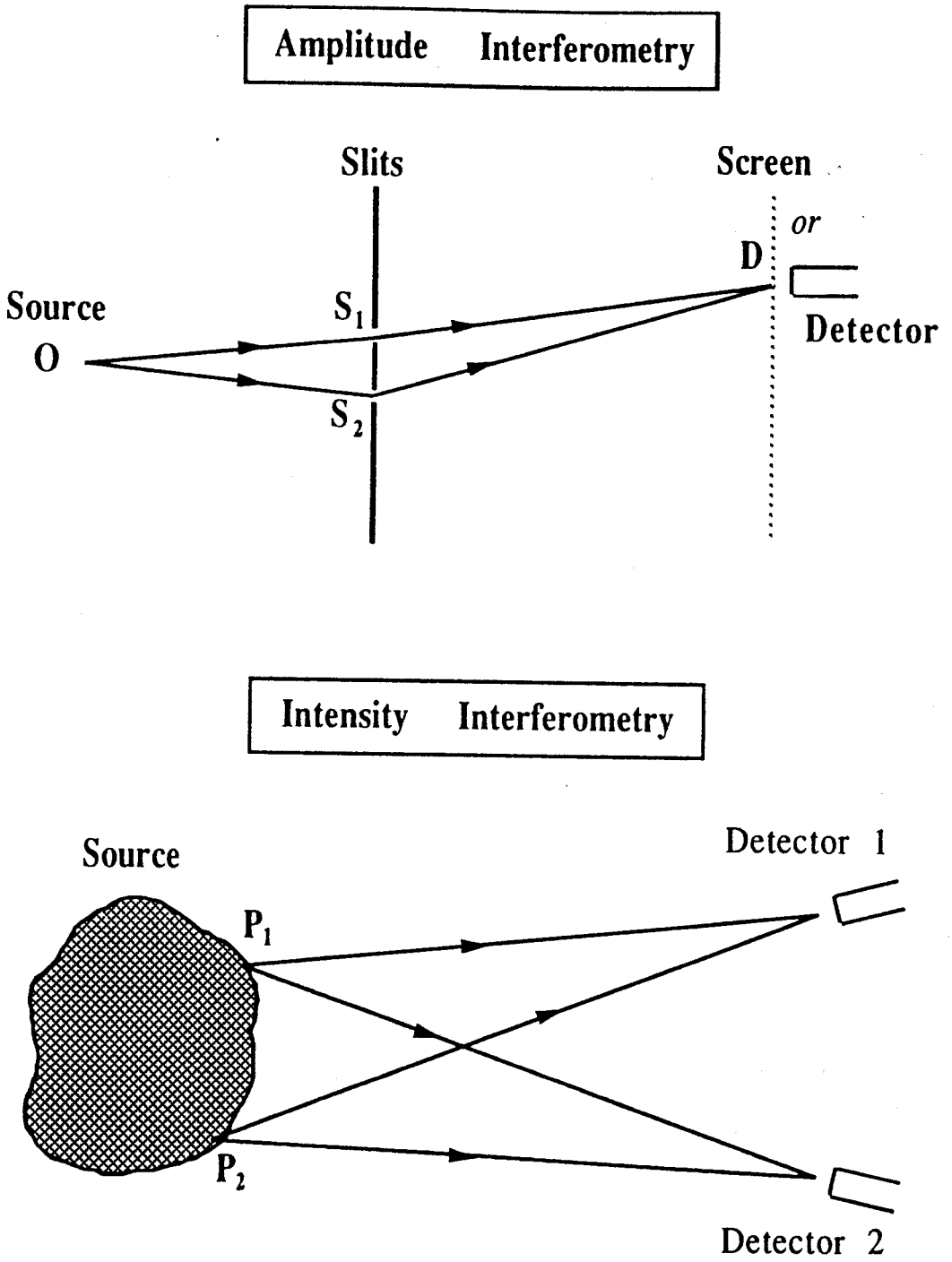

Figure 1.1: Schematic diagram of (1) an amplitude interferometer (upper part) and (2) an intensity interferometer (lower part).

correlated lower frequency signal and idler photons. The time interval between the signal and idler photons were accurately measured to be about 100fs [Hong 87]. Further experiments demonstrated the non-classical and non-local behaviors of photons [Ou 89, Ou 90]. Based upon two-particle interferometry technique, new experiments were proposed to test the fundamental question of completeness of quantum mechanics [Fran 89, Horn 89].

The study of pion correlations in proton-anti-proton annihilation by Golderhaber et. al [Gold 59, Gold 60] marked the first application of intensity interferometry using pions in subatomic physics. Since the origin of pion correlations was understood due to Bose-Einstein statistics, two-pion intensity interferometry was mostly referred to as Bose-Einstein correlation. Following extensive theoretical work [Shur 73, Cocc 74, Kopy 74, Yano 78, Gyul 79], two-pion intensity interferometry has become a valuable tool to study various properties such as chaoticity (the degree of incoherence), radius, lifetime and shape of the pion emitting source in elementary particle collisions as well as nuclear collisions [Boal 90]. Promisingly, it may be able to probe the formation of quark-gluon plasma which is a new state of matter to be created in the ultra-relativistic heavy-ion collisions [Bert 89].

Two-proton intensity interferometry was put forward by Koonin in order to probe the space-time structure of the collision dynamics in medium-to-high energy nuclear reactions [Koon 77]. Since protons are fermions, the anti-symmetrization of two-proton wavefunctions results in an anti-correlation. However, two-proton correlations are mainly dominated by correlations resulting from final state interactions including strong and Coulomb interactions. It was shown that the shape of two-proton correlation functions at small relative momenta (less than 50MeV/c) is very sensitive to the source size. Two-proton correlations have subsequently been measured to investigate the space-time

characteristics of the emitting source in heavy-ion induced reactions at a wide range of energies [Boal 90].

1.2 Intermediate Energy Heavy-Ion Collisions

Heavy-ion collisions at intermediate energy (E/A=20-200MeV) has become an active area of research using heavy-ion accelerators [Gelb 87, Bord 90, Greg 86]. The goal of research is to understand the thermodynamical properties of nuclear matter under extreme conditions and the nuclear dynamics leading to thermal equilibration. It is a difficult and challenging task because of the unique complexity involved with the finite nuclear system which interacts strongly and evolves on a very short time scale.

The dynamics and thermodynamics of nucleus-nucleus collisions are largely governed by the bombarding energy and the impact parameter. At low energy of a few MeV per nucleon, heavy-ion collisions are dominated by the nuclear mean field and one-body dissipation. Peripheral collisions are characterized by quasi-elastic and deeply inelastic collision. Central collisions lead to complete fusion of projectile and target, and the process can be well described by the formation of compound nucleus and its decay by statistical evaporation of particles and γ-rays [Birk 83].

Relativistic heavy-ion collisions at high energy ($E/A \geq 0.5$ GeV) are dominated by individual nucleon-nucleon collisions as the nucleon mean-free path becomes short and comparable to nucleonic size. The geometrical concept in the participant-spectator model proves to be valid. Thermal equilibrium may be rapidly obtained within the volume of participant nucleons to which statistical models may be applicable [DasG 81, Cser 86, Stoc 86, Stöc 86].

Heavy-ion collisions at intermediate energy represent the transition region in which both nuclear mean field and nucleon-nucleon collsions are important. The incomplete fusion model combines mechanisms of both low energy and high energy collisions. The partially fused system can be highly excited. As the

emission of particles prior to the attainment of full statistical equilibrium of the composite system is observed to be important, it remains an open question to know accurately how much excitation energy is deposited into the composite system. The knowledge of the excitation energy is essential to determine the decay of the system in a statistical approach. At low excitation energy, the excited system undergoes binary sequential decays. As the excitation energy increases, multi-fragment emissions become important. At even higher excitation energy, the system may approach its limit of stability and explode into its constituents. A nuclear liquid-gas phase transition of the excited system is expected to occur. Therefore, systematic study of the final products of collisions can provide information on the properties of hot nuclei of temperature T=0-10MeV and density of approximately 0.1 to 1.5 times normal nuclear density.

Significant progress has been made recently in both experimental measurements and theoretical studies to understand intermediate energy heavy-ion collisions. More exclusive experiments were carried out to measure most of the final reaction products including γ rays, neutrons, light charged particles, intermediate mass fragments and fission fragments using high efficiency detector arrays and/or 4π detectors [Tsan 89, Kim 89, Pias 91, Bowm 91, DeSo 91, Sobo 91]. A complete characterization of the final states of the collsion may be possible experimentally. Microscopic models have been based upon computer simulations of the transport equation of nucleons under the influence of nuclear mean field, nucleon-nucleon collision, and phase-space blocking due to Pauli principle [Bert 88]. They provided useful insights into the dynamics leading to statistical thermalization. To extract any information on the thermodynamical property of nuclear matter (e.g. the nuclear equation of state) from the measurement of reaction products, we need a good understanding of both the dynamical and the statistical aspects of the collision and develop and test microscopic models capable of describing the space-time evolution of the reaction.

We have exploited the two-proton correlation function as an observable to test space-time geometries of intermediate energy heavy-ion collisions predicted by dynamic models such as the Boltzmann-Uehling-Uhlenbeck model, as it was originally proposed in Reference [Koon 77].

1.3 Two-proton Intensity Interferometry

Two protons, emitted at small relative momenta from an excited nuclear system, carry information about the space-time characteristics of the emitting source since the relative two-proton wave function reflects the interplay of the mutual Coulomb and nuclear interactions and the exclusion due to Pauli principle [Boal 90, Koon 77, Prat 87, Gong 91a]. The attractive S-wave nuclear interaction leads to a pronounced maximum in the two-proton correlation function at relative momentum, $q \approx 20$ MeV/c, when the average distance upon emission is of the order of 10 fm or less. The long-range Coulomb interaction and the Pauli exclusion principle give rise to a minimum at $q \approx 0$ MeV/c. The detailed shape of two-proton correlation functions has to be calculated by incorporating correctly all the physical ingredients.

The average distance between the two protons upon emission depends on the spatial dimension and the lifetime of the emitting system. Consider two protons with an average velocity, v, emitted from a static source of radius, r, and lifetime, τ. After emission, the separation between the two protons is $r+v\tau$. For the decay of equilibrated compound nuclei with temperatures below 5 MeV, estimated emission times are larger than several hundred fm/c [Frie 83]. As a consequence, the average distance between emitted protons is much larger than the size of the emitting nucleus and the effects of the Coulomb interaction and the Pauli principle should dominate. On the other hand, non-equilibrium proton emission in intermediate energy heavy-ion collisions is calculated to proceed on much shorter time scales [Aich 85, Cass 88] and average proton separations may

reflect the spatial dimension of the emitting system rather than the emission rate. Here, the nuclear interaction should be prominent.

Figure 1.2 illustrates the apparent sources expected for emission from short-lived and long-lived nuclear systems [Bert 89]. For correlations at small relative momenta, the detected protons have nearly the same final momenta directed towards the detection system. The dots in the figure illustrate the locations of protons moving towards the detector with a given momentum, $\vec{p}$. Protons emitted from a short-lived source (upper part) occupy a small region of space, but protons emitted from a long-lived source (lower part) occupy a large and elongated region of space [Prat 87, Awes 88, Bert 89]. The direction of elongation is along the direction of $\vec{p}$. In general, reduced correlations are expected for emission from long-lived sources due to the larger apparent source size. Moreover, for an elongated source, the Pauli anti-correlation should be less in the longitudinal (elongated) direction than in the transverse (non-elongated) direction due to the directional dependence of anti-symmetrization effects [Koon 77, Prat 87, Awes 88] which are important for $|\vec{q}\cdot\vec{r}| \approx h$, where $\vec{q}$ and $\vec{r}$ denote the relative momentum and position vectors upon emission. The longitudinal correlation function (for which the relative momentum, $\vec{q} = \frac{1}{2}(\vec{p}_1 - \vec{p}_2)$, is parallel to total momentum, $\vec{P} = \vec{p}_1 + \vec{p}_2$) of a long-lived source may therefore be enhanced as compared to the transverse correlation function (for which $\vec{q}$ is perpendicular to $\vec{P}$), unless the apparent source region becomes so large that sensitivity to anti-symmetrization effects is lost.

1.4 Motivation

In most measurements of two-proton correlation functions, implicit summations over the relative angle, $\Psi = \cos^{-1}(\vec{P}\cdot\vec{q}/Pq)$, between relative and total momenta of the proton pair were performed. While such measurements did not explore the shape of the source function, they did corroborate the qualitative expectations based upon the lifetime arguments outlined above. Two-proton

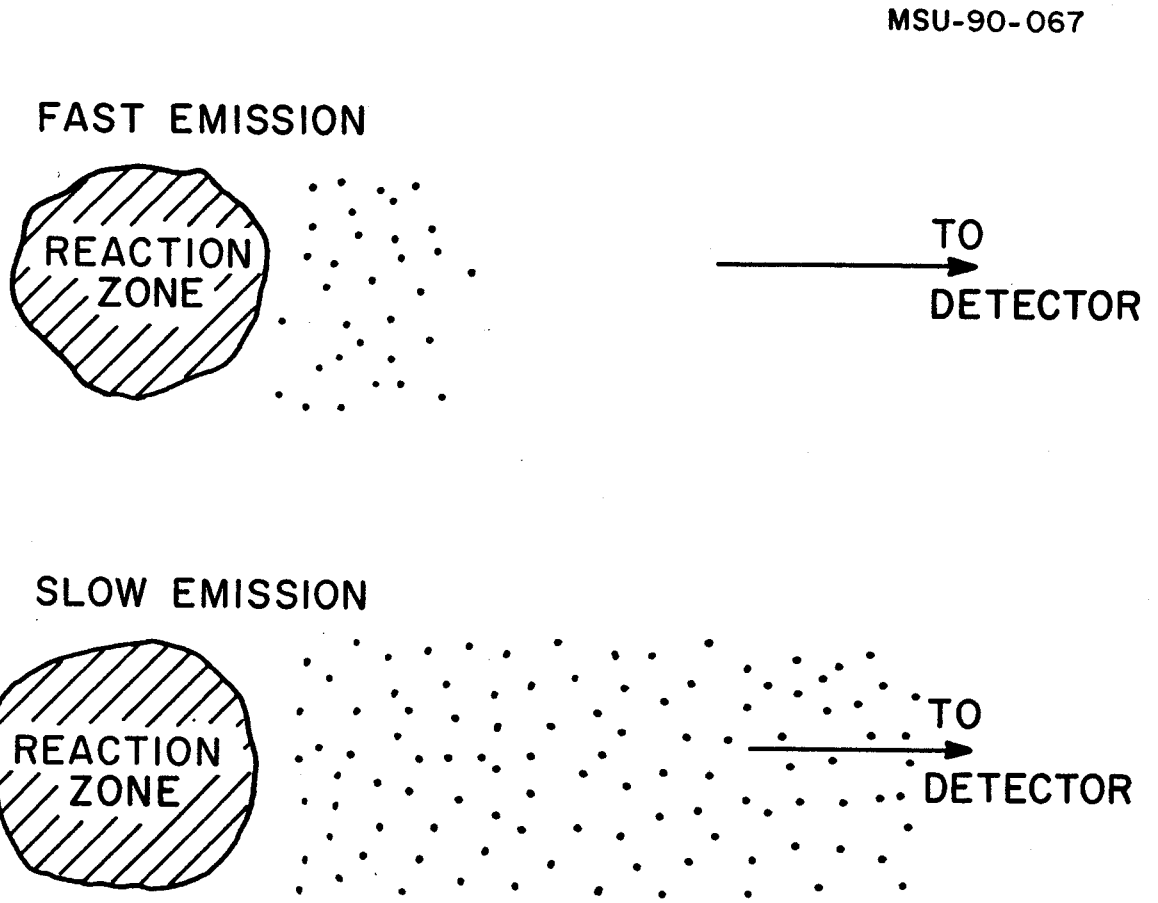

Figure 1.2: Illustration of source functions for emission from short-lived (upper part) and long-lived (lower part) nuclear systems. The dots indicate the locations of protons of a given momentum after the last proton has been emitted.

correlation functions measured in kinematic regions dominated by evaporation from equilibrated reaction residues [DeYo 89, Ardo 89, DeYo 90, Gong 90b] exhibit a minimum at q≈0 MeV/c, but no maximum at q≈20 MeV/c. The shapes of these correlation functions could only be described by assuming emission from long-lived compound nuclei or, alternatively, from short-lived systems of unphysically large dimensions. In contrast, two-proton correlation functions measured in kinematic regions dominated by fast non-equilibrium emissions exhibit a clear maximum at q≈20 MeV/c [Zarb 81, Lync 83, Gust 84, Poch 86, Chen 87a, Chen 87b, Poch 87, Fox 88, Awes 88, Cebr 89, Queb 89, Gong 90b, Gong 90c] which becomes more pronounced with increasing kinetic energy of the emitted protons [Lync 83, Poch 86, Chen 87b, Poch 87, Awes 88, Gong 90b, Gong 90c]. The shapes of these correlation functions could be described in terms of short-lived sources with dimensions comparable to those of the respective compound nuclei; emission from systems with even smaller dimensions was required for the description of correlation functions measured for the most energetic protons [Lync 83, Poch 86, Chen 87b, Gong 91b].

More recently, longitudinal and transverse correlation functions were measured, both for non-equilibrium [Awes 88] as well as equilibrium emissions [Ardo 89, Gong 90b]. None of these investigations found definitive evidence for elongated source shapes. For the case of equilibrium emission, these findings were shown to be consistent with theoretical correlation functions predicted by the Weisskopf formula for evaporation from equilibrated compound nuclei [Ardo 89, Gong 90b].

In order to elucidate similarities and differences of two-proton correlation functions for equilibrium and non-equilibrium emission processes, we performed measurements at $\theta_{lab} \approx 25°$ for ^{14}N induced reactions on ^{27}Al and ^{197}Au at E/A = 75 MeV and for ^{129}Xe induced reactions on ^{27}Al and ^{122}Sn at E/A = 31 MeV. When light projectiles impinge on heavy target nuclei, emission at forward

angles is dominated by non-equilibrium processes and emission at backward angles is dominated by equilibrium processes [Poch 87, Queb 89, Ardo 89]. Taking advantage of this angular dependence, we studied non-equilibrium emission in "forward kinematics" for the reactions $^{14}N + ^{27}Al$ and $^{14}N + ^{197}Au$ at E/A = 75 MeV and equilibrium emission in "inverse kinematics" for the reaction $^{129}Xe + ^{27}Al$ and for the nearly-symmetric reaction $^{129}Xe + ^{122}Sn$ at E/A = 31 MeV. The measurements were performed with identical detector geometries, energy calibrations and energy thresholds.

Two-proton correlation functions have been calculated by applying the Wigner function formalism [Koon 77, Prat 87, Gong 91a] to one-body phase-space distribution predicted by the Boltzmann-Uehling-Uhlenbeck transport equation as well as the Weisskopf formula. Comparisons between the measured and calculated two-proton correlation functions provide tests of the space-time structure of specific reaction models. Non-equilibrium emission predicted with good numerical accuracy $^{14}N + ^{27}Al$ reaction at E/A = 75 MeV. Particle emission rates predicted by the Weisskopf formula were tested for the ^{129}Xe induced reactions at E/A = 31 MeV.

1.5 Organization

In Chapter 2, we describe various tests and performances of the CsI(Tl) detetctor developed for this experiment. Details of the experimental setup are outlined in Chapter 3. Subsequently, Chapter 4 explains the data analysis procedures for particle identification, energy calibration, time-walk correction and detector efficiency correction.

In Chapter 5, the inclusive single-proton cross sections are shown. They are fitted in terms of moving-source parametrizations and compared to BUU model predictions for pre-equilibrium emissions in reactions $^{14}N + ^{27}Al$ and $^{14}N + ^{197}Au$ at E/A =75 MeV.

In Chapter 6, we present a brief derivation of the Wigner function formalism which relates the two-particle correlation function to the single particle Wigner function. The sensitivity of two-proton correlation functions to source radii and emission time scales is illustrated by performing calculations for a number of simple source parametrizations. Approximations underlying the Wigner function formalism are examined in comparison with the classical trajectory calculations.

The measured two-proton correlation functions are presented in Chapter 7 and analyzed in terms of Gaussian sources of negligible lifetime to allow comparisons with previous measurements.

Chapter 8 gives a brief review of the Weisskopf formula used for the calculation of particle evaporation from equilibrated compound nuclei, together with some numerical results. The measured two-proton correlation functions for equilibrium emissions are compared to predictions of the Weisskopf evaporation model.

In Chapter 9, we begin with a brief review of the basic assumptions underlying the derivation of the Boltzmann-Uehling-Uhlenbeck transport equation, and then discuss the impact parameter averaging procedure and a few numerical calculations. The measured two-proton correlation functions for non-equilibrium emissions are compared to predictions of the BUU model. We further explore the sensitivity of predicted two-proton correlation functions to the equation of state of nuclear matter, in-medium nucleon-nucleon cross section and the impact parameter of the collision.

A summary and conclusions are finally given in Chapter 10. Most results of this thesis were published in referred journals [Gong 88, Gong 90a, Gong 90b, Gong 90c, Gong 91a, Gong 91b, Gong 91c].

CHAPTER 2. THE CSI(TL) DETECTOR

2.1 General Considerations

The study of intermediate energy heavy-ion reactions often requires the detection of light charged particles (p, d, t, α, ...) emitted with energies ranging from the exit channel Coulomb barriers up to several hundred MeV. For moderate resolution requirements, plastic scintillators are adequate. Better resolution can be obtained with inorganic scintillators such as NaI(Tl), for which energy resolutions of the order of one percent have been achieved for light charged particles of about 100 MeV energy [Poch 87].

Particle detectors using NaI(Tl) scintillators have a number of disadvantages. The crystals are hygroscopic and must be hermetically sealed, typically with a thin entrance window (≈ 8μm Havar). Small pinholes in the entrance window can lead to deteriorations of the detectors with time when they are stored in air. The use of thicker entrance windows leads to higher detection thresholds and a loss of resolution. The detectors usually employ photomultipliers for photon detection. In general, photomultipliers exhibit rather poor long-term stability. Although it is possible to monitor gain drifts with accuracies of the order 1%, the procedures used are rather time consuming and cumbersome [Chit 86b, Poch 87].

The use of CsI(Tl) scintillators promises to overcome some of these difficulties [Knol 89, Gras 85a]. The crystals have superior thermal and mechanical properties (see Table 2.1). Since they are only slightly hygroscopic, they do not have to be hermetically sealed. Furthermore, their spectral response is well matched to that of silicon photodiodes [Gras 85a] which exhibit excellent

Table 2.1: Properties of NaI(Tl) and CsI(Tl) scintillators.

Scintillator	CsI(Tl)	NaI(Tl)	Units
Maximum Emission Wavelength, λ_{max}	540	415	nm
Refractive Index @λ_{max}	1.80	1.85	
Pulse 10-90% Rise Time	4.0	0.5	μs
Decay Constant, τ_f/τ_s	0.4-0.7/7.	0.23	μs
Total Light Yield	52000	38000	Photons/MeV
$(dE/dx)_{min}$	5.6	4.85	MeV/cm
Radiation Length, X_0	1.86	2.59	cm
Hardronic Interaction Length, λ	36.4	41.3	cm
Specific Gravity, ρ	4.51	3.67	gm/cm^3
Melting Point, T_m	621	651	^0C
Hygroscopicity	slightly	yes	
Thermal and Mechanical Resistance	excellent	poor	

long-term stability (see Figure 2.21 below) when read out with good quality charge sensitive preamplifiers [Bluc 86]. A number of investigations using small volume crystals have pointed out these generally attractive features [Vies 86, Meij 87, Kreu 87, Gras 85a, Gras 85b]. In fact, energy resolutions of the order of 1% were reported for α-particles of 100 MeV energy [Vies 86]. However, the use of CsI(Tl) scintillator does have obvious disadvantages due to rather slow time response of the scintillator. The detector usually has poor time resolution and count-rate tolerance.

At the beginning of our detector development, we tested a small volume CsI(Tl) scintillator ($1\times2\times4cm^3$) read out by a PIN diode of $1\times1cm^2$ active area using a commercial charge-sensitive preamplifier (Canberra 2003). Standard electronics was set up with a amplifier (Tennelec TC241) and a Multi-Channel-Analyzer (Canberra MCA-85). Figure 2.1 shows the measured energy spectrum of γ-rays from a ^{60}Co radioactive source. The FWHM resolutions are 6.0%, 5.6%, and 4.4% for E_γ = 1.173 MeV, 1.332 MeV, and 2.505 MeV, respectively. The inset magnifies the pile-up peak originated from two lower energy γ-rays detected in the crystal in coincidence. We built another detector by using a cubic CsI(Tl) crystal ($2\times2\times2cm^3$), a larger PIN diode of $2\times2cm^2$ active area, and a homemade charge-sensitive preamplifier. The γ-ray energy spectra measured with this detector is shown in Figure 2.2 for a ^{137}Cs source (E_γ = 0.662 MeV) (upper part) and for a ^{60}Co source (E_γ = 1.173, 1.332 MeV) (lower part). Indicated in the figure are the FWHM energy resolutions, which are very comparable to the energy resolutions of the γ-rays measured by a standard NaI(Tl) detector read out by a photomultiplier tube [Gras 85a]. Assuming that the total resolution (σ_{tot}) consists of the intrinsic resolution (σ_{intr}) and the electronic noise (σ_{noise}), we obtained that $\sigma_{intr} = \sqrt{(\sigma_{tot})^2-(\sigma_{noise})^2}$. In the upper part of Figure 2.2, for an example, σ_{tot} = 59 keV, σ_{noise} = 46 keV, and then σ_{intr} = 37 keV. The intrinsic detector resolution is somewhat less than the electronic noise level of the pre

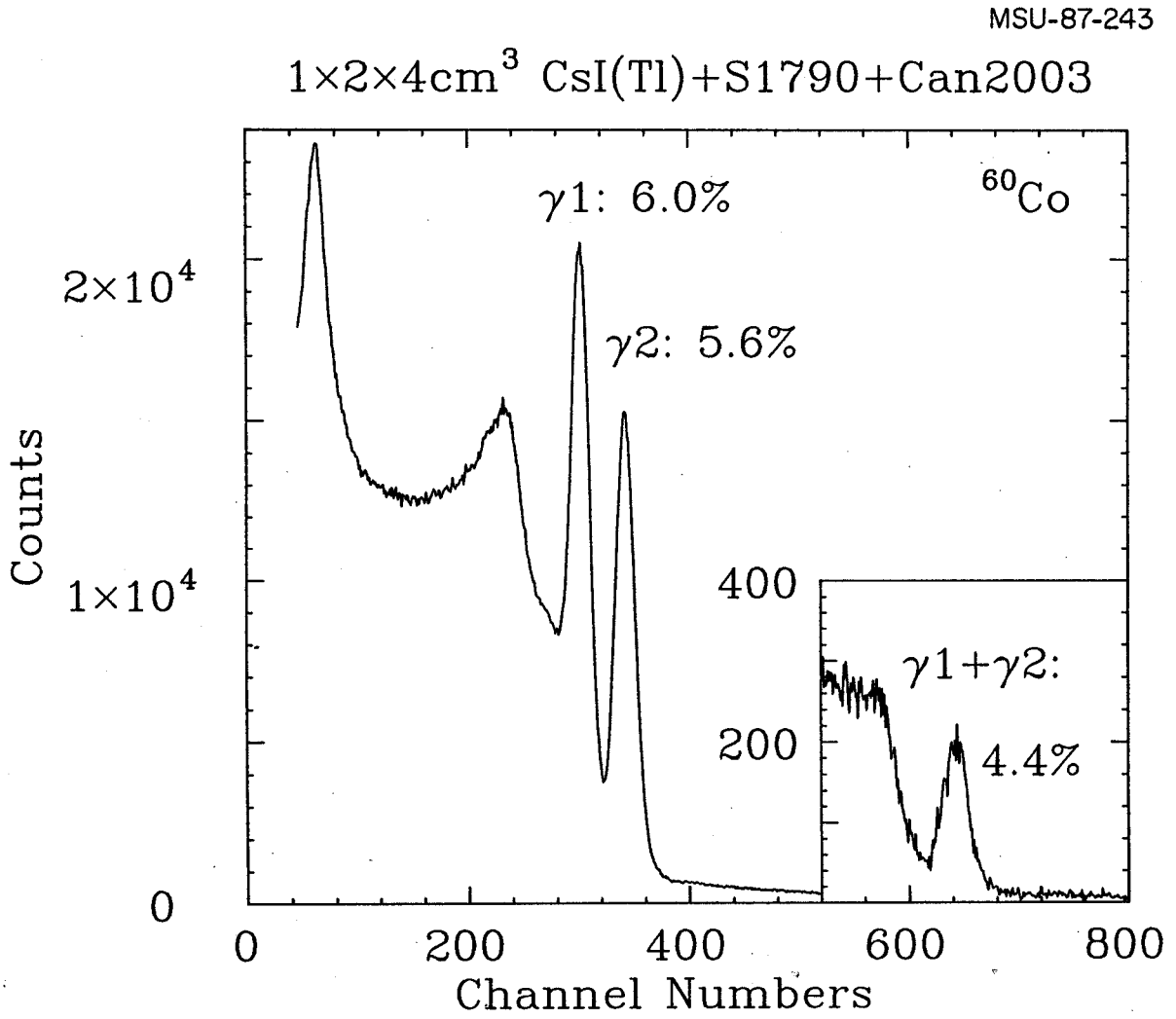

Figure 2.1 : Measured energy spectrum of γ-rays from a ^{60}Co source with a small volume CsI(Tl) scintillator (1×2×4 cm^3) read out by a Hamamatsu PIN diode (S1790: 1×1 cm^2), where a commercial charge-sensitive preamplifier (Canberra 2003) was used.

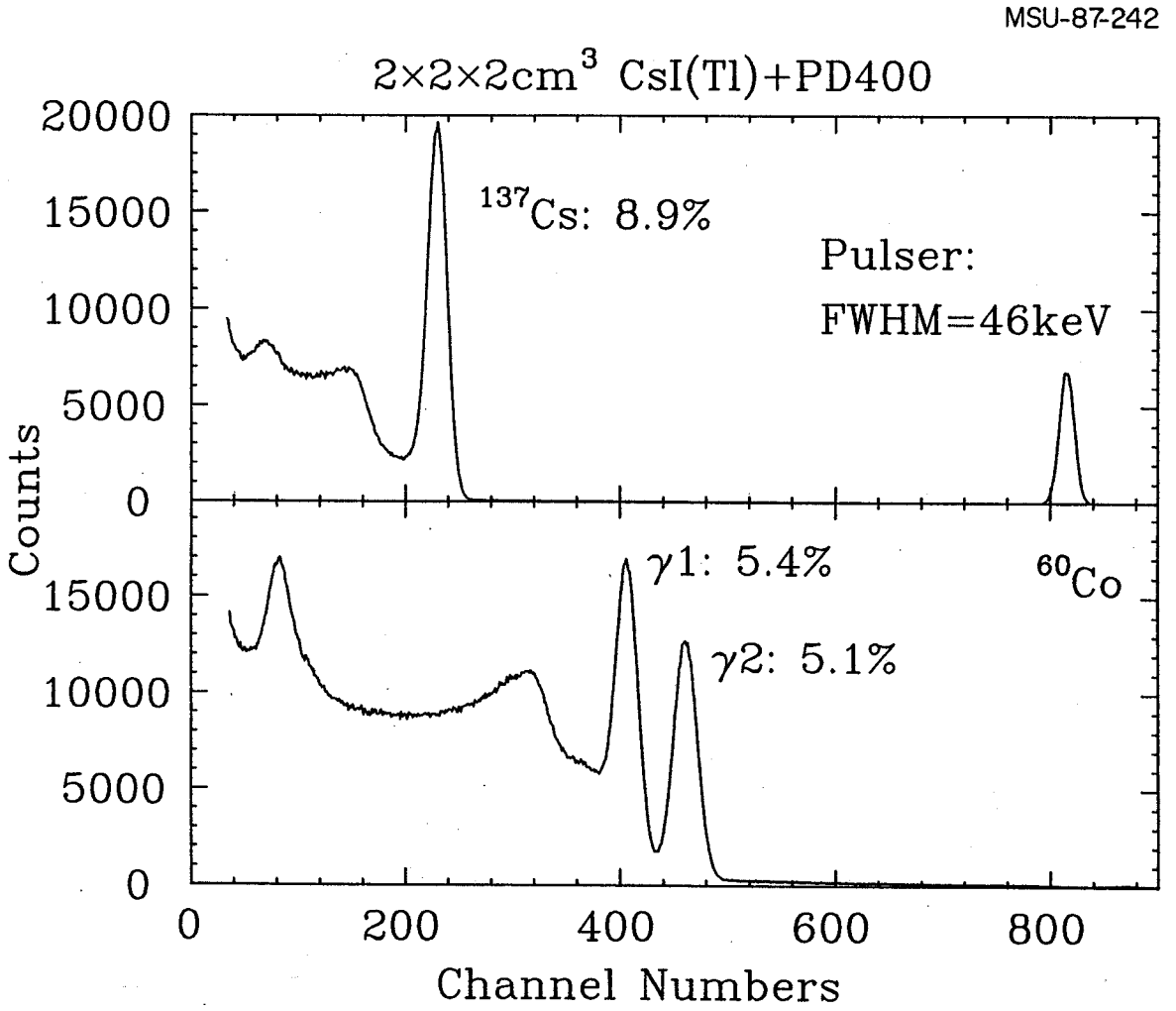

Figure 2.2 : Measured energy spectra of γ-rays from a ^{137}Cs source (upper part) and a ^{60}Co source (lower part) with a small cubic CsI(Tl) crystal (2×2×2 cm^3) read out by a Hamamatsu PIN diode (2×2 cm^2), where a homemade charge-sensitive preamplifier was used.

-amplifier. Reduction of the electronic noise in the preamplifier should lead to even better detector resolution.

Though small volume CsI(Tl) crystals have demonstrated excellent detection resolution, our objective is to use rather large volume cylindrical crystals of typical dimensions of 38 mm diameter and 100 mm length for a 56 element detector array. We have performed detailed resolution tests for a number of large volume CsI(Tl) scintillators read out by a $2\times2cm^2$ PIN diode. Resolutions of 1% have been achieved for protons of 50 MeV. However, in general, the resolution was found to be limited by local nonuniformities causing variations of the scintillation efficiency of several percent.

2.2 Description of the CsI(Tl) Detector.

Our CsI(Tl) crystals were manufactured by BICRON corporation. They are cylinders of identical physical dimensions (diameter = 38 mm, length = 100 mm), which can stop, for example, protons up to energies of about 190 MeV and alpha particles up to energies of about 780 MeV.

The structure of the CsI(Tl) detector is depicted in Figure 2.3. We used a clear lucite light guide of 12 mm length connected to the rear flat surface of the CsI(Tl) crystal which had been polished with a tissue moistened with alcohol. Good optical coupling with sufficient mechanical rigidity was obtained using RTV 615 silicon rubber for the interfaces between the CsI(Tl) crystal and the light guide, and between the light guide and the photon detectors. Most measurements were performed using a square shaped PIN diode of $2\times2cm^2$ active area for photon detection. In several instances, the diode was replaced by a photomultiplier with a circular photocathode of 38 mm diameter to verify that our results were not an artefact of the square geometry of the active area of the PIN diode.

The detailed response of the detector assembly depends on the treatment of the scintillator surface. Some of our test results will be discussed in the next

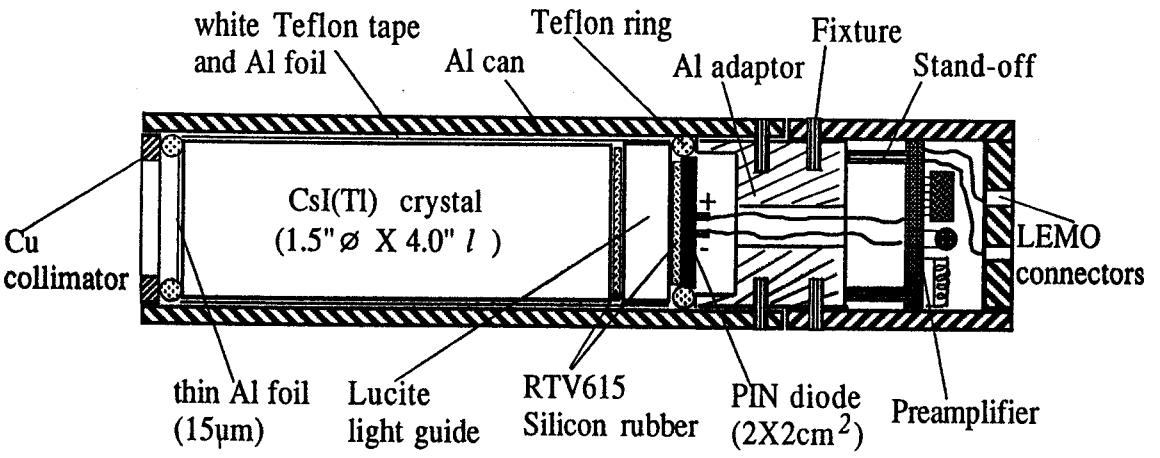

Figure 2.3 : Anatomic diagram of the CsI(Tl) detector.

section. Our standard treatment consists in sanding with fine paper (#320-#400) all the outer surfaces of the assembly (i.e. crystal and light guide). The sides are sanded by movements parallel to the cylinder axis; the front surface is sanded by circular motions. Teflon tape is wrapped around the sides of the detector assembly; the front face of the crystal is covered by an aluminum foil of 15 μm thickness. A light intransparent aluminum foil is wrapped around the layers of teflon tape. The detector is then inserted into an aluminum can which provides mechanical protection and the housing of the preamplifier.

Our $2\times2cm^2$ PIN diode is a prototype supplied by Hamamatsu corporation. It has a leakage current of about 5 nA at room temperature and at an operating bias of 60 V. Because of slight heating, operation in vacuum resulted in an increase of leakage current. In our detector array, cooling lines were installed to remove excessive heat and maintain the detectors at constant temperature (about 15 °C). It was measured [Gras 85a] that the temperature dependence of the light yield of CsI(Tl) scintillator read out by photodiode shows a flat maximum around 30-40 °C and has a temperature coefficient of 0.3%/ °C at 20 °C. The diode has a capacitance of 135 pF at full bias. Its area-to-capacitance ratio is better by about a factor of two as compared to the standard $1\times1cm^2$ PIN diodes such as the Hamamatsu S1723 and S1790 diodes. For low level signals one can expect an improved signal-to-noise ratio. However, the actual improvement does not track the area-to-capacitance ratio because the use of a larger diode of area comparable to that of the light guide results in a non-negligible reduction of the reflecting surface of the light guide (which is wrapped with teflon tape). The signals measured with the $2\times2cm^2$ PIN diode were about a factor of 2 larger than those measured with $1\times1cm^2$ PIN diodes.

The photodiode was furnished without a protecting window at the front face. We, therefore, applied an optically clear epoxy (EPO-TEK 301-2, by Epoxy Technology Inc.) to the surface of the PIN diode to protect the silicon wafer and

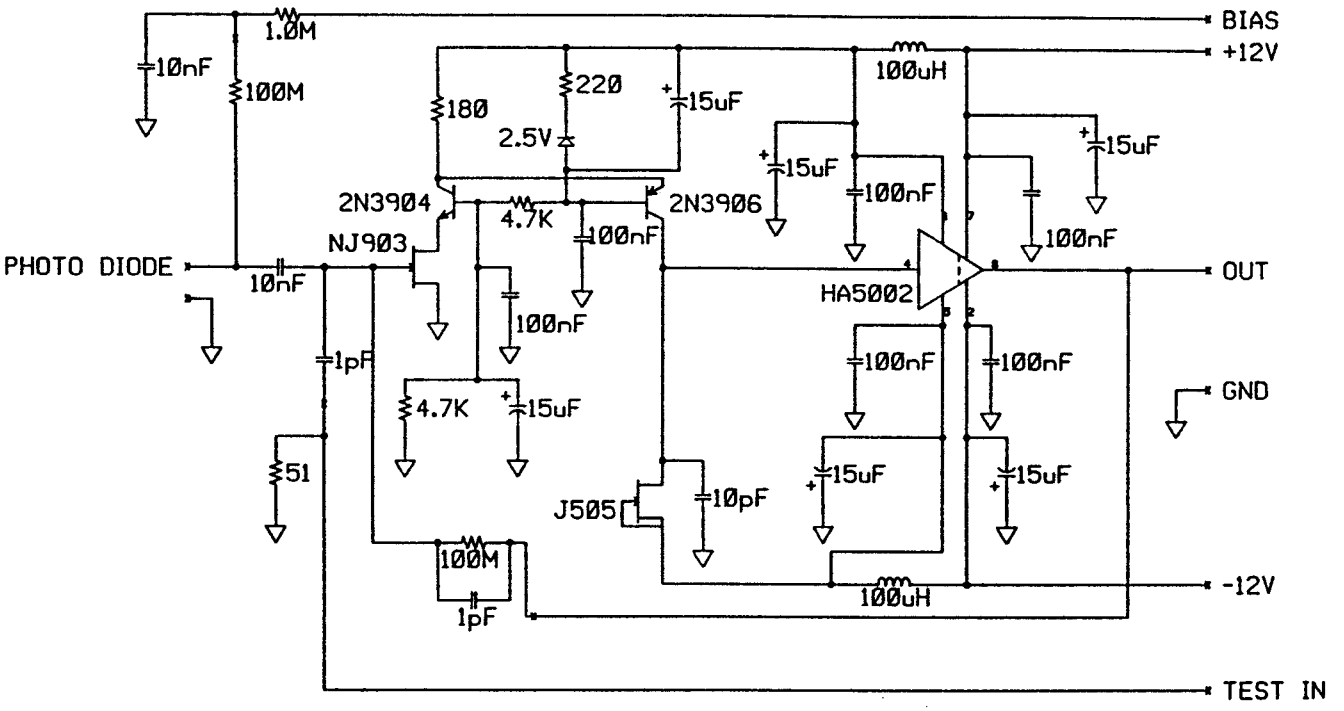

Figure 2.4: Schematics of the preamplifier used for the readout of the PIN diode. The preamplifier is mounted on a circuit board of 38 mm diameter.

allow repeated optical couplings with different detectors. To provide the necessary mechanical stability, the diode was mounted on a substrate made of Boron Nitride. The diodes were operated for months without measurable deterioration of its performance.

A low cost preamplifier of good resolution and low power dissipation was designed by M.R. Maier at the NSCL and its schematics is shown in Figure 2.4. Its risetime of $\tau_r = 0.2$ μs is smaller than the fast decay component of the fluorescent light of CsI(Tl) (about 0.4 μs). The power dissipation of 0.5 watt is sufficiently low to allow operation of the preamplifier in vacuum without overheating the diode. The preamplifier noise at full-width-half-maximum (FWHM) corresponds to a charge of 2000 electrons using an input capacitance of 130 pF and a shaping time constant of 1.4 μs for the subsequent amplification with a spectroscopy amplifier. For our CsI(Tl) detector assembly, this noise figure corresponds to a resolution of about 300 keV for α-particles of 5.5 MeV, the exact value depending on the light output of individual crystals.

2.3 Resolution Test of Individual Detectors

In this section, we describe a series of tests for a number of crystals concerning their resolution for energetic light particles and the position sensitivity of the detector response. For these measurements a ΔE surface barrier detector of 400 μm thickness and 450 mm^2 active area (ORTEC TB-27-450-400) was placed in front of the CsI detecor. In order to unambiguously identify intrinsic properties of individual crystals each crystal was provided with a well defined frame of reference, which was kept fixed with respect to the individual crystal throughout our measurements. Our choice of reference frame is depicted in Figure 2.5.

For the purpose of book-keeping the crystals were labelled with numbers. We present representative results obtained for detectors #1 and #3 during test runs with energetic light particles and from bench tests with collimated radioactive sources.

For the bench test, we used a ^{137}Cs γ-ray source which was collimated by a 3 mm diameter lead collimator of about 6 cm thickness. The collimated γ-ray source was mounted on a movable platform. The position of the collimator was determined with an accuracy of better than 0.05 mm. During these measurements the position of the CsI-detector was kept fixed. The measurements were performed with semi-gaussian pulse shaping using a peaking time of 6μs for the main amplifier. Typically, the FWHM resolution for the 662 keV line of ^{137}Cs was of the order of 25%; it is affected by photon statistics and electronic noise. Therefore, these measurements had to be performed with good statistical accuracy. For an accurate determination of the peak position, it was necessary to subtract the background due to noise and Compton scattering. Because of the excellent stability of the PIN diode, peak shifts of less than 0.2 % could be detected by measuring the ^{137}Cs peak with high statistical accuracy (typically larger than 2×10^4 counts in the photopeak).

Most measurements of detector responses were performed with a beam of 96 MeV α-particles delivered by the K500 cyclotron of the NSCL. For these measurements, the CsI(Tl) crystals were mounted as the stopping detectors of ΔE-E telescopes, the ΔE detector being a 400 μm thick silicon surface barrier detector with an active area of 450 mm^2. Gold and polycarbon, $(CH_2)_n$, targets of 2 and 1 mg/cm^2 thickness were used to obtain alpha particles and protons of known energy. The scattered particles were collimated by a 12.5 mm thick block of copper with a circular hole of 3 mm diameter. For these measurements, the position of the collimator was kept fixed in the laboratory and the telescope was moved with respect to the collimator exposing different points of the detector entrance window to scattered particles of fixed energy. The distance between the collimator and the target was 40 cm; the kinematic smearing for recoil protons was less than 1% in all cases. The absolute resolution of the ΔE-silicon detector ($\leq$50 keV) is considerably better than that of the CsI(Tl) detector.

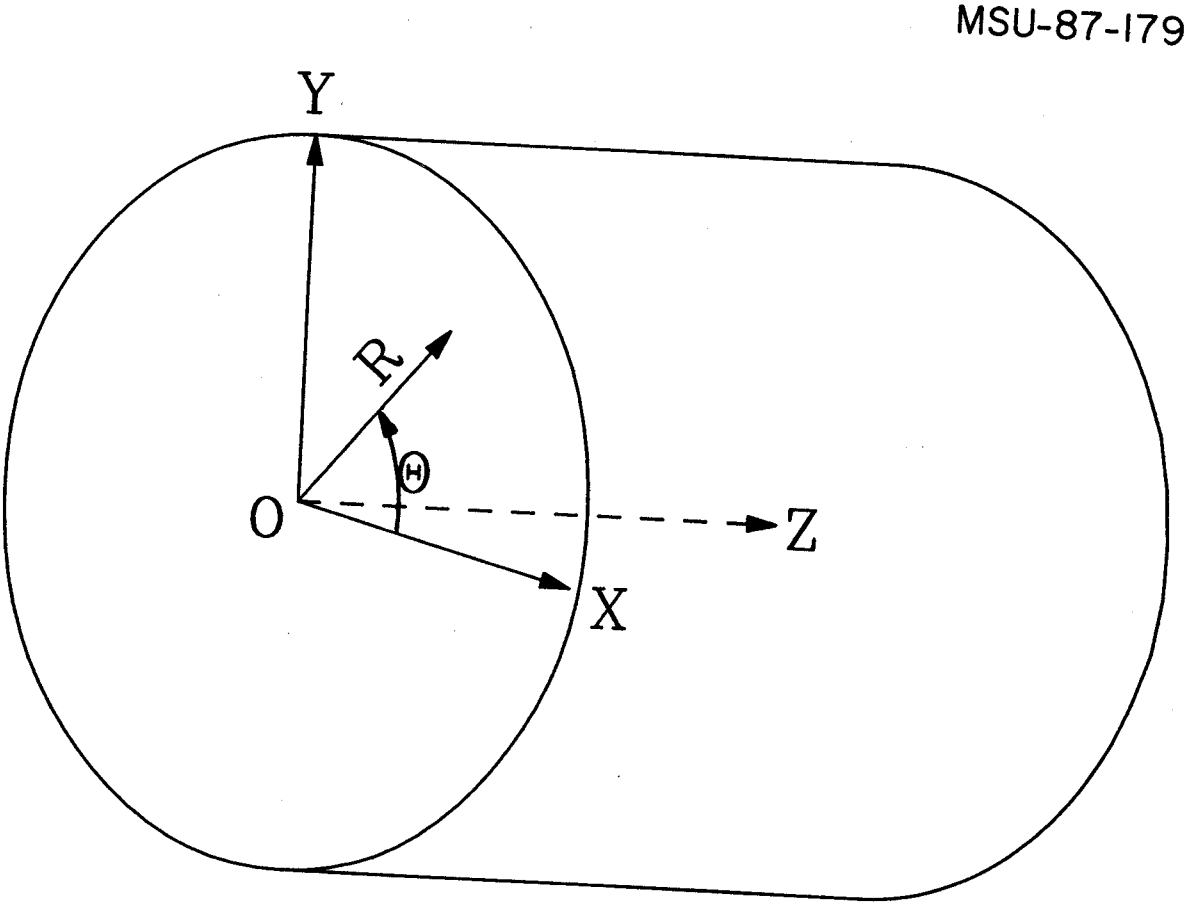

Figure 2.5 : Crystal-fixed frame of reference for γ-ray scanning tests.

One can, therefore, largely eliminate the effects of energy loss variations in the ΔE-detector due to straggling or detector inhomogeneities by adding the ΔE and E signals. By this procedure one can determine the intrinsic resolution of the CsI(Tl) detector with good accuracy.

Tests were also performed at the Indiana University Cyclotron Facility. A direct, low intensity beam of 200 MeV protons was degraded by passing it through an aluminum absorber and then collimating it with 50 mm thick Cu collimators with circular holes of 3 or 25 mm diameter, respectively. For these collimator sizes, outscattering of the particles is of minor importance. In these measurements no silicon ΔE-detector was used.

Results for Crystal #1

This crystal was of clear transparent appearance with a few tiny imperfections in the bulk material. For the results presented here, crystal #1 was packaged following the procedure outlined in Section 2.2 with the single exception that the detector surfaces were not sanded by us. The crystal had been ordered from the factory with its front and rear faces polished and the cylinder mantle unpolished.

Figure 2.6 shows a scan of the detector response obtained by moving the collimated radiation source (scattered protons and α-particles as well as γ-rays) parallel to the X-axis of the crystal entrance window. Plotted is the percentage shift of the peak location measured at position X as compared to the peak position measured at the center, X=0. The exact magnitude of the measured shift depends on the nature of the detected radiation. This can be expected from the different penetration depths of γ-rays, protons and α-particles. For all three measurements, the detector exhibits a response which is distinctly left-right asymmetric with respect to the cylinder axis, X=0. For the measurements with the collimated ^{137}Cs source, the signal to (electronic) noise ratio is considerably worse than for measurements with energetic particles. As a consequence, the experimental

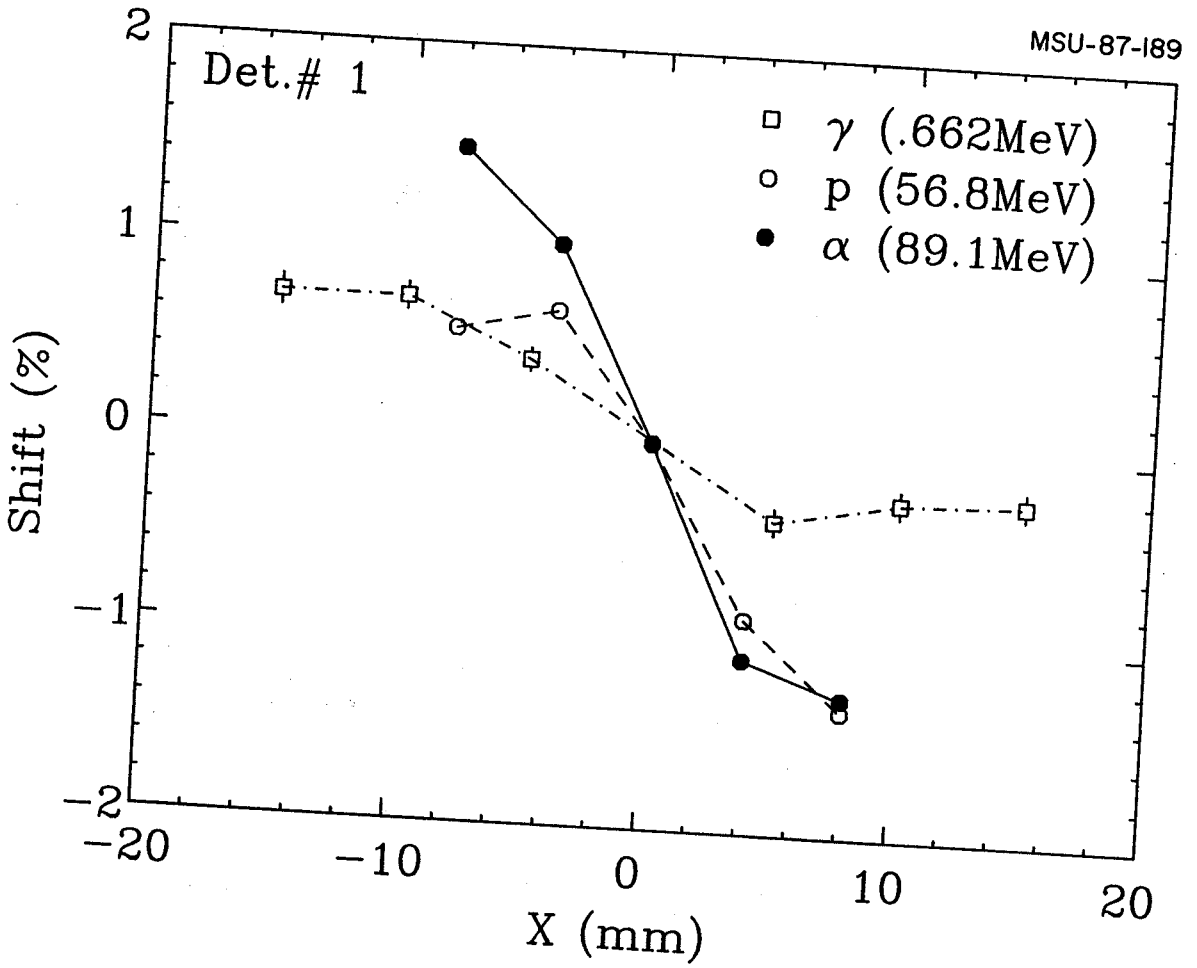

Figure 2.6 : Left-right asymmetric response of crystal #1 for collimated γ-rays of 662 keV, protons of 56.8 MeV, and α-particles of 89.1 MeV. Shown is the relative shift of the peak centroid as a function of the X-coordinate of the collimator, keeping Y=0. The data are normalized to the peak position measured for X=Y=0.

uncertainties for the γ-ray measurements are larger. Due to Compton scattering and variations of the penetration depths the effective volume in which scintillation is produced is larger for γ-rays than for particles. The larger sampling volume might slightly reduce the sensitivity of tests with γ-rays. However, it is important that the approximate magnitude of the asymmetry can be well established with a simple bench test using γ-rays. This allows testing of individual crystals without having to take recourse to expensive accelerator time.

With a collimator of 3 mm diameter, the detector exhibits an excellent energy resolution of the order of 1% for α-particles of 94 MeV. Because of the strong position dependence of the detector response, the energy resolution is considerably worse if a larger collimator is used. With a collimator of 20 mm diameter a double humped peak structure was observed with a FWHM resolution of about 3%.

Different treatments of the front face of the crystal #1 were investigated. The front surface was polished, sanded, covered with aluminum foil, aluminized mylar, or teflon tape. Although the detailed detector response is affected by these treatments, we were unable to eliminate the underlying left-right asymmetry. The effects of surface treatments will be illustrated in some more detail for a different crystal, #3, which exhibited a less asymmetric response at one end of the crystal.

It was verified that the asymmetric response of the detector was not due to the square shape of the photon detector. As an example, Figure 2.7 shows measurements with a collimated γ-ray source for a different crystal, #2, performed using a PIN diode and a photomultiplier tube as photon detectors. Both measurements give very similar results: the response of this particular crystal is relatively flat for a scan along the X-axis and shows a pronounced asymmetry for a scan along the Y-axis.

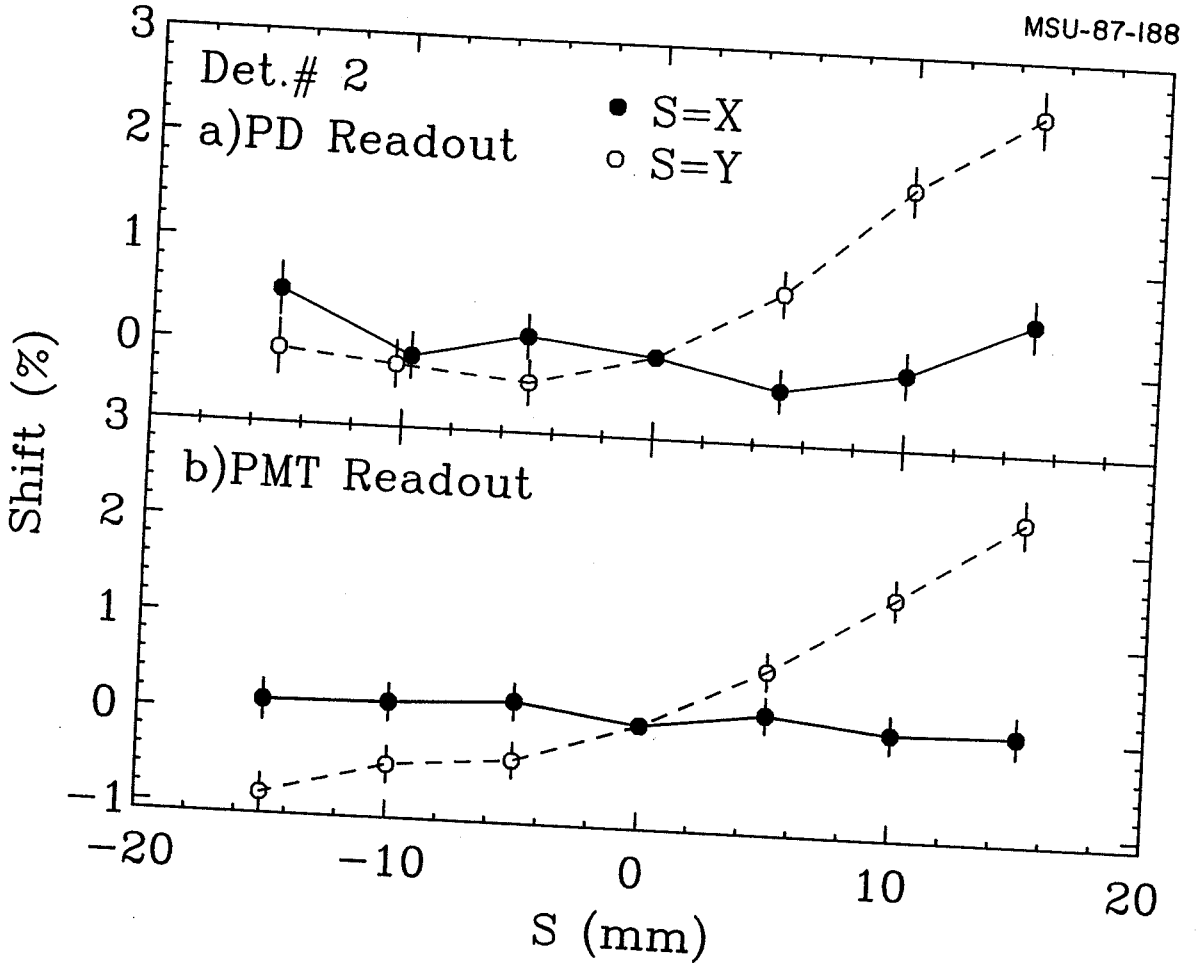

Figure 2.7 : Position sensitive response of crystal #2 for collimated γ-rays. The open points show measurements as a function of the Y-coordinate of the collimator keeping X=0; the solid points show the dependence on the X-coordinate keeping Y=0. Part a) and b) show measurements using a square PIN diode and a photomultiplier with circular photocathode, respectively.

Results for Crystal #3

This crystal was of slightly opaque appearance. As compared to crystal #1, it had a reduced light output. Initial tests revealed that the response of the detector was nearly symmetric with respect to the cylinder axis. This detector was then chosen for rather detailed investigations concerning the treatment of surfaces as well as its resolution for energetic light particles, including protons of 178 MeV energy.

Figure 2.8 shows the response to collimated γ-rays for the original (untreated) crystal as it arrived from the factory and for the crystal with the front surface and the cylinder mantle sanded. For the untreated detector (with a polished front surface) the light collection efficiency decreases as the radiation source is removed from the cylinder axis, see Figure 2.8b. A considerably more uniform response is obtained when the crystal is sanded, see Figure 2.8a. The major effect of sanding the surfaces of the detector is the removal of a reflection symmetric position sensitivity along the X and Y directions, which could be caused by variations of the effective solid angle for light collection due to total internal reflection at the side surfaces.

We have investigated whether sanding of the front surface introduces significant dead layers which could affect the energy resolution for low energy charged particles. Within experimental uncertainties, the energy resolution for collimated α-particles of 5.5 MeV energy was found to be the same for polished and sanded entrance windows. In addition, the signal amplitudes were very similar for the two different surface treatments. Therefore, we conclude that no major damages are introduced by also sanding the front surface of the detector. An optimally uniform response is obtained for diffusely reflecting detector surfaces. It should be noted that different treatments of the cylinder mantle can significantly alter the light collection efficiency as a function of the Z-coordinate. Such a dependence is of minor concern for the detection of charged particles

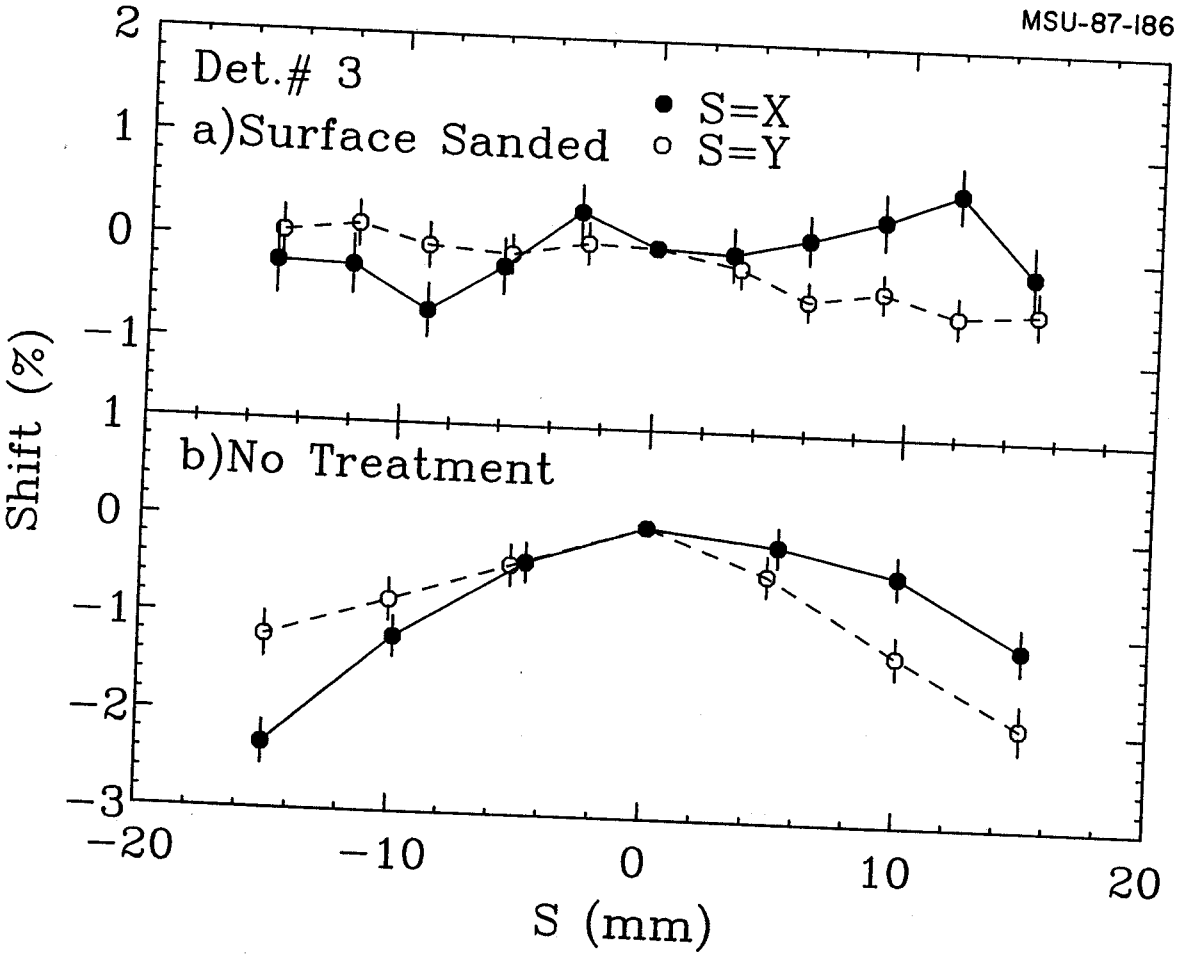

Figure 2.8 : Position sensitive response of crystal #3 for collimated γ-rays. The open points show measurements as a function of the Y-coordinate of the collimator keeping X=0; the solid points show the dependence on the X-coordinate keeping Y=0. Part (a): Standard sanding treatment of the reflecting surfaces; part (b): original detector with polished front face.

entering through the front window: it merely introduces nonlinearities in the energy calibration of the detector without significantly affecting the energy resolution. Quite generally, scintillation detectors have nonlinear energy calibrations due to the dependence of the differential light output on ionization density [Poch 87, Vies 86].

Figure 2.9 shows the response of the elements of the ΔE-E telescope to α-particles of 92 MeV restricted by a 3 mm collimator moved along the X-axis of the crystal. The upper part of the figure shows the response of the ΔE-detector which shows clear evidence of a convex shape with an inhomogeneity of the order of 8%. The center part of the figure shows the complementary response of the CsI detector. After summation of the ΔE and E signals, the total response of the telescope is obtained to be flat within 0.5%.

Figure 2.10 shows energy spectra of protons and α-particles emitted at $\Theta=20°$ from a polycarbon target $(CH_2)_n$ irradiated with 96 MeV α-particles. In order to reduce kinematical broadening of the elastic scattering peaks a collimator of 3 mm diameter was used. The energy resolution (FWHM) of the telescope is 1.0% for 55 MeV protons and 0.8% for 92 MeV α-particles. Due to the rather uniform response of crystal #3, the detector resolution is of comparable quality for larger collimators. For 95 MeV α-particles (obtained from the elastic scattering on Au), a resolution of 0.9% was measured with a collimator of 20 mm diameter, see Figure 2.11. Figure 2.12 shows the energy calibration of the detector. Good linearity is observed over the range of energies measured. Consistent with previous measurements [Vies 86], α-particles exhibit a significant pulse height defect as compared to protons.

The tests described so far probe only a small fraction of the crystal. In order to test the response to more penetrating radiation, we performed measurements with protons of 178 MeV. Using a collimator of 3 mm in diameter a resolution (FWHM) of 1.4% was obtained. When a 25 mm diameter collimator was used, the

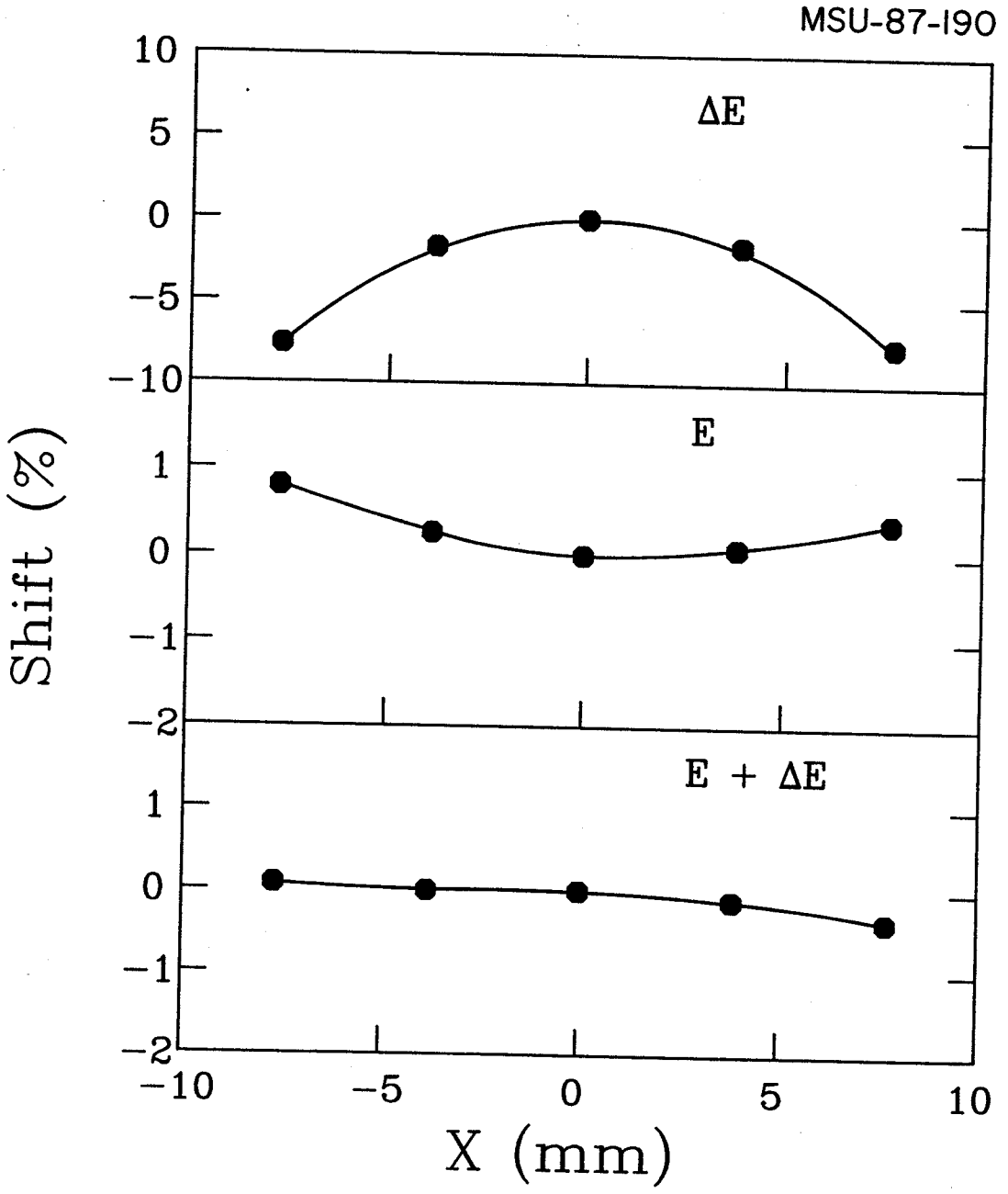

Figure 2.9 : Percentage shift of the ΔE, E, and summed ΔE+E signals as a function of the X-coordinate of the particle collimator, keeping Y=0. (Crystal #3)

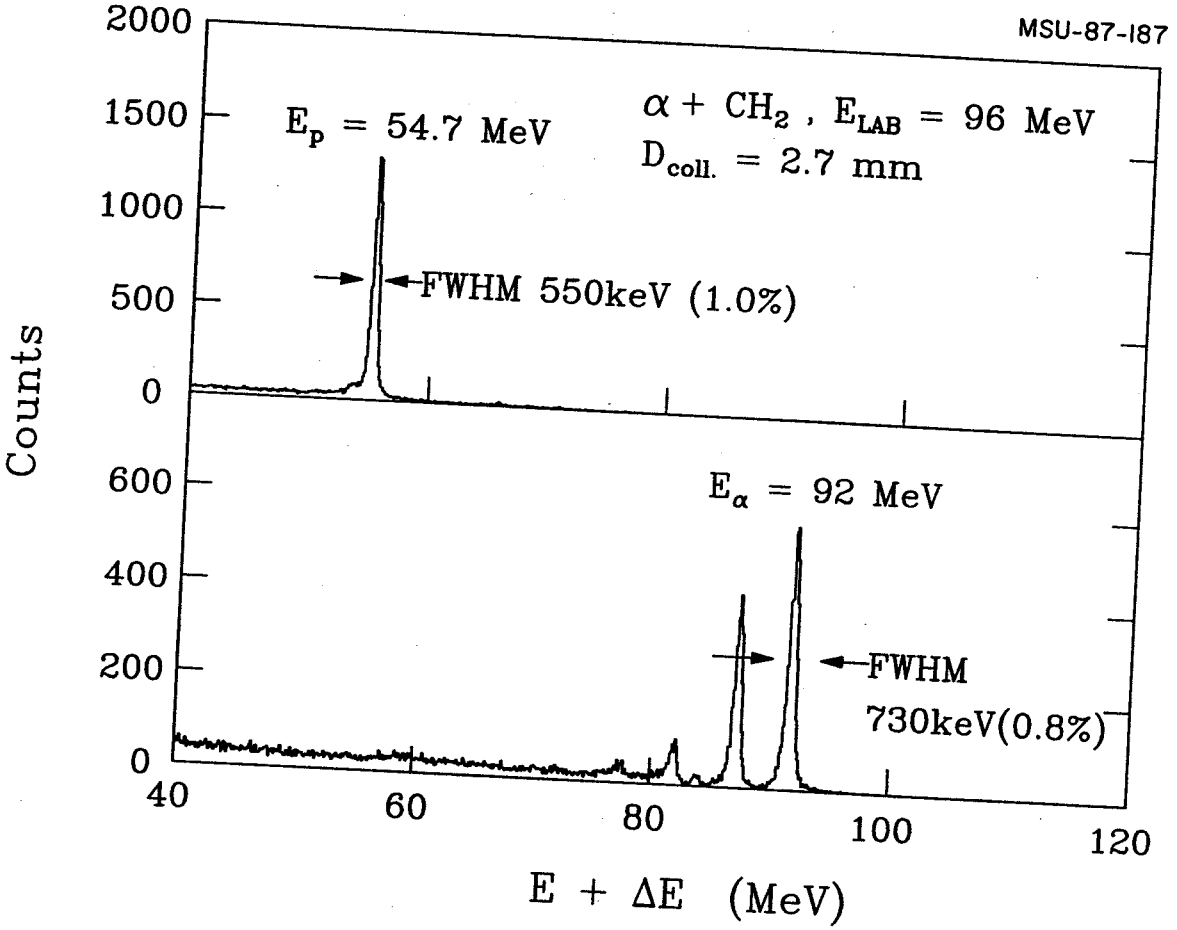

Figure 2.10: Energy spectra of protons and α-particles obtained at Θ=20° for reactions induced by 96 MeV α-particles on a CH_2 target. The detector collimator was 3 mm in diameter. (Crystal #3)

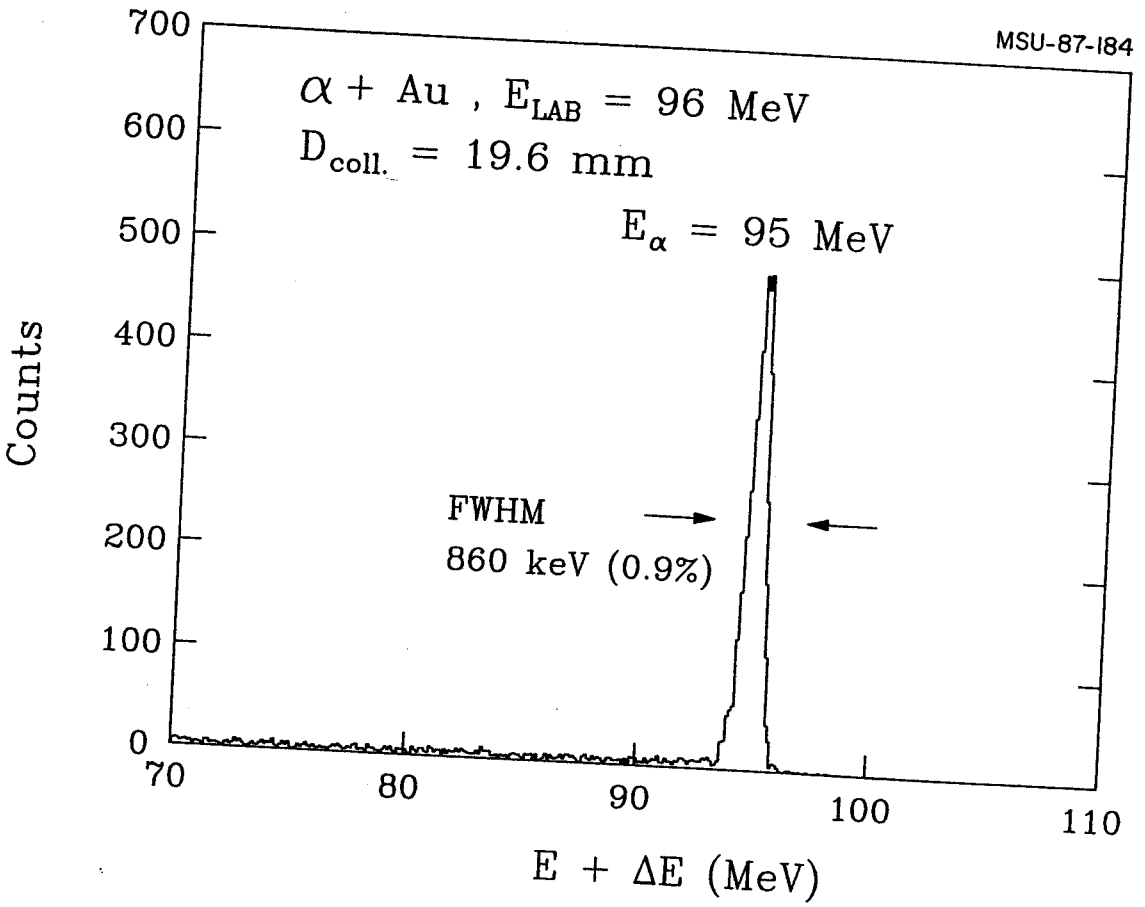

Figure 2.11: Energy spectrum of α-particles detected at Θ=20° for the α+Au reaction at 96 MeV. A collimator of 20 mm diameter was used. (Crystal #3)

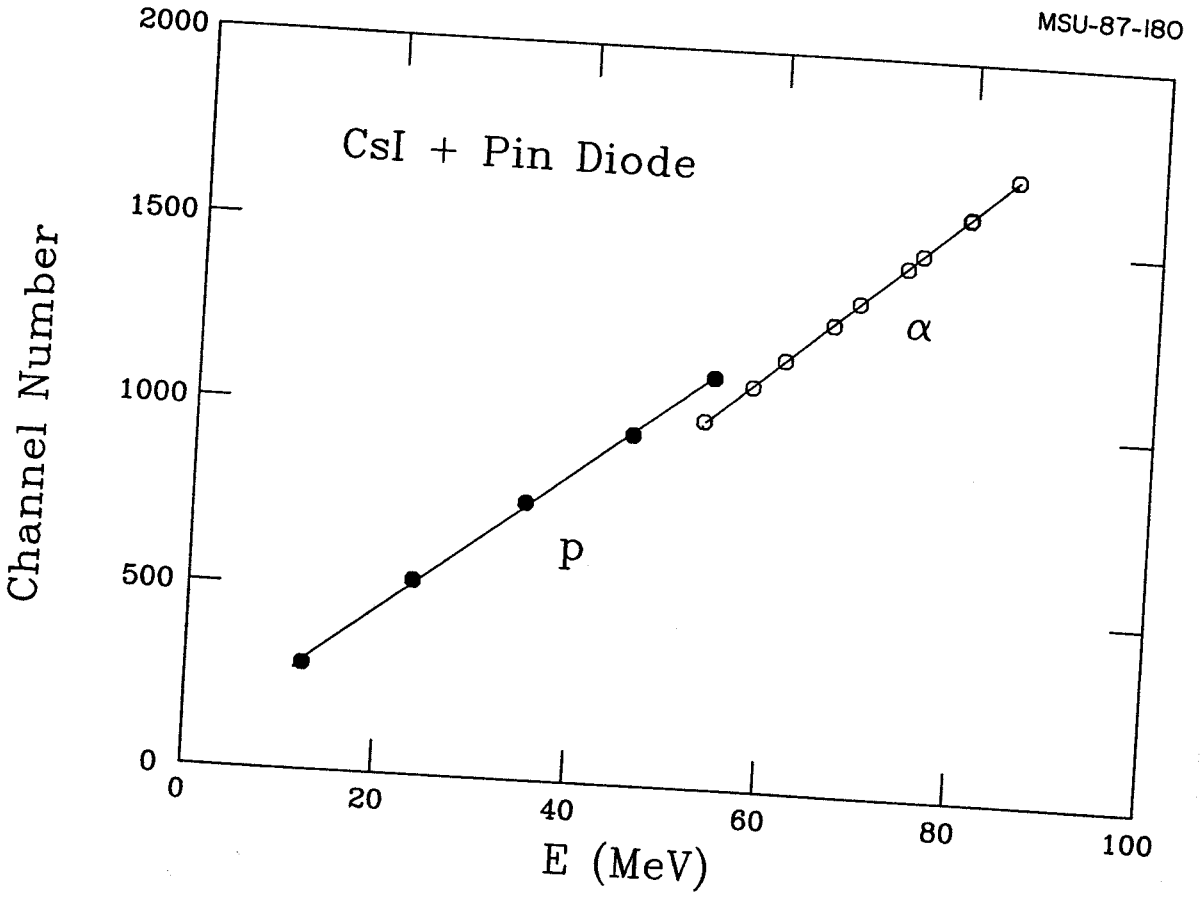

Figure 2.12: Energy calibration for crystal #3.

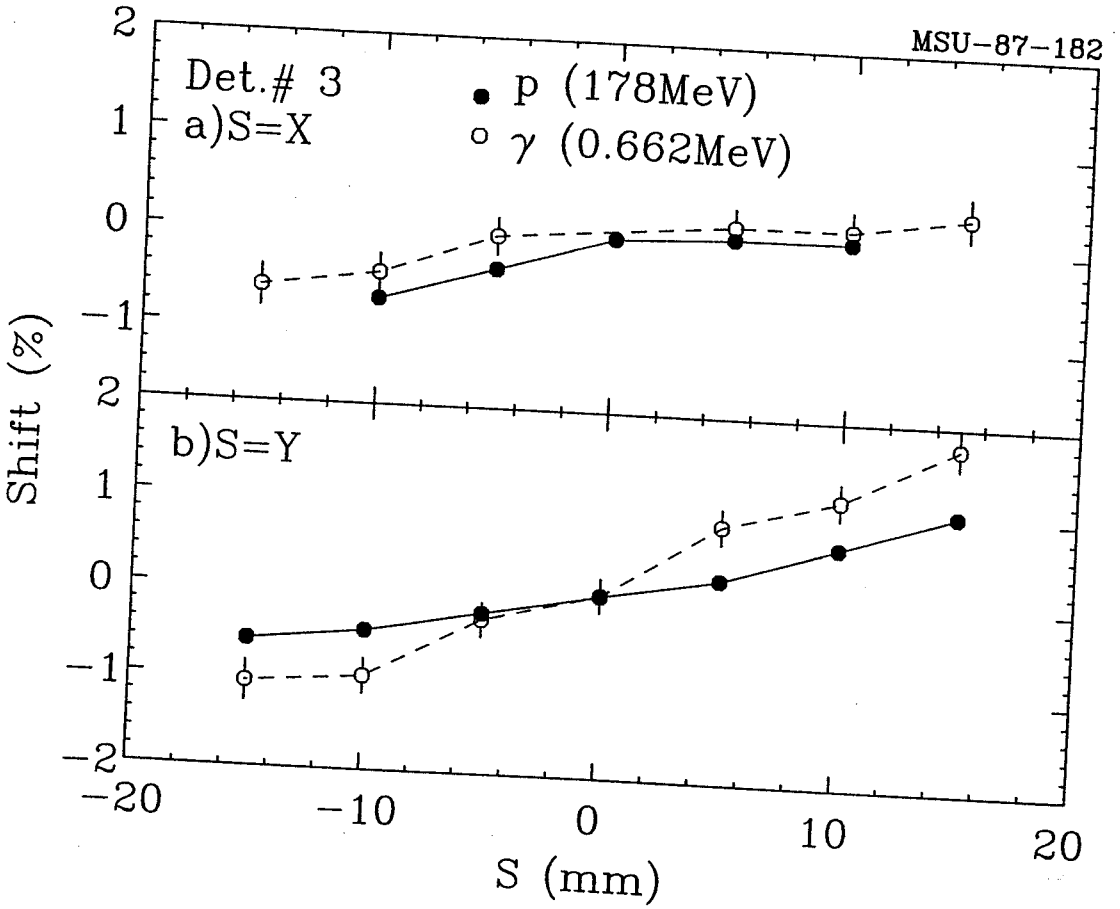

Figure 2.13: Position sensitive response of crystal #3 as detected by collimated protons of 178 MeV (solid points) entering the front face (Z=0) of the crystal with the PIN diode mounted at the rear end (Z=112 mm) and by collimated γ-rays (open points) entering the rear face (Z=100 mm) of the crystal with the PIN diode mounted at the front end (Z=-12 mm). Part (a) shows measurements as a function of the X-coordinate of the collimator keeping Y=0; part (b) shows measurements as a function of the Y-coordinate of the collimator keeping X=0.

energy resolution was 1.7%. Scans of the detector response along the X and Y directions revealed non-trivial variations of the peak position as a function of position, see solid points in Figure 2.13. Reduced position sensitivities were measured for protons degraded to lower energy (≈146 MeV). In order to verify that the position sensitivity of the detector was associated with the properties of the crystal itself and not an artefact of our detector assembly, we removed the light guide and PIN diode from the crystal and attached it at to the former entrance window (Z=0 mm coordinate). After applying our standard surface treatment and packaging, we measured the response of the crystal by injecting collimated γ-rays through the rear window of the crystal (Z=100 mm coordinate). The measurements are shown by the open points in Figure 2.13. We observe a pronounced asymmetry in the detector response which tracks the qualitative features observed for 178 MeV protons. Of course there are quantitative differences since the two tests sample different (though partly overlapping) regions of the crystal. However, they do confirm that the variations in the scintillation efficiencies are due to inhomogeneities in the rear part of the crystal.

In summary, our results indicate that the resolution of large volume CsI(Tl) crystals is mainly limited by local inhomogeneities of the crystal response (most probably due to non-uniform doping of Tl concentrations). Improved fabrication techniques might overcome these limitations.

2.4 Pulse Shape Discrimination

In this section, we describe the timing characteristics of the detector and compare light particle identification spectra obtained with the ΔE-E technique using a 400 μm thick transmission surface barrier detector of 450 mm^2 active area (ORTEC TB-27-450-400) with those obtained by pulse shape discrimination technique. Special attention will be paid to the degradation of particle identification by pulse shape discrimination technique at higher count rates.

Particle identification spectra obtained with the ΔE-E technique are shown in Figures 2.14 and 2.15. For these measurements the preamplified PIN diode signals were shaped with a standard semi-Gaussian bipolar filter using a peaking time of 3 μs for the unipolar output. (This corresponds to a time constant of 1.4 μs.) The particle identification spectra were linearized by using a standard particle identification (PID) function:

$$PID \propto (E+\Delta E)^{1.8} - E^{1.8} . \qquad (2.1)$$

The PID spectra were then integrated over an interval of 45-70 MeV for the energies of the detected particles. Figure 2.14 shows the quality of particle identification which can be obtained with planar ΔE detectors. In these measurements inhomogeneities of the ΔE detector were reduced to a negligible level by using a collimator of 3 mm diameter in front of the telescope. Between protons and deuterons a peak-to-valley ratio of about 100 can be obtained; the separation between ^{3}He and ^{4}He is even better. When a larger collimator is used the inhomogeneities of our ΔE-detector are not negligible and the particle identification deteriorates somewhat, see Figure 2.15. In this figure, particle identification spectra are shown for two different count rates, 10^3 and 1.4×10^4 counts per second (cps), using a collimator of 20 mm diameter. (In our measurements sizeable contributions to the count rate of the CsI(Tl) detector are due to γ-rays and neutrons.) At count rates of the order of 10^3-10^4 cps, the particle identification is of good quality, it degrades slightly with increasing count rate.

It has been known for many years that the temporal decay of the CsI(Tl) light output depends on the ionization density of the detected particles [Stor 58]. The fluorescent light has two major decay time constants. In a good approximation the

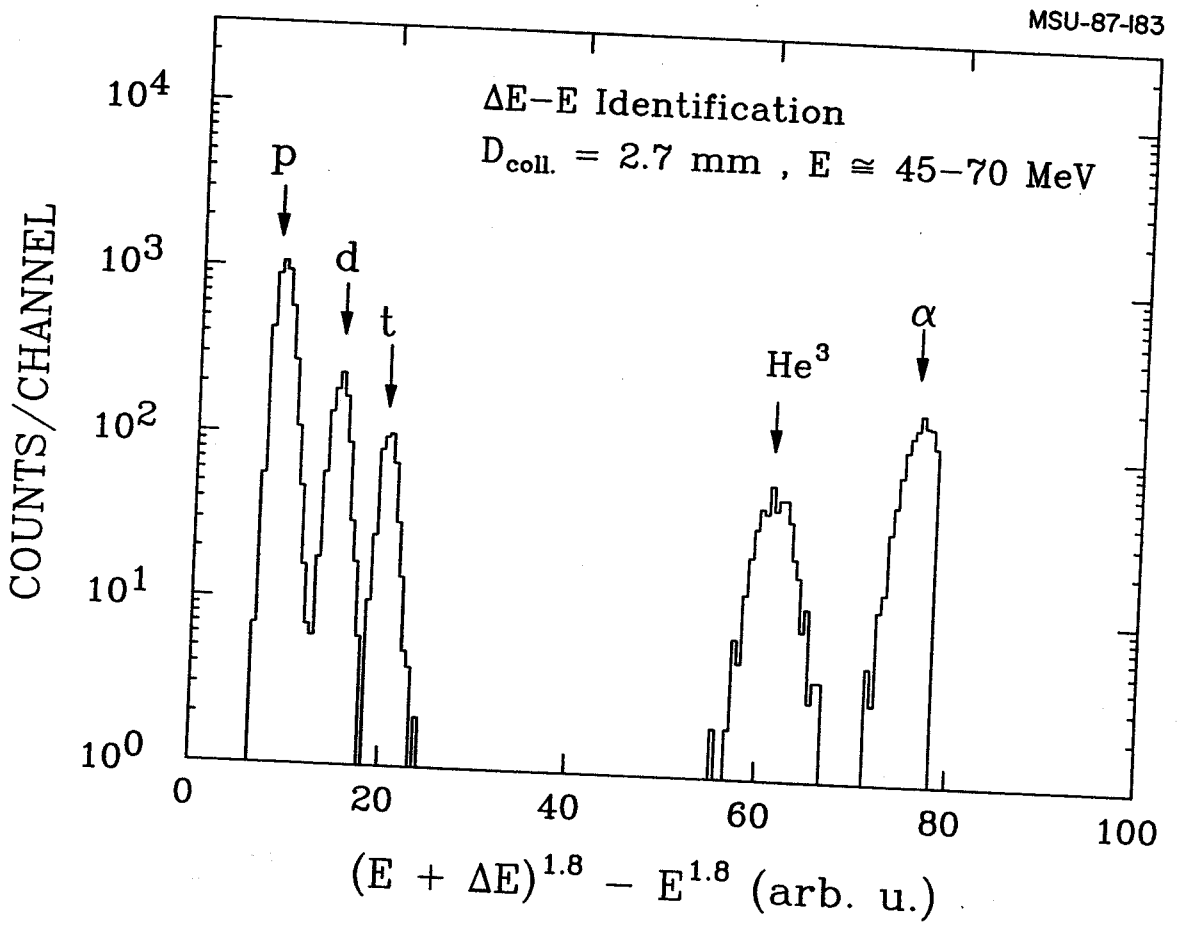

Figure 2.14: Particle identification spectrum obtained with the ΔE-E technique and employing the linearization function PID = $(E+\Delta E)^{1.8} - E^{1.8}$. The interval of energy integration was 45-70 MeV. To eliminate inhomogeneities of the ΔE-silicon detector, a collimator of 3 mm diameter was used.

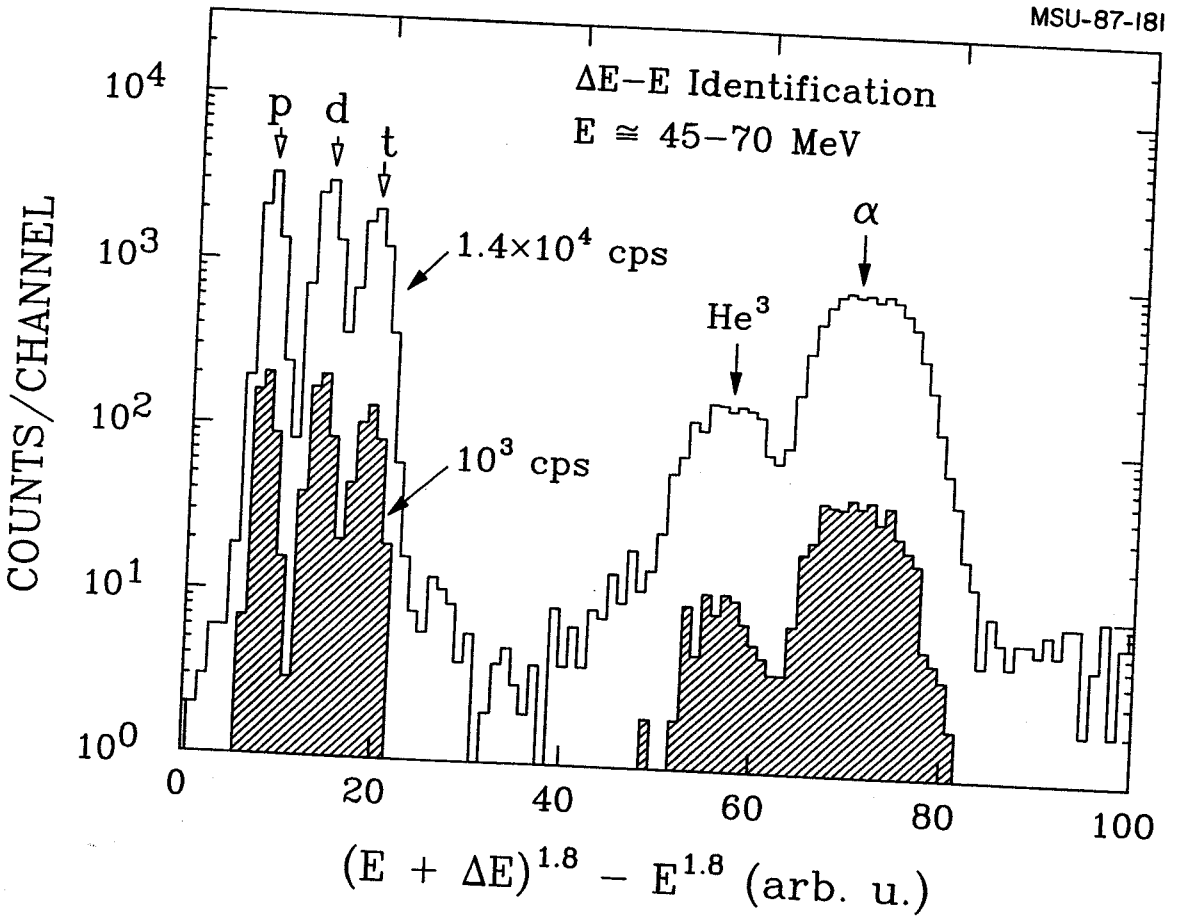

Figure 2.15: Particle identification spectrum obtained with the ΔE-E technique and employing the linearization function PID = $(E+\Delta E)^{1.8} - E^{1.8}$. The interval of energy integration was 45-70 MeV. A collimator of 20 mm diameter was used. Identification spectra are shown for the count rates of 10^3 cps (shaded histogram) and 1.4×10^4 cps (upper histogram).

decay of the scintillation pulse can be expressed as [Stor 58, Alar 86]:

$$L(t) = L_s \exp(-t/\tau_s) + L_f \exp(-t/\tau_f) \ . \qquad (2.2)$$

While the slow time constant, $\tau_s \approx 7$ μs, is independent of the ionization density generated by the detected particle, both the detailed value of the fast time constant, $\tau_f \approx$ 0.4-0.7 μs, as well as the relative intensity, L_f/L_s, are known to exhibit such a dependence. It is, therefore, possible to discriminate between different charged particles via pulse shape discrimination techniques [Kreu 87, Alar 86, Bigg 61].

Figure 2.16 shows particle identification spectra obtained via pulse shape discrimination for two count rates, 10^3 and 1.4×10^4 cps. For these data, we measured the time difference, ΔT, between the time derived with a constant fraction discriminator from a fast signal of the PIN diode, shaped with 400 ns differentiation and 100 ns integration constants, and the zero-cross-over time of a slow doubly differentiated signal shaped with a semi-gaussian bipolar filter (ORTEC 572) using a time constant of 3 μs. (A theoretical analysis, using measured time constants for different particle species and the noise characteristics of the filter network, predicts an optimum pulse shape discrimination for time constants between 2-3 μs, assuming that pile-up effects are negligible.) At low count rates, the pulse shape discrimination technique yields good separation between hydrogen isotopes and somewhat marginal separation between ^{3}He and ^{4}He. However, the quality of particle separation deteriorates rather rapidly with increasing count rate. This effect can be understood as due to the sensitivity of the zero-cross-over of the slow signal to pile-up. The ΔE-E technique is clearly superior, especially at higher count rates. Nevertheless, pulse shape discrimination can provide useful results in low count rate applications encountered, for example, in detector arrays of high granularity in which each module subtends only a small solid angle. In addition, it can be used to

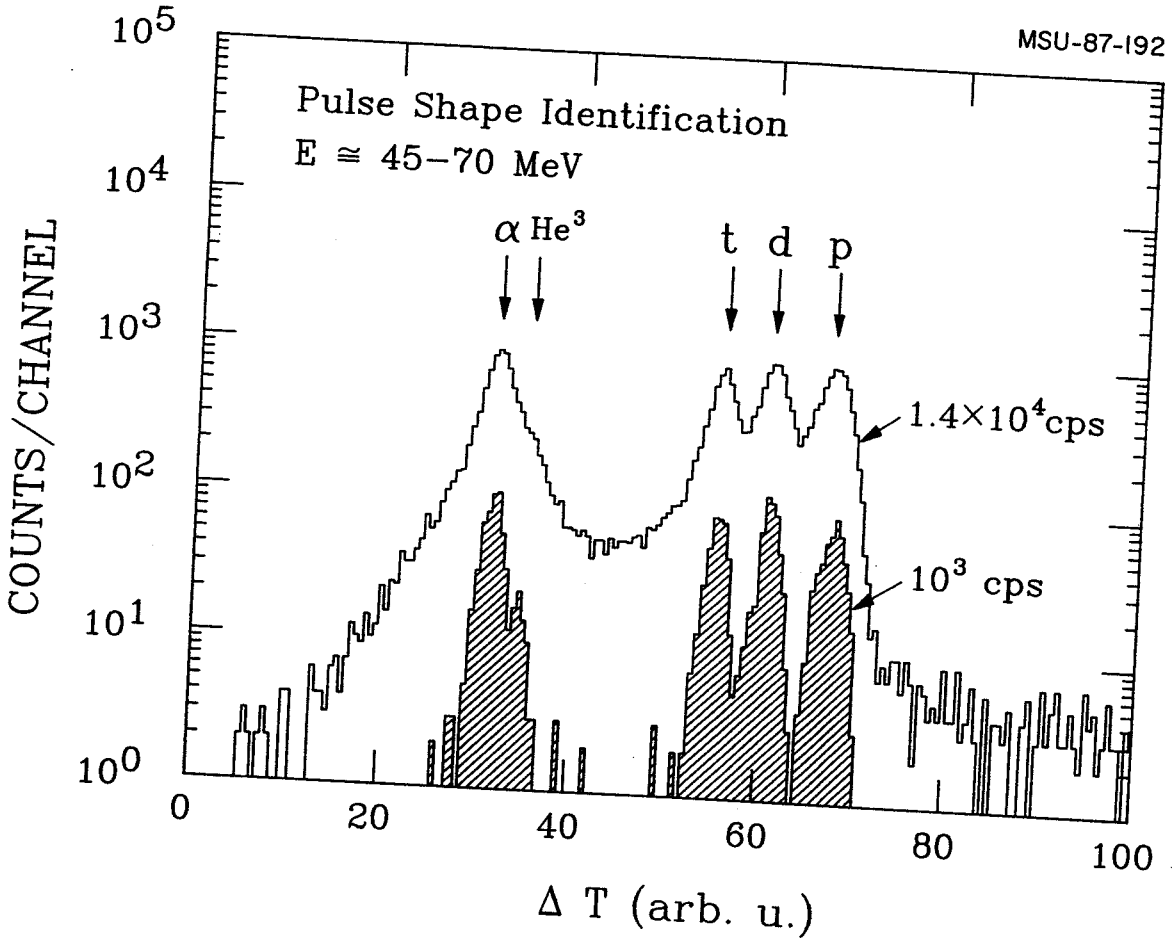

Figure 2.16: Particle identification spectra obtained with the pulse shape discrimination technique. The interval of energy integration was 45-70 MeV. A collimator of 20 mm diameter was used. Identification spectra are shown for the count rates of 10^3 cps (shaded histogram) and 1.4×10^4 cps (upper histogram).

discriminate between different hydrogen isotopes of very high energy in applications where dynamic range considerations dictate the use of thin ΔE detectors less suitable for the separation of protons, deuterons, and tritons.

Since the particle identification efficiency of the ΔE-E technique is close to 1, one can determine the efficiency of the pulse shape discrimination (PSD) technique by setting gates corresponding to various particles in the PID-E matrix and then sorting the gated data into the ΔT-E matrix. The efficiency of the PSD technique can then be defined in terms of the ratio

$$\varepsilon_{psd} = N_{PSD}/N_{PID}, \tag{2.3}$$

where N_{PID} denotes the total number of counts sorted for a given gate in the PID-E matrix and N_{PSD} is the number of events which fall into the appropriate region in the ΔT-E matrix.

We have measured the dependence of ε_{psd} as a function of count rate in the CsI(Tl) detector #3 using time constants of 2 and 3 μs in a semi-gaussian filter network. The results obtained for p, d, t, and α-particles are shown in Figure 2.17. For both shaping times, the pulse-shape discrimination efficiency decrease strongly as a function of count rate. At count rates of the order of 10^3 cps, $\varepsilon_{psd} \approx$ 95-100%, the exact value depending on shaping constant and particle type. At count rates of the order of 10^4 cps, $\varepsilon_{psd} \approx$ 70-80%, i.e. between 20% to 30% of the particles are misidentified. Such misidentifications can pose a serious handicap for high resolution coincidence measurements since the number of correctly identified particle pairs depends quadratically on ε_{psd}: For ε_{psd} = 75%, only 56% of the coincident particle pairs will be identified correctly.

Some improvements of the count rate dependence of the pulse shape discrimination efficiency might be obtained by using pulse shaping by double delay-line differentiation because of its faster baseline recovery characteristics.

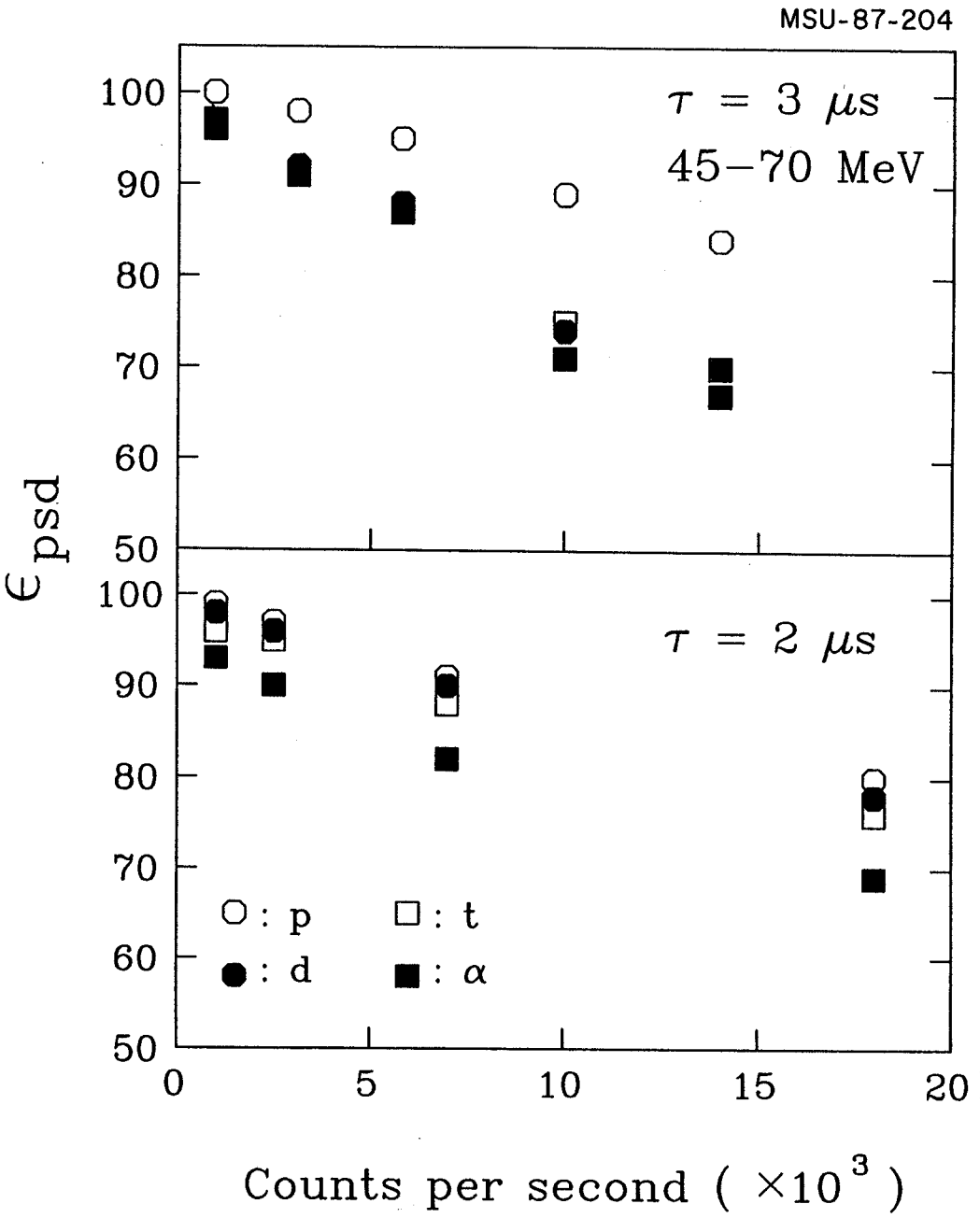

Figure 2.17: Particle identification efficiency as a function of count rate in the CsI detector obtained with the pulse shape discrimination technique. The slow pulse shaping was performed using a semi-gaussian bipolar filter of shaping time constants of 3 μs (upper part) and 2 μs (lower part). The interval of energy integration was 45-70 MeV. A collimator of 20 mm diameter was used.

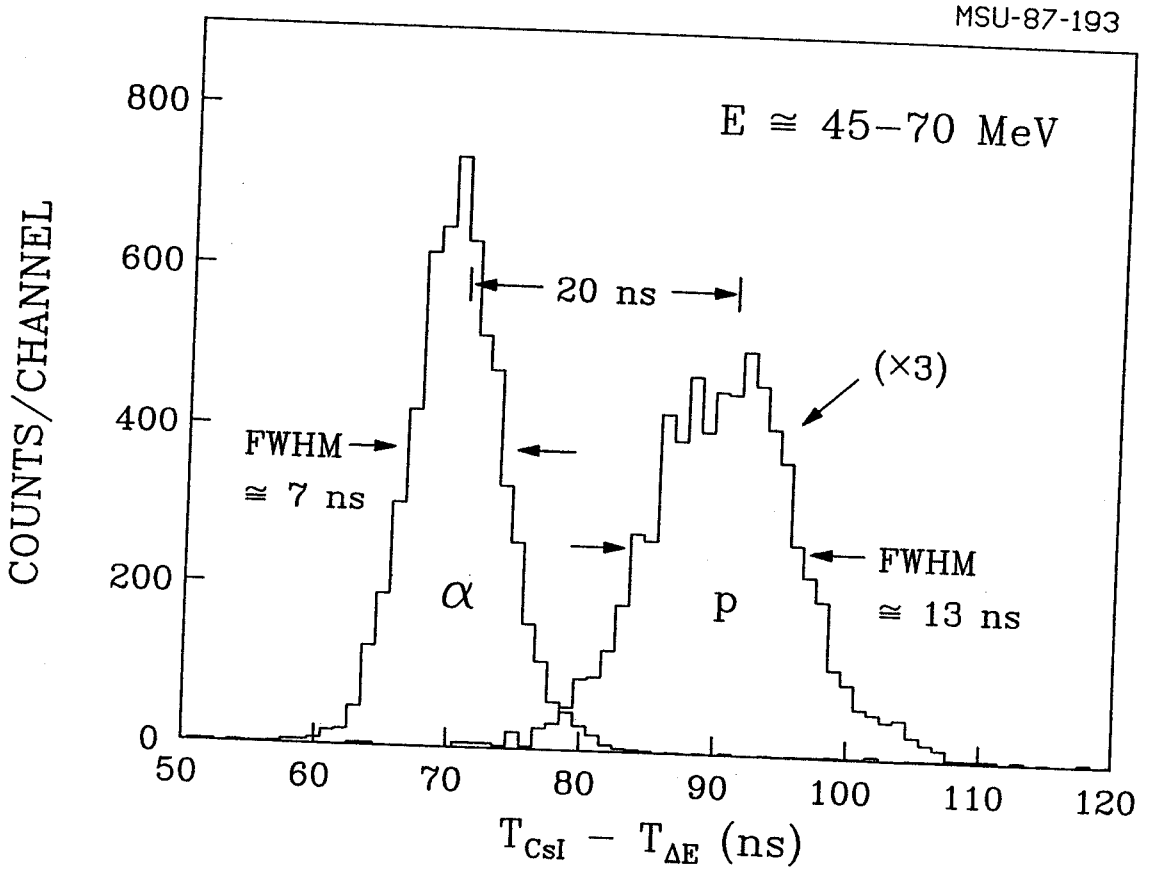

Figure 2.18: Relative timing between the CsI(Tl) E and the silicon ΔE detectors using constant fraction discriminators. The interval of energy integration was 45-70 MeV.

However, one cannot expect to match the excellent count rate dependence achieved for the ΔE-E technique, since the amount of time during which the baseline is occupied will not change considerably. The ΔE-E technique is less sensitive to count rate since the time constant in the main shaping amplifier for the ΔE signal can be kept small; it could even be reduced with respect to the value of 1.4 μs adopted for our measurements since electronic noise is not the limiting factor.

The rather poor count rate characteristic of the pulse shape discrimination technique is intimately connected to the fact that even the faster of the two components of the fluorescent light of CsI(Tl) is sufficiently slow to cause severe pile-up problems. Another consequence of the slow CsI(Tl) light response is the quality of the timing that one can obtain from such a detector. With mono-energetic protons of 178 MeV, time resolutions of the order of 4 ns were obtained with the constant fraction technique. This value is close to the optimum value which can be expected from our detector: at lower energies, the signal to noise ratio becomes worse and the time resolution will deteriorate. Further problems arise from the existence of different decay constants for different particle species which cause additional walk problems when one uses charge integrating preamplifiers. To illustrate this problem, Figure 2.18 shows the time difference derived from the signals of the CsI(Tl) E and the silicon ΔE detectors using constant fraction timing techniques. The particle dependent walk is clearly visible.

2.5 Quality Tests of CsI(Tl) Scintillators

The resolution of large volume CsI(Tl) detectors was found to be limited by local crystal nonuniformities which caused significant variations of the light output efficiency. The magnitude of the local variations of light output efficiency can vary significantly between individual crystals. It can be assessed with an inexpensive bench test in which the position dependent response to collimated γ-rays is measured (see Section 2.3). In order to make detectors of satisfactory

quality for a 56 element hodoscope, we have tested a large number of CsI(Tl) scintillators manufactured by BICRON corporation. Based upon extensive measurements with collimated γ-ray scanning, we compared crystals grown by a previous technique to crystals grown with a newly developed process showing considerably better uniformity of scintillation efficiency.

All crystals tested were cylinders of 38 mm diameter and 102 mm length. They are packed according to the structure depicted in Figure 2.3. The response of all detectors was tested with 662 keV γ-rays from a ^{137}Cs source collimated by a 3 mm diameter lead collimator of about 6 cm thickness. The collimated γ-rays entered through the flat front face of the CsI(Tl) crystals in a direction parallel to the cylinder axis. As a quantitative measure for the non-uniformities of scintillation response, we evaluated the maximum shift of the centroid of the photopeak as the collimator moved along a circle of 1 cm radius centered at the axis of the cylindrical CsI(Tl) crystals. The measured shifts of the photopeak were normalized to the response for irradiation at the center of the circular entrance window.

Techniques used for the growth of CsI(Tl) (and other alkali halides) on a commercial scale are not documented in the open literature, but are based on years of research and development in material purification and growth furnace design. Techniques described in Reference [Birk 64] make it possible to grow good quality crystals of small size and on a small scale. The growth of large volume crystals ($\geq$100 ℓ) on a monthly schedule requires a detailed understanding of the interplay between purity of starting material, growth furnace design, and growth rates.

The two different sets of crystals described here represent an old and a new growth process. BICRON began growing CsI(Tl) in 1985 using the old process. The resulting crystals were acceptable for Compton suppression shields and phoswich [NaI(Tl)/CsI(Tl)] applications. Under close examination with a finely

collimated γ-ray beam these crystals were found to have pulse height variations of as much as 6% over distances of the order of 1 cm. Our test results for a large sample of such crystals are shown by the unshaded histogram in Figure 2.19. These scintillators exhibit a broad distribution in scintillation uniformity.

Analysis of the crystals from the old growth process revealed severe internal stress and strain. Fluorescent emission under strong photo excitation did not show wide variations. An immediate correction was to further customize the Stockbarger furnace and to reduce the diameter of the crystals from 19 inches to 6 inches to improve the control of thermal gradients in the crucible full of molten material. Thermal gradients at the liquid/solid interface must be large and the vertical plane within the furnace at which crystal growth occurs must be constant.

The performance of crystals grown with the new technique is encouraging. They exhibit much better scintillation uniformities, see the shaded histogram in Figure 2.19. Attempts to go to larger, more useful diameters have led to new purification processes and additional furnace changes. Yields of high quality crystal material are low. In Figure 2.19, 37 crystals measured with "Shift[%]" less than or equal to 1% were accepted and used for our purpose.

There is a close relation between scintillation uniformity and energy resolution when photon statistics or electronic noise cease to be limiting factors. When used for the detection of energetic light charged particles, the majority of crystals grown with the old technique will yield detectors with only modest energy resolution. Crystals grown with the new technique exhibit exceptional energy resolutions for energetic light particles, see Figure 2.20 for illustration. The energy spectra shown in the figure were obtained by irradiating a polycarbonate foil with α-particles of 160 MeV incident energy. For these measurements, a ΔE-E detector telescope was used which consisted of a 300 μm thick planar silicon ΔE-detector and a CsI(Tl) E-detector grown with the new technique. The sharp peaks

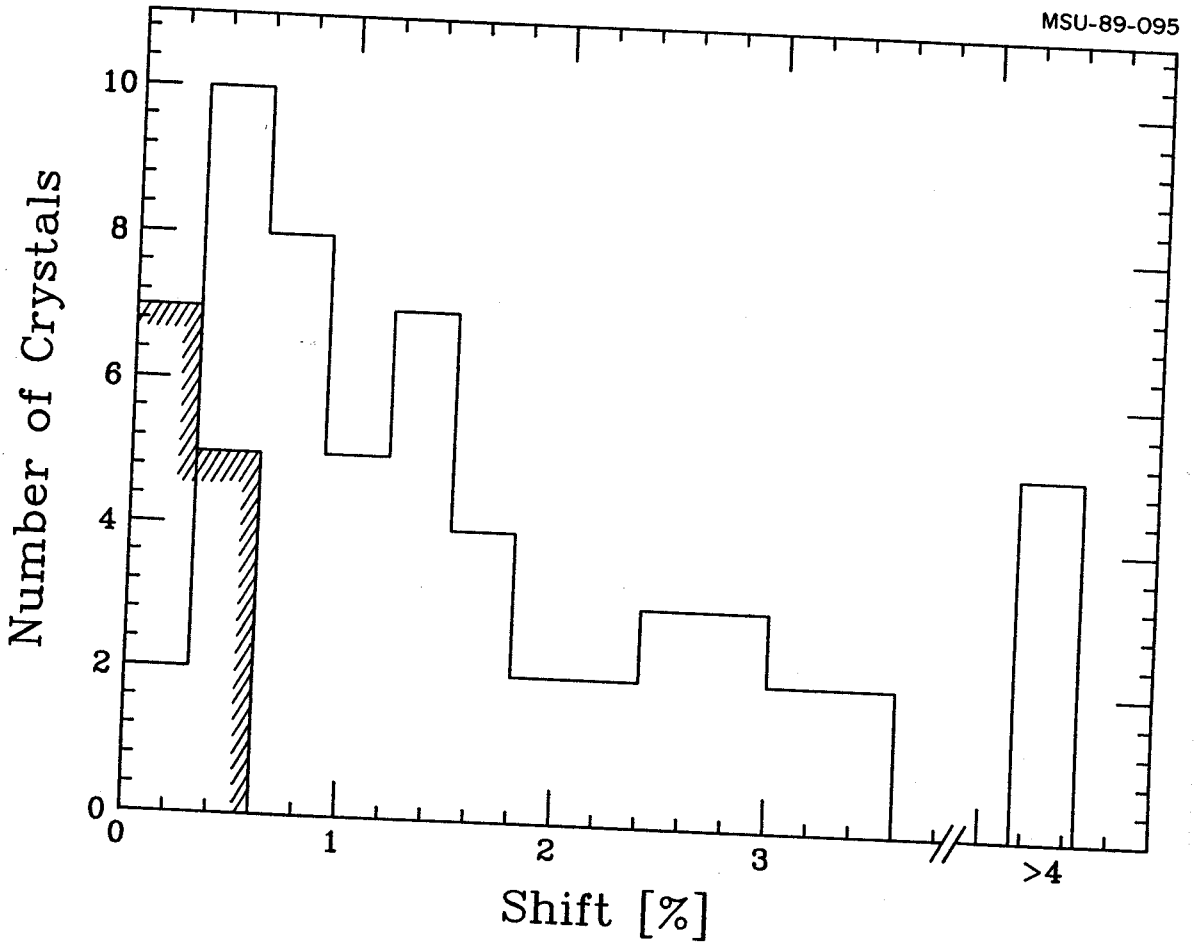

Figure 2.19: Maximum variations of scintillation response observed for collimated γ-rays entering the detector front face at various points located on a circle of 1 cm radius and centered at the detector axis. The shaded histogram shows the measurements for detectors produced with the new growth technique; the unshaded histogram shows measurements for detectors fabricated with the old technique.

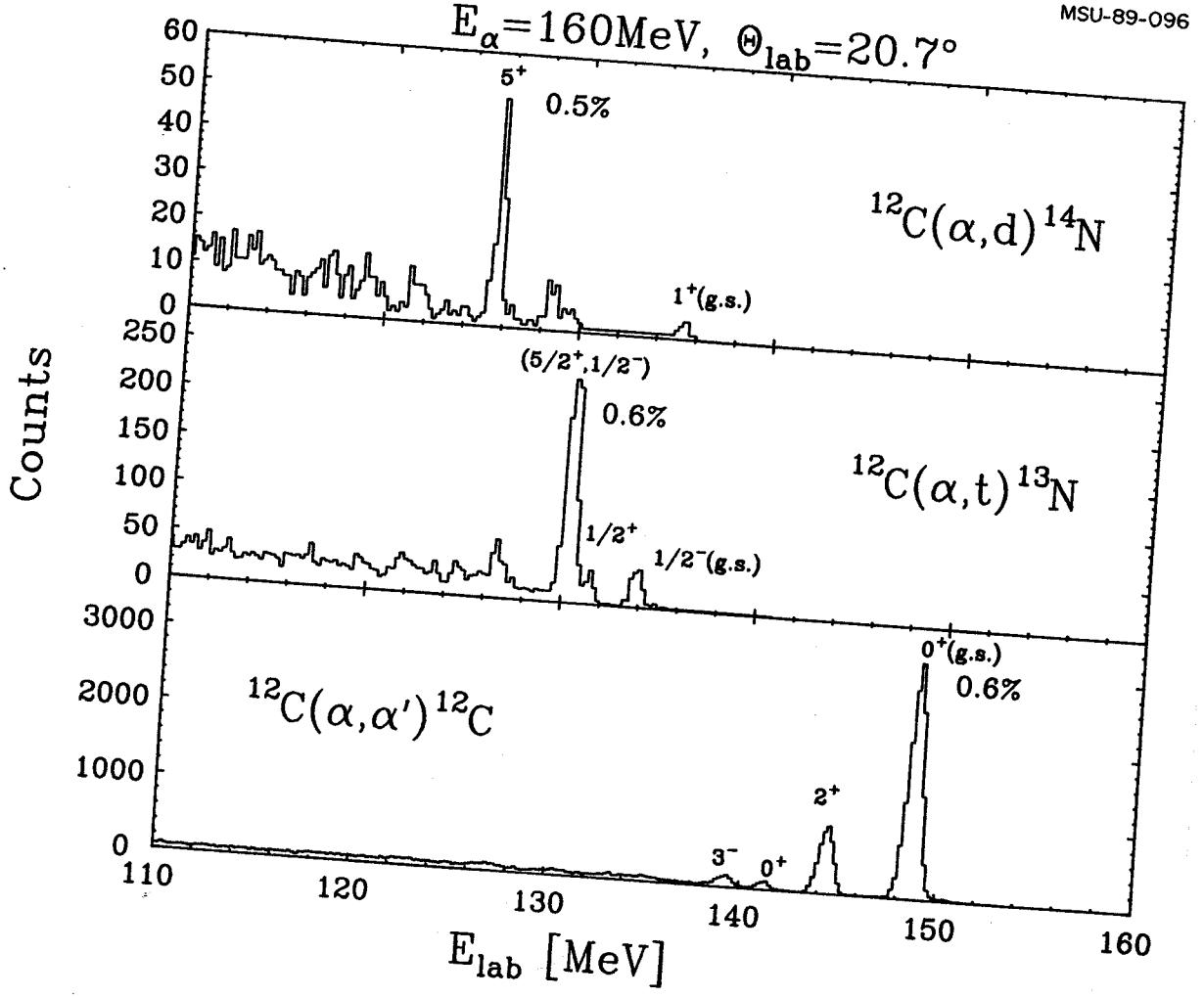

Figure 2.20: Energy spectra measured with a CsI(Tl) detector produced with the new technique.

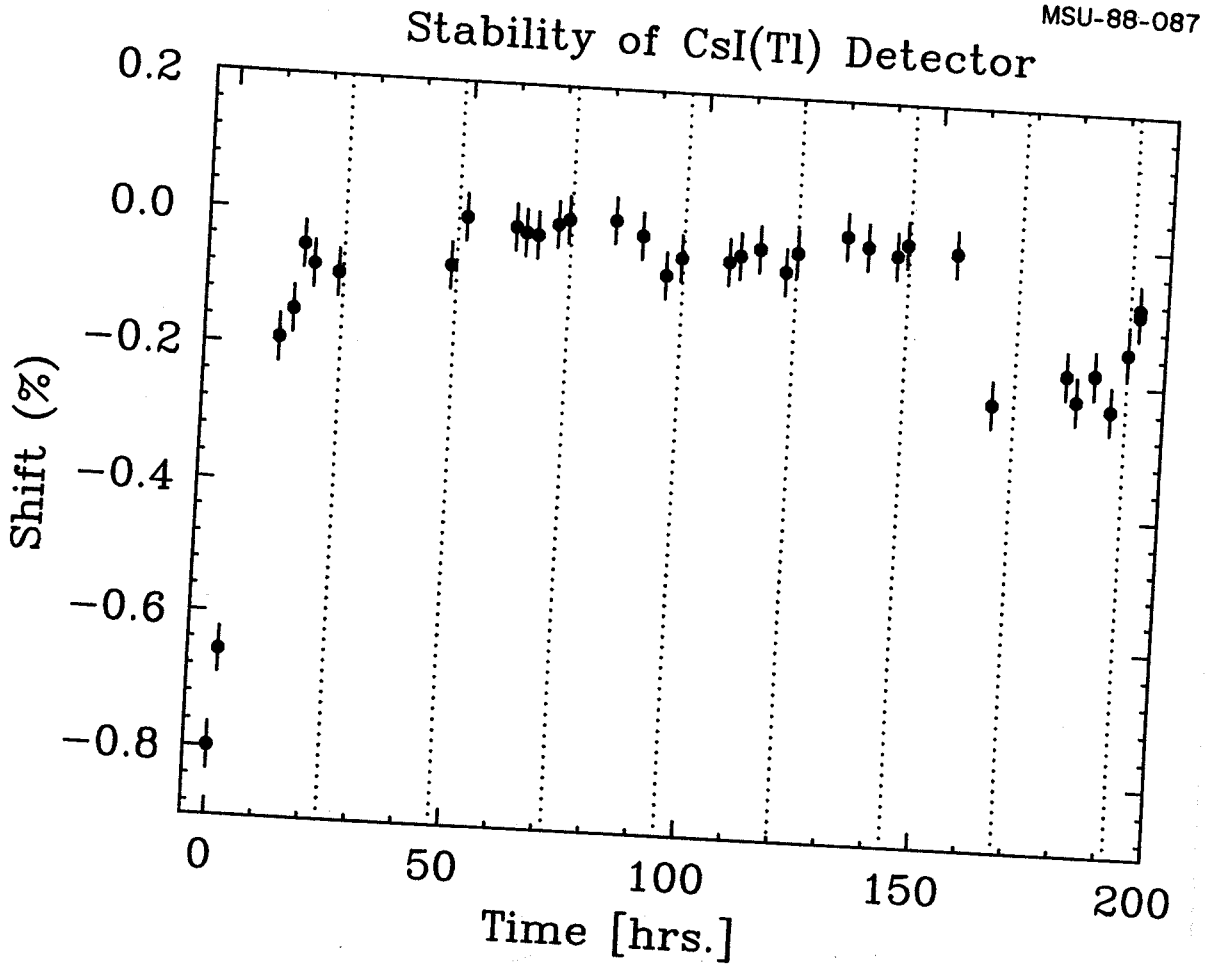

Figure 2.21: The stability of pulse-height of a CsI(Tl) detector.

resulting from the $^{12}C(\alpha,d)$, $^{12}C(\alpha,t)$ and $^{12}C(\alpha,\alpha)$ reactions indicate excellent detector resolutions of 0.5-0.6% (FWHM). For this particular CsI(Tl) crystal, a maximum peak shift of 0.6% was measured with our γ-ray scanning test. The measured electronic noise was about 300 keV.

Finally, to illustrate the degree of pulse-height stability, Figure 2.21 gives an example for one typical CsI(Tl) detector. Except for the initial phase-in period of a few hours during which the temperature of the detector and its assciated electronics had to stabilize, the pulse height remained constant within 0.5% up to 8 days. The gain stability of our actual CsI(Tl) detectors was measured to be of comparable quality during the whole experiment for up to one month.

In summary, our investigations have shown that improved fabrication techniques have allowed the production of large volume CsI(Tl) detectors with excellent energy resolution and excellent long-term stability when photodiode readout is used.

CHAPTER 3. EXPERIMENTAL DETAILS

3.1 Mechanical Setup

The experiment was performed in the 92 inch scattering chamber of the National Superconducting Cyclotron Laboratory of Michigan State University using beams from the K1200 cyclotron. Light particles were detected with ΔE-E telescopes consisting of silicon ΔE-detectors and CsI(Tl) or NaI(Tl) E-detectors.

The detectors were arranged in two seperate hodoscopes. The geometrical placement of these hodoscopes is indicated in the schematic drawing shown in Figure 3.1.

One hodoscope with 37 Si-CsI(Tl) telescopes was centered at $\theta=25°$ and $\phi=0°$ (where θ and ϕ denote the polar and azimuthal angles with respect to the beam axis) and at a distance of 105 cm from the target. Its front face geometry is shown in Figure 3.2. (Due to the low yield of CsI(Tl) crystals grown by the new technique [Gong 90a] at BICRON Corp., we were not able to fully implement the 56 element hodoscope at the time of this experiment.) Each telescope of this hodoscope subtended a solid angle of $\Delta\Omega=0.37$ msr and consisted of a 300 μm thick planar surface barrier detector of 450 mm^2 active area and a cylindrical CsI(Tl) scintillator (length= 10cm, diameter= 4cm) read out by a 400 mm^2 PIN diode [Gong 88]. The nearest neighbor spacing between adjacent detectors was $\Delta\theta=2.6°$. The CsI(Tl) detector array was kept at a constant temperature around 15°C degree with an ethanol refrigerator and had excellent gain stability (better than 1% over a time period of one month).

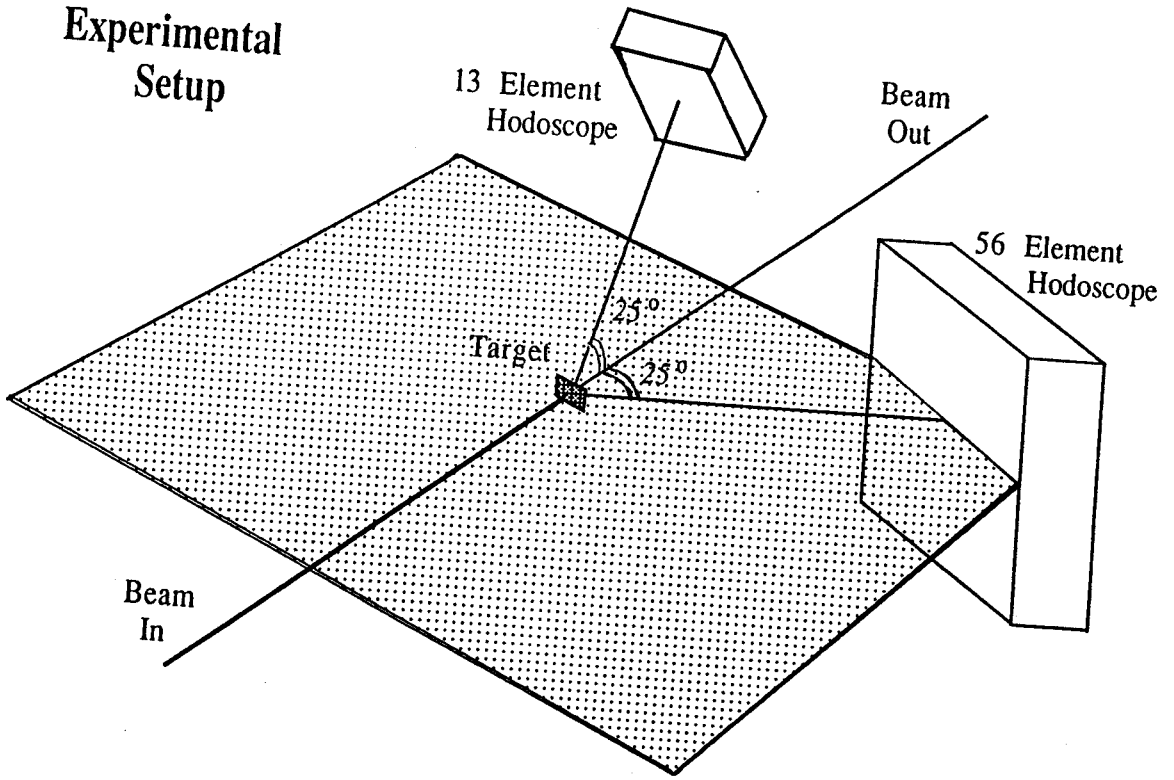

Figure 3.1: Schematic view of the experimental setup with two hodoscopes being used.

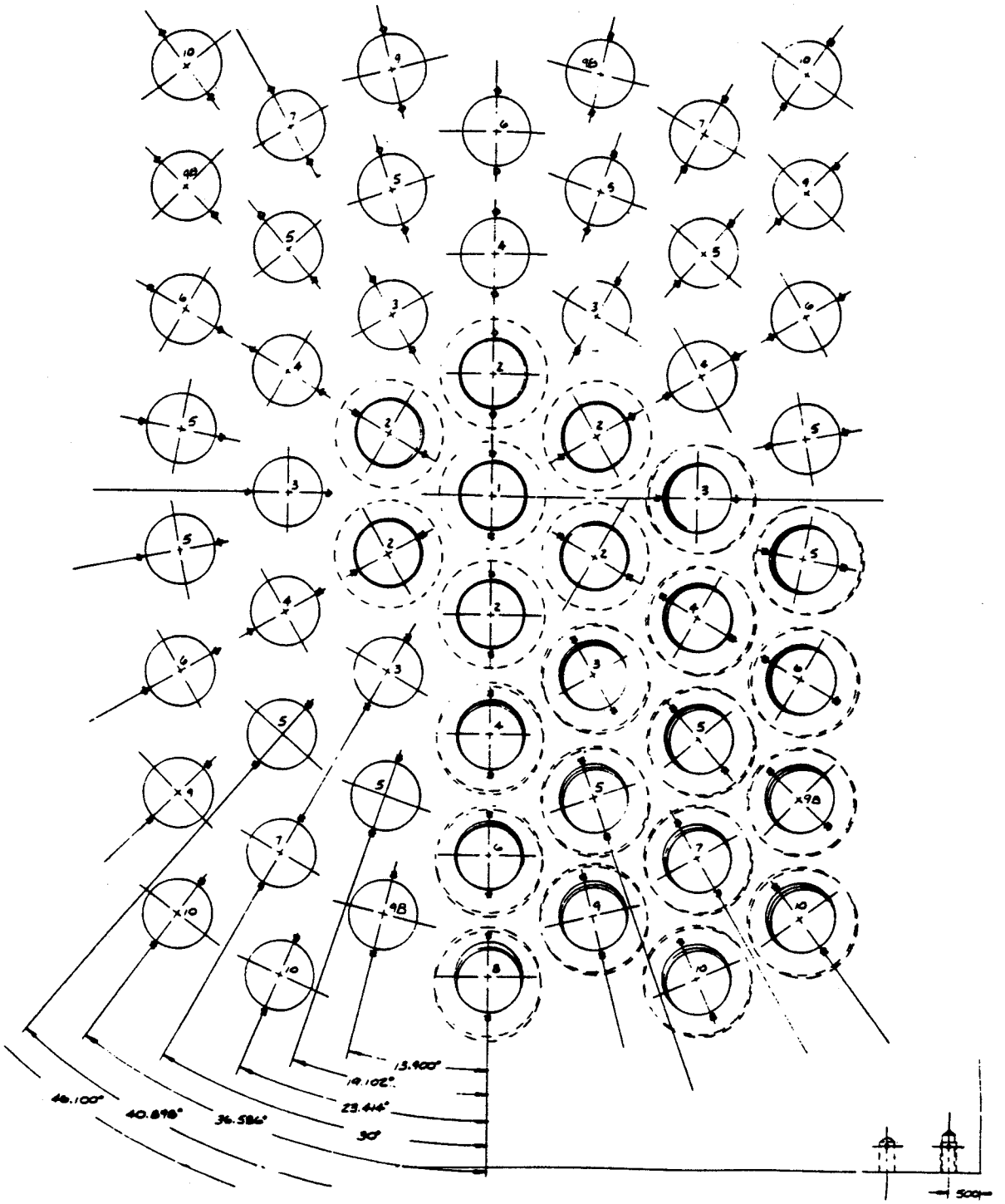

Figure 3.2: Schematic view of the front face of the 56 element hodoscope.

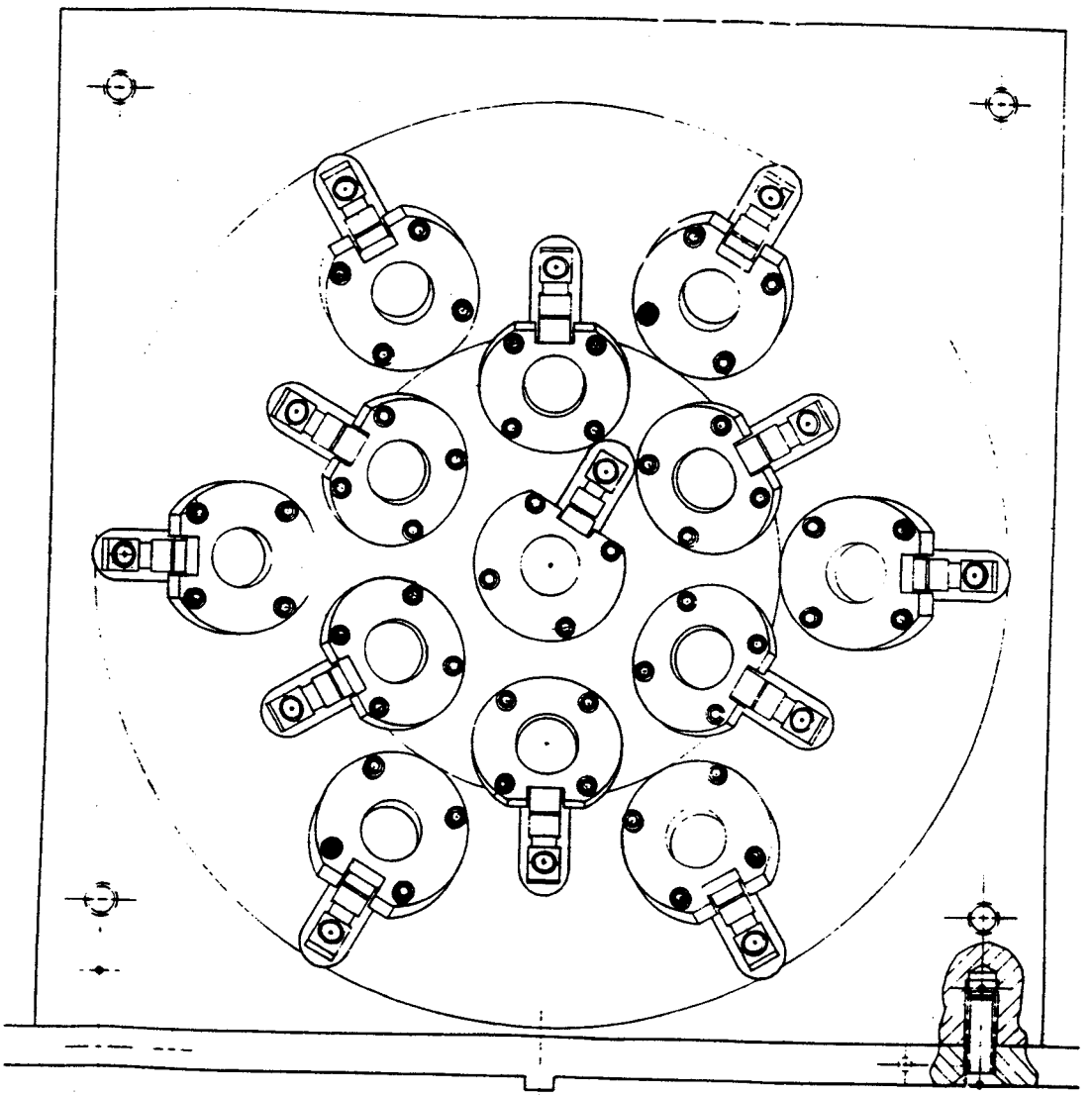

Figure 3.3: Schematic view of the front face of the 13 element hodoscope.

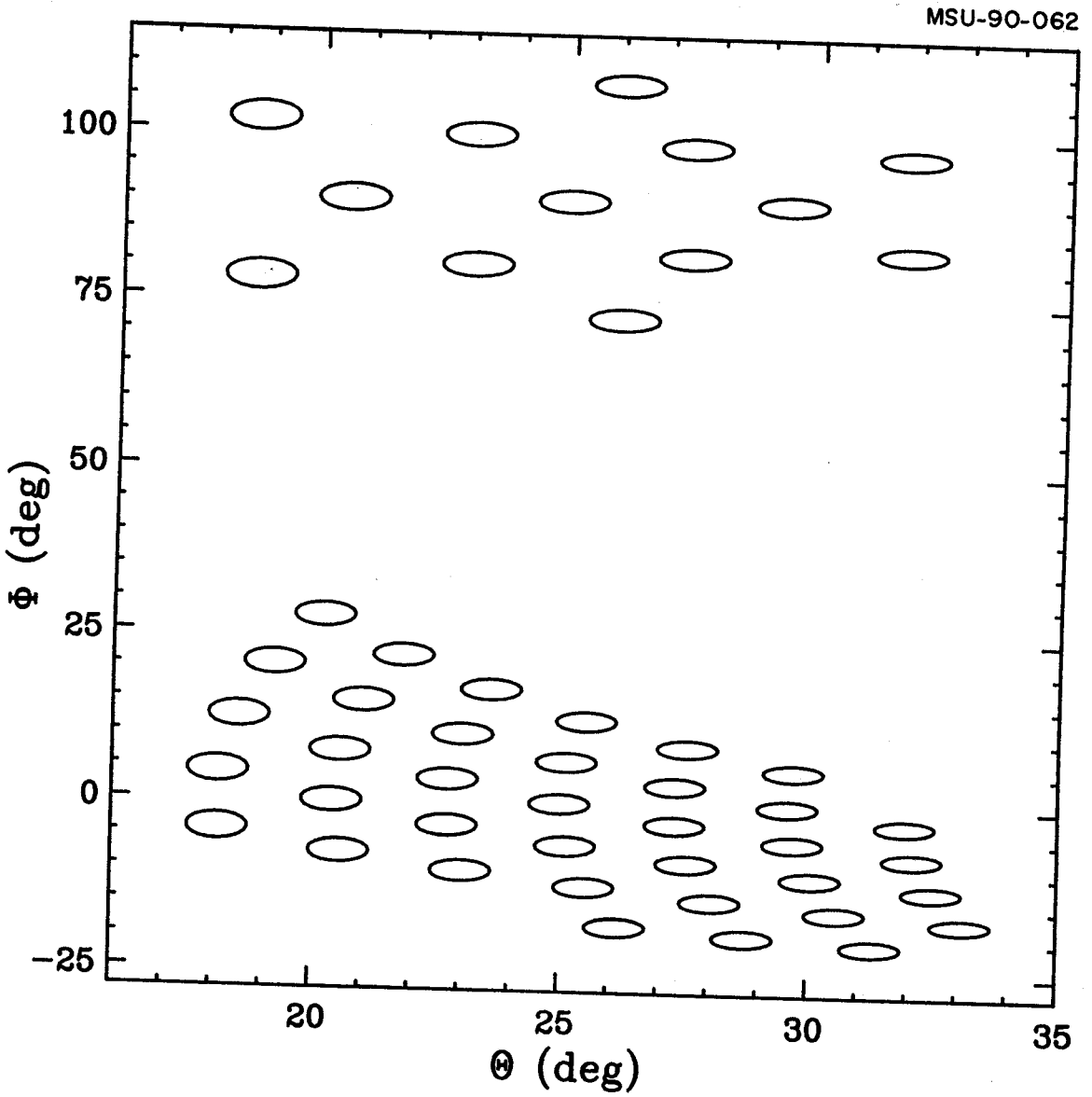

Figure 3.4: Polar coordinates of 50 ΔE-E telescopes used in the experiment.

The other hodoscope with 13 Si-NaI(Tl) telescopes was centered at θ=25° and ϕ=90° and at a distance of 60 cm from the target. Its front face geometry is shown in Figure 3.3. Each telescope of this array subtended a solid angle of $\Delta\Omega$=0.5 msr and consisted of a 400 μm thick Si surface barrier detector of 200 mm^2 active area and a cylindrical NaI(Tl) scintillator (length= 10cm, diameter= 4cm) read out by a photomultiplier tube. The nearest neighbor spacing between adjacent detectors was $\Delta\theta$=4.4°. Gain drifts of the individual photomultiplier tubes were measured by a light pulser system as well as by changes in the location of the particle identification lines in the ΔE-E matrix [Poch 87]. These gain drifts were determined in the off-line analysis and corrected with an overall accuracy of better than 2%.

Figure 3.4 shows the polar angles covered by individual telescopes in the the θ-ϕ plane.

3.2 Electronics

The principle for the electronic processing of all detector signals is sketched in Figure 3.5. The analog signals from either Si solid-state detector or CsI(Tl)/NaI(Tl) scintillation detector were first amplified by charge-sensitive pre-amplifiers (PA). They were further shaped and amplified by amplifiers (A). The slow outputs of the amplifiers were digitized by peak-sensing ADCs and read out and recorded later on magnetic tape as the energy information. The fast outputs of the amplifiers were converted to logic signals by either Constant-Fraction-Discriminators (CFD) or Leading-Edge-Discriminators (LED). Figure 3.6 depicts the sequences in processing NIM logic signals for a Si-NaI(Tl) telescope (upper part) and a Si-CsI(Tl) telescope (lower part), respectively. In order to detect high energy protons which deposit little energy in the transmission Si detectors, two thresholds of lower energy, E_L, and higher energy, E_H, were set for the fast E-outputs from NaI(Tl)/CsI(Tl) detectors. The valid telescope event was then defined as: $(\Delta E'_{Si} \bullet E_L + E'_L \bullet E_H)$ for a Si-CsI(Tl) telescope and $E_L \bullet (\Delta E_{Si} + E_H)$ for a

Note:

PA ——— Preamplifier

A ——— Amplifier

CFD ——— Constant Fraction Discriminator

LED ——— Leading Edge Discriminator

FIFO ——— Fan-In-Fan-Out

QDGG —— Quad Delay Gate Generator

DGG ——— Dual Gate Generator

~~~~ —— time-delay cable (not resistor)

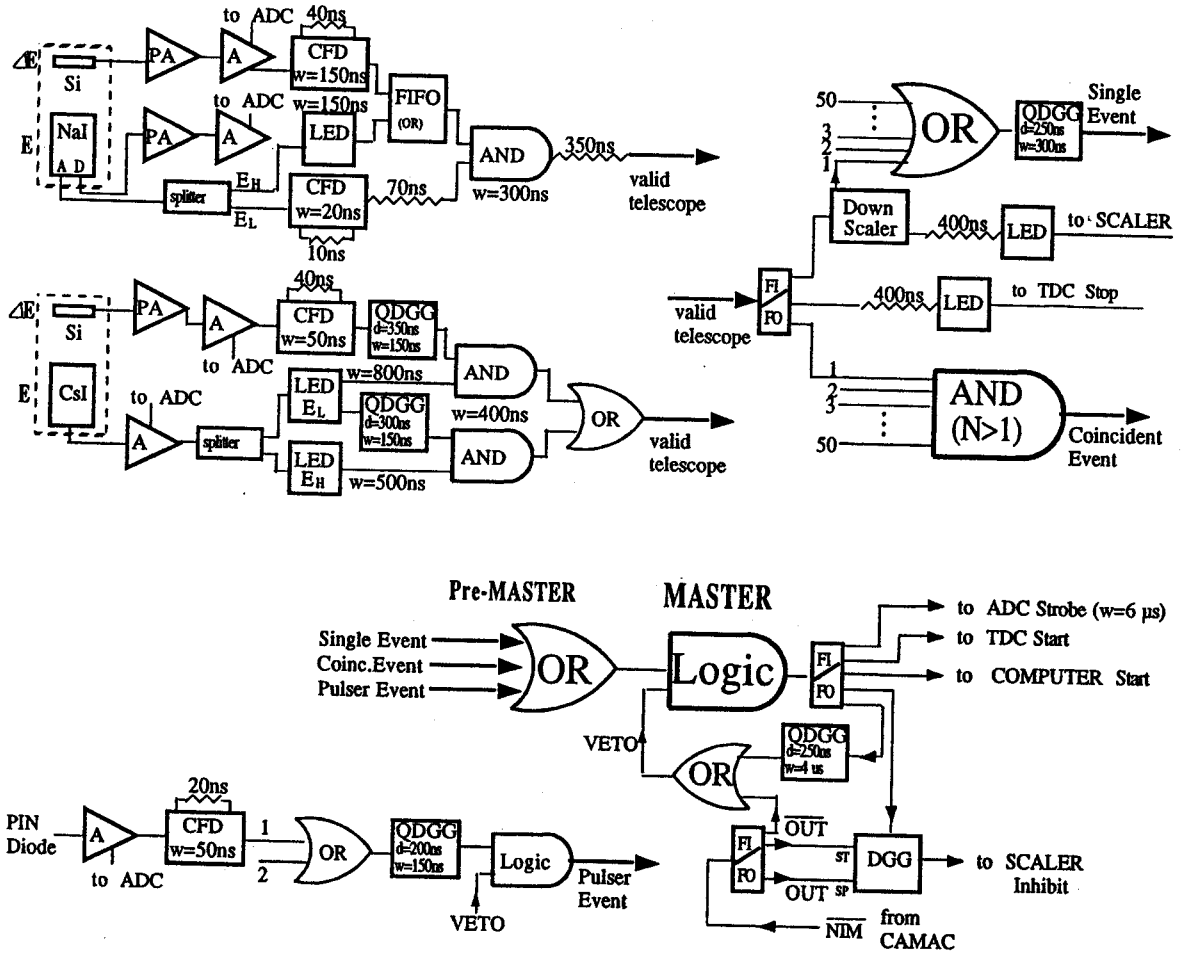

Figure 3.5: Block diagram of the electronic circuits and trigger logic.
~~~~

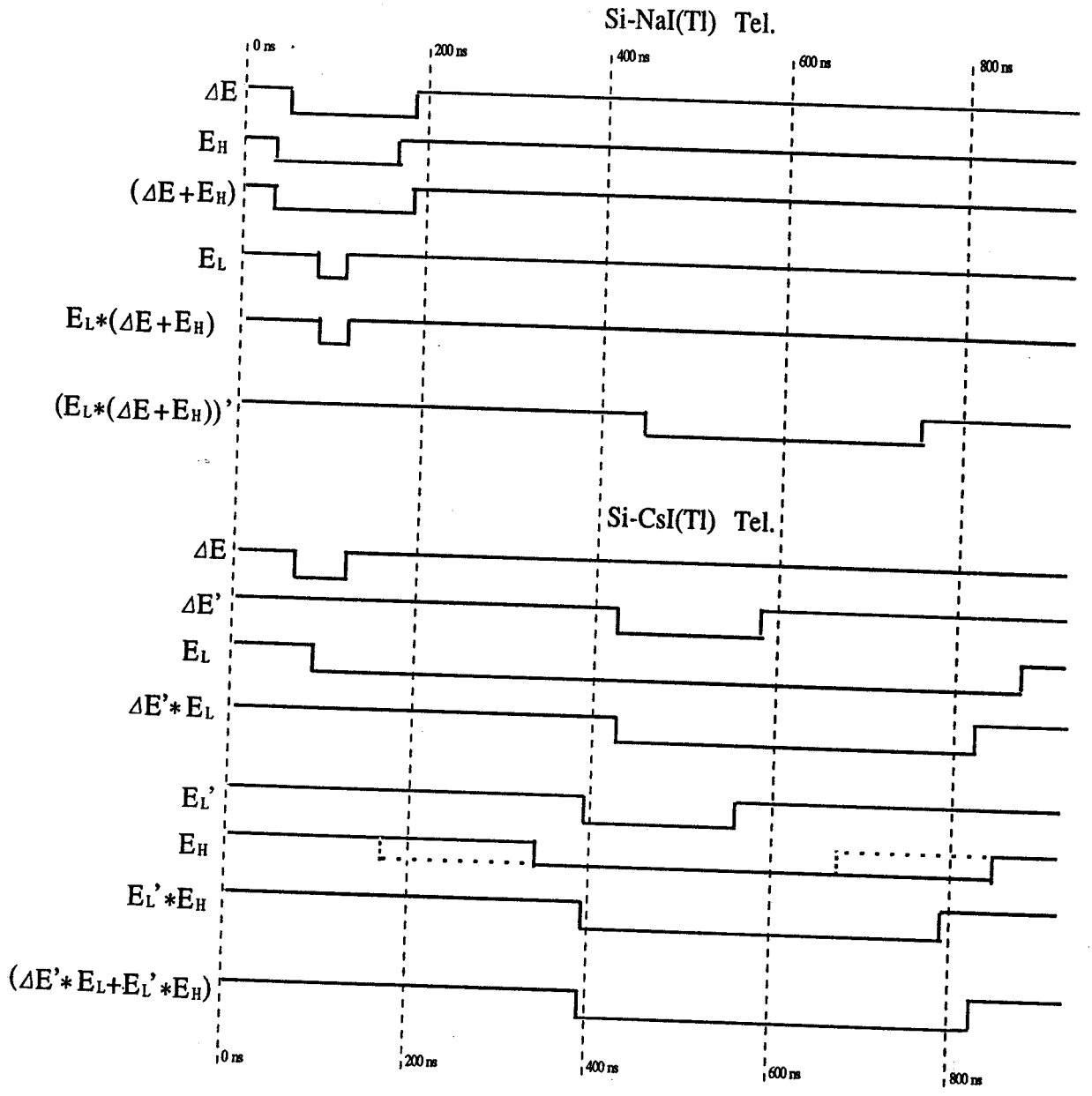

Figure 3.6: Diagram for processing the logic signals in a Si-NaI(Tl) or Si-CsI(Tl) telescope.

Si-NaI(Tl) telescope, where the primes indicated the delay-and-stretch operations on the corresponding signals. Advantage was taken of faster timing responses of Si detector in the Si-CsI(Tl) telescope and NaI(Tl) detector in the Si-NaI(Tl) telescope. The timing information of a valid telescope event was therefore determined by ΔE_{Si} or E_L(CsI) (when ΔE_{Si} was not present) in the Si-CsI(Tl) telescope or by E_L(NaI) in the Si-NaI(Tl) telescope. For protons, E_L was about 5 MeV and E_H about 30 MeV.

The logic signal of a valid telescope event was fanned out to (1) the coincidence multiplicity unit to register as a coincidence event when at least two telescopes fired within the coincidence timing window (around 400 ns); (2) the multiple-OR module to register as a single event after a certain factor of down-scaling; (3) Scalers and TDC Stop to register event rate and timing after appropriate delays.

Electronic pulser signals were provided for all pre-amplifiers in addition to the light pulser system for photomultiplier tubes. They were very useful for testing electronic modules and trigger logic. Gains shifts were monitored by the pulser events and corrected for in the off-line analysis wherever necessary.

Coincidence and down-scaled singles data were taken simultaneously, together with pulser events taken at much lower rate. A VETO circuit was incorporated to prevent ADC conversions during computer busy period. The MASTER logic thus defined provided trigger signals for TDC Start, ADC Strobe, and Computer Start. BIT registers were used to keep track of what type of event occurred and which detector fired.

3.3 Reactions

Four nuclear reactions with heavy ion beams were measured in the experiment. For reactions induced by ^{129}Xe at E/A=31 MeV, we used ^{27}Al and ^{122}Sn targets with areal densities of 5.6 and 5.3 mg/cm^2, respectively. For reactions induced by ^{14}N at E/A=75 MeV, we used ^{27}Al and ^{197}Au targets

with areal densities of 15.0 and 15.9 mg/cm^2, respectively. Typical beam intensities on target were approximately 5×10^9 ^{14}N(5+) ions per second and 1×10^8 ^{129}Xe(23+) ions per second. The beam spots on target had elongated shapes of typically 1-2 mm width and 2-3 mm height.

For the purpose of energy calibrations of individual detectors, a $(CH_2)_n$ target (25.4μm thick) was used to scatter α-particles of 160, 116, and 90 MeV incident energy after passing through Al degraders with thickness of 0, 880, and 1250 mg/cm^2, respectively. Resulting from two-body reaction kinematics, mono-energetic light particles such as protons, deuterons, tritons, ^{3}He, and ^{4}He were measured at various laboratory angles.

During the experiment, raw data were sampled periodically and diagnostic spectra were monitored on line to insure that all detectors were functioning well and good quality data were recorded on magnetic tape.

CHAPTER 4. DATA REDUCTION

In this chapter, we explain the offline data-reduction procedures used for identifying particle, calibrating energy, correcting time-walk, and correcting detector efficiency.

4.1 Particle Identification

Using the ΔE-E telescope, charged particles can be clearly identified [Goul 75] on the two-dimensional map of ΔE (the energy loss in the thin transmission detector) v.s. E (the energy loss in the stopping detector). However, we did not set the particle gates in the ΔE-E map because excessively large computer memory is required for sufficient channel resolution. Instead, we used a linearization function [Shim 79] to transform the ΔE-E map into a PID-E map where PID is the value of the corresponding linearization function.

For illustration, Figure 4.1 shows typical PID-E plots for a Si-NaI(Tl) telescope in the left panel and for a Si-CsI(Tl) telescope in the right panel. The PID function for a Si-NaI(Tl) telescope was defined as:

$$PID = 100 \bullet [\log(b \bullet \Delta E) + (b-1) \bullet \log(E + c \bullet \Delta E) - 0.7]. \quad (4.1)$$

where c=0.5, b=1.5-0.18 •ΔE/t, and t=400μm (the Si detector thickness). The PID function for a Si-CsI(Tl) telescope was similarly defined as:

$$PID = 80 \bullet [\log(b \bullet \Delta E) + (b-1) \bullet \log(E + c \bullet \Delta E) - 2.5]. \quad (4.2)$$

where c=0.5, b=1.825-0.18 •ΔE/t, and t=300μm (the Si detector thickness). To set particle gates unambiguously for the isotopes of Li and Be in the CsI(Tl) detector, we magnified their existing regions by using another PID function which was

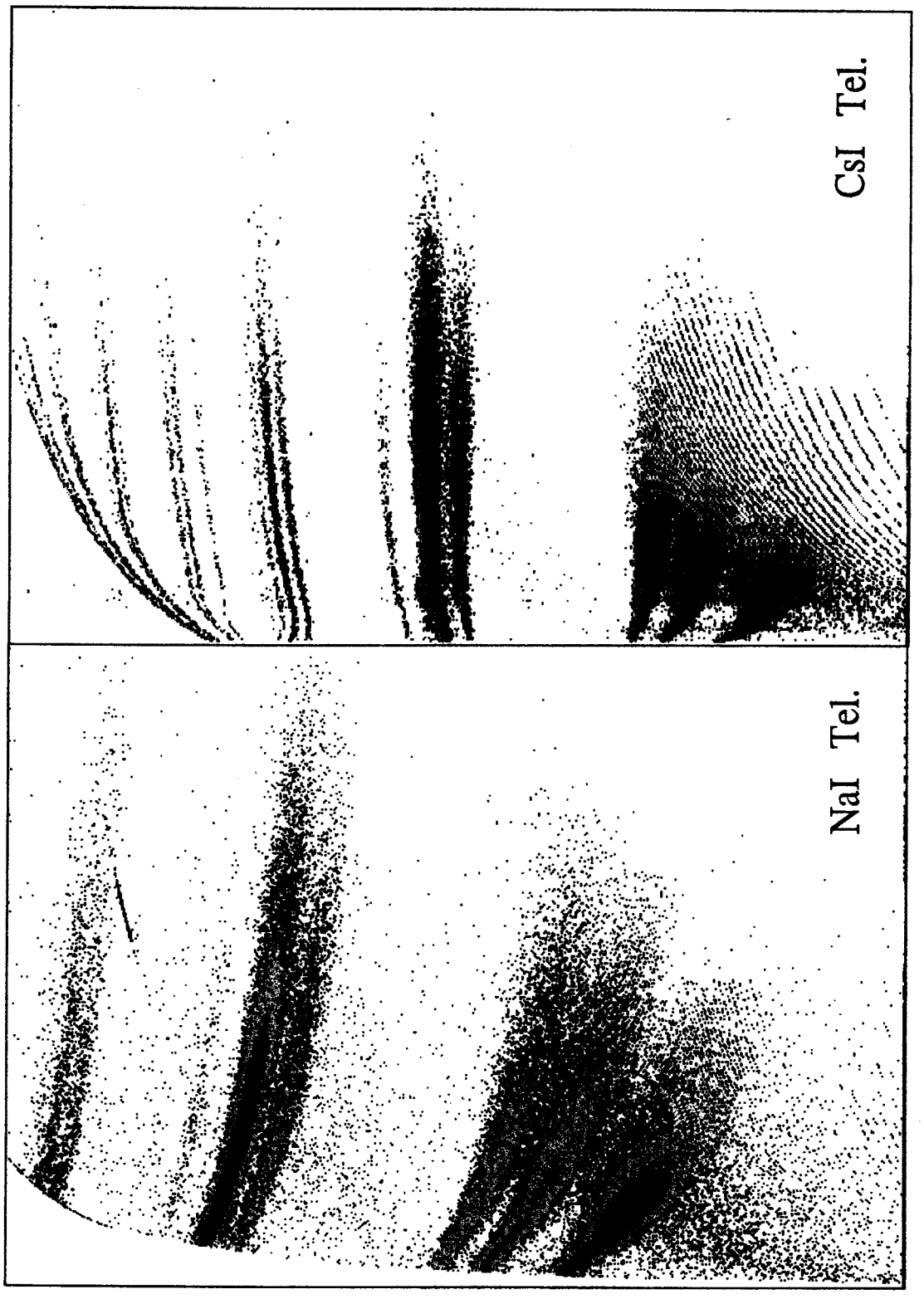

Figure 4.1: Two-dimensional plots of PID v.s. E for a Si-NaI(Tl) telescope (left panel) and for a Si-CsI(Tl) telescope (right panel) whereon particle gates were set.

defined as:

$$PID = 220 \bullet [\log(b \bullet \Delta E) + (b-1) \bullet \log(E + c \bullet \Delta E) - 5.5]. \quad (4.3)$$

where c=0.5, b=1.65-0.18 $\bullet \Delta E/t$, and t=300μm (the Si detector thickness).

In Figure 4.1, it is clear that p, d, t, ^{3}He, ^{4}He, ^{6}He, and ^{6}Li, and ^{7}Li, are identified in the Si-NaI(Tl) telescope and p, d, t, ^{3}He, ^{4}He, ^{6}He, ^{6}Li, ^{7}Li, ^{8}Li, ^{9}Li, ^{7}Be, ^{9}Be, ^{10}Be, and B are identified in the Si-CsI(Tl) telescope.

4.2 Energy Calibration

Because of their high linearity, the ΔE-Silicon detectors were simply calibrated by a precision electronic pulsers and by means of 5.5 MeV α particles from a ^{241}Am source. Once calibrated by the 5.5 MeV α particles, the pulser would inject known amounts of charge through a calibrated capacitor into a Si preamplifier. By setting the pulser at several amplitudes ΔE_i, we obtained the corresponding peaks $N_i(\Delta E)$ on the ΔE-ADC spectrum. A linear fit by the equation:

$$\Delta E_i = a \bullet N_i(\Delta E) + b, \quad (4.4)$$

provided the desired energy calibration coefficients (a, b) for a Si-detector.

Energy calibrations for NaI(Tl) or CsI(Tl) scintillator detectors were more involved. Previous energy calibrations for NaI(Tl) [Chen 88] were performed by directing secondary charged particles of known rigidities into each telescope. This method allowed the simultaneous calibrations for different particles of precisely-known incident energies. Unfortunately, this technique could not be used in the present setup as a magnetic beam analysis setup was not available. Alternative energy-calibration methods had to be employed for our detectors.

4.2.1 Two-body Reaction Kinematics

A $(CH_2)_n$ target of 25.4μm thickness was bombarded by α-particles of 160, 116, and 90 MeV incident energy after passing through the Al degraders with thickness of 0, 880, and 1250 mg/cm^2 during the calibration run. Calibration

points could be obtained in most telescopes by detecting mono-energetic light-charged particles (p,d,t, ^{3}He, ^{4}He) from scatterings or direct reactions such as:

$$p(^{4}He,p)^{4}He, \quad (4.5)$$

$$p(^{4}He,d)^{3}He, \quad (4.6)$$

$$^{12}C(^{4}He,d)^{14}N, \quad (4.7)$$

$$^{12}C(^{4}He,t)^{13}N, \quad (4.8)$$

$$p(^{4}He,^{3}He)d, \quad (4.9)$$

$$^{12}C(^{4}He,^{3}He)^{13}C, \quad (4.10)$$

$$^{12}C(^{4}He,^{4}He)^{12}C. \quad (4.11)$$

Other beams or targets were also used to supply a few extra calibration points for p and ^{4}He in the following scatterings:

$$p(^{20}Ne,p)^{20}Ne, \quad (4.12)$$

$$^{197}Au(^{4}He,^{4}He)^{197}Au. \quad (4.13)$$

Typical energy spectra of light-charged particles were already shown in Figures 2.10, 2.11, and 2.20. Recoil protons in Equation (4.5) or recoil deuterons in Equation (4.6) had broader peak widths than the real detector resolution because of kinematical smearing in detectors of finite angular acceptance. In all cases, the peak centroids were extracted to establish energy calibrations. Meanwhile, the corresponding energy values of all peaks were calculated by two-body kinematics. Typical energy calibrations derived from this technique are shown in Figure 4.2 for a CsI(Tl) detector and in Figure 4.3 for a NaI(Tl) detector.

For the energy calibration of protons in the NaI(Tl) detector (N04), a quadratic polynomial fit was performed [Chen 88], indicated by solid line in Figure 4.3. Included in the fit was one special point on the X-axis, which was the ADC channel offset (N_{offset}) determined from pulser calibrations. Since no data were available at higher energy, a linear extrapolation was used for E > 60MeV as indicated by the dashed line (obtained by a linear fit to all available

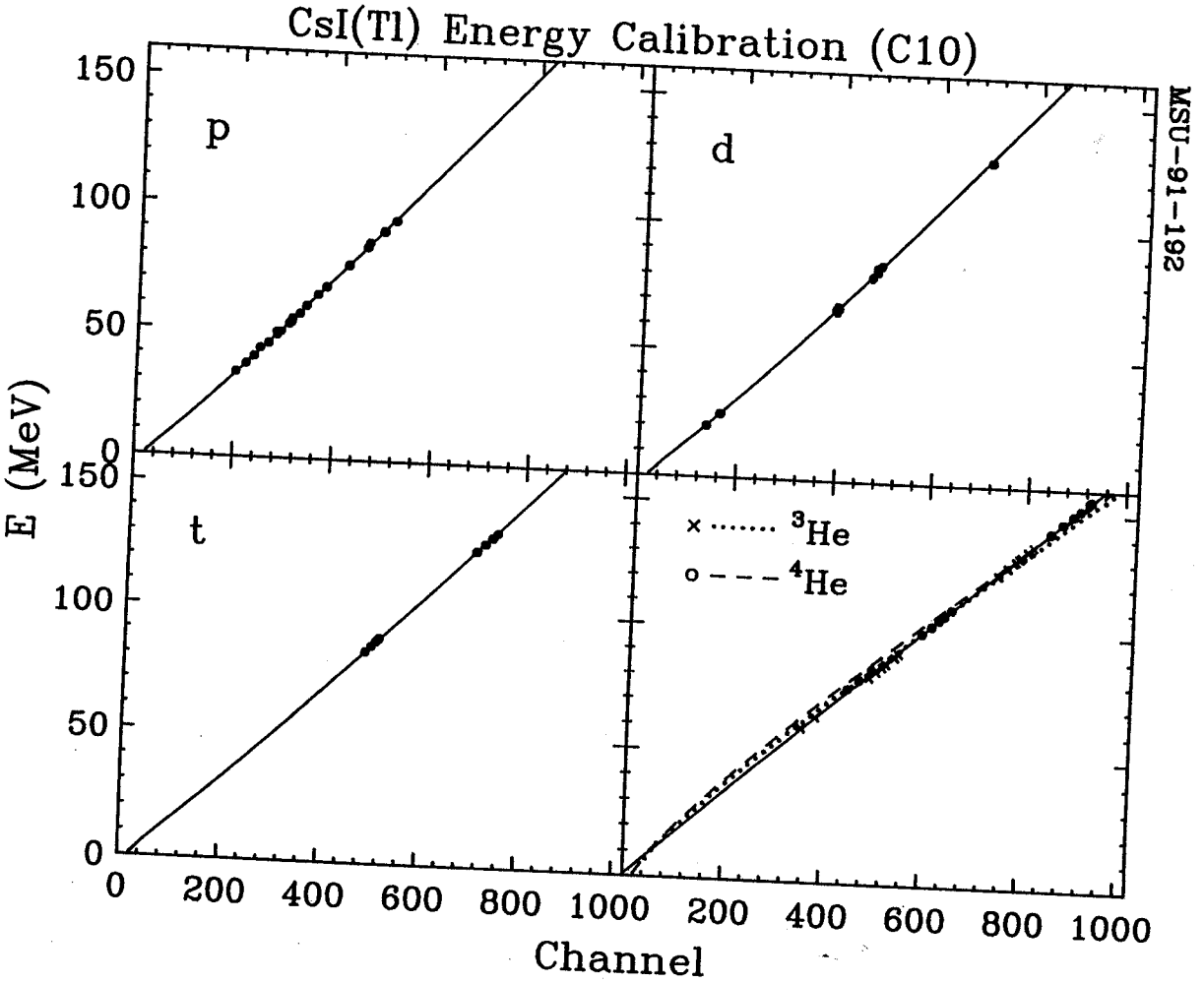

Figure 4.2 : Energy calibration of protons, deuterons, tritons, ^{3}He and ^{4}He for a CsI(Tl) detector (C10) obtained by two-body reaction kinematics. The curves are explained in the text.

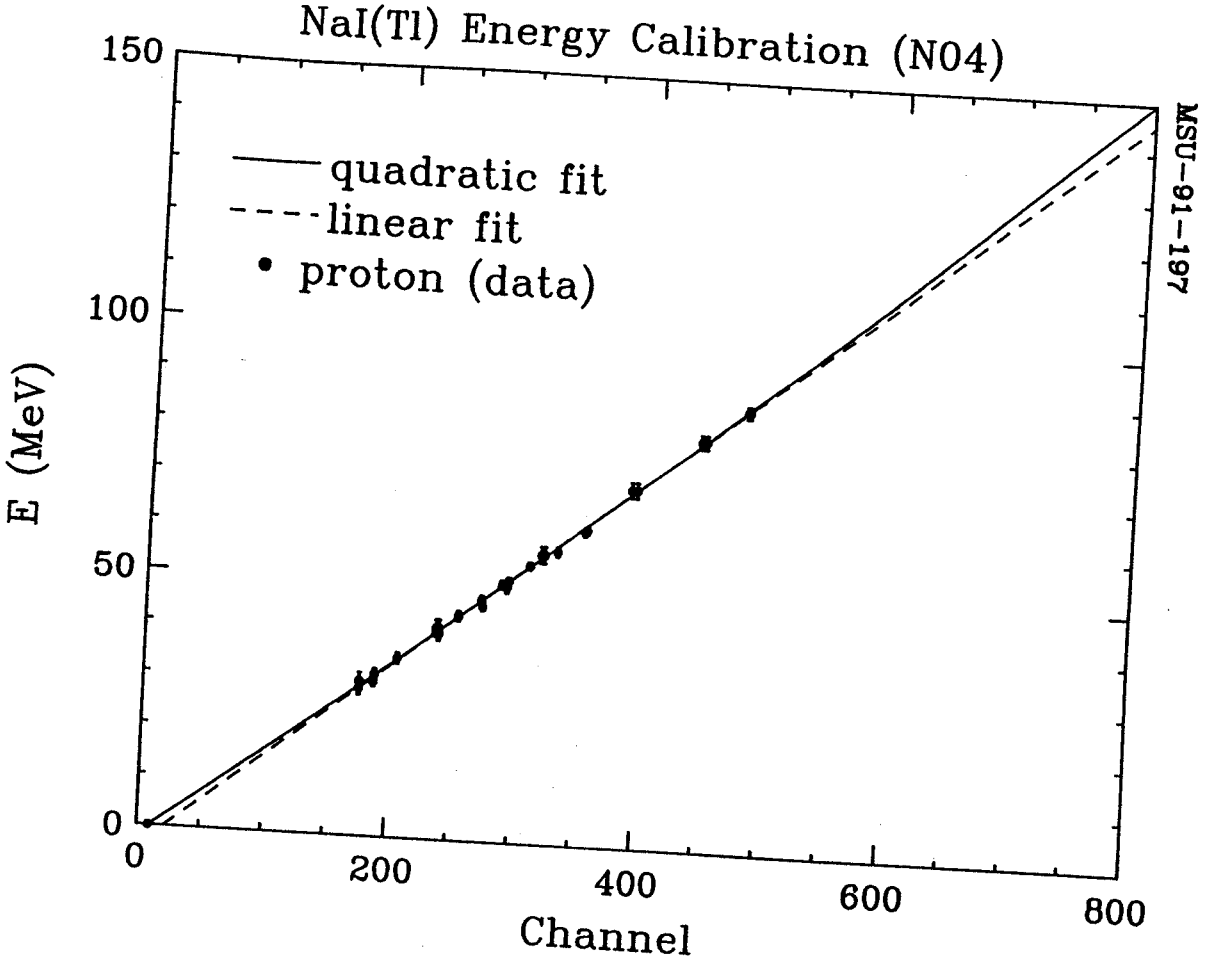

Figure 4.3 : Energy calibration of protons for a NaI(Tl) detector (N04) obtained by two-body reaction kinematics. The curves are explained in the text.

Table 4.1: Fit parameters for energy calibrations of various particles in a typical NaI(Tl)/CsI(Tl) detector (N04/C10) using the equation: $E\ (MeV) = A + B \bullet N(E) + C \bullet N(E)^2$.

Isotope	A	B	C	Comment
p,d,t	-1.575	0.1721	0.2158e-4	E≤60MeV, NaI(Tl)
p,d,t	-3.941	0.1868	0.0	E>60MeV, NaI(Tl)
^{3}He	0.629	0.199	0.0	NaI(Tl)
^{3}He	-0.258	0.168	0.0	CsI(Tl)
^{4}He	3.677	0.193	0.0	NaI(Tl)
^{4}He	1.548	0.166	0.0	CsI(Tl)
^{6}He	4.524	0.199	0.0	NaI(Tl)
^{6}He	2.643	0.167	0.0	CsI(Tl)
^{6}Li, ^{7}Li	13.507	0.214	0.0	NaI(Tl)
^{6}Li, ^{7}Li	8.523	0.178	0.0	CsI(Tl)
^{8}Li, ^{9}Li	11.891	0.177	0.0	CsI(Tl)
^{7}Be	20.505	0.181	0.0	CsI(Tl)
^{9}Be, ^{10}Be	19.705	0.195	0.0	CsI(Tl)
B	33.181	0.198	0.0	CsI(Tl)

data). The fitting coefficients are listed in Table 4.1 for this detector.

Energy calibrations of p,d,t, ^{3}He and ^{4}He are shown in the upper left and right panel and in the lower left and right panel of Figure 4.2, respectively, for the CsI(Tl) detector (C10). The points and crosses were measured data points, and the curves were calculated responses for p,d,t , ^{3}He and ^{4}He together with a line fit for ^{3}He and ^{4}He only.

The scintillation response to charged particles can be described [Birk 64] by a relation between dL/dx, the differential light output, and dE/dx, the stopping power of incident particles. Commonly referred to is the empirical Birk's formula:

$$dL/dx = \frac{S \bullet dE/dx}{1 + kB \bullet dE/dX} \quad , \tag{4.14}$$

where S is the scintillation efficiency, k is the relative quenching probability, and B•dE/dx is the density of damaged molecules along the track of the penetrating particle. The functional values of dL/dE v.s. dE/dx are listed [Birk 64, Pink 89] in Table 4.2, which were used for calculating light outputs for p,d,t, ^{3}He and ^{4}He in CsI(Tl) detectors.

For a particle of given energy E, the light output L(E) can then be calculated by the following integral:

$$L(E) = \int_0^{R(E)} \frac{dL}{dE}\left(\frac{dE}{dx}\right) \bullet \frac{dE}{dx}\, dx, \tag{4.15}$$

where dE/dx was the stopping power in the layer between x and x+dx and R(E) was the stopping range, both of which were calculated from Ziegler's parametrizations [Zieg 77]. L(E) was then associated with the ADC channel N(E) by the linear relationship:

$$N(E) = N_{offset} + \eta \bullet L(E). \tag{4.16}$$

Table 4.2: Differential light output, dL/dE, of CsI(Tl) scintillator v.s. differential energy loss, dE/dx (MeV/mg/cm^2).

dE/dx	0.001	0.002	0.003	0.004	0.005	0.006	0.007	0.008
dL/dE	0.980	0.980	0.985	1.000	1.010	1.018	1.030	1.042
dE/dx	0.009	0.010	0.020	0.030	0.040	0.050	0.060	0.070
dL/dE	1.057	1.071	1.198	1.255	1.241	1.201	1.175	1.141
dE/dx	0.080	0.090	0.100	0.200	0.300	0.400	0.500	0.600
dL/dE	1.108	1.085	1.057	0.849	0.717	0.613	0.540	0.500
dE/dx	0.700	0.800	0.900	1.000	2.000	10.000	20.000	100.00
dL/dE	0.465	0.435	0.415	0.400	0.300	0.170	0.140	0.100

Here, η is the normalization constant which is the same for p, d, and t and slightly different for ^{3}He and ^{4}He.

Figure 4.2 compares the calculated responses to the measured data. The calculations have satisfactorily reproduced the energy calibration data for p, d, t and therefore provide the final energy calibrations for these particles. However, the calculations, indicated by dotted and dashed curves, respectively for ^{3}He and ^{4}He, did not go through the data points at all energies and showed larger non-linearity at low energies. The discrepancy might be related to the fact that fast scintillation component of CsI(Tl) is known to depend on dE/dx. In our analysis, we had adopted the simple linear fit to the measured ^{3}He and ^{4}He calibration points. This is justified by the quality of the fits.

4.2.2 Energy-loss Calculations

One of the advantages of using a ΔE-E telescope to measure charged particles is that some energy calibrations can be accomplished in the off-line analysis when calibration beams of well known energy are not available. With this technique, one uses the known ΔE calibration and ΔE detector thickness to deduce the energy deposited in the CsI(Tl)/NaI(Tl) detector.

Figures 4.4 and 4.5 show the centroids of particle identification lines in the ΔE-E maps for representative Si-CsI(Tl) and Si-NaI(Tl) telescopes, respectively. For a specific particle, each point represents N(E), the centroid position of the E-ADC channel numbers corresponding to N(ΔE), a narrow bin of ΔE-ADC channels. A function can be defined by:

$$N(E) = f(N(\Delta E)). \qquad (4.17)$$

For a charged particle (Z,A) of given incident energy (E), we calculated [Zieg 77, Zieg 85, Hube 90] the energy losses: ΔE in Si detector of known thickness and E in NaI(Tl)/CsI(Tl) detector. The energy calibration of N(E) v.s. E was then established through Equations (4.4) and (4.17). Using this procedure, we were able

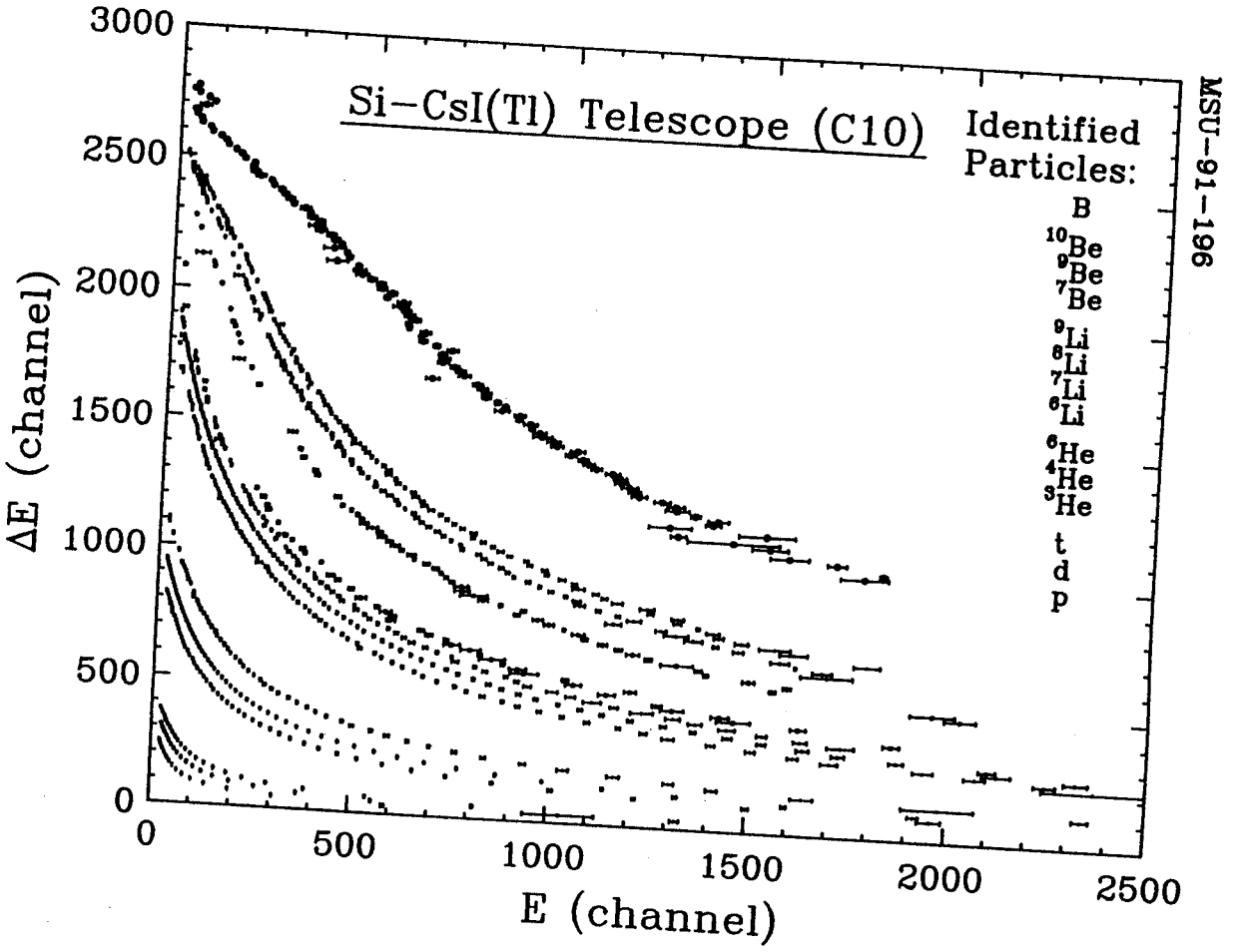

Figure 4.4 : Two-dimensional map of ΔE (the energy loss in Si. detector) v.s. E (the energy loss in CsI(Tl) detector) which was used for the off-line energy calibrations of all identified particles in a CsI(Tl) detector (C10).

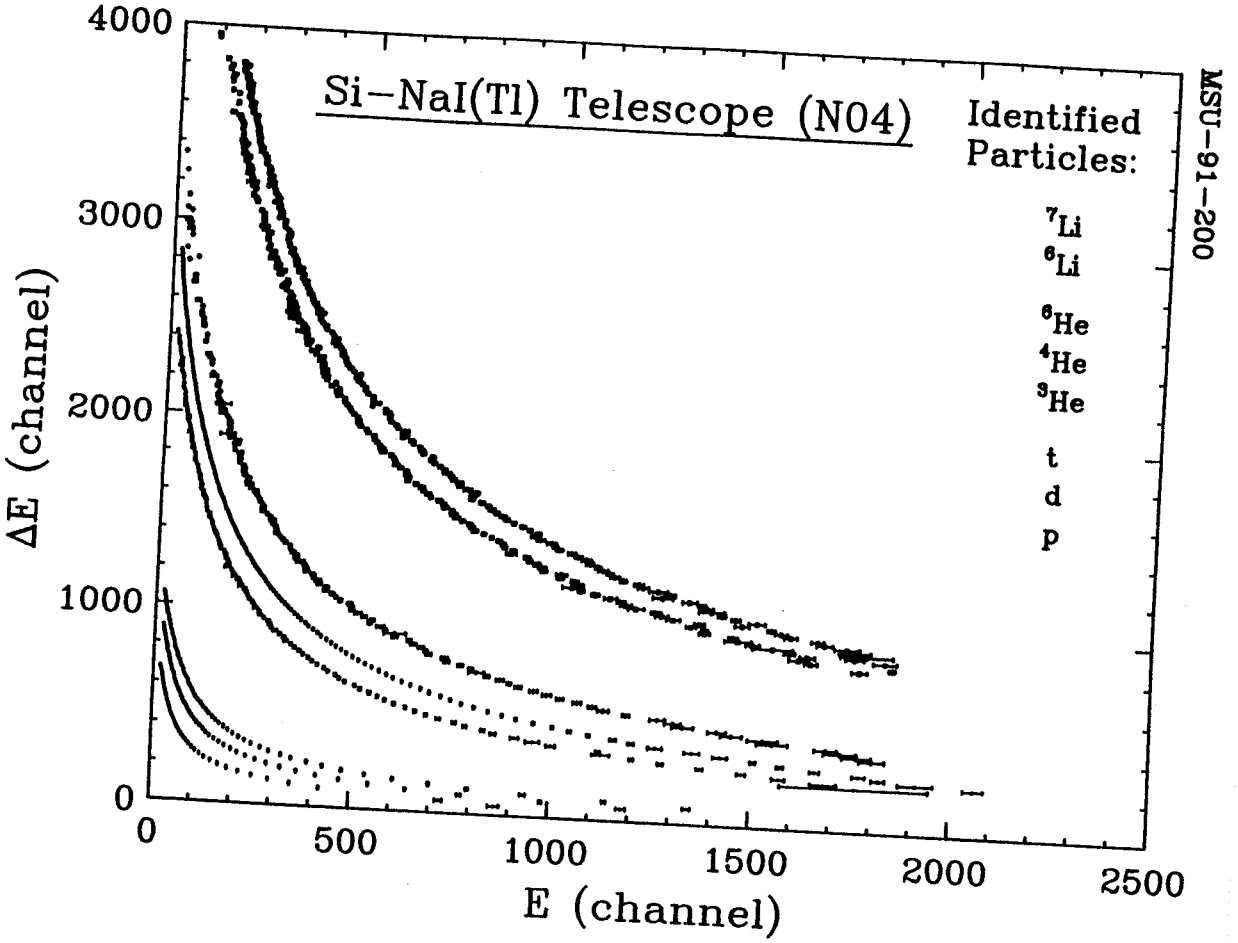

Figure 4.5 : Two-dimensional map of ΔE (the energy loss in Si. detector) v.s. E (the energy loss in NaI(Tl) detector) which was used for the off-line energy calibrations of all identified particles in a NaI(Tl) detector (N04).

to calibrate almost all particles for the energy ranges of interest. Typical examples are given in Figures 4.6-8 for the CsI(Tl) detector (C10) and in Figures 4.9-10 the NaI(Tl) detector (N04).

In Figure 4.6, the solid points are the same data as shown in Figure 4.2, which were obtained from two-body reaction measurements, while the open points and crosses are derived from energy-loss calculations. After adjusting the thickness of the Si-detector within 5%, we achieved remarkable agreement between the two calibration procedures for protons, deuterons, and tritons. It should be pointed out that the two-body reaction technique mainly provided data points at high energies, and the energy-loss calculation technique supplied most data points at low energies. Data points at very high energy given by the second technique were less reliable since the numerical interpolation or extrapolation had large uncertainty. As seen from Figure 4.4 and 4.5, the ΔE-E curves become flat at large N(E), this technique therefore loses its sensitivity. For the Helium particles, we adopted the simple linear fits which could represent all data rather well.

Energy calibrations of the Lithium, Beryllium, and Boron particles were obtained by the energy-loss calculations only, as shown in Figure 4.7. For simplicity, linear fits were used. The fitting coefficients are listed in Table 4.1. In Figure 4.8, energy calibrations of p, ^{4}He, ^{7}Li, ^{7}Be, and B are compared for the CsI(Tl) detector (C10). The non-linear behavior of proton response with respect to other particles was not well understood and was observed for almost all detectors. It might be related to light collection efficiency for particles stopping at different ranges.

In the same way, we obtained the energy calibrations of p,d,t, ^{3}He, ^{4}He, ^{6}He, ^{6}Li, and ^{7}Li for the NaI detector (N04) as shown in Figures 4.9-10. We had used the same proton energy calibration as discussed in Section 4.2.1 for deuterons and tritons since they showed very similar responses. Energy calibrations for ^{3}He,

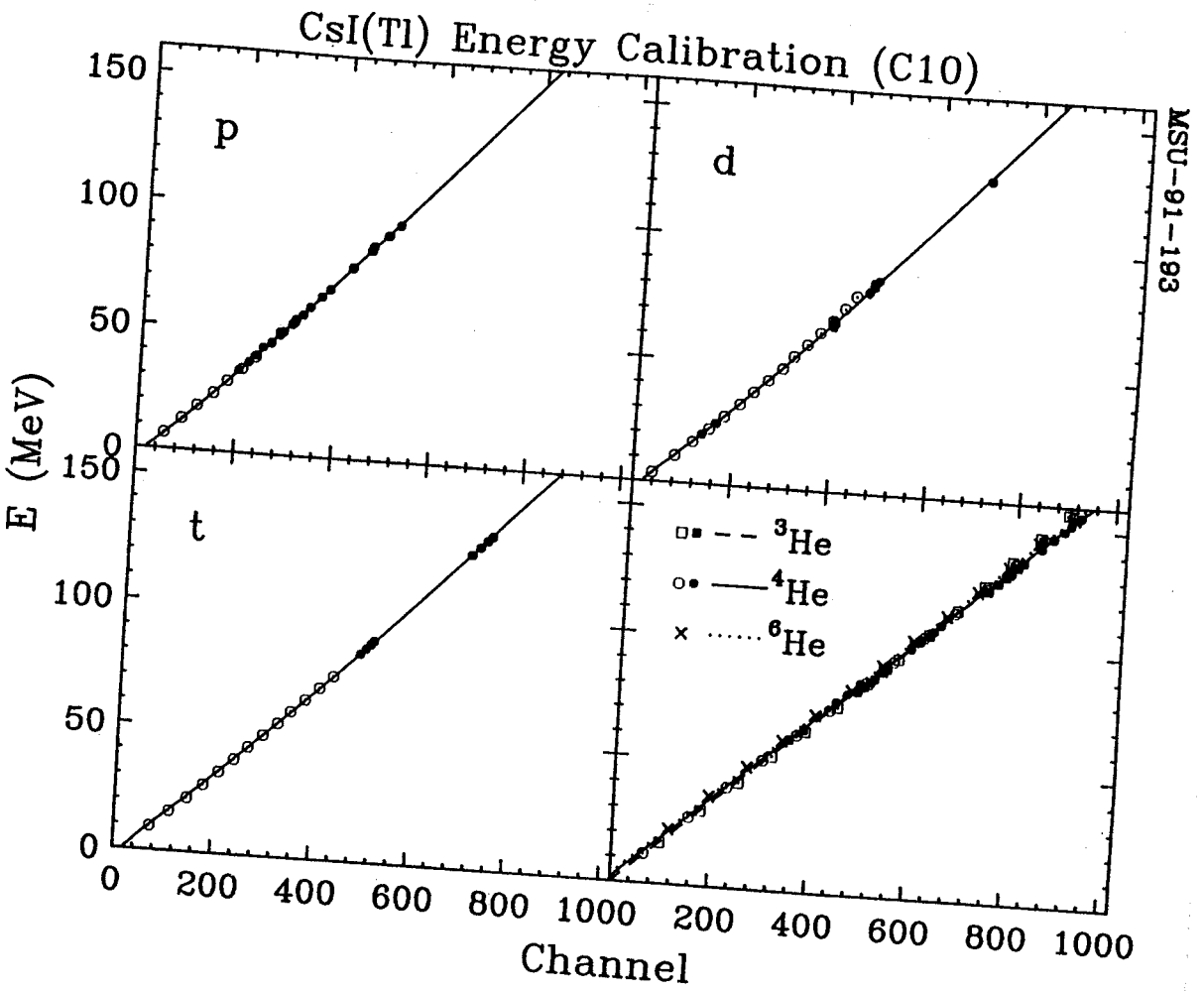

Figure 4.6 : Energy calibration of protons, deuterons, tritons, ^{3}He, ^{4}He, and ^{6}He for a CsI(Tl) detector (C10) obtained by both two-body reaction kinematics (solid points) and energy-loss calculations (open points). The curves are explained in the text.

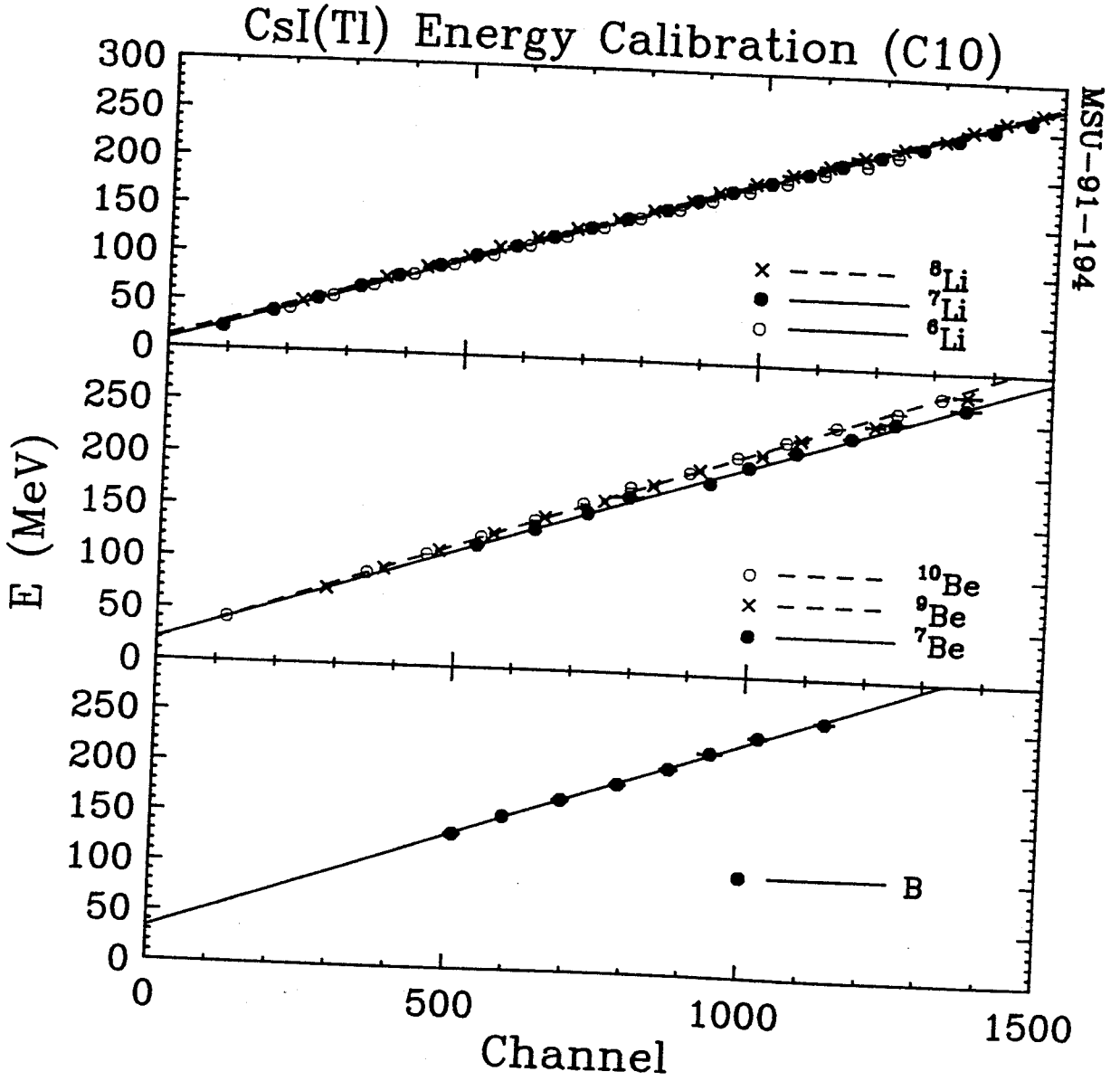

Figure 4.7 : Energy calibration of ^{6}Li, ^{7}Li, ^{8}Li, ^{7}Be, ^{9}Be, ^{10}Be, and B for a CsI(Tl) detector (C10) obtained by energy-loss calculations. The curves are linear fits to the data points. See text for explanations.

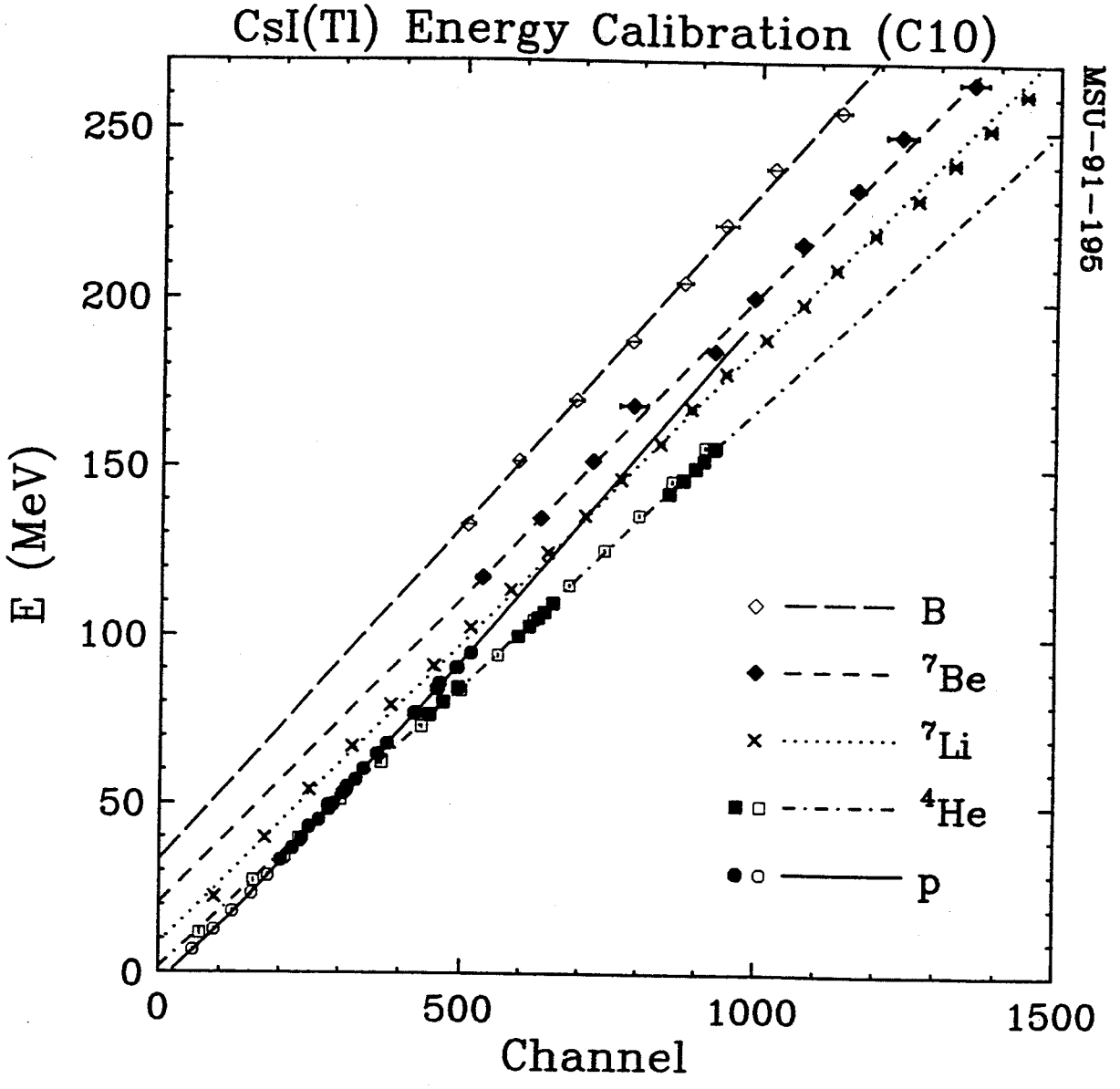

Figure 4.8 : Comparison of energy calibrations for particles such as proton, ^{4}He, ^{7}Li, ^{7}Be, and B measured in a CsI(Tl) detector (C10). The curves are the corresponding fits. See text for explanations.

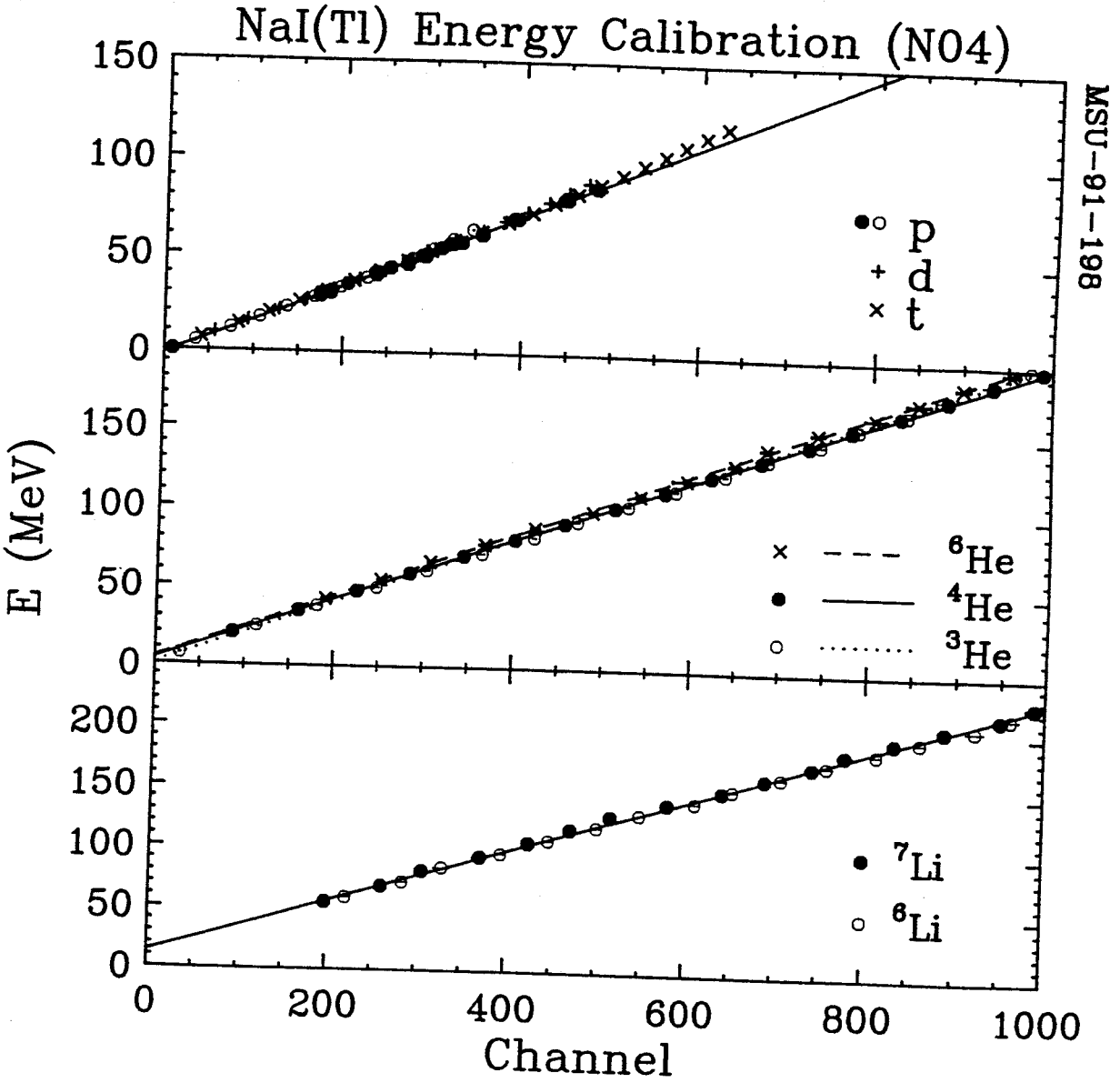

Figure 4.9 : Energy calibration of protons, deuterons, tritons, ^{3}He, ^{4}He, ^{6}He, ^{6}Li, and ^{7}Li for a NaI(Tl) detector (N04) obtained by energy-loss calculations. The curves are corresponding fits to the data points. See text for explanations.

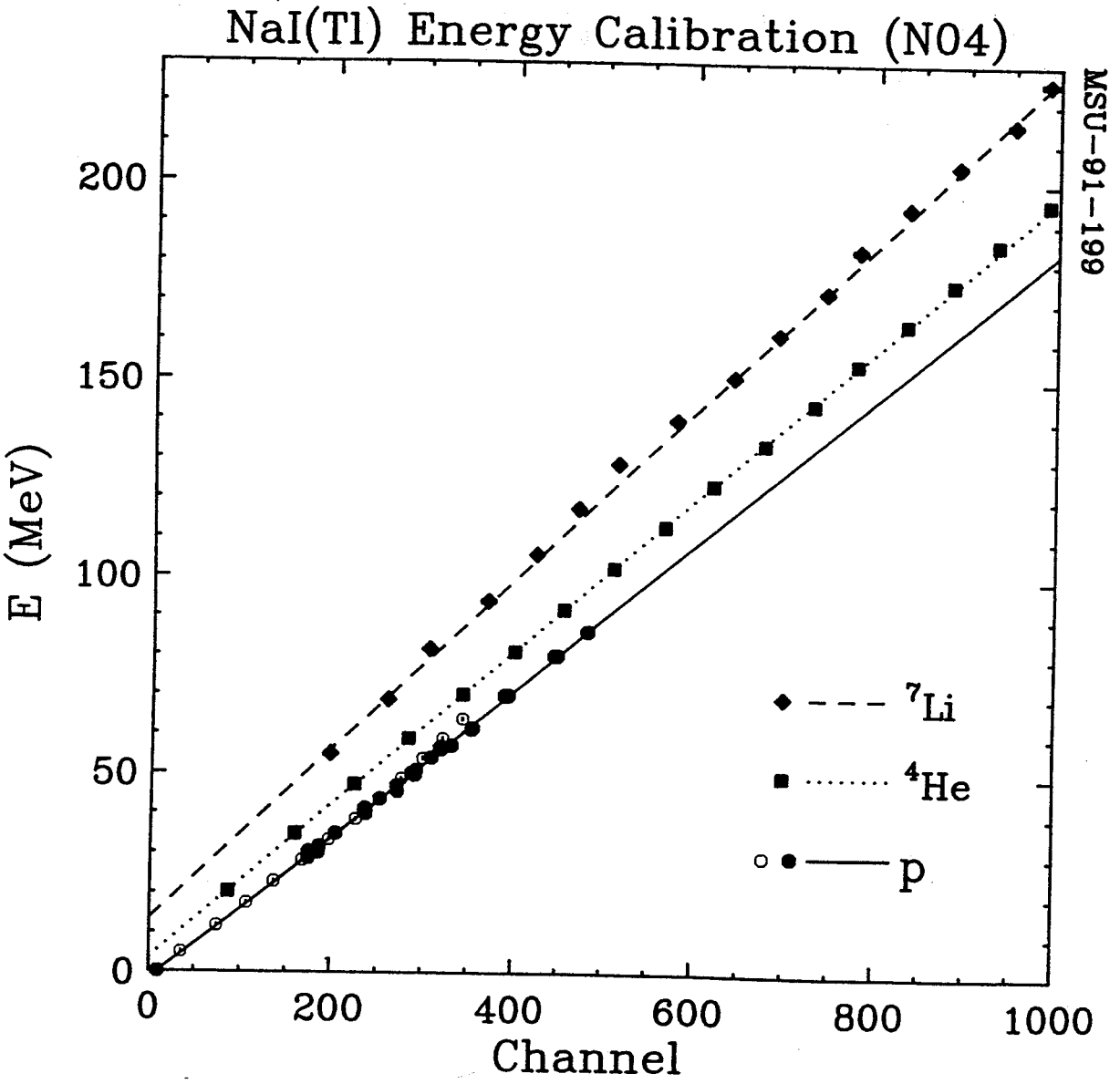

Figure 4.10: Comparison of energy calibrations for particles such as proton, ^{4}He, and ^{7}Li measured in a NaI(Tl) detector (N04). The curves are the corresponding fits. See text for explanations.

^{4}He, ^{6}He, ^{6}Li, and ^{7}Li particles were once again fitted by straight lines. The fitting parameters are again listed in Table 4.1.

The accuracy of this calibration technique is mainly limited to (1) the accuracy of the energy-loss calculation; (2) the accuracy of thickness measurement for any foil or detection media; (3) the accuracy of energy calibration for the Si detector; (4) the accuracy of numerical interpolation or extrapolation in using Equation (4.17).

4.3 Time-walk Corrections

In two-particle coincidence measurements, it is essential to seperate real coincidence events coming from one single projectile-target interaction from random coincidence events due to two or more projectile-target interactions. Random event contaminations are corrected by constructing the relative time spectrum between any two telescopes and by setting appropriate time gates.

It is well known that the time response of NaI(Tl) scintillators is fast (τ_d=0.23μs, τ_r=0.5μs) and that of CsI(Tl) scintillators is very slow (τ_d=1.0μs, τ_r=4μs) (see Table 2.1). While constant-fraction-discriminators (CFD) were used in the timing circuits for the NaI(Tl) detectors, it was not economical and practical to use CFDs for the CsI(Tl) detectors in this experiment. Instead, we employed simple leading-edge-discriminators (LED) (see Figure 3.5). Consequently, a large time-walk became inevitable for the CsI(Tl) detectors in contrast to the negligible time-walk for the NaI(Tl) detectors as shown respectively in the right and left panel of Figure 4.11. Here the time difference between a detector and the down-scaled RF signal ($T-T_{RF}$) is plotted against the stopping energy signal (E). Each band represents one beam burst. To simplify the analysis for the CsI(Tl) detector, we straightened the curved response of CsI(Tl) detector.

After making this kind of walk correction for the CsI(Tl) detectors and aligning the zero-time with each other among all detectors, the relative time spectra were constructed. They are displayed in Figures 4.12 for 75MeV/nucl.

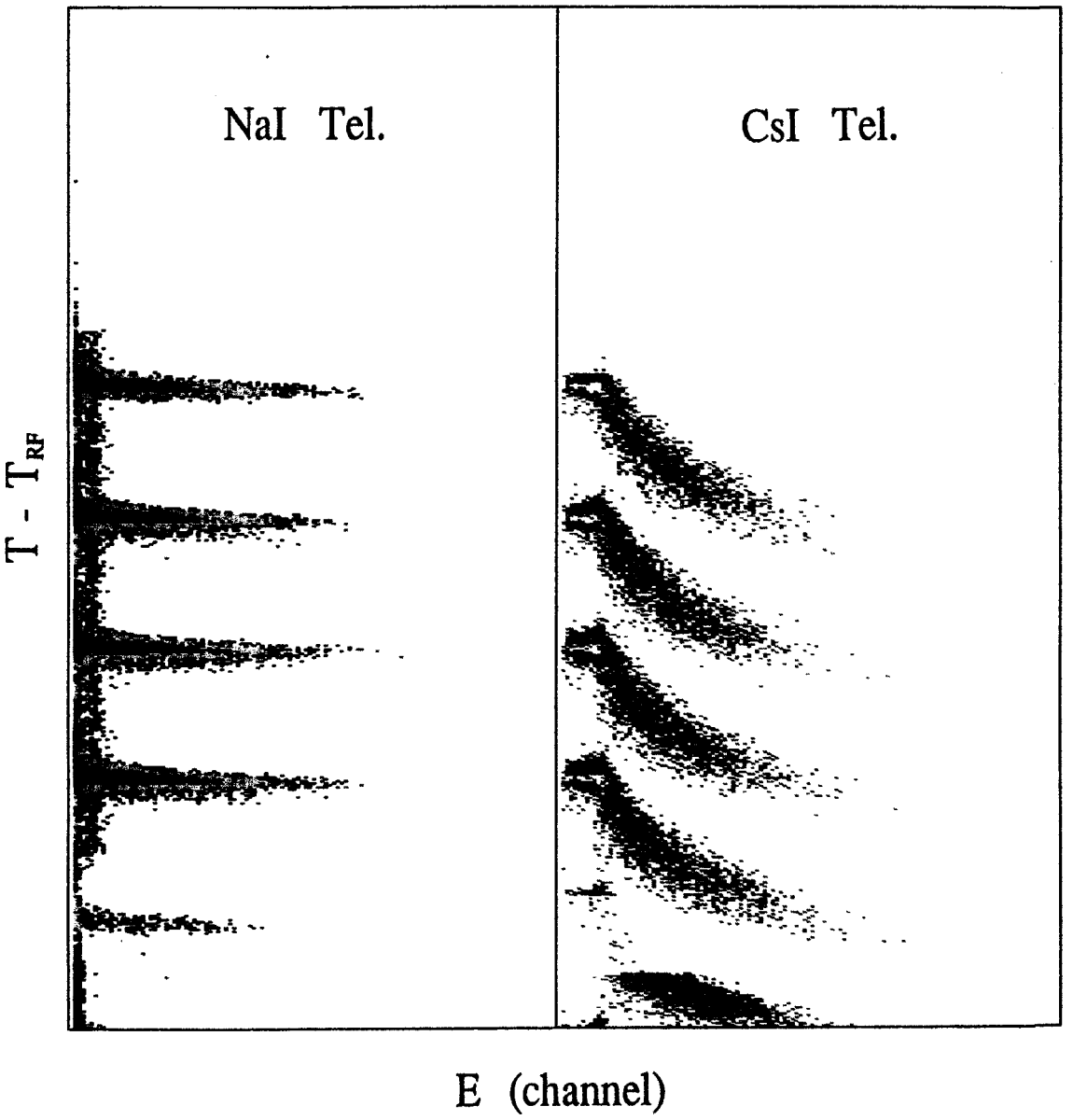

Figure 4.11: Two-dimensional plots of ($T - T_{RF}$) v.s. E for a Si-NaI(Tl) telescope (left panel) and for a Si-CsI(Tl) telescope (right panel) where necessary time-walk corrections were made.

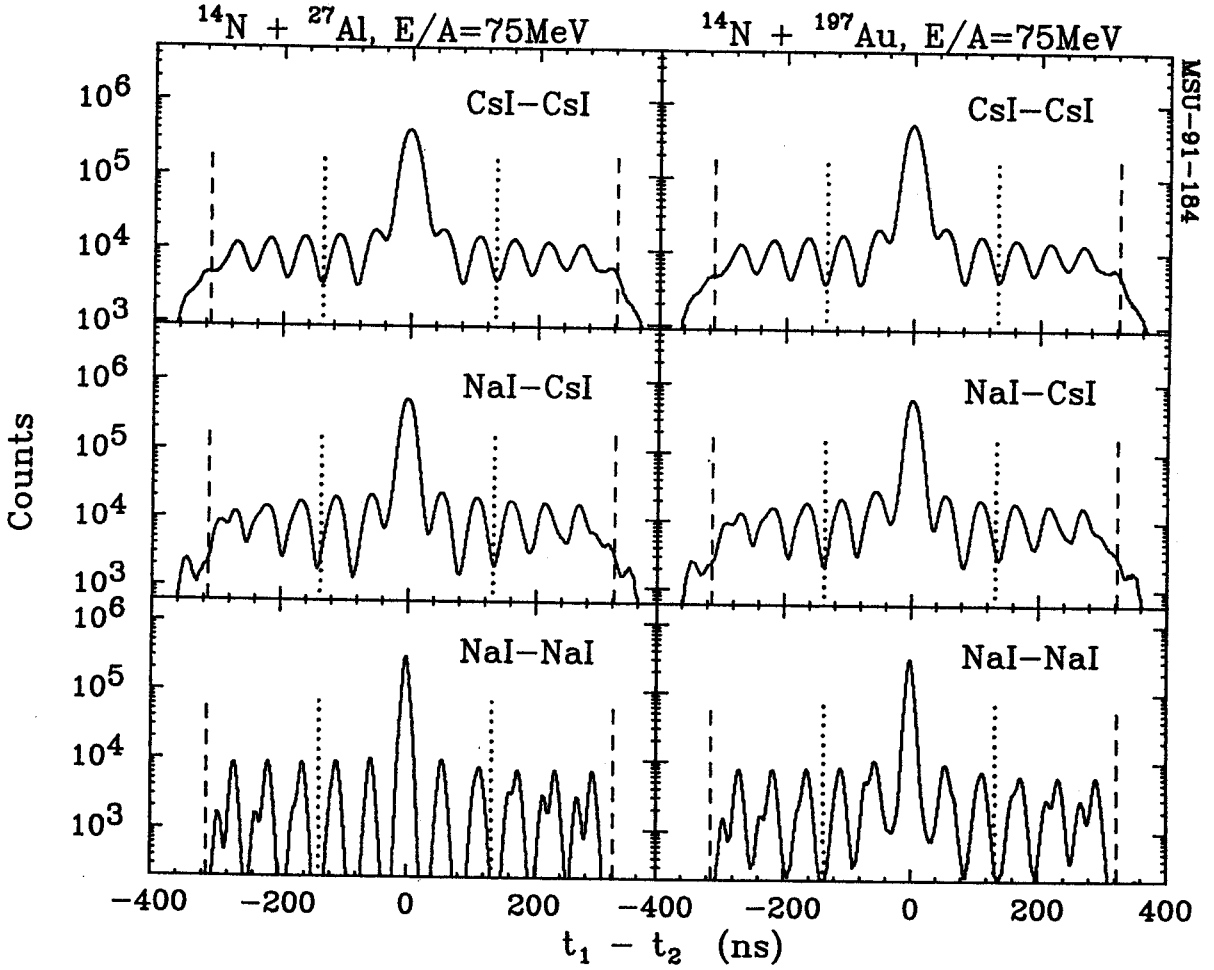

Figure 4.12: Relative timing spectra between any two telescopes in the 75MeV/nucl. ^{14}N induced reactions on ^{27}Al (left part) and on ^{197}Au (right part). Timing gates for real and random coincident events are indicated by vertical lines.

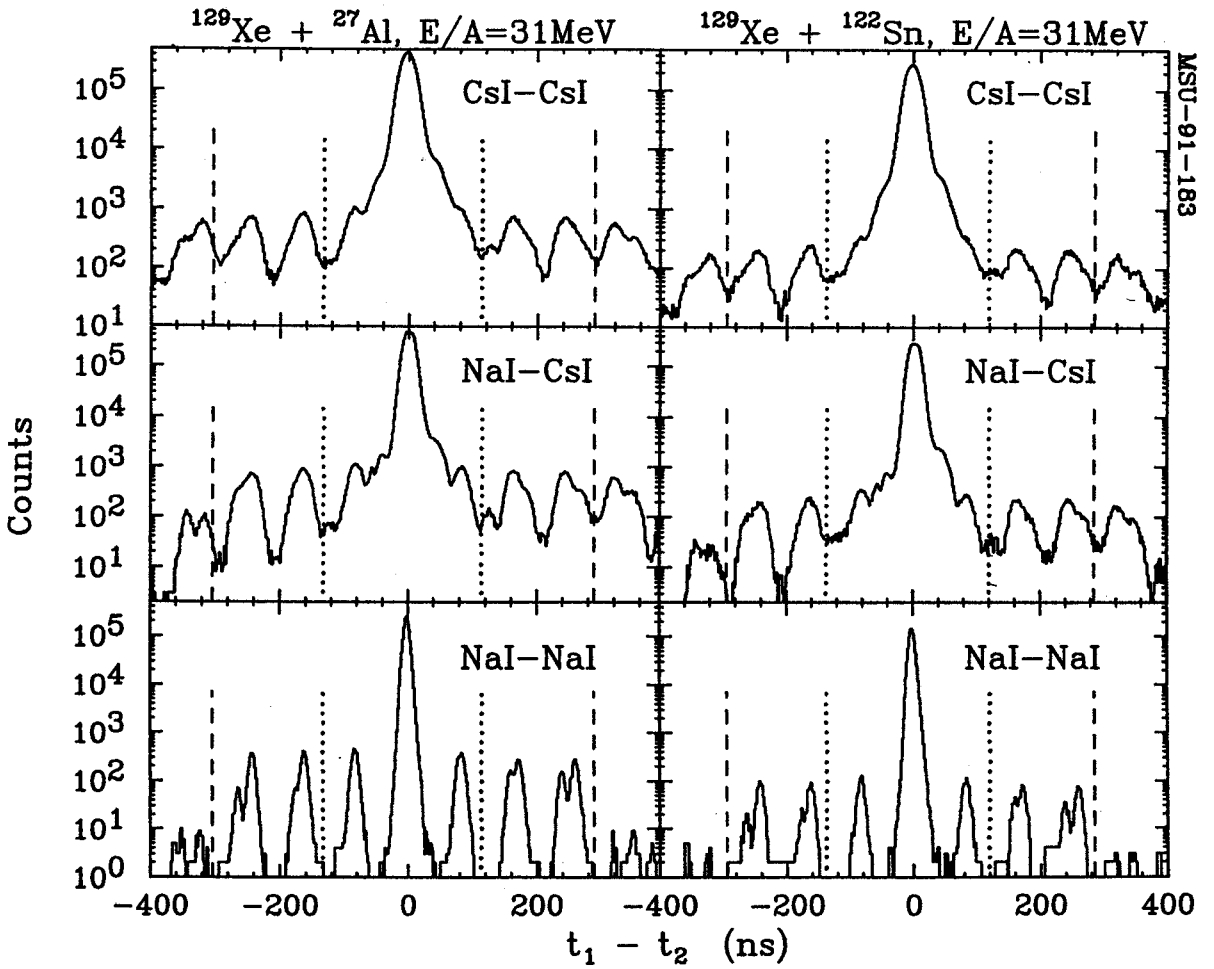

Figure 4.13: Relative timing spectra between any two telescopes in the 31MeV/nucl. ^{129}Xe induced reactions on ^{27}Al (left part) and on ^{122}Sn (right part). Timing gates for real and random coincident events are indicated by vertical lines.

^{14}N induced reaction on ^{27}Al (left parts) and on ^{197}Au (right parts) and in Figure 4.13 for 31MeV/nucl. ^{129}Xe induced reaction on ^{27}Al (left parts) and on ^{122}Sn (right parts), respectively. Three categories of the relative time spectrum were defined as (1) between two CsI(Tl) detectors (upper panel); (2) between NaI(Tl) and CsI(Tl) detector (middle panel); (3) between two NaI(Tl) detectors (lower panel). For each reaction, the relative time spectra of different category had very similar peak structures except that the NaI(Tl) detector showed better time resolutions than the CsI(Tl) detectors. The highest peak in the center contains real coincidence events and also a random contamination, while the side peaks of about equal height arise from random coincidence events.

To be on the safe side, we have defined the "real" coincidence events (N'_{real}) by the events locating between two dotted lines and the random coincident events (N'_{random}) by the events lying between the dotted and the dashed lines on both left and right hand sides. Assuming that the number of random peaks contained in N'_{real} is m'_{real} and N'_{random} included m_{random} random peaks, the corrected real coincidence events are:

$$N_{real} = N'_{real} - N'_{random} \cdot m'_{real} / m_{random}. \qquad (4.18)$$

One can estimate from Figure 4.12 and 4.13 that the ratio of N_{random} over N_{real} was about 5% for ^{14}N induced reactions and about 0.3% for ^{129}Xe induced reactions. After random correction, the numbers of real two-proton coincidence events, $N_{real} = 2.25\times10^{6}$, 1.94×10^{6}, 1.13×10^{6}, and 0.46×10^{6} for the reactions ^{14}N + ^{197}Au, ^{14}N + ^{27}Al, ^{129}Xe + ^{27}Al, and ^{129}Xe + ^{122}Sn, respectively.

4.4 Corrections due to Nuclear Reaction Loss

Energetic light-charged particle can undergo nuclear reactions with target nuclei in a detector. When such a nuclear reaction occurs, the particle's energy is generally not measured correctly due to non-vanishing Q-value and the emission of neutrons and γ-rays. This poses a small inefficiency problem for the detector. In this section, we discuss corrections for detection losses due to nuclear reactions of light charged-particles entering CsI(Tl)/NaI(Tl) scintillators.

The total reaction cross section for heavy-ion collisions in the intermediate energy range can be parametrized as [Kox 87]:

$$\sigma_R = \pi R_{int}^2 \bullet (1 - \frac{B_c}{E_{cm.}}), \tag{4.19}$$

where $E_{c.m.}$ is the c.m. energy and B_c is the Coulomb barrier of the projectile-target system. They are given by:

$$E_{c.m.} = E_{lab} \bullet A_t/(A_p+A_t) \text{ and } B_c = Z_p Z_t e^2/[r_c(A_p^{1/3}+A_t^{1/3})], \tag{4.20}$$

with r_c=1.3fm, Z_p (Z_t) and A_p (A_t) are the atomic and mass number of projectile (target) nuclei. The interaction radius, R_{int}, can be divided into volume and surface terms as:

$$R_{int} = R_{vol} + R_{surf}. \tag{4.21}$$

The volume radius is given by

$$R_{vol} = r_0 (A_p^{1/3} + A_t^{1/3}), \tag{4.22}$$

and the surface radius is parametrized as

$$R_{surf} = r_0 \left(a \frac{A_p^{1/3} \cdot A_t^{1/3}}{A_p^{1/3} + A_t^{1/3}} - c \right) + D, \qquad (4.23)$$

where $r_0 = 1.1$ fm, $a = 1.85$, $D = 5Z_p(A_t - 2Z_t)/(A_p A_t)$ due to neutron skin excess, and c is empirically parametrized by the formula [Town 88]:

$$c = 1.91 - 16.0 \cdot \exp(-0.7274 \cdot E^{0.3493}) \cdot \cos(0.0849 \cdot E^{0.5904}), \qquad (4.24)$$

with $E = E_{lab}/A_p$ being the laboratory kinetic energy of projectile in units of MeV/nucleon.

We first obtain the stopping range (S in units of mgr/cm^2) for a particle incident on CsI(Tl)/ NaI(Tl) detectors by using Ziegler's parametrization [Zieg 77]. The detector depth is then devided into many thin slices within the particle's stopping range. In the i-th slice of detector ($\Delta x = S/N$), we use the thin-target approximation to calculate the nuclear reaction rates by:

$$R_i(Cs) = n_0(Cs) \cdot \Delta x(Cs) \cdot \sigma_R^i(Cs), \qquad (4.25)$$

$$R_i(I) = n_0(I) \cdot \Delta x(I) \cdot \sigma_R^i(I), \qquad (4.26)$$

where $n_0(Cs) = 6.022 \times 10^{-7}/A(Cs)$, $n_0(I) = 6.022 \times 10^{-7}/A(I)$, both in units of $[cm^2/mgr/mb]$, and $\Delta x(Cs) = \Delta x \cdot A(Cs)/[A(Cs) + A(I)]$, $\Delta x(I) = \Delta x \cdot A(I)/[A(Cs) + A(I)]$.

Finally, the total probability of nuclear reaction loss is obtained by

$$R_{tot} = 1 - \prod_{i=1}^{N} [1 - R_i(Cs)] \cdot [1 - R_i(I)]. \qquad (4.27)$$

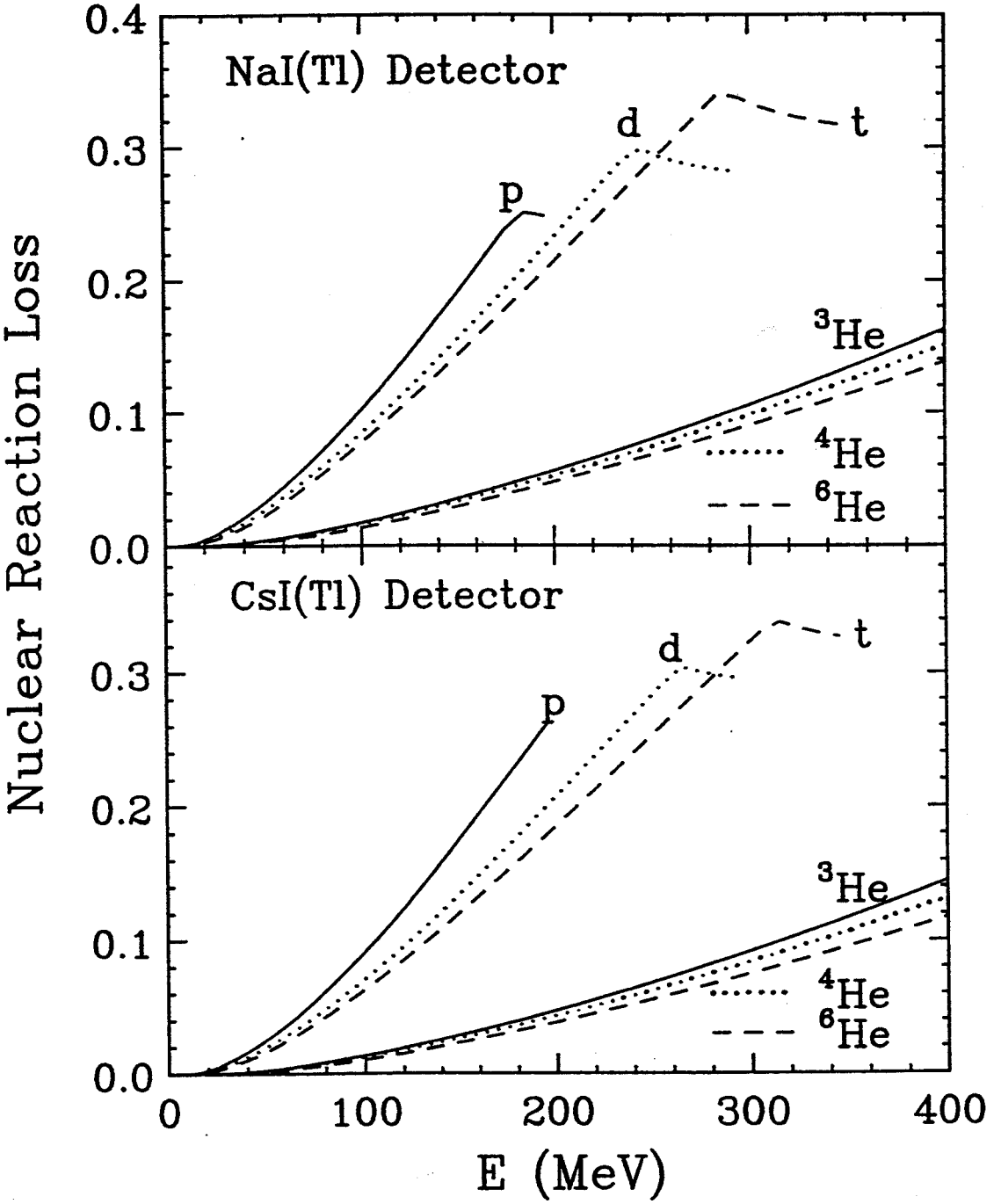

Figure 4.14: The probabilities of nuclear reaction loss for light-charged particles detected by a 10cm long NaI(Tl) or CsI(Tl) scintillator.

Figure 4.14 shows the calculated probability of nuclear reaction loss for light-charged particles (p, d, t, ^{3}He, ^{4}He, ^{6}He) entering a 10cm long NaI(Tl) detector (upper part) and a 10cm long CsI(Tl) detector (lower part). Typically, a proton of 150MeV energy has about 20% probability of nuclear reaction inside the detector. At the energies of interest, the probability of nuclear reaction is smaller for the Helium particles and negligible for heavier fragments. By comparison, the probability of nuclear reaction is slightly larger in NaI(Tl) detector than in CsI(Tl) detector since NaI(Tl) has less stopping power and the particles have a longer range than in CsI(Tl).

CHAPTER 5. SINGLE-PROTON ENERGY SPECTRA

5.1 Inclusive Energy Spectra

Examples of inclusive energy spectra for protons detected at the extreme angles covered by our detector array, $\theta_{lab} = 18°$ and $33°$, are shown in Figure 5.1. Spectra measured for reactions induced by ^{129}Xe and ^{14}N projectiles are shown in the left and right panels, respectively. In order to gain qualitative insight and allow comparisons with other data, we have fit these cross sections with the moving source parametrisations. We have to caution, however, that the extracted parameters are not uniquely determined by our data and must not be over-interpreted since our measurements covered only a small range of angles.

For the ^{14}N-induced reactions, we have chosen a simple three-source parametrization, representing isotropic Maxwellian contributions from a target-like source, a projectile-like source, and an intermediate velocity nonequilibrium source:

$$\frac{d^2\sigma}{d\Omega\, dE} = \sum_{i=1}^{3} N_i \sqrt{E-U_c} \cdot \exp\{-[E-U_c+E_i-2\sqrt{E_i(E-U_c)}\cdot\cos\theta]/T_i\}. \qquad (5.1)$$

Here, N_i and T_i are relative normalization and kinetic temperature parameters, respectively. The energy E_i is the kinetic energy of a particle co-moving with the i-th source, $E_i = \frac{1}{2} mc^2\beta_i^2$. The Coulomb energy, U_c, corrects for the Coulomb repulsion from heavy reaction residues assumed at rest in the laboratory rest frame.

The solid curves displayed in the right hand panels of Figure 5.1 show fits

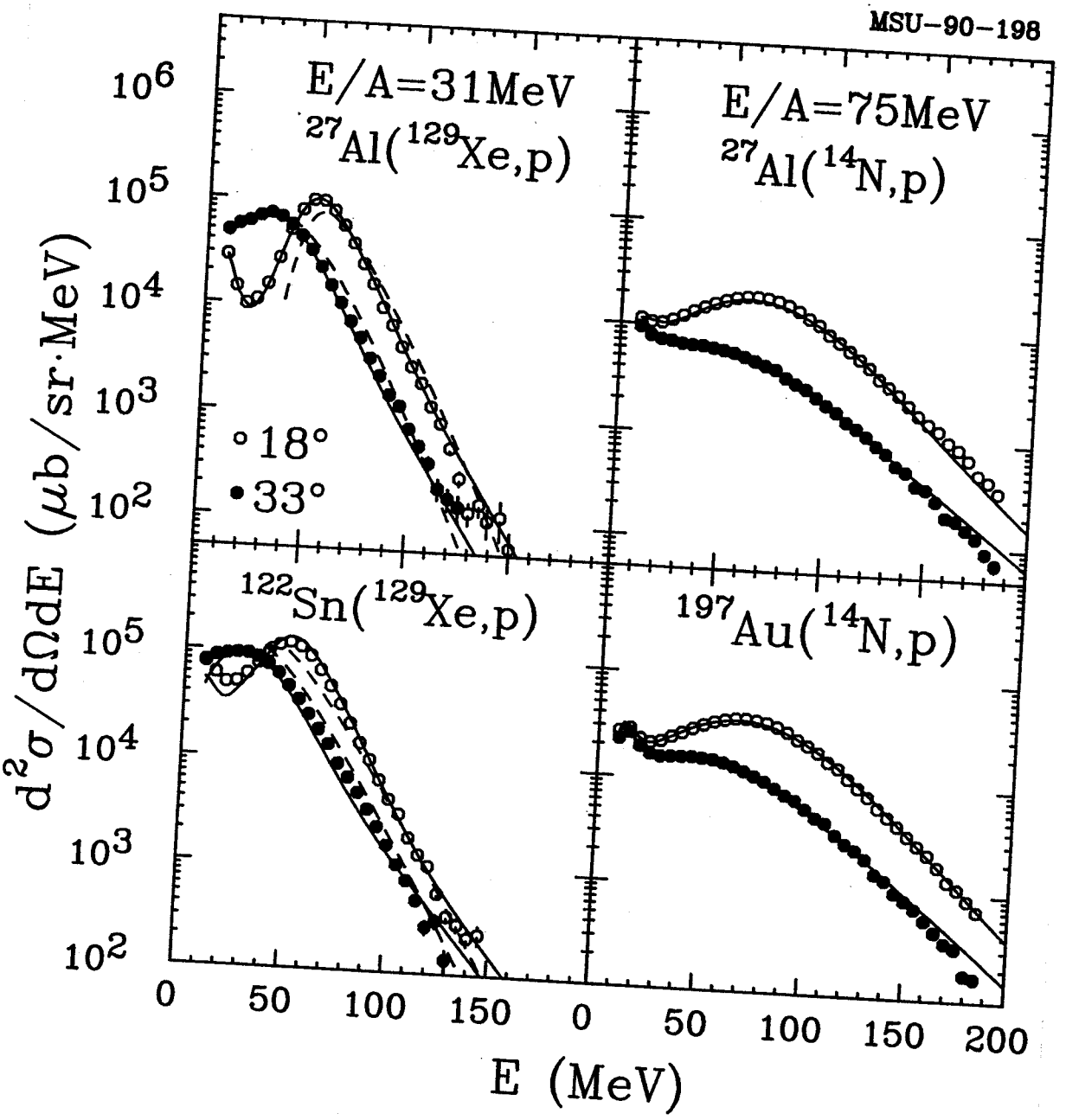

Figure 5.1: Inclusive proton cross sections measured, at θ_{lab}=18° and 33°, for the reactions ^{129}Xe+^{27}Al and ^{129}Xe+^{122}Sn at E/A=31 MeV (left hand panels) and the reactions ^{14}N+^{27}Al and ^{14}N+^{197}Au at E/A=75 MeV (right hand panels).

Table 5.1: Fit parameters used for the description of the inclusive single- proton cross sections shown in Figure 5.1. The spectra for the ^{14}N and ^{129}Xe-induced reactions were fitted by Equations (5.1) and (5.2), respectively.

The normalization constants, N_i, are given in units of $[mb/(sr \bullet MeV^{3/2})]$, U_c, Δ_c, and T_i are all in units of [MeV]. Also given are the velocities, β_{pro} and β_{cn}, of the projectile and the compound nucleus, respectively.

Reaction	β_{pro}	β_{cn}	U_c	Δ_c	i	N_i	β_i	T_i
$^{14}N+^{27}Al$	0.40	0.14	1.72	-	1	4.67	0.371	6.04
				-	2	1.62	0.200	19.59
				-	3	3.98	0.073	4.62
$^{14}N+^{197}Au$	0.40	0.026	8.57	-	1	8.52	0.376	5.88
				-	2	4.55	0.200	18.10
				-	3	22.81	0.025	3.84
$^{129}Xe+^{27}Al$	0.26	0.21	5.18	2.0	1	52.40	0.234	4.07
					2	3.91	0.213	8.94
$^{129}Xe+^{27}Al$	0.26	0.21	7.25	2.0	1	36.57	0.213	6.0
$^{129}Xe+^{122}Sn$	0.26	0.13	4.23	2.0	1	66.05	0.241	4.25
					2	7.13	0.130	13.92
$^{129}Xe+^{122}Sn$	0.26	0.13	9.88	2.0	1	58.0	0.130	9.13

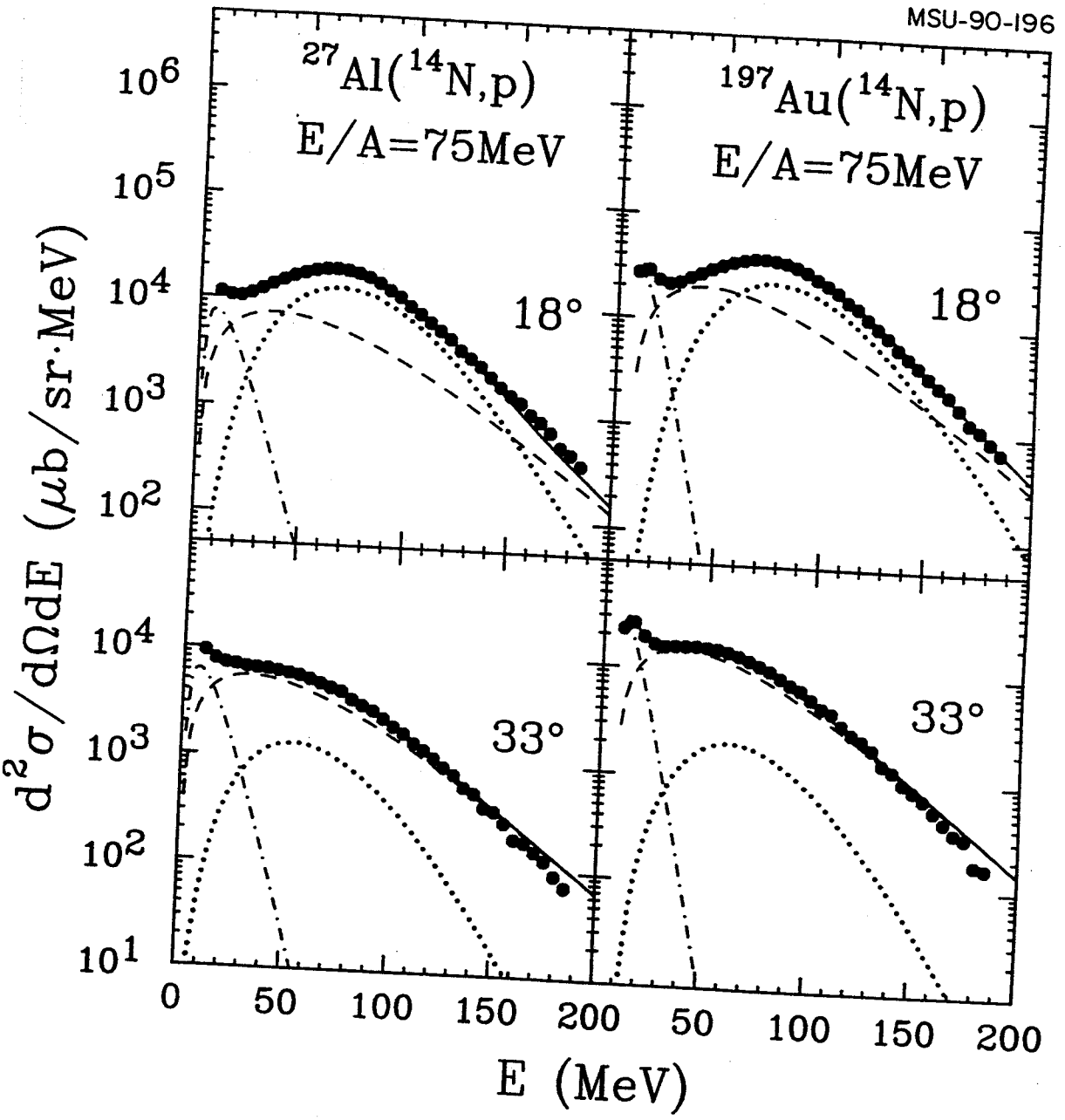

Figure 5.2: Decomposed three moving source fits to inclusive proton energy spectra measured, at θ_{lab}=18° and 33°, for 75 MeV/nucl. ^{14}N induced reactions on ^{27}Al (left two panels) and on ^{197}Au (right two panels).

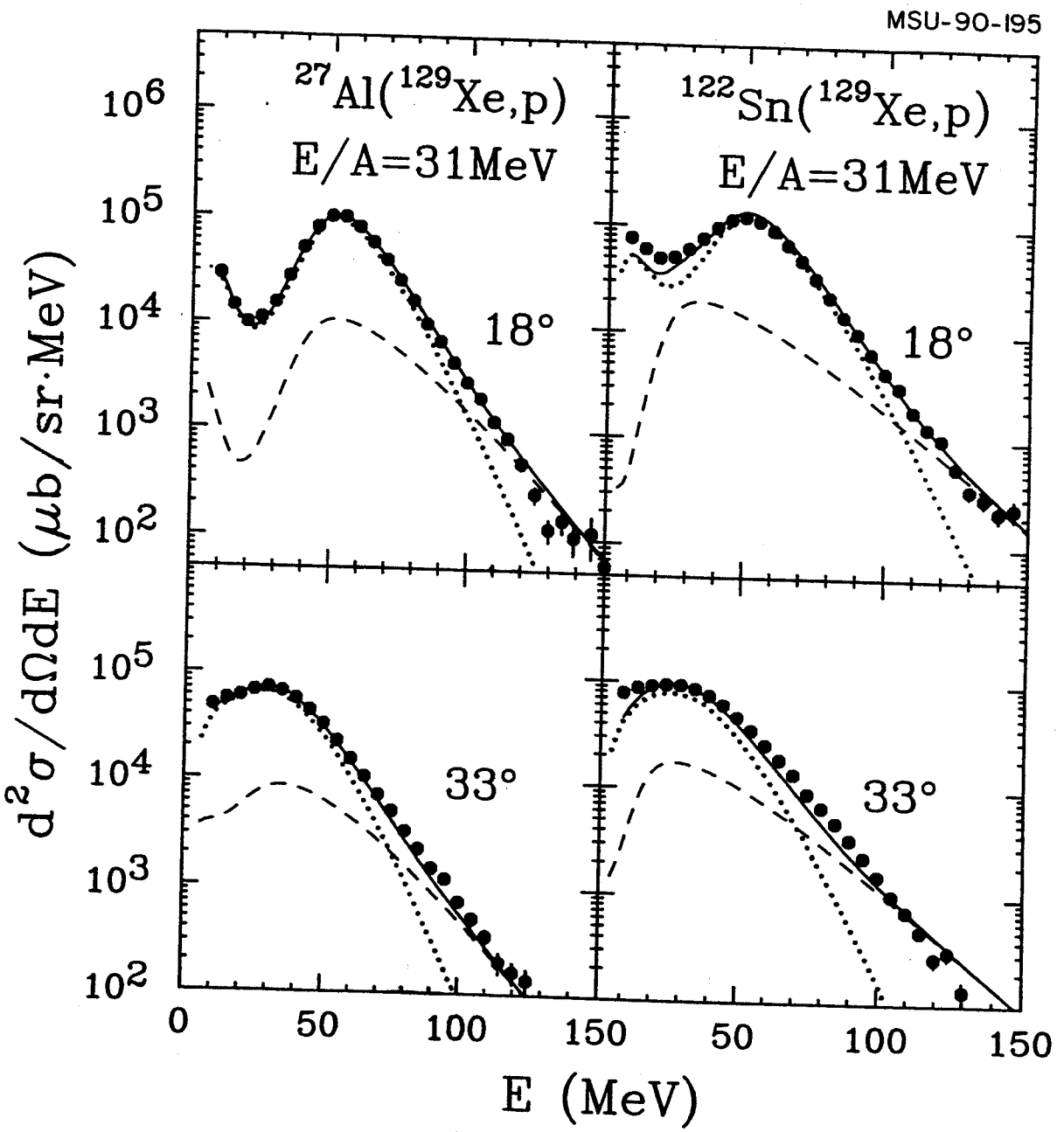

Figure 5.3: Decomposed two moving source fits to inclusive proton energy spectra measured, at θ_{lab}=18° and 33°, for 31 MeV/nucl. ^{129}Xe induced reactions on ^{27}Al (left two panels) and on ^{122}Sn (right two panels).

obtained with this parametrization; the parameters are listed in Table 5.1. To illustrate the relative importance of contributions from various moving sources, the fits were decomposed into contributions from target- and projectile-like source and intermediate velocity source, indicated by dot-dashed, dotted, and dashed lines, respectively, in Figures 5.2 and 5.3. The spectra can be rather well described by assuming emission from target- and projectile-like sources with temperature parameters of about 4 to 6 MeV and by including a non-equilibrium component described, as before [Chen 87b, Poch 87, Gelb 87] in terms of an intermediate velocity source characterized by a high kinetic temperature parameter, T≈18-20 MeV. Particularly for the $^{14}N + ^{197}Au$ reaction, the fits indicate significant evaporative contributions from a target-like source to the low-energy portion of the spectrum.

For the Xe-induced reactions, fusion-like and projectile-like residues have large velocities in the laboratory rest frame, and emission from these two sources is strongly forward focussed. In comparison, contributions from target-like residues are of minor importance at our detection angles. Furthermore, non-equilibrium emission may be expected to be small. Therefore, we adopted a two-source parametrization representing emission from projectile- and fusion-like sources. For these sources, the simple Coulomb correction adopted in Equation (5.1) is inappropriate since the heavy reaction residues have large velocities with respect to the laboratory rest frame. Furthermore, the measurements include energies which lie below the projectile and compound nucleus Coulomb barriers. Hence, the sharp truncation of the energy spectra for sub-barrier energies is inappropriate. For these reasons, we adopted a parametrization similar to that used in Reference [Fiel 86]:

$$\frac{d^2\sigma}{d\Omega\, dE} = \sum_{i=1}^{2} N_i \int_{U}^{U} dU \frac{\exp[-(U-U_c)^2/2\Delta_c^2]}{\Delta_c \sqrt{2\pi}} \sqrt{E(1-U/E_{cm,i})}\, e^{-(E_{cm,i}-U)/T_i} \quad (5.2)$$

Here, $E_{cm,i} = E + E_i - 2\sqrt{E_i E}\cdot\cos\theta$ and $E_i = \frac{1}{2} m c^2 \beta_i^2$; the integration limits were chosen as $U_1 = \max(0, U_c - 5\Delta_c)$ and $U_2 = \min(E_{cm,i}, U_c + 5\Delta_c)$. In Equation (5.2), the Coulomb field is assumed to be stationary in the rest frame of the emitting source, and an average is performed over an ensemble of Coulomb barriers using Gaussian weighting factors.

The fitted spectra are shown as solid lines in the left hand panels of Figure 5.1. The spectra can be rather well described by assuming evaporative emission from a fusion-like source and a projectile-like source. The decomposition of source contributions is presented in Figure 5.3, where dashed lines indicate fusion-like sources and dotted lines indicate projectile-like sources. (For the $^{129}Xe + ^{27}Al$ reaction, fusion-like sources have velocities very similar to the projectile velocity, $\beta \approx 0.26$. For the $^{129}Xe + ^{122}Sn$ reaction, fusion-like sources have approximately half the beam velocity.) The fits shown by the solid curves indicate strong contributions from decays of excited projectile residues. The inclusion of a projectile-like source largely improves the fits at lower energies. At these energies, the calculations are sensitive to details of the parametrization of the ensemble of Coulomb barriers. Again, it must be stressed that the extracted source parameters are not uniquely determined because of the small angular range covered by our detector array. In order to illustrate some of the existing uncertainties, we have also described the tail of the energy spectra ($E \geq 40$ MeV) by assuming emission from a single source moving with the velocity of the compound nucleus. These calculations are shown by the dashed curves in the left hand panels of Figure 5.1; the parameters are listed in Table 5.1.

It should be kept in mind that the moving source parametrization does not offer a unique interpretation of the single-particle inclusive cross sections. The adopted parametrizations should, therefore, be viewed with a "grain of salt". Nevertheless, the calculations indicate possible contributions from a number of different sources which cannot be disentangled without ambiguity.

5.2 Comparison with BUU Calculations

With respect to our future discussion, it is instructive and useful to compare the single-proton cross sections measured for the ^{14}N-induced reactions with those predicted by BUU calculations [Baue 87]. Comparisons of the BUU theory to the experimental two-proton correlation functions will be presented later in Chapter 9.

In Figure 5.4, the solid points represent the measured single-proton cross sections for the reactions $^{14}N + ^{27}Al$ (upper panel) and $^{14}N + ^{197}Au$ (lower panel); cross sections predicted by BUU calculations are shown by open points. For the emission of energetic protons, the cross sections predicted by the BUU calculations are in rather good agreement with the data. However, at lower energies, $E \leq 70$ MeV, the predicted cross sections are larger than the measured ones. At least part of this discrepancy may be attributed to the fact that the present calculations do not incorporate cluster formation and emission. The formation and emission of clusters is expected to be particularly important when the phase space density is high, i.e. at low kinetic energies. In these regions of phase space, the flux of emitted nucleons will appear, in part, in the form of bound clusters. On the basis of these qualitative arguments, one can expect that proton cross sections predicted by BUU calculations should be larger than the experimental cross sections for free protons; the effect should be most pronounced for protons of low energies.

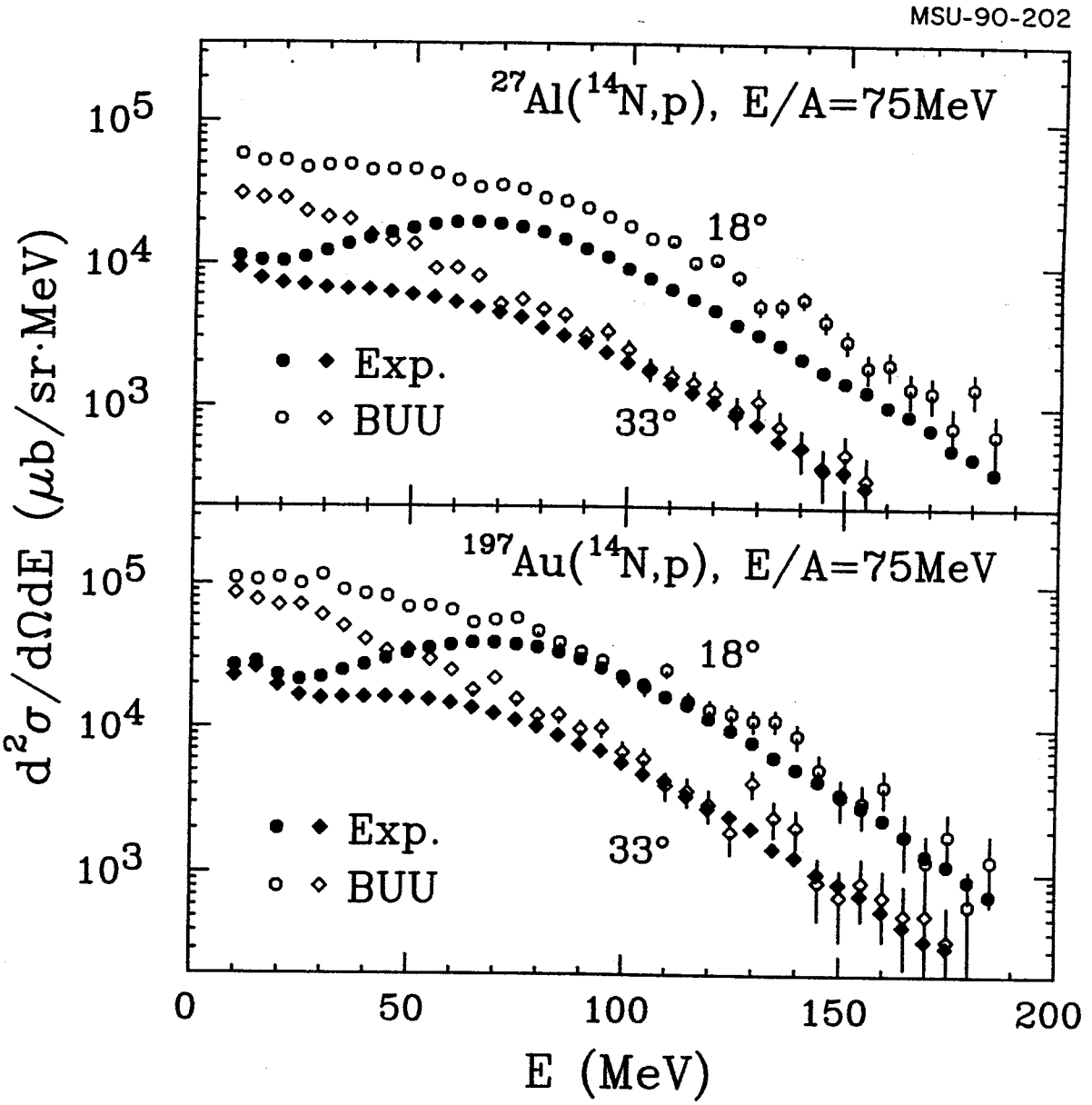

Figure 5.4: Single-proton cross sections calculated with the BUU theory (open points) are compared to experimental cross sections (solid points) for the reactions ^{14}N+^{27}Al (top panel) and ^{14}N+^{197}Au (bottom panel) at E/A=75 MeV. Circular and diamond shaped symbols indicate laboratory angles of 18° and 33°, respectively.

CHAPTER 6. TWO-PROTON CORRELATION FUNCTION

In this chapter, we give a brief derivation of the general formalism which allows the calculation of two-proton correlation functions from the knowledge of the single-particle phase-space density. The sensitivity of two-proton correlation functions to source radii and lifetimes is illustrated by means of simple analytical source parametrizations.

6.1 Theoretical Formalism

A number of formalisms have been published [Boal 90] which derive two-particle correlation functions from the knowledge of the emission function, $g(\vec{p},x)$, i.e. the probability of emitting a particle with momentum $\vec{p}$ from space-time point $x=(\vec{r},t)$. The derived expressions differ only in minor details and the predicted results are similar. Here, we derive an expression for the correlation function in most general terms assuming complete knowledge of all two-particle quantum mechanical matrix elements. We then introduce and justify approximations which allow practical calculations. For simplicity, we will restrict ourselves to the important case of correlations between two identical particles.

In the following, we will use four-vector notation to keep our formulae compact and manageable. However, our formalism is not relativistically covariant.

Our final expression for the two-particle correlation function is identical to the expressions given in References [Koon 77, Prat 87]:

$$R(\vec{P},\vec{q})+1 = C(\vec{P},\vec{q}) = \frac{\Pi(\vec{p}_1,\vec{p}_2)}{\Pi(\vec{p}_1)\Pi(\vec{p}_2)} =$$

$$= \frac{\int d^4x_1 d^4x_2 g(\vec{P}/2, x_1)\, g(\vec{P}/2, x_2)\, |\phi(\vec{q}, \vec{r}_1 - \vec{r}_2 - (t_1 - t_2)\vec{P}/2m)|^2}{\int d^4x_1 g(\vec{P}/2, x_1) \int d^4x_2 g(\vec{P}/2, x_2)} . \quad (6.1)$$

Here, $\Pi(\vec{p}_1, \vec{p}_2)$ and $\Pi(\vec{p}_i)$ denote the two-particle and single-particle emission probabilities, $\vec{P}$ and $\vec{q}$ are the total and relative momenta, $\vec{P} = \vec{p}_1 + \vec{p}_2$ and $\vec{q} = (\vec{p}_1 - \vec{p}_2)/2$, respectively, and ϕ is the relative wave function.

This expression was given in Reference [Koon 77] without derivation. It was derived in Reference [Prat 87] by using the sudden approximation for which the particles are assumed to be on shell in their final state and the mutual interaction is switched on suddenly. Equation (6.1) was then derived assuming the thermal wavelength is much smaller than the size of the system. These approximations are not very well justified. Here, we start from the full quantum-mechanical expression for two-particle emission and show how, under most circumstances, we can justify a few approximations which lead to Equation (6.1). Results obtained in many other formalisms are similar. For instance, in the literature on two-pion interferometry the function $g(\vec{P}/2, x)$ is often replaced by something similar, for example, $[g(\vec{p}_1, x) \cdot g(\vec{p}_2, x)]^{1/2}$. As long as the relative momentum $|\vec{q}|$ is much smaller than a characteristic momentum, $|\vec{p}|$, of $g(\vec{p}, x)$ (such as $|\vec{p}| \approx \sqrt{3mT}$, where T is the temperature of the emitting system), there is little difference between the formalisms.

The complete matrix element for the creation of the n-body final state includes all information necessary for the calculation of correlation functions. Here we will derive an approximation in which the correlation function will only depend on properties of the one-body emission probability which can be extracted from the one-body matrix elements.

We start out by first considering the probability for creating two particles with final momenta $\vec{p}_1$ and $\vec{p}_2$ from sources 1 and 2 at space-time points x_1 and x_2:

$$\Pi(\vec{p}_1,\vec{p}_2) = |\int d^4x_1 d^4x_2 M_1(x_1)M_2(x_2)U(x_1,x_2:\vec{p}_1,\vec{p}_2)|^2 . \qquad (6.2)$$

Here, $U(x_1,x_2:\vec{p}_1,\vec{p}_2)$ is the evolution operator for particles created at x_1 and x_2 which end up in the asymptotic momentum states $\vec{p}_1$ and $\vec{p}_2$. The matrix element $M_i(x_i)$ creates the particle at x_i and the remaining collision products into a state which henceforth does not interact with the particle. In Equation (6.2), we have assumed that the particles are emitted independently. This allows the factorization of the matrix element for two-body emission into the product of single-body elements.

By squaring the matrix elements and transforming to the new coordinates x_i (mean) and δx_i (relative), we obtain

$$\Pi(\vec{p}_1,\vec{p}_2) = \int d^4x_1 d^4\delta x_1 d^4x_2 d^4\delta x_2 S_1(x_1,\delta x_1)S_2(x_2,\delta x_2)\bullet .$$

$$W_{p_1,p_2}(x_1,\delta x_1,x_2,\delta x_2). \qquad (6.3)$$

where

$$W_{\vec{p}_1,\vec{p}_2}(x_1,\delta x_1,x_2,\delta x_2) = U^{\dagger}(x_1+\delta x_1/2,x_2+\delta x_2/2:\vec{p}_1,\vec{p}_2)\bullet$$
$$U(x_1-\delta x_1/2,x_2-\delta x_2/2:\vec{p}_1,\vec{p}_2), \qquad (6.4)$$

and

$$S_1(x_1,\delta x_1) = M_1^{\dagger}(x_1+\delta x_1/2)M_1(x_1-\delta x_1/2). \qquad (6.5)$$

The expression becomes physically more transparent when the dependences on δx_i are replaced by dependences on the momenta, k_i, through four-dimensional Wigner transforms. As a result, we obtain:

$$\Pi(\vec{p}_1,\vec{p}_2) = \int d^4x_1 d^4x_2 d^4k_1 d^4k_2 \tilde{S}_1(x_1,k_1)\tilde{S}_2(x_2,k_2)\tilde{W}_{\vec{p}_1,\vec{p}_2}(x_1,k_1,x_2,k_2), \qquad (6.6)$$

with the Wigner transforms $\tilde{S}$ and $\tilde{W}$ defined by:

$$\tilde{S}_i(x_i,k_i) = \int d^4\delta x S_i(x_i,\delta x) e^{i\delta x \bullet k_i}, \qquad (6.7)$$

and

$$\tilde{W}_{\vec{p}_1,\vec{p}_2}(x_1,k_1,x_2,k_2) =$$

$$\int d^4\delta x_1 d^4\delta x_2 W_{\vec{p}_1,\vec{p}_2}(x_1,\delta x_1,x_2,\delta x_2) e^{-i\delta x_1 \bullet k_1 - i\delta x_2 \bullet k_2}. \qquad (6.8)$$

For non-interacting distinguishable particles, the time evolution operators, U, in Equation (6.2) become simple exponentials, and we obtain from Equation (6.4) the relation $W_{\vec{p}_1,\vec{p}_2} = \exp(i\delta x_1 \bullet p_1 + i\delta x_2 \bullet p_2)$. In this case, we can see from Equation (6.8) that $\tilde{W}_{\vec{p}_1,\vec{p}_2}(x_1,k_1,x_2,k_2) = \delta^4(p_1-k_1)\,\delta^4(p_2-k_2)$, as expected: Non-interacting distinguishable particles retain their four-momentum after the emission.

The functions $\tilde{S}(x,k)$ are the quantum mechanical analogues of the emission probability for particles with four-momentum k from space-time point x. This can be seen from the following argument. Performing the same steps as above, but now for the single particle distributions, and making use of the relation $\tilde{W}_{\vec{p}}(x,k) = \delta^4(p-k)$, we obtain the result:

$$\Pi(\vec{p}) = \int d^4x d^4k\, \tilde{S}(x,k)\delta^4(p-k)\,. \qquad (6.9)$$

From here on, we will imply the on-shell condition $p^0 = E(\vec{p})$ when referring to the 0^{th} component of the asymptotic momentum. Equation (6.9) shows that the emission probability is given by:

$$g(\vec{p},x) = \tilde{S}(x,p)\,. \qquad (6.10)$$

In order to obtain an expression for $\tilde{W}_{\vec{p}_1,\vec{p}_2}(x_1,k_1,x_2,k_2)$, we assume that the first emitted particle propagates freely for a time ($t_2 - t_1$) before it interacts with the second particle which is created at t_2. With this assumption, the evolution operator,

$$\tilde{U}(\vec{k}_1,t_1,\vec{k}_2,t_2:\vec{p}_1,\vec{p}_2) = (2\pi)^{-6} \int d^3x_1 d^3x_2 U(x_1,x_2:\vec{p}_1,\vec{p}_2) e^{-i\vec{k}_1\bullet\vec{x}_1 - i\vec{k}_2\bullet\vec{x}_2}, \quad (6.11)$$

for momentum states, $\vec{k}_i$, evolving into the true scattering states, $\vec{p}_i$, can be written as

$$\tilde{U}(\vec{k}_1,t_1,\vec{k}_2,t_2:\vec{p}_1,\vec{p}_2) = \Phi(\vec{k}_1,\vec{k}_2:\vec{p}_1,\vec{p}_2)\bullet\exp[iE_{12}t_2 + iE_1(t_1-t_2)] . \quad (6.12)$$

Here E_{12} is the total kinetic energy of the proton pair, and Φ is the projection of the total wave function on the plane wave states $\vec{k}_1$ and $\vec{k}_2$.

If the emissions of the two particles are not far apart in time, the assumption of time-ordered emission entering Equation (6.12) becomes questionable due to the uncertainty principle.

One can now calculate $\tilde{W}$ in terms of the wave function projection Φ:

$$\tilde{W}_{\vec{p}_1,\vec{p}_2}(x_1,k_1,x_2,k_2) =$$

$$\int d\delta t_1 d^3\delta\vec{k}_1 d\delta t_2 d^3\delta\vec{k}_2 \tilde{U}^{\dagger}(\vec{k}_1+\delta\vec{k}_1/2,t_1+\delta t_1/2,\vec{k}_2+\delta\vec{k}_2/2,t_2+\delta t_2/2:\vec{p}_1,\vec{p}_2)$$

$$\bullet\tilde{U}(\vec{k}_1-\delta\vec{k}_1/2,t_1-\delta t_1/2,\vec{k}_2-\delta\vec{k}_2/2,t_2-\delta t_2/2:\vec{p}_1,\vec{p}_2)$$

$$= \int d^3\delta k_1 d^3\delta k_2 d^3R_1 d^3R_2 \delta(k_1^0-E_1)\delta[k_2^0-(E_{12}-E_1)] f_2(\vec{k}_1,\vec{k}_2,\vec{R}_1,\vec{R}_2:\vec{p}_1,\vec{p}_2)$$

$$e^{-i\delta\vec{k}_1\bullet(\vec{x}_1+\vec{k}_1(t_2-t_1)/m-\vec{R}_1) - i\delta\vec{k}_2\bullet(\vec{x}_2-\vec{R}_2)} . \quad (6.13)$$

Here, the symbol k_i^0 is the 0-th component of the four vector k_i. To arrive at the second part of Equation (6.13), we performed Fourier transforms and made the linear approximation for the energy, $E(\vec{k}+\delta\vec{k}) \approx E(\vec{k}) + \delta\vec{k}\bullet\vec{k}/m$. The function f_2 introduced into Equation (6.13) is the Wigner decomposition of the total two-particle density matrix:

$$f_2(\vec{k}_1,\vec{k}_2,\vec{R}_1,\vec{R}_2:\vec{p}_1,\vec{p}_2) = \int d^3\delta k_1 d^3\delta k_2 \exp(-i\delta\vec{k}_1\vec{R}_1 - i\delta\vec{k}_2\vec{R}_2)$$

$$\Phi^*(\vec{k}_1+\delta\vec{k}_1/2,\vec{k}_2+\delta\vec{k}_2/2:\vec{p}_1,\vec{p}_2)\Phi(\vec{k}_1-\delta\vec{k}_1/2,\vec{k}_2-\delta\vec{k}_2/2:\vec{p}_1,\vec{p}_2)$$

$$= \int d^3\delta x_1 d^3\delta x_2 \exp(-i\delta\vec{x}_1\vec{k}_1 - i\delta\vec{x}_2\vec{k}_2)$$

$$\Phi^*(\vec{R}_1+\delta\vec{x}_1/2,\vec{R}_2+\delta\vec{x}_2/2:\vec{p}_1,\vec{p}_2)\Phi(\vec{R}_1-\delta\vec{x}_1/2,\vec{R}_2-\delta\vec{x}_2/2:\vec{p}_1,\vec{p}_2). \qquad (6.14)$$

We insert Equation (6.13) into the expression for the two-particle probability, Equation (6.6), perform the integration over k_i^0 and obtain

$$\Pi(\vec{p}_1,\vec{p}_2) = \int d^3\delta k_1 d^3\delta k_2 d^3R_1 d^3R_2 d^3k_1 d^3k_2 d^4x_1 d^4x_2 \tilde{S}(x_1,E_1,\vec{k}_1)\tilde{S}(x_2,E_{12}-E_1,\vec{k}_2)$$

$$f_2(\vec{k}_1,\vec{k}_2,\vec{R}_1,\vec{R}_2:\vec{p}_1,\vec{p}_2)e^{-i\delta\vec{k}_1\bullet(\vec{x}_1+\vec{k}_1(t_2-t_1)/m-\vec{R}_1) - i\delta\vec{k}_2\bullet(\vec{x}_2-\vec{R}_2)} \qquad (6.15)$$

If we had used a different "reasonable" formula for Equation (6.12) or kept more terms in the expansion of $E(\vec{k}+\delta\vec{k})$, we would have obtained the same formula as Equation (6.15) except that the partition of energy into the source at x_1 and the source at x_2 would have been different. These details are not important since they will be absorbed into the approximation of the next paragraph.

In order to make the formalism tractable, that is depend only on $\tilde{S}(\vec{x}, E, (\vec{k}_1+\vec{k}_2)/2)$, we now make the assumption that the product of the matrix elements

$\tilde{S}_1 \bullet \tilde{S}_2$ depends weakly on the partition of the four-momentum. In order for the particles to interact, x_1 and x_2 must be very close together. The function $\tilde{S}$ should then have the same momentum dependence at both points. If the momentum dependence is thermal, then the product of the Boltzmann distributions has no dependence on k_1-k_2. Even for arbitrary momentum dependence, the product $\tilde{S}_1 \bullet \tilde{S}_2$ has, to first order, no dependence on relative momentum. If we do not make the approximation of weak dependence on the partition of four-momentum, the formalism is intractable, unless we know quantum details of the emission matrix $\tilde{S}(k,x)$ for $k^0 \neq E(\vec{k})$. This assumption allows us to integrate over $d^3\delta k_i$ and d^3R_i and express the two-particle probability as:

$$\Pi(\vec{p}_1,\vec{p}_2) = \int d^3k_1 d^3k_2 d^4x_1 d^4x_2 \tilde{S}(x_1,E_{12}/2,(\vec{k}_1+\vec{k}_2)/2)\tilde{S}(x_2,E_{12}/2,(\vec{k}_1+\vec{k}_2)/2)$$

$$f_2(\vec{k}_1,\vec{k}_2,\vec{x}_1+\vec{k}_1(t_2-t_1)/m,\vec{x}_2;\vec{p}_1,\vec{p}_2)\,. \qquad (6.16)$$

Since the total momentum of the pair is conserved during the evolution towards their asymptotic momentum states, we can substitute $\vec{k}_1+\vec{k}_2=\vec{p}_1+\vec{p}_2:=\vec{P}$. We obtain:

$$\Pi(\vec{p}_1,\vec{p}_2) = \int d^3k_1 d^3k_2 d^4x_1 d^4x_2 \tilde{S}(x_1,P/2)\tilde{S}(x_2,P/2)$$

$$f_2(\vec{k}_1,\vec{k}_2,\vec{x}_1+\vec{k}_1(t_2-t_1)/m,\vec{x}_2;\vec{p}_1,\vec{p}_2)\,. \qquad (6.17)$$

The emission function $\tilde{S}$ is evaluated at the four-momentum $P=(E(\vec{P}),\vec{P})$. In general, the 0-th component of this four-vector is not equal to E_{12}. However, as long as $\vec{p}_1$-$\vec{p}_2$ is small, this difference can be neglected. This approximation allows us now to replace the function $\tilde{S}(x,P/2)$ with the single particle emission probability $g(\vec{P}/2,x)$, see Equation (6.10). We can now calculate the two-particle probability in terms of single particle probabilities. It is prudent to make the same

approximations in the expression for the single- particle emission probabilities. Then the correlation function for non-interacting particles will remain at unity even when $\vec{p}_1$-$\vec{p}_2$ is not small.

Dividing the two-particle emission probability from Equation (6.17) by the single particle emission probabilities thus yields for the two-particle correlation function:

$C(\vec{P},\vec{q}) =$

$$\frac{\int d^4x_1 d^4x_2 d^3k_1 d^3k_2 g(\vec{P}/2, x_1)\, g(\vec{P}/2, x_2)\, f_2(\vec{k}_1, \vec{k}_2, \vec{x}_1 + \vec{k}_1(t_2-t_1)/m, \vec{x}_2 : \vec{p}_1, \vec{p}_2)}{\int d^4x_1 d^3k_1 g(\vec{P}/2, x_1)\, f_1(\vec{k}_1, \vec{x}_1 : \vec{p}_1) \int d^4x_2 d^3k_2\, g(\vec{P}/2, \vec{x}_2) f_1(\vec{k}_2, \vec{x}_2 : \vec{p}_2)} \tag{6.18}$$

Using the definition of the Wigner decompositions, Equation (6.14), and the fact that the two-particle wave function can be factored into the center-of-mass wave function multiplied by the relative wave function,

$$\Phi(\vec{x}_1, \vec{x}_2 : \vec{p}_1, \vec{p}_2) = \exp[-i(\vec{p}_1+\vec{p}_2)(\vec{x}_1+\vec{x}_2)/2]\, \phi[(\vec{p}_1-\vec{p}_2)/2, \vec{x}_1-\vec{x}_2], \tag{6.19}$$

one finds for the integrals over the Wigner functions f_1 and f_2:

$$\int d^3k_i f_1(\vec{k}_i, \vec{x}_i : \vec{p}) = 1, \tag{6.20}$$

$$\int d^3k_1 d^3k_2 f_2(\vec{k}_1, \vec{k}_2, \vec{x}_1, \vec{x}_2 : \vec{p}_1, \vec{p}_2) = \int d^3(k_1+k_2) d^3\left(\frac{k_1-k_2}{2}\right) f_2(\vec{k}_1, \vec{k}_2, \vec{x}_1, \vec{x}_2 : \vec{p}_1, \vec{p}_2)$$

$$= \int d^3(k_1+k_2) d^3\left(\frac{k_1-k_2}{2}\right) \delta^3(\vec{P}-\vec{k}_1-\vec{k}_2)$$

$$\int d^3\delta r \exp[i\delta\vec{r}\bullet(\vec{k}_1-\vec{k}_2)/2]\, \phi^*(\vec{q}, \vec{x}_1-\vec{x}_2+\delta\vec{r}/2)\phi(\vec{q}, \vec{x}_1-\vec{x}_2-\delta\vec{r}/2)$$

$$= |\phi(\vec{q},\vec{x}_2-\vec{x}_1)|^2 . \qquad (6.21)$$

Inserting these relations into Equation (6.18) now yields our final result which was already given in Equation (6.1).

The central assumption underlying our derivation is the approximation $\tilde{S}(x,E,\vec{k}) \approx \tilde{S}(x,E,(\vec{k}_1+\vec{k}_2)/2)$. This approximation becomes exact when the emission function $\tilde{S}(x,k)$ is broad, i.e. when its characteristic momentum is much larger than the relative momentum or the momentum spread of the resonance. In intermediate energy heavy-ion collisions this is an appropriate assumption since the characteristic momenta are of the order of magnitude of a few hundred MeV/c and the relative momenta of interest are smaller than 50 MeV/c. (The important momentum components for the ^{2}He "resonance" lie below 100 MeV/c.) If we keep the momentum dependence in Equation (6.15), expanding $\vec{k}_i$ about $\vec{P}/2$, we can show that this dependence cancels out in first order. Thus we expect the formalism to give very close to the correct answer, unless the characteristic momentum of the emission becomes quite small. Our derivation does not rely on the assumption that the system be semi-classical and that the thermal wavelength be much shorter than the size of bound states or even the size of the emitting system. Our result is valid as long as the product of $\tilde{S}_1 \cdot \tilde{S}_2$ depends only on $\vec{k}_1+\vec{k}_2$ and not $\vec{k}_1-\vec{k}_2$. For systems which sample many states, such as a thermal system, this is a good assumption. Since usually there is no knowledge of the matrix elements as a function of k^0, these approximations are the best we can do. Luckily, since we are interested in correlations for small relative momenta and since the characteristic momenta of the protons are sufficiently high, these are excellent approximations.

The correlation function $C(\vec{P},\vec{q})$ depends only on the final relative positions of all the particles with momentum $\vec{P}/2$. To make this more clear, we write Equation (6.1) as:

$$C(\vec{P},\vec{q}) = \int d^3r\ F_{\vec{P}}(\vec{r})\,|\,\phi(\vec{q},\vec{r})\,|^2, \tag{6.22}$$

where $\vec{r} = \vec{r}_1 - \vec{r}_2$ is the relative coordinate of the emitted particles. The function $F_{\vec{P}}(\vec{r})$ is defined by:

$$F_{\vec{P}}(\vec{r}) = \frac{\int d^3R f(\vec{P}/2, \vec{R}+\vec{r}/2, t_>)\, f(\vec{P}/2, \vec{R}-\vec{r}/2, t_>)}{|\int d^3r' f(\vec{P}/2, \vec{r}', t_>)|^2}. \tag{6.23}$$

where $\vec{R} = \frac{1}{2}(\vec{r}_1 + \vec{r}_2)$ is the center-of-mass coordinate of the two particles. The Wigner function $f(\vec{p},\vec{r},t_>)$ is the phase-space distribution of particles of momentum $\vec{p}$ at position $\vec{r}$ at some time, $t_>$, after both particles have been emitted:

$$f(\vec{p},\vec{r},t_>) = \int_{-\infty}^{t_>} dt\, g(\vec{p},\vec{r}-\vec{p}(t_>-t)/m,t). \tag{6.24}$$

For a given momentum $\vec{P}$, the correlation has three degrees of freedom, $\vec{q}$, which are a function of $F_{\vec{P}}(\vec{r})$. The most we can hope to extract from the correlation function is $F_{\vec{P}}(\vec{r})$, the normalized probability of two protons with the same momentum $\vec{P}/2$ being separated by $\vec{r}$. We have shown in the derivation above that the calculation of $F_{\vec{P}}(\vec{r})$ requires only the knowledge of the single-particle phase-space distributions or the emission probability $g(\vec{p},\vec{r},t)$.

6.2 Illustrative Calculations and Discussions

In this section, we will discuss the physical information contained in two-proton correlation functions, such as the source size and lifetime, and point out characteristic signatures of slowly-cooling and explosive sources, respectively. The function $F_{\vec{P}}(\vec{r})$, Equation (6.23), contains significant information about the dynamics of the collision. For instance, a long lived source will lead to an extended separation when $\vec{r}$ is parallel to the velocity $\vec{P}/2m$. Thus in addition to the spatial extent of $F_{\vec{P}}(\vec{r})$ one gains insight into the lifetime of the source [Prat 87].

The $\vec{P}$ dependence yields insight into the dynamics of the collision. Both the size and the lifetime can depend on the total momentum. Cooling [Prat 87, Frie 83, Boal 86] is signified by increasingly large lifetimes for particles with smaller energies. We discuss this later in the section on the compound nucleus. Collective explosive flow is signaled by short lifetimes and shrinking apparent source dimensions for increasing energy [Prat 87]. There should be a transition in reaction mechanisms, from evaporative to exploding, at excitation energies near the nuclear binding energy. This is the dynamical equivalent of the liquid-gas phase transition. At low excitation, nuclei slowly evaporate particles, cooling like a hot liquid drop. At sufficiently high excitation, nuclei explode and expand like a gas [Prat 87].

The relative wave function, $\phi(\vec{q},\vec{r})$, is influenced by three different effects: identical particle interference, short range hadronic interaction, and the Coulomb repulsion of the protons. Additionally, it is affected by the weighting factors for the partition of various spin states. We briefly discuss how these effects contribute to the correlation function and how the resulting correlations can be used to determine $F_{\vec{P}}(\vec{r})$.

To calculate the relative wave function numerically, we solved the Schrödinger equation for the $\ell=0$ and $\ell=1$ partial waves with Coulomb and the Reid soft-core potential [Reid 68]. We used the full Coulomb wave function [Mess 76], $\phi_c(\vec{q},\vec{r})$, and added the modification $\delta\phi(\vec{q},\vec{r})$ which is the contribution to the relative wave function from the first two partial waves minus the contribution which would have occurred if the strong interaction were absent. The two-proton relative wave function, $\phi(\vec{q},\vec{r})$, is then obtained by

$$|\phi(\vec{q},\vec{r})|^2 = w_s \bullet |{}^1\phi(\vec{q},\vec{r})|^2 + w_t \bullet |{}^3\phi(\vec{q},\vec{r})|^2, \qquad (6.25)$$

where ${}^1\phi(\vec{q},\vec{r})$ and ${}^3\phi(\vec{q},\vec{r})$ are the singlet and triplet ^{2}He spatial wave functions, respectively and w_s and w_t are the spin weighting factors for the singlet and triplet ^{2}He, respectively. In most cases, two-proton spins are assumed to be statistically distributed so that $w_s=1/4$ and $w_t=3/4$. This assumption is followed in our analysis.

For identical non-interacting particles, the squared wave function has the form: $|\phi(\vec{p},\vec{r})|^2 \propto (1\pm\cos(2\vec{p}\cdot\vec{r}))$. In that case, the inverse Fourier transform of the correlation function would yield the complete three-dimensional function $F_{\vec{P}}(\vec{r})$. For spin-half particles, the correlation function is reduced to one half at $|\vec{q}|=0$ [Kopy 72] and returns to unity with a width of $q_x \approx 1/R_x$. Experiments that gate on the direction of the relative momentum can then determine all three spatial dimensions of $F_{\vec{P}}(\vec{r})$.

Coulomb interactions yield a dip in the correlation function which goes to zero as $\vec{q}$ approaches zero. As long as the characteristic dimensions of $F_{\vec{P}}(\vec{r})$ are much smaller than the two-proton Bohr radius of 58 fm, the shape of the dip does not depend on the shape or size of the source but only on the Gamov factor. For larger sources, the Coulomb interaction, too, provides information about both the source size and, to a weak degree, on the shape. The Coulomb dip in the correlation function at $|\vec{q}|=0$ will diminish for large sources. The most unfortunate aspect of the Coulomb interaction is that the Coulomb dip lessens the number of available pairs at small relative momentum, making it more difficult to see the effects of identical particle interference.

Strong interactions provide excellent gauges of the size of smaller sources, $R \lesssim 10$ fm. The ^{2}He "resonance" appears as a bump in the two-proton correlation function at $q \approx$ 20 MeV/c. (Strictly speaking, the ^{2}He "resonance" is not a resonance, since the phase shift does not increase by 90°, but only by about 60°.) The size of the bump is proportional to the percentage of pairs whose relative

position is within the size of the nearly bound state. Thus the height goes roughly as R^{-3}. This provides a very sensitive test of the size, but not of the shape.

As was recently pointed out [Zhu 91], two-proton spin distribution could be distributed non-statistically in fast break-up reactions of light projectile nuclei. In such cases, the spin weighting factors can be different from $w_s=1/4$, $w_t=3/4$ and the shape of correlation function will be modified accordingly.

For typical source sizes of about 5 fm, all the above effects are important. Choosing a distribution $F_{\vec{P}}(\vec{r})$ that fits the correlation function requires more than just the appropriate size as measured by a single parameter. One must have $F_{\vec{P}}(\vec{r})$ correct for large $\vec{r}$ in order to fit the correlation function at low $\vec{k}$ in the Coulomb dip and one must have $F_{\vec{P}}(\vec{r})$ correct at small $\vec{r}$ in order to fit the height of the correlation function. If the source is not so large that the Coulomb dip erases the effect of identical particle interference, the shape must be chosen correctly as well to fit the correlation function for different directions of $\vec{q}$. Thus all the physical characteristics of $F_{\vec{P}}(\vec{r})$ can be tested with correlation measurements provided that all effects due to quantum statistics and final state interactions are properly taken into account. In the following subsections we illustrate some these qualitative expectations by calculations performed for simple analytical emission sources.

6.2.1 Spherical Sources of Negligible Lifetime

The relative importance of anti-symmetrization and the nuclear and Coulomb interactions depends on the size of the emitting system. In order to provide a quantitative comparison of these effects, we have calculated two-proton correlation functions for Gaussian sources of negligible lifetime,

$$g(\vec{p},\vec{r},t) = \rho(r)\delta(t-t_0) = \rho_0 \exp(-r^2/r_0^2)\delta(t-t_0), \qquad (6.26)$$

in which the nuclear interaction and the Pauli principle were turned off successively. These calculations are compared in Figure 6.1 for a number of

representative radius parameters (r_0 = 2.5, 5, 10, 20 fm) . The solid curves show the results of the full calculations which include the nuclear and Coulomb interactions and the Pauli exclusion principle. The dotted lines show calculations for which the nuclear interaction has been turned off; these calculations still include quantum effects of the two-proton Coulomb interaction and the anti-symmetrization of the relative wave function. The dashed curves represent calculations for which both the nuclear interaction and the anti-symmetrization of the relative wave function have been turned off. (These latter calculations differ from classical Coulomb trajectory calculations [DeYo 89, DeYo 90, Elma 91] since the Coulomb repulsion between the two protons is treated quantum mechanically. For large source dimensions or emission from long-lived sources, this difference should be of minor importance.) For radius parameters, $r_0 \lesssim 10$ fm, both the anti-symmetrization of the relative wave function and the nuclear interaction have important effects on the detailed shape of the calculated correlation functions. For much larger source dimensions, $r_0 \gtrsim 20$ fm, the Coulomb interaction dominates and the neglect of the Pauli principle and the nuclear interaction can be justified [DeYo 89, DeYo 90, Elma 91].

Furthermore, we have calculated two-proton correlation functions for Gaussian source of negligible lifetime with three different assumptions about the spin weighting factors (w_s,w_t) in Equation (6.25) in order to assess the relative

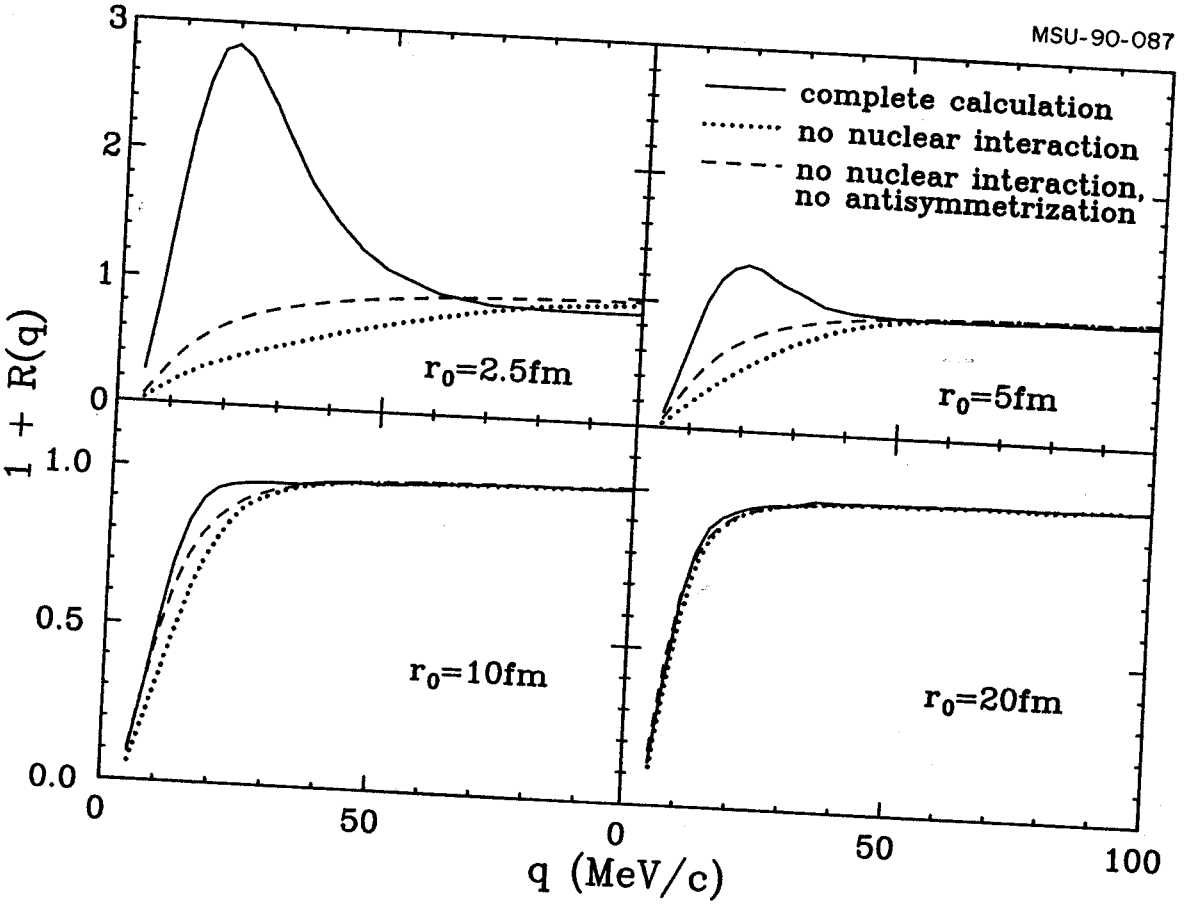

Figure 6.1: Two-proton correlation functions calculated for Gaussian sources of negligible lifetime with representative radius parameters, r_0 =2.5, 5, 10, 20 fm. The solid curves show the result of the full calculations; the dotted curves show calculations for which the nuclear interaction is neglected; the dashed curves shown calculations for which the nuclear interaction and the Pauli principle are neglected.

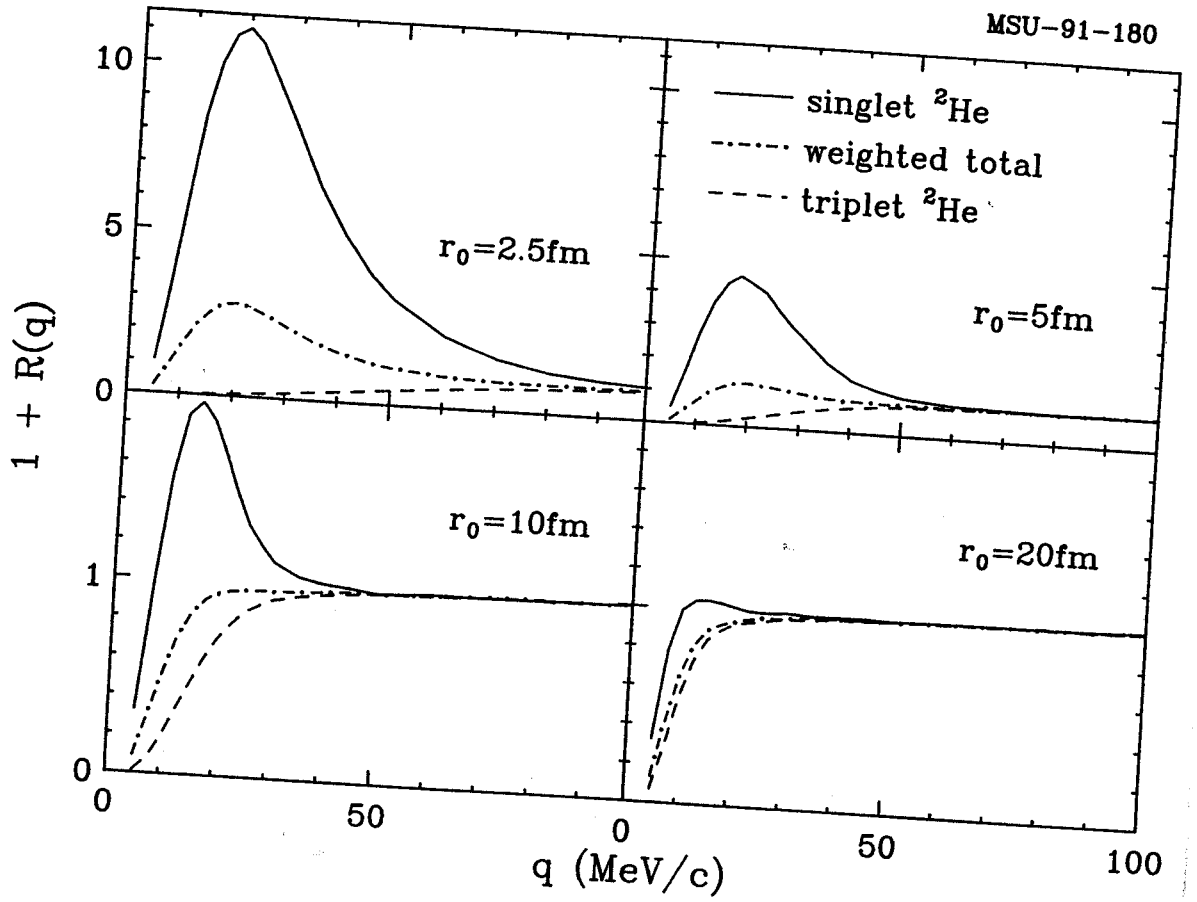

Figure 6.2: Two-proton correlation functions calculated for Gaussian sources of negligible lifetime with representative radius parameters, r_0=2.5, 5, 10, 20 fm. Assuming the two-proton relative wavefunction to be: $|\phi|^2 = w_s \bullet |^1\phi|^2 + w_t \bullet |^3\phi|^2$, the solid, dotdashed and dashed curves show calculations for (1) w_s = 1 and w_t = 0, (2) w_s = 1/4 and w_t = 3/4, (3) w_s = 0 and w_t = 1, respectively.

importance of singlet and triplet spin states. In Figure 6.2, solid and dashed curves represent the calculated two-proton correlation functions for the singlet (S = 0: $w_s = 1$, $w_t = 0$) and triplet (S = 1: $w_s = 0$, $w_t = 1$) ^{2}He spin states, respectively. The dot-dashed curves are the averaged calculations using $w_s = 1/4$ and $w_t = 3/4$. Four representative radius parameters (r_0 = 2.5, 5, 10, 20 fm) are used to see the dependence of the spin-state effect on the emission-source sizes. For radius parameters, $r_0 \leq 5$ fm, the singlet two-protons have very strong correlations around $q \approx 20$ MeV/c and the triplet two-protons show large anti-correlations. These are consistent with the respective proton-proton potentials [Reid 68]. At larger radii, the singlet two-proton correlations become weak and the peak shifted to q less than 20 MeV/c, and the anti-correlations for triplet two-protons are smaller, too. Overall, the correlation peak at q≈20MeV/c is most dominated by the singlet spin state.

Most analyses of fast-particle-emission processes [Zarb 81, Lync 83, Gust 84, Chen 87a, Chen 87b, Poch 86, Poch 87, Fox 88, Awes 88, Cebr 89] have used sources of negligible lifetime with spherically symmetric Gaussian density distributions, Equation (6.26). For spherically symmetric sources, the shape of the two-proton correlation function is rather insensitive to details of the density profile. To illustrate this point, we compare the shapes of two-proton correlation functions calculated for sources of negligible lifetime with Gaussian, Equation (6.26), and uniform sharp-sphere density distributions,

$$g(\vec{p},\vec{r},t)=\rho_0\,\Theta(r)\Theta(R_s-r)\,\delta(t-t_0). \qquad (6.27)$$

In Equation (6.27), R_s is the sharp sphere radius and $\Theta(x)$ is the unit step function which vanishes for negative arguments. The solid and dotted curves in Figure 6.3 represent calculations performed with Eqs. (6.26) and (6.27), respectively. In these calculations, the radius parameters have been adjusted to match the magnitudes

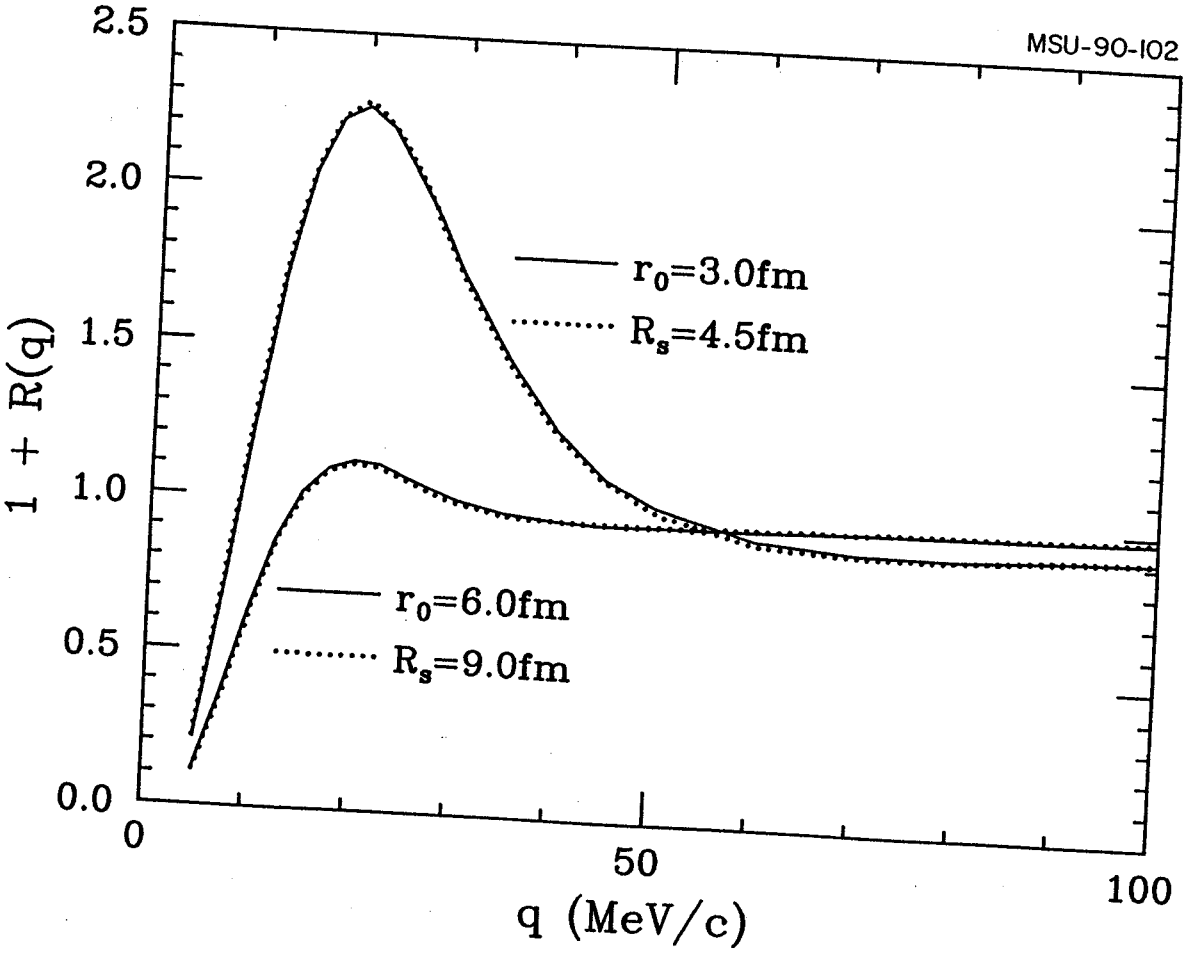

Figure 6.3: Two-proton correlation functions calculated for sources of negligible lifetime assuming Gaussian (solid lines) and sharp sphere (dotted lines) density distributions. The radius parameters, r_0 and R_s, are indicated.

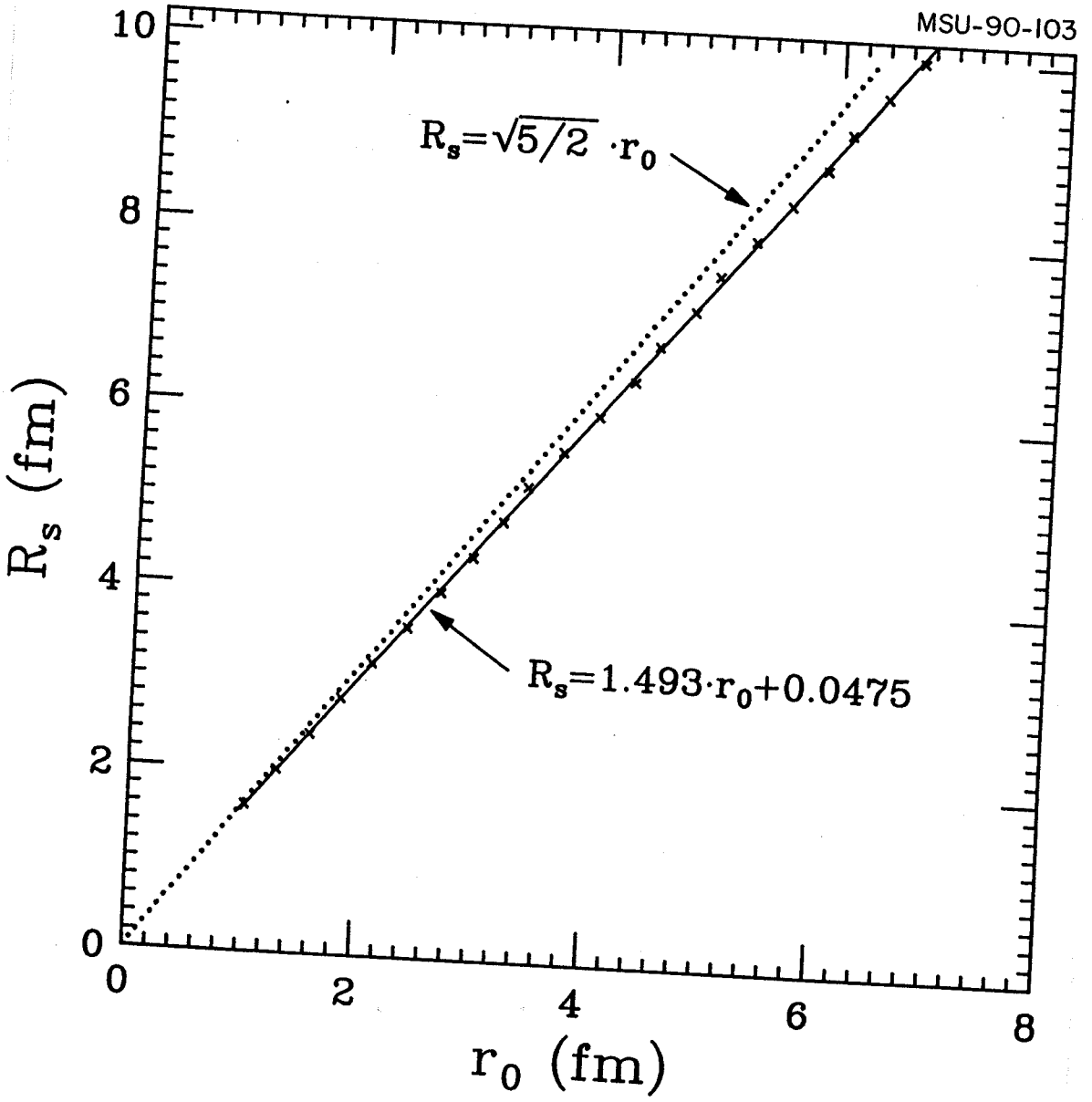

Figure 6.4: Relation between radius parameters, r_0 and R_s, of Gaussian and sharp sphere density distributions for which equivalent two-proton correlation functions are obtained in the limit of negligible lifetime. Crosses indicate results of numerical calculations, the solid line represents a linear fit, and the dotted curve shows the relation $R_s=\sqrt{(5/2)}\, r_0$ used in the literature [Boal 90].

of the maxima at q≈20 MeV. The correlation functions calculated for these rather different density profiles are virtually identical in shape.

Previously, Gaussian source parameters, r_0, have been translated [Boal 90] into equivalent sharp-sphere radii, R_s, by employing the approximate relation, $R_s \approx \sqrt{(5/2)}\, r_0$. This relation can be justified by equating the rms radii of the two density distributions. Equivalent radii, r_0 and R_s, of the two density profiles can also be defined by the requirement that the calculated correlation functions have maxima of identical height. Such equivalent radii are indicated by ×-shaped symbols in Figure 6.4. These equivalent radii can be rather well described by the relation $R_s = 1.493 r_0 + 0.0475$ fm; this relation is represented by the solid curve in Figure 6.4. For comparison, the analytically derived relation, $R_s = \sqrt{(5/2)}\, r_0$, is indicated by the dotted curve; it is a surprisingly good approximation.

6.2.2 Spherical Sources of Finite Lifetime

In order to illustrate the sensitivity of the shapes of two-proton correlation functions to the lifetime of the emitting system, we have performed calculations under the simplifying assumption that particles are emitted from a spherical volume of radius R_s according to a simple exponential law,

$$g(\vec{p},\vec{r},t) \propto \rho_0 \Theta(r)\Theta(R_S - r)\Theta(t) p e^{-p^2/2mT - t/\tau}, \qquad (6.28)$$

where T and τ denote the (constant) source temperature and lifetime, respectively.

Calculations for two-proton correlation functions, integrated over all relative orientations between $\vec{P}$ and $\vec{q}$, are shown in Figure 6.5. The parameters used in these calculations are given in the figure. The upper panel of the figure illustrates the sensitivity to the lifetime of the emitting system for proton pairs of total

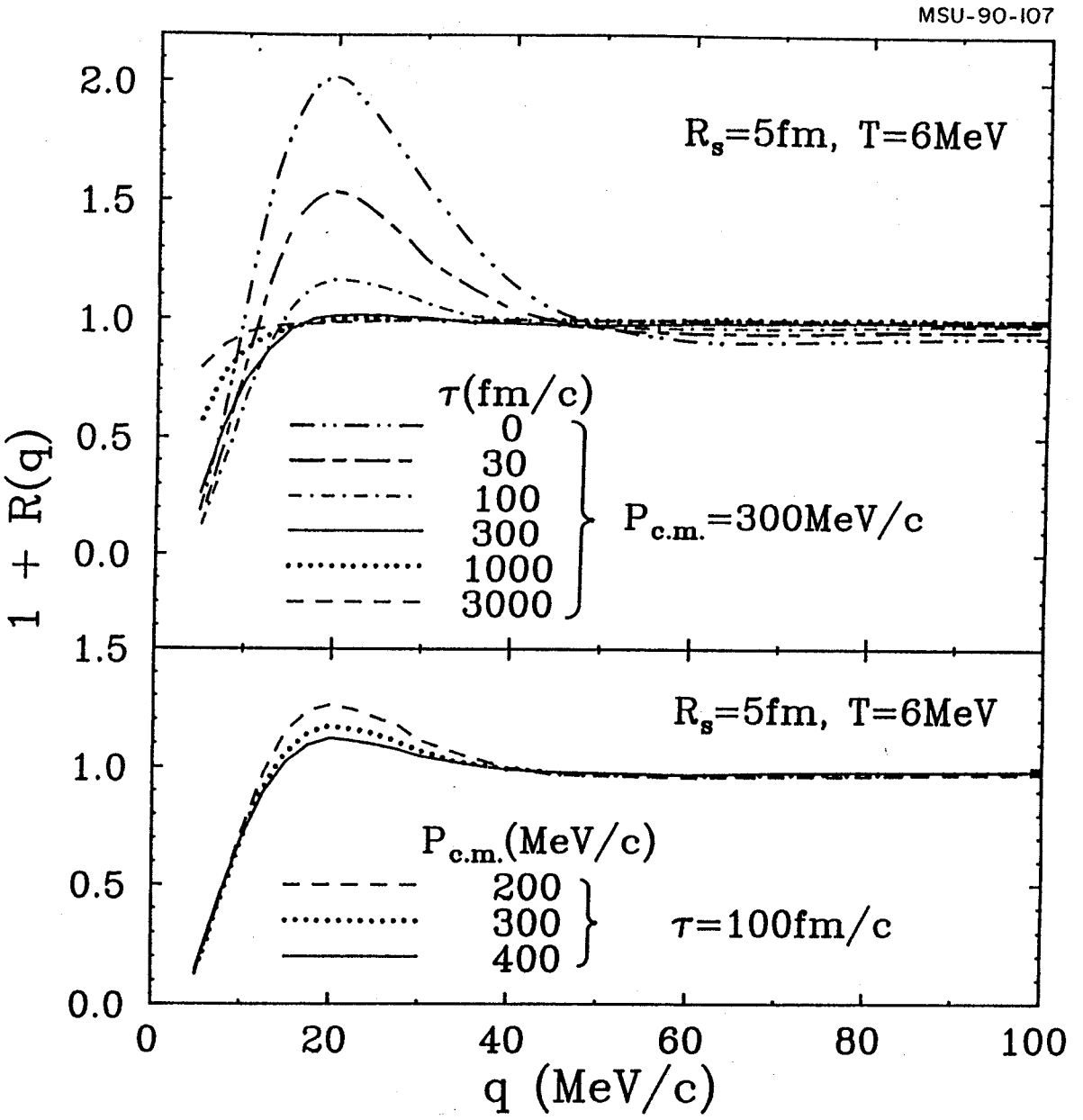

Figure 6.5: Two-proton correlation functions predicted for emission from spherical sources of radius R_s=5 fm, decaying isotropically with fixed life-time, Equation (6.28). The top and bottom panels depict the dependence on life-time, τ, and total momentum, $P_{c.m.}$, respectively.

momentum, $P_{c.m.}$ = 300 MeV/c, measured in the rest frame of the emitting source. The calculated two-proton correlation functions exhibit considerable sensitivity to lifetimes of the order of 30-3000 fm/c. For much shorter lifetimes, the shape of the correlation function becomes dominated by the spatial dimension of the emitting system; for much longer lifetimes the correlations disappear. The lower panel of Figure 6.5 illustrates how the correlation function depends on the total momentum of the emitted proton pairs for the case of a fixed lifetime, τ=100 fm/c. The calculated correlations become more pronounced for smaller total momenta, i.e. for particles emitted with lower kinetic energies. This dependence can be understood in terms of the spatial extent of the Wigner distribution. The longitudinal dimension of the apparent source is of the order of $(P_{c.m.}/2m_p)\tau$, where m_p denotes the proton mass. For fixed lifetime, τ, this quantity increases for larger values of $P_{c.m.}$ and the correlation function becomes attenuated. Such a momentum dependence stands in contrast to experimental observations [Lync 83, Chen 87a, Chen 87b, Poch 86, Poch 87, Awes 88, Gong 91b] and is opposite to that calculated for emission from compound nuclei for which the effects of cooling produce a strong momentum dependence of the effective decay times (see also the discussion in Chapter 8).

Figure 6.6 illustrates the dependence of the two-proton correlation function on the angle, $\Psi = \cos^{-1}(\vec{P}\bullet\vec{q}/Pq)$, between the relative and total momentum vectors of the two-proton pair. As was done in the experimental analysis [Gong 91b], we define longitudinal and transverse correlation functions by the cuts $|\cos\Psi| \geq 0.77$ (Ψ=0°-40° or 140°-180°) and $|\cos\Psi| \leq 0.5$ (Ψ=60°-120°), respectively. Different panels of Figure 6.6 show longitudinal and transverse correlation functions calculated for different lifetimes τ=0, 10, 30, 100, 300, 1000 fm/c. In these calculations, the total momentum of the proton pair was kept constant at $P_{c.m.}$=300 MeV/c. For very short lifetimes, $\tau \lesssim 10$ fm/c, the apparent source is essentially

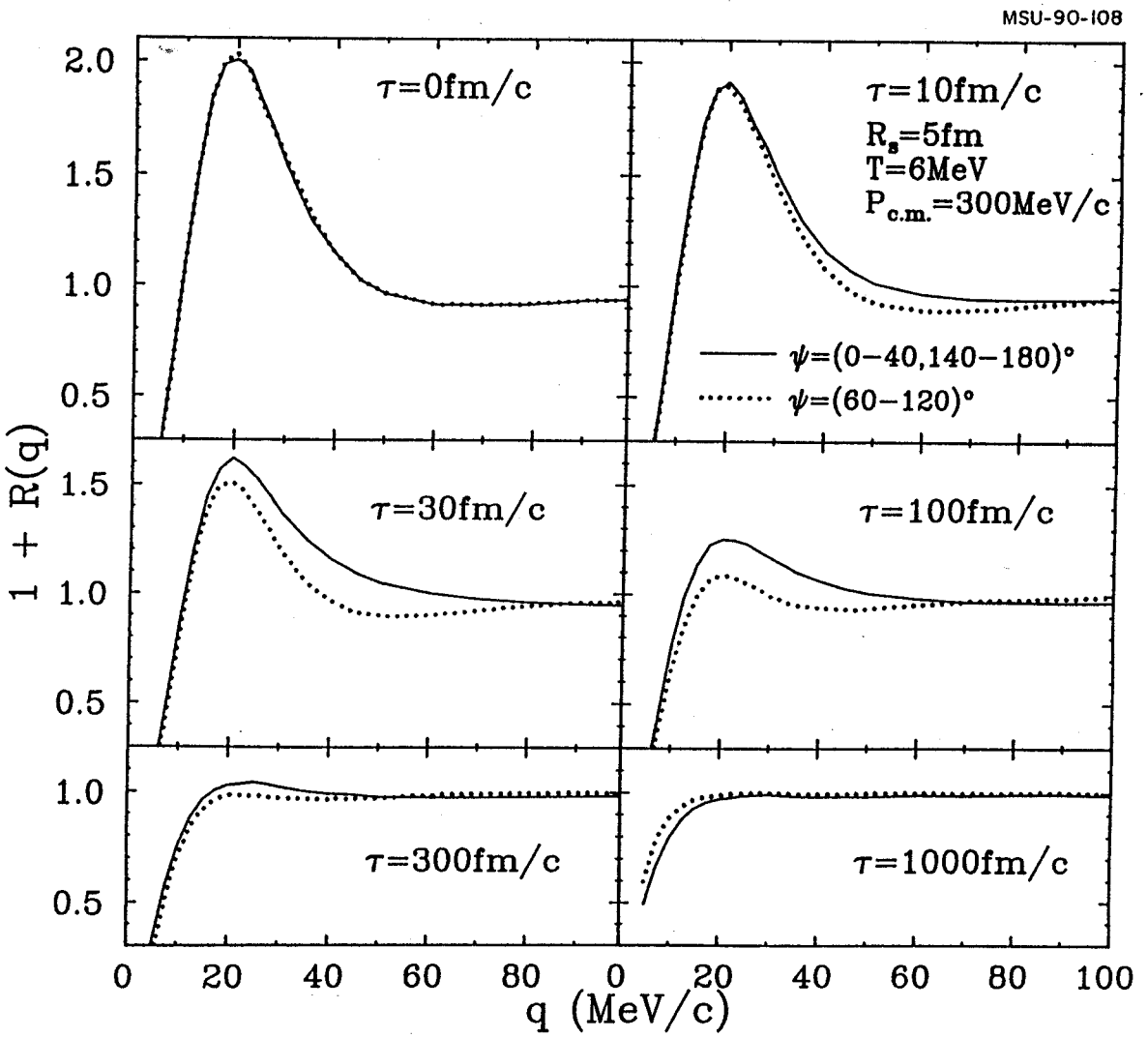

Figure 6.6: Longitudinal and transverse correlation functions calculated for emission from sources decaying with constant lifetimes, Equation (6.28). The parameters used in these calculations are indicated in the figure.

spherical in shape and life-time effects are negligible for the calculation of the two-proton correlation function. For an intermediate time-window, $\tau \approx$30-300 fm/c, longitudinal and transverse correlation functions are sensitive to the lifetime of the emitting system. For larger lifetimes, $\tau \gtrsim 1000$ fm/c, this sensitivity is essentially lost as the average separation between emitted particles becomes so large that anti-symmetrization effects become negligible. In fact, for extremely large lifetimes the effect is reversed because Coulomb induced correlations contain a weak amount of directional information. The Coulomb force is parallel to the relative displacement of the protons; therefore, the Coulomb hole in the correlation function will be strongest when the relative momentum is parallel to the longest dimension of the pair's separation. For long-lived sources this is the longitudinal direction. Comparisons of longitudinal and transverse correlation functions yield the strongest sensitivity to the lifetime of the emitting system on the order of 30-300 fm/c. By more judicious choices of the gates on $P_{c.m.}$, one may stretch the sensitivity of such measurements beyond these rough boundaries.

6.3 Comparison with Classical Trajectory Calculation

Two-proton correlation functions have been used to study emission time scales of evaporative emission processes [DeYo 89, Ardo 89, DeYo 90, Gong 90b, Elma 91, Gong 91b]. Two different techniques have been used to calculate two-proton correlation functions. One technique is based upon the Wigner function formalism outlined in Section 6.1, and the other employs classical trajectory calculations [DeYo 89, DeYo 90, Elma 91]. As it is not clear whether and under which conditions the two approaches yield similar (or identical) results, we have performed numerical calculations for a simplified source function in order to make quantitative comparisons between the two approaches and explore the validity of the approximations underlying different theoretical treatments.

Similar to Equation (6.28), we used a simple source function corresponding to thermal emission from the surface of a sharp sphere of radius R:

$$g(\vec{p},\vec{r},t) \propto (\hat{r}\bullet\hat{p})\Theta(\hat{r}\bullet\hat{p})\delta(r-R_S)\Theta(t)\Theta(E-V_S)(E-V_S)e^{-(E-V_S)/T - t/\tau} . \qquad (6.29)$$

Here, $\hat{r}$ and $\hat{p}$ are unit vectors parallel to $\vec{r}$ and $\vec{p}$; $E=p^2/2m$; $V_S = Z_S e^2/R_S$ is the Coulomb barrier. Calculations were performed with the parameters: $Z_S = 78$, $R_S =$ 8 fm, T = 4 MeV, and τ = 200, 500, 1000 fm/c. We have chosen a relatively low temperature parameter to emphasize the emission of low-energy protons pertinent to evaporative emission from hot compound nuclei.

In the Wigner function formalism, the two-particle correlation function depends only on the final relative positions of all the particles with momentum $\vec{P}/2$. It is derived under the assumptions that the final-state interaction between the two protons dominates and that final-state interactions with the remaining system are negligible, that the single-particle phase-space distribution varies only slowly over particle momenta $P/2\pm q$, and that the correlation functions are determined by the two-body density of states as corrected by the interactions between the two particles.

For a long-lived source, we assume that the Coulomb force is the only interaction between two protons. After integrating over all relative orientations between $\vec{P}$ and $\vec{q}$, we obtained the classical approximation to Equation (6.22) as: [Kim 91a, Kim 91b]

$$1+R(\vec{P},\vec{q}) = \int d^3r\, F_{\vec{P}}(\vec{r})\,[\,1-me^2/q^2r\,]^{1/2} . \qquad (6.30)$$

Classical trajectory calculations similar to References [Kim 91a, Kim 91b] were performed for proton emissions. The final-state Coulomb interaction with the emitting system was incorporated ($Z_S = 78$), or neglected ($Z_S = 0$). Recoil effects were taken into account (the mass of the emitting system was taken as $M_S = 197$ u). The emission function in the rest frame of the emitting system, Equation 6.29, was sampled by Monte-Carlo techniques. For trajectory calculations in which the

Coulomb interaction with the emitting system was taken into account ($Z_S = 78$), the Coulomb parameter in Equation (6.29) was set to $V_S = 0$. For calculations in which the Coulomb interaction with the emitting nucleus was turned off, the Coulomb parameter $V_S = 78e^2/R_S$ was used in Equation (6.29) to ensure close similarity of the asymptotic kinetic energy spectra for all calculations. Upon emission, the particle trajectories were calculated by integrating Newton's equations, and the asymptotic particle momenta were stored as coincidence events and as single-particle spectra. These simulated events were treated in the same manner as the measured data to generate two-proton correlation functions according to Equation (7.1).

Correlation functions calculated with various approximations are compared in Figure 6.7 for emission times of τ=200fm/c (upper part), 500fm/c (middle part), and 1000fm/c (lower part). The solid curves represent the correlation functions calculated with the Wigner function formalism by including nuclear and Coulomb interactions and anti-symmetrization of wave-function. The dotted curves represent the same calculations except that the nuclear interaction was turned off. Comparison between these two calculations indicates that the nuclear interaction is important for life-times $\tau \lesssim 500$ fm/c.

The dashed curves in Figure 6.7 represent calculations with the Wigner function formalism in which the two protons are assumed to be spinless and distinguishable particles experiencing only Coulomb interaction. The relative wave function is given by the (non-antisymmetrized) Coulomb scattering wave-function. The dot-dashed curves show the results obtained with Equation (6.30). For the lifetimes considered, the classical approximation provides an excellent approximation for the calculations of angle integrated correlation functions

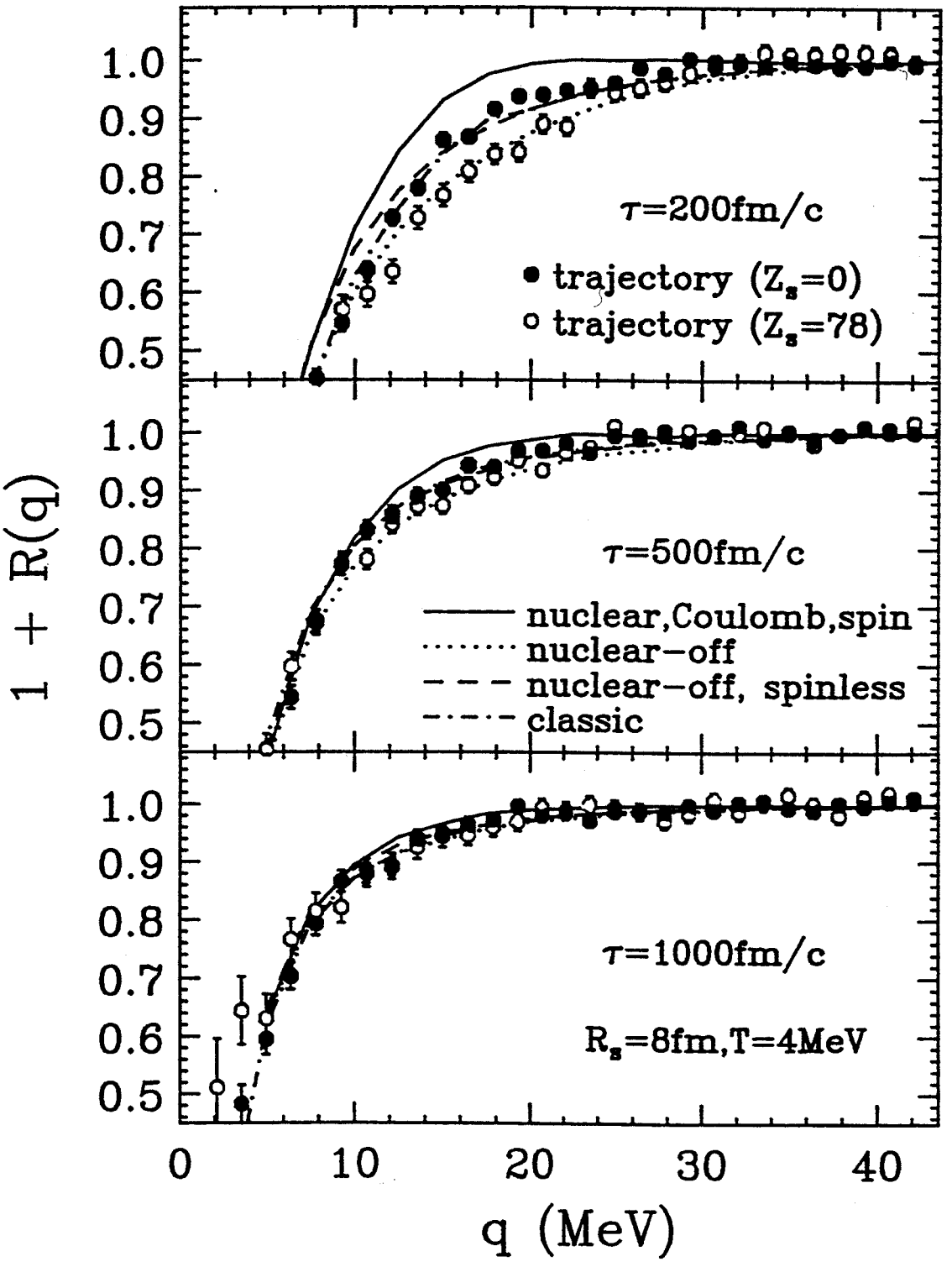

Figure 6.7: Two-proton correlation functions for a schematic source, Equation (6.29), representing thermal surface emission with fixed life-times, τ=200fm/c (upper part), τ=500fm/c (middle part), and τ=1000fm/c (lower part). The parameters are indicated in the figure. Different symbols and curves are explained in the text.

arising from Coulomb final-state interactions between distinguishable particles, even if they are as light as protons. (Note, however, that anti-symmetrization effects can only be safely neglected for $\tau \gtrsim 1000$ fm).

The open points in Figure 6.7 show the results of classical trajectory calculations incorporating the Coulomb interaction with the emitting system (Z_S=78). For comparison, the solid points show results obtained by turning off the Coulomb interaction with the emitting source (Z_S=0). (These latter calculations are not necessarily identical with results obtained from Equation (6.30) as they do not rely on the approximation, implicit in the Wigner function formalism, of using only the one-body phase-space density at the center-of-mass velocity of the two-proton pair.) The differences between the two trajectory calculations are small. For short emission time scales (τ=200 fm/c), however, they are not negligible. (This conclusion depends on the shape of the energy spectrum: Coulomb distortions in the field of the heavy reaction residue decrease for the emission of more energetic protons.) For large emission time scales, τ=1000 fm/c, all calculations agree to a good degree of accuracy.

In summary, our investigation suggests that the neglect of the two-proton nuclear interaction and the anti-symmetrization of the two-proton wave-function leads to comparable or larger inaccuracies than the neglect of the Coulomb interaction with the emitting heavy residue. For large emission times $\tau \gtrsim 1000$ fm/c, pertinent for the decay of low-temperature compound nuclei, the classical formula, Equation (6.30), provides an excellent approximation for the calculation of angle integrated two-proton correlation functions and gives virtually identical results to the classical trajectory calculations.

CHAPTER 7. TWO-PROTON CORRELATION FOR THE GAUSSIAN SOURCE

The experimental two-particle correlation functions, R(q), are presented as a function of relative momentum, q, using the definition:

$$\Sigma Y_{12}(\vec{p}_1,\vec{p}_2) = C_{12}\,(1+R(q))\,\bullet\,\Sigma Y_1(\vec{p}_1)Y_2(\vec{p}_2)\,. \qquad (7.1)$$

Here, $\vec{p}_1$ and $\vec{p}_2$ are the laboratory momenta of particles 1 and 2; $q=\frac{1}{2}\,|\,\vec{p}_1-\vec{p}_2\,|$ is the relative momentum of the particle pair; $Y_{12}(\vec{p}_1,\vec{p}_2)$ is the coincidence yield; and $Y_1(\vec{p}_1)$ and $Y_2(\vec{p}_2)$ are the single particle yields. For each experimental gating condition, the sums on both sides of Equation (7.1) are extended over all energy and detector combinations corresponding to the given bins of q. The normalization constant, C_{12}, is determined by the requirement that R(q)=0 for large relative momenta.

Theoretical correlation functions are calculated with Equations (6.22-24). In most previous analyses, $g(\vec{p},\vec{r},t)$ was parametrized in terms of a simple Gaussian source of negligible lifetime,

$$g(\vec{P}/2,\vec{r},t) = \rho_0\,\delta(t)\exp\left[-r^2/r_0{}^2(P)\right]\,, \qquad (7.2)$$

where the radius parameter was allowed to be momentum dependent. To allow comparisons with the previous analyses and to systematize our data, we will adopt this parametrization for the calculations presented in this Chapter.

7.1 Angle- and Energy-integrated Correlation Functions

Two-proton correlation functions corresponding to sums over all detectors and all proton energies above the applied software energy threshold of 10 MeV are compared in Figure 7.1. The correlation functions measured for the reactions $^{14}N + ^{27}Al$ and $^{14}N + ^{197}Au$ exhibit pronounced maxima at relative momenta $q \approx 20$ MeV/c, see top panels of Figure 7.1. Small but significant differences exist at small relative momenta where the minimum at $q \approx 0$ MeV/c is more pronounced for the ^{27}Al than for the ^{197}Au target. The correlation functions measured for the ^{129}Xe-induced reactions do not exhibit a pronounced maximum at $q \approx 20$ MeV/c, but only a minimum at $q \approx 0$ MeV/c, see bottom panels of Figure 7.1. The correlation functions measured for the reactions $^{129}Xe + ^{27}Al$ and $^{129}Xe + ^{122}Sn$ have very similar shapes. On the other hand, the correlation functions measured for ^{14}N and ^{129}Xe induced reactions are strikingly different, corroborating previously observed differences between correlation functions measured for equilibrium and nonequilibrium emission processes in slightly different reactions [DeYo 89, Queb 89, Ardo 89, DeYo 90]. For orientation, the solid lines show theoretical correlation functions predicted for Gaussian sources of negligible lifetime. For the reactions induced by ^{14}N and ^{129}Xe, radius parameters of $r_0 = 4.4$ and 70 fm were used, respectively. These source parameters should be compared to the equivalent radius parameters for Al and Au nuclei, $r_0(Al) \approx 2.5$ fm and $r_0(Au) \approx 4.4$ fm , which are obtained from tabulated [Brow 84] r.m.s. charge radii using the approximate relation $r_0 = \sqrt{(2/3)}\, r_{rms}$. For the ^{14}N-induced reactions a source radius of $r_0 = 4.4$ fm is not necessarily unreasonable. However, it is astonishing that this radius parameter exhibits no obvious dependence on the size of the target nucleus. A purely geometrical interpretation of the correlation function is, therefore, in doubt. For the large source parameter, $r_0 \approx 70$ fm, used to describe the correlation functions

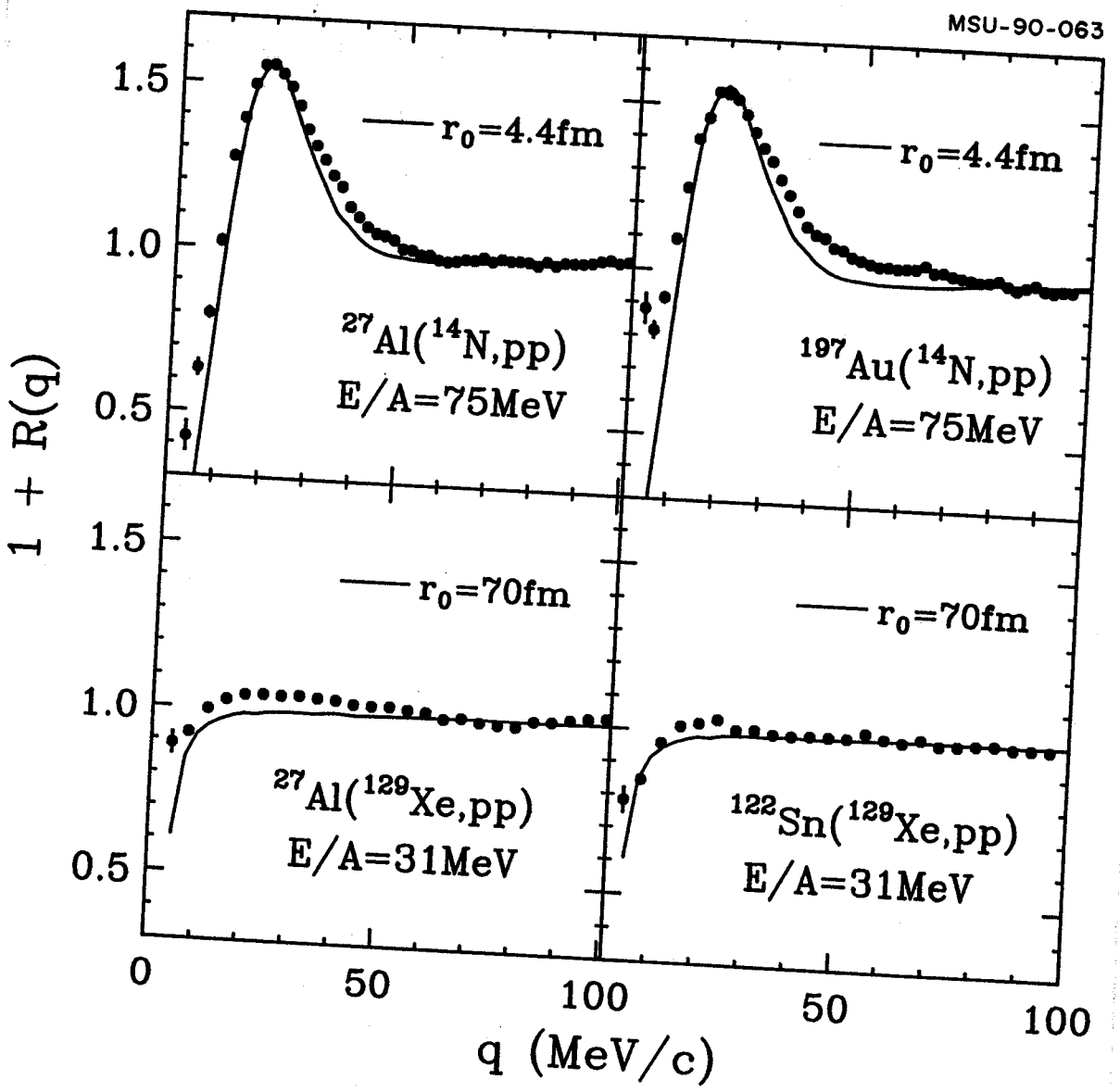

Figure 7.1: Comparison of energy integrated two-proton correlation functions measured for the reactions $^{14}N+^{27}Al$ and $^{14}N+^{197}Au$ at E/A=75 MeV (top panels) and the reactions $^{129}Xe+^{27}Al$ and $^{129}Xe+^{122}Sn$ at E/A=31 MeV (bottom panels). The solid curves represent correlation functions predicted for Gaussian sources of negligible lifetime with the indicated radius parameters, r_0.

measured for the ^{129}Xe induced reactions, a purely geometrical interpretation is clearly unphysical and the lifetime of the emitting system must play a major role.

7.2 Dependence on Total Momentum

Two-proton correlation functions are known to exhibit strong dependences on the energy of the emitted particles [Lync 83, Chen 87a, Chen 87b, Poch 86, Poch 87, Awes 88, Gong 90b, Gong 90c], or, equivalently, on the total momentum, $\vec{P} = \vec{p}_1 + \vec{p}_2$, of the coincident proton pair. Figure 7.2 shows two-proton correlation functions for two representative momentum gates, measured for the reactions ^{129}Xe + ^{27}Al (upper panel) and ^{129}Xe + ^{122}Sn (lower panel). The momentum gates represented by the solid and open points correspond to protons emitted with kinetic energies below and above the compound nucleus Coulomb barriers, respectively. For the ^{129}Xe + ^{27}Al reaction, the two momentum gates, P=480-570 and 660-750 MeV/c, select protons with kinetic energies of $E_{c.m.} \approx$ 5-10 and 15-23 MeV, respectively, in the center-of-mass frame of reference (i.e. the rest frame of the compound nucleus). For the ^{129}Xe + ^{122}Sn reaction, the two momentum gates, P=270-540 and 540-660 MeV/c, select protons with kinetic energies of $E_{c.m.} \approx$ 1-15 and 15-27 MeV, respectively. As can be expected from qualitative time scale arguments, sub-barrier emission results in a reduction of the minimum at q≈0 MeV/c. Furthermore, correlation functions at sub-barrier energies can suffer enhanced attenuations and/or distortions from sequential decays of primary fragments emitted in particle unbound states [Frie 83] and from deflections in the Coulomb field of the heavy reaction residue. Because of these additional complications, we will refrain from a more detailed analysis of two-proton correlation functions for protons emitted with sub-barrier energies. Calculations of two-proton correlation functions for evaporative processes will be presented in Chapter 8.

The correlation functions measured for the ^{14}N-induced reactions exhibit a more pronounced dependence on the total momentum of the detected proton

pairs. Figures 7.3 and 7.4 show correlation functions for representative ranges of the total momentum, P, for the reactions $^{14}N + {}^{27}Al$ and $^{14}N + {}^{197}Au$, respectively. Consistent with previous measurements, the maximum at $q \approx 20$ MeV/c becomes more pronounced for larger total momenta, i.e. for the emission of more energetic particles. For the lowest momentum gate, P=270-390 MeV/c, the correlation functions are distinctly different for the two targets. For the ^{27}Al target, a clear maximum at $q \approx 20$ MeV/c is measured. For the ^{197}Au target, on the other hand, this maximum is barely visible and the shape of the correlation function resembles that measured for evaporative processes.

The solid curves in Figures 7.3 and 7.4 show correlation functions calculated for Gaussian sources of negligible lifetime, Equation (7.2), using momentum dependent source parameters shown in Figure 7.5. In these calculations, appropriate averages over total momentum were performed, and the resolution of the hodoscope was taken into account. The overall trends of the data are well described. However, the shapes of the measured correlation functions are not reproduced in all details. The peaks of the calculated correlation functions are slightly narrower than the peaks of the measured correlation functions. The disagreement is particularly evident in the region around $q \approx 30$-40 MeV/c. In addition, for the $^{14}N + {}^{197}Au$ reaction, the adopted parametrization fails to reproduce the exact shape of the minimum at $q \approx 0$ MeV/c for the low momentum gate, P = 270-390 MeV/c.

In order to provide a simple description of the momentum dependence of the two-proton correlation functions measured for the ^{14}N-induced reactions, we have constructed experimental correlation functions for a number of narrow gates placed on the total momentum, P. Each such correlation function was characterized in terms of a Gaussian source, Equation (7.2), by requiring that

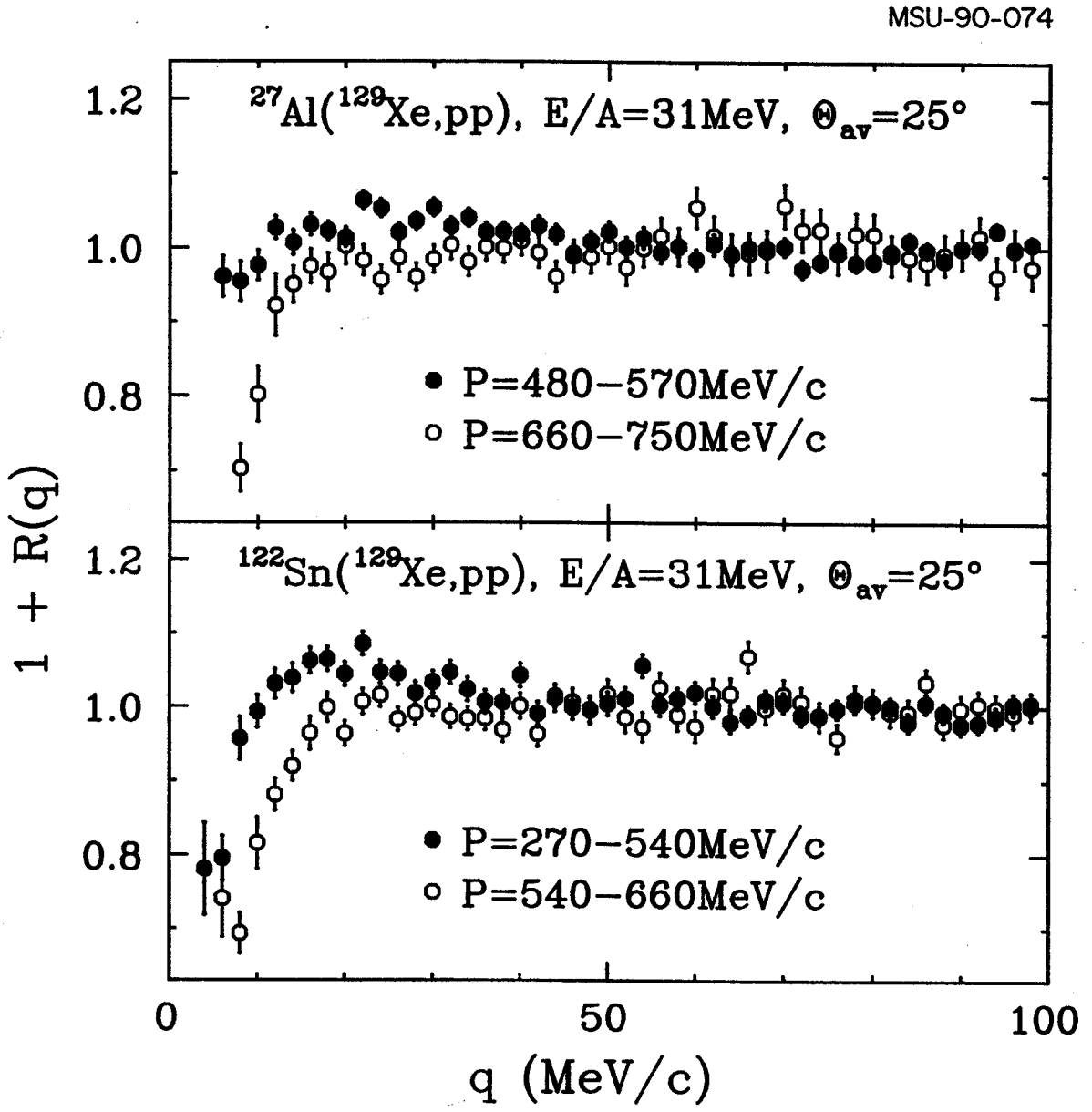

Figure 7.2: Two-proton correlation functions measured for the reactions ^{129}Xe+^{27}Al and ^{129}Xe+^{122}Sn at E/A=31 MeV. The gates on the total momenta, P, of the coincident proton pairs are indicated; solid and open points represent center-of-mass energies below and above the compound nucleus Coulomb barriers.

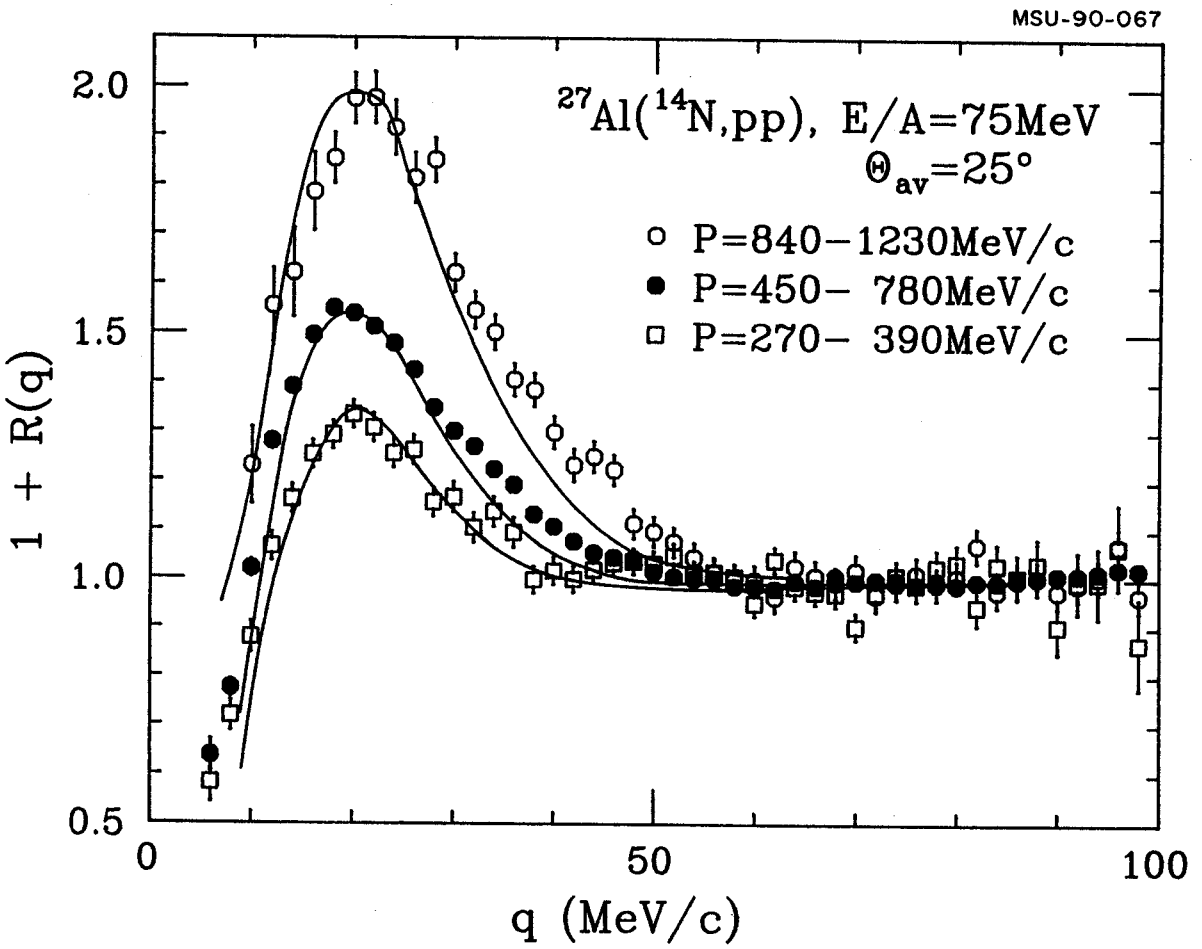

Figure 7.3: Two-proton correlation functions measured for the reaction $^{14}N+^{27}Al$ at E/A=75 MeV. The gates placed on the total momenta, P, of the coincident particle pairs are indicated. The solid curves represent calculations for Gaussian sources of negligible lifetime assuming a dependence of the radius parameter, r_0, on total momentum, P, as shown by the open points in Figure 7.5 and folded with the response of the experimental apparatus.

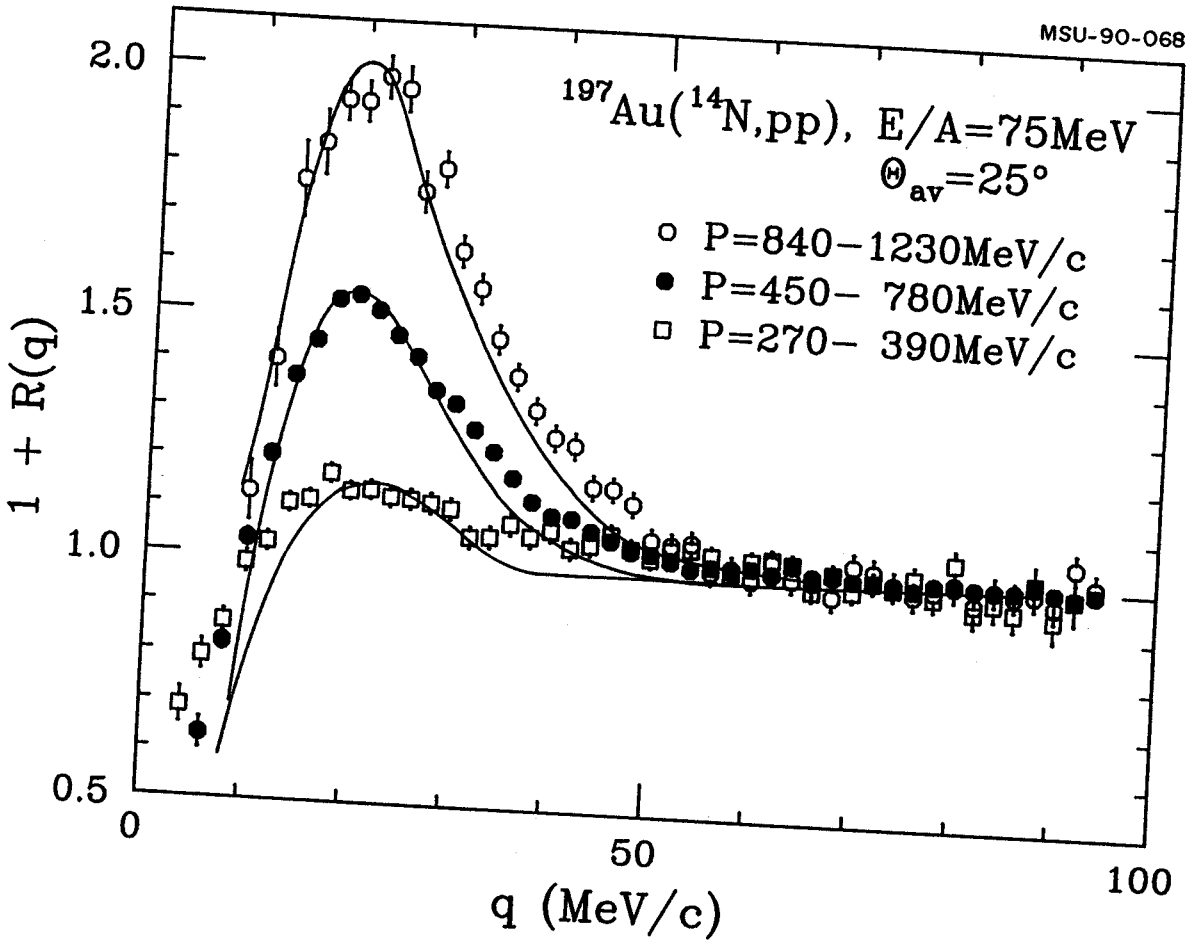

Figure 7.4: Two-proton correlation functions measured for the reaction $^{14}N+^{197}Au$ at E/A=75 MeV. The gates placed on the total momenta, P, of the coincident particle pair are indicated. The solid curves represent calculations for Gaussian sources of negligible lifetime assuming a dependence of the radius parameter, r_0, on total momentum as shown by the solid points in Figure 7.5 and folded with the response of the experimental apparatus.

the correlation function calculated for this source could reproduce the height of the maximum of the measured correlation function. The dependence of the extracted radius parameters on the total momentum of the detected particle pair, $r_0(P)$, is shown in Figure 7.5. The error bars indicate estimated systematic errors. For the $^{14}N + ^{197}Au$ reaction, the adopted parametrization fails to reproduce the shape of the minimum at $q \approx 0$ MeV/c for the low momentum gates, P<350 MeV/c. Here, the assumed monotonic dependence of the radius parameter on total momentum appears to be inadequate, and one may have to mix in additional contributions from much larger sources or, alternatively, from long-lived evaporative processes to fit the shape of the minimum at $q \approx 0$ MeV/c. Because of the inherent ambiguities of such an approach, we did not pursue this possibility. Instead, we have indicated these possible contributions by open-ended error bars.

We wish to comment that the radius parameter, $r_0(P)$, cannot be interpreted at face value since the lifetime effect must be present for emissions of low energy protons. Even though correlation functions are calculated without lifetime, this approach is used only to summarize and display the full momentum dependence and some subtle target dependence of two-proton correlation functions.

While the average correlation functions measured for the $^{14}N + ^{27}Al$ and $^{14}N + ^{197}Au$ reaction are very similar (see Figure 7.1), significant differences surface when one explores the dependence on the total momentum of the proton pairs. Such more subtle differences, already apparent in the raw data shown in Figures 7.3 and 7.4, are clearly revealed in Figure 7.5. For the $^{14}N + ^{197}Au$ reaction, the extracted source dimensions exhibit a nearly monotonic increase with decreasing total momentum of the detected proton pair. For the $^{14}N + ^{27}Al$ reaction, on the other hand, the extracted source dimensions are rather constant over the range of P≈400-750 MeV/c. The extracted source dimensions are

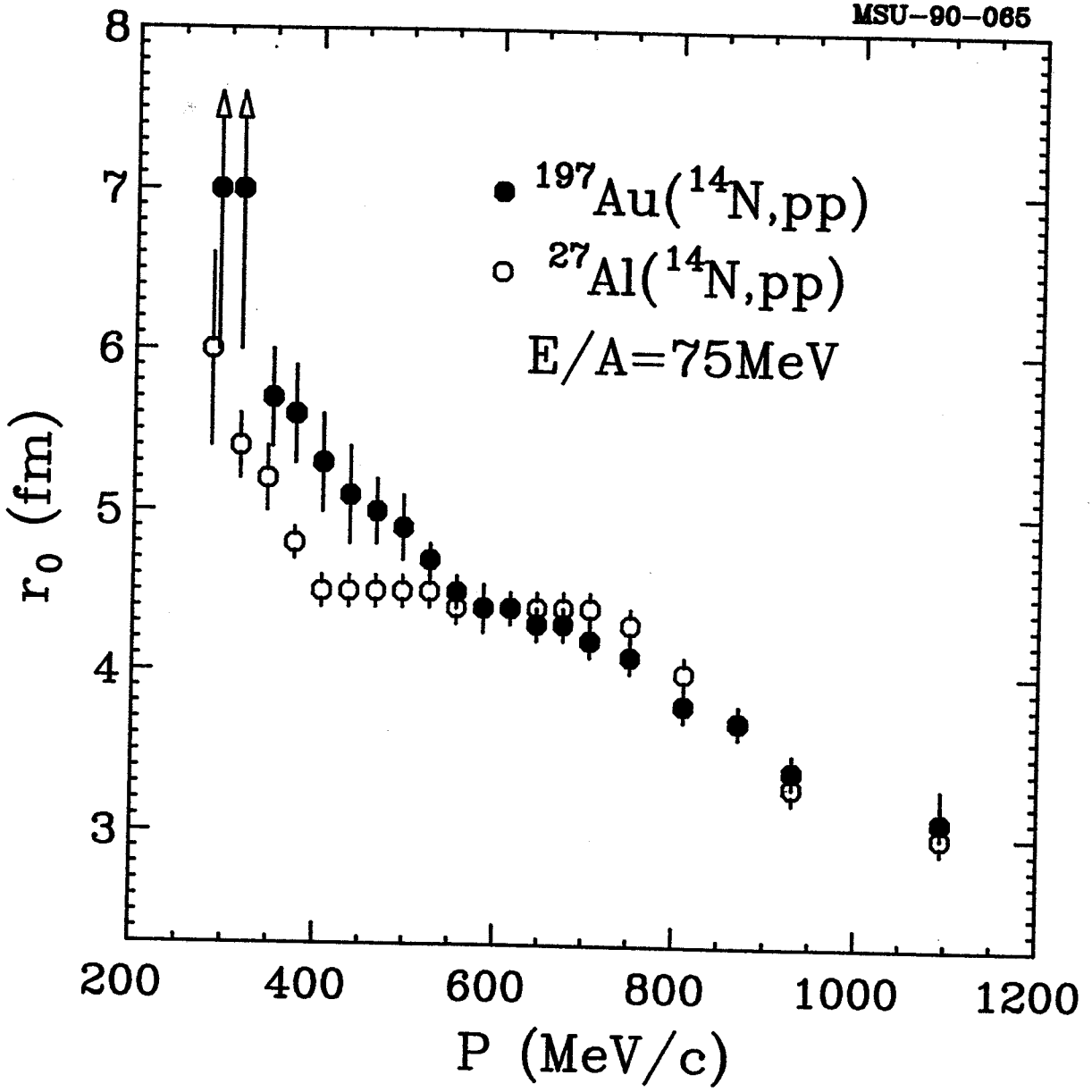

Figure 7.5: Radius parameters, r_0, for Gaussian sources of negligible lifetime extracted from two-proton correlation functions gated by different total momenta, P, of the coincident particle pairs for ^{14}N induced reactions on ^{27}Al and ^{197}Au at E/A=75 MeV. The error bars indicate estimated systematic errors.

comparable for the two targets at high total momenta, $P \gtrsim 800$ MeV/c, indicating that very energetic particles are emitted by comparable processes. At low total momenta, $P \lesssim 500$ MeV/c, the extracted source dimensions are considerably larger for the reactions on ^{197}Au than for the reactions on ^{27}Al, most likely indicating larger contributions from slow evaporation processes for the ^{197}Au target.

As more two-proton correlation measurements become available, interesting systematic trends emerge. Figure 7.6 shows the radius parameters for Gaussian source of negligible lifetime extracted from ^{3}He + Ag(natural) at E/A = 67 MeV [Zhu 91], ^{40}Ar + ^{197}Au at E/A = 60 MeV [Poch 87], and ^{14}N + ^{197}Au at E/A = 75 MeV (this work, see Figure 7.5), as a function of v/v_{beam}, the ratio of v, the mean velocity of the two-proton pairs, to v_{beam}, the beam velocity. The solid curve is an interpolation to the data obtained for the ^{14}N + ^{197}Au reaction. The dashed and dotdashed lines are obtained by scaling the solid line with multiplicative factors of $(3/14)^{1/3}$ and $(40/14)^{1/3}$ for the reactions ^{3}He + Ag and ^{40}Ar + ^{197}Au, respectively. The good agreement between extrapolated and measured source radii at $v/v_{beam} \geq 0.7$ for both ^{3}He and ^{40}Ar induced reactions suggests that the spatial extent of the emitting region for energetic protons scales with the radius of the light projectile impinging on a heavy target. For lower energy protons emitted from an evaporative source on a long time scale, the extracted radius parameters may not represent the source size but rather reflect the lifetime of the emitting system (see Section 6.2.2 and Chapter 8). This qualitative argument is in accordance with the observation that the scaling of the measured source radii with the radius of the projectile does not apply at $v/v_{beam} < 0.7$.

It is interesting to note that similar source-size scaling with the projectile radius has been observed from two-pion intensity interferometry in relativistic nucleus-nucleus collisions [Bart 86].

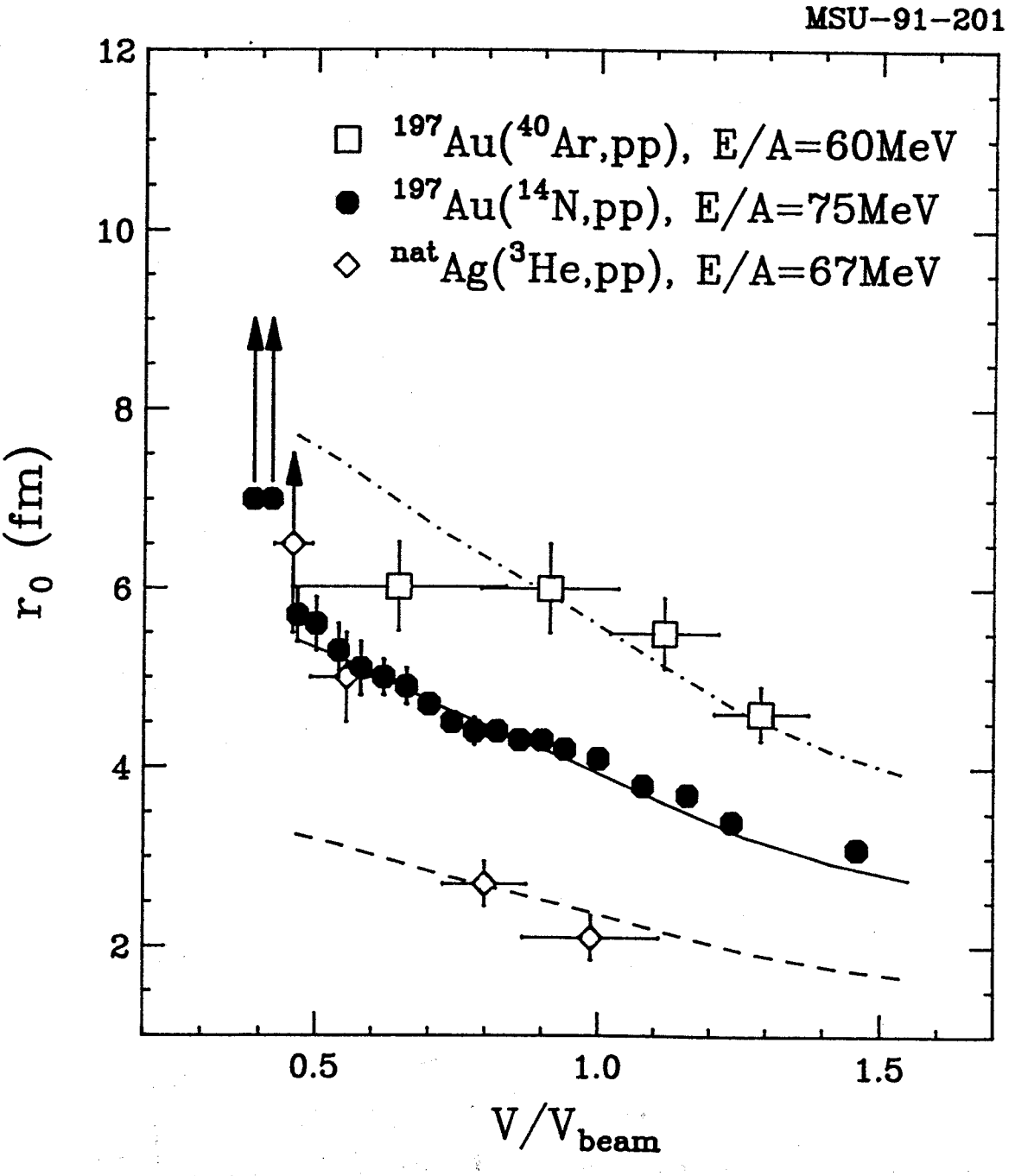

Figure 7.6: Systematics of Gaussian source radii, $r_0(v/v_{beam})$, extracted from various asymmetric reactions. The points and curves are explained in the text.

7.3 Effect of Instrumental Resolution

In order to evaluate instrumental distortions of the measured correlation functions, we have simulated the response of our experimental apparatus by taking its known energy and angular resolution into account. The solid curves in Figure 7.7 show the undistorted correlation functions, calculated for Gaussian sources with the indicated radius parameters. The points are results of Monte Carlo calculations in which the angular and energy resolutions of the experimental apparatus are taken into account. In these calculations, the coincidence yield was taken as

$$Y_{12}(\vec{p}_1,\vec{p}_2) = (1+R(q))\, Y_1(\vec{p}_1)Y_2(\vec{p}_2)\,, \qquad (7.3)$$

where the singles yields, $Y_1(\vec{p}_1)$ and $Y_1(\vec{p}_2)$, were taken from the single particle yields measured for the $^{14}N+^{27}Al$ reaction and R(q) was calculated by assuming a Gaussian source of negligible lifetime, Equation (7.2), with the radius parameters given in the figure. Both singles and coincidence distributions were smeared by the energy and angular resolution of the experimental apparatus and sorted in the same way as the experimental data, using three representative momentum gates. The simulated correlation functions are in close agreement with the original, undistorted correlation function. Except at very small relative momenta, line shape distortions caused by the resolution of the experimental apparatus are negligible. Note, in particular, the absence of visible distortions in the region of q $\approx$ 30-40 MeV/c where the Gaussian-source fits deviate from the experimental correlation functions (see also Figures 7.3 and 7.4).

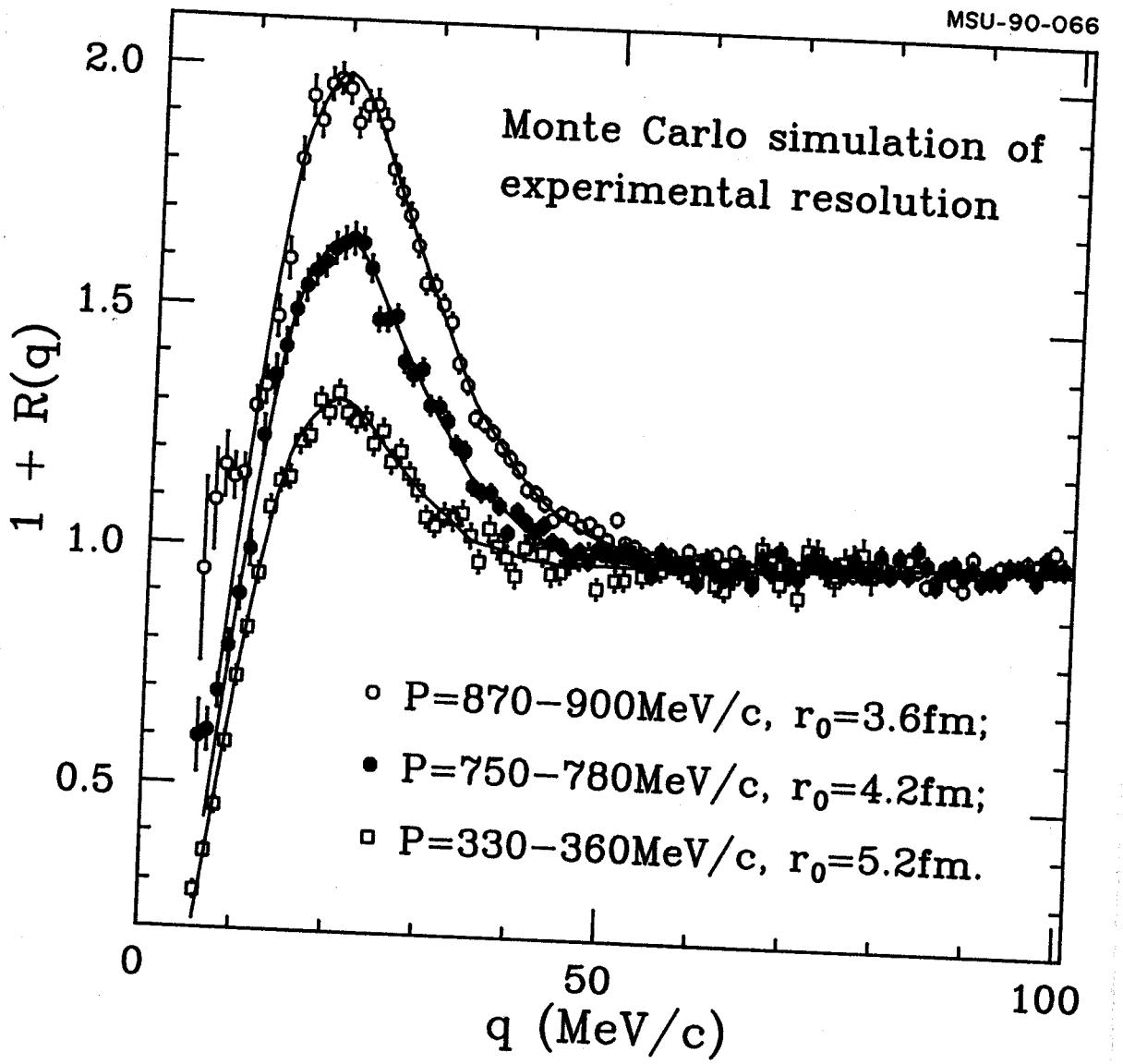

Figure 7.7: Monte-Carlo simulation for the response of the experimental apparatus. The curves show the undistorted correlation functions assumed for the indicated gates on total momentum, P. The points represent the calculated response of the apparatus after taking the energy and angular resolution effects into account. The error bars show the statistical accuracy of the Monte-Carlo calculations.

CHAPTER 8. TWO-PROTON CORRELATION FOR EVAPORATIVE EMISSION

Two-proton correlation functions for particle evaporation from long-lived compound nuclei can be calculated by using the Wigner-function formalism [Prat 87, Gong 91a], Equations (6.22-24). We have used the statistical model of Reference [Frie 83] to construct Wigner functions for evaporative emission from equilibrated compound nuclei.

8.1 Statistical Evaporation Model

In this model, the average particle emission is calculated from a generalized Weisskopf formula and cooling of the compound nucleus is calculated from the average mass and energy emission rates [Frie 83]. Sub-barrier emission is not incorporated because of the use of the sharp cut-off approximation for the inverse cross sections. For simplicity, the level density is approximated by that of an ideal Fermi gas at the density of normal nuclear matter.

The generalized Weisskopf formula gives the probability per unit time and energy intervals of emitting a particle, b, with energy, E, at time, t, from a compound nucleus, c:

$$\frac{d^2N_b}{dEdt} = (2S_b+1)\frac{m_b \pi R_b^2}{\pi^2 \hbar^3}(E-V_b)\Theta(E-V_b)\exp\left[\frac{-E+Z_b F(T,\rho_\pi)+N_b F(T,\rho_\nu)-B_b}{T}\right]. \quad (8.1)$$

Here, S_b, m_b, Z_b, N_b, and E denote the spin, mass, charge, neutron number,

and energy of the emitted particle; T is the temperature of the compound nucleus; $F(T,\rho_\pi)$ and $F(T,\rho_\nu)$ are the Helmholtz free energies per particle for protons and neutrons, respectively, and $\Theta(x)$ is the unit step function. The free energies were calculated by assuming that the nucleons behaved like an ideal Fermi gas with a density of $\rho = 0.145$ fm^{-3}. The height of the Coulomb barrier, V_b, was taken as the Coulomb energy between the daughter nucleus and the emitted fragment when they are separated by the absorption radius, R_b. For simplicity, the absorption radius was calculated as:

$$R_b = r_0 [(A_c - A_b)^{1/3} + A_b^{1/3}] \; ; r_0 = 1.2 \text{ fm} . \qquad (8.2)$$

Here, A_c and A_b denote the mass numbers of the parent nucleus, c, and the emitted particle, b, respectively. The binding energy, B_b, is the difference in masses of the parent nucleus and that of the daughter nucleus and the emitted particle. The masses of parent and daughter nuclei were calculated from a liquid-drop formula:

$$M(A,Z) = Z m_p c^2 + (A-Z) m_n c^2 - [\, 14.1A - 13A^{2/3} - 0.595 Z^2 A^{-1/3} - 19(A-2Z)^2/A \,] \qquad (8.3)$$

The spatial distribution of emission points was chosen to be uniform in the two coordinates transverse to the velocity of the emitted particles; the third coordinate was chosen such that the emission point corresponds to the surface of the sphere of radius R_b. For particles with energies very near the Coulomb barrier, this is not a particularly satisfying choice. These particles undergo a significant change in their trajectory due to the Coulomb field of the compound nucleus. Distortions of two-proton correlation functions by deflections of the emitted protons in the Coulomb field of the daughter nucleus are manifestations of long range three-body effects. Such effects are not incorporated in the formalism presented in Chapter 6. We also neglected effects due to angular momentum

coupling which, for rapidly rotating compound nuclei, could modify the extracted radii by up to 20% [Koon 89].

If the spatial separation between emitted protons is much larger than the two-proton Bohr radius of 58 fm, one can neglect the identical-particle interference of the emitted protons and their strong mutual interaction, and also the quantum nature of their mutual Coulomb repulsion. Under these conditions, one can calculate correlation functions from the classical Coulomb trajectories, where the electric field of both protons and that of the compound nucleus are taken into account [DeYo 89]. For compound nuclei with excitation energies below about 2.0 MeV/nucleon, emission time scales are sufficiently large that the above conditions are satisfied; classical trajectory calculations should provide a good approximation (see the discussions in Section 6.3).

For increasingly high excitation energies, the time scales for emission become shorter. As the protons are emitted closer to one another, the quantum nature of the Coulomb interaction, identical particle statistics, and the strong interaction become important in that order. Fortunately, Coulomb deflections in the field of the compound nucleus become less important for particles emitted with kinetic energies significantly above the Coulomb barrier. For collisions with sufficient energy to dissolve the nuclei, $E/A \gtrsim 50$ MeV, the neglect of three-body effects for the two-proton relative wave function should provide a good approximation. At these energies, the effects of the strong interaction and identical particle interactions dominate. These effects can only be calculated by a full quantum treatment of the relative wave function.

8.2 Model Calculations

It is instructive to explore the sensitivity of the calculated correlation functions to various parameters and momentum cuts. The following illustrative calculations are performed for narrow ranges of the total momenta, $P_{c.m.}$, of the emitted particle pairs. (The momenta, $P_{c.m.}$, are defined with respect to the compound nucleus rest frame.)

The shape of the two-proton correlation function depends on the time-scale governing the emission of the detected particles. For particle emission from equilibrated compound nuclei, this time scale depends on the level density and, therefore, on the initial temperature. Because of cooling via particle emission, the time scale also depends on the energy of the emitted particles. In Figures 8.1 and 8.2, such dependences are illustrated for the decay of highly excited ^{156}Ho nuclei. Figure 8.1 shows the calculated time dependence of the respective emission processes, i.e. the relative probability per unit time for the emission of the specified protons. The predicted two-proton correlation functions are shown in Figure 8.2. The top panels in the two figures present calculations for initial temperatures T = 5, 10, and 20 MeV, keeping the total momentum of the two-proton pair fixed at $P_{c.m.} = 400 \pm 10$ MeV/c. (This momentum bin selects protons of kinetic energy $E_{c.m.}/A \approx 21$ MeV in the compound nucleus rest frame.) At low temperatures, $T \lesssim 5$ MeV, the decay times are large and the predicted correlation functions exhibit only a minimum at $q \approx 0$ MeV/c. With increasing temperature, the decay times decrease and the minimum at q = 0 MeV/c becomes more pronounced. For very hot nuclear systems, $T \gtrsim 20$ MeV, the calculated emission time scales become so short that the two-proton nuclear interaction becomes significant and the maximum in the correlation function at $q \approx 20$ MeV/c emerges. The bottom panels of Figures 8.1 and 8.2 show calculations for different total momenta, $P_{c.m.}$, and fixed initial temperature, T = 10 MeV. Because of cooling of the compound nucleus, particles of higher energy are emitted on faster

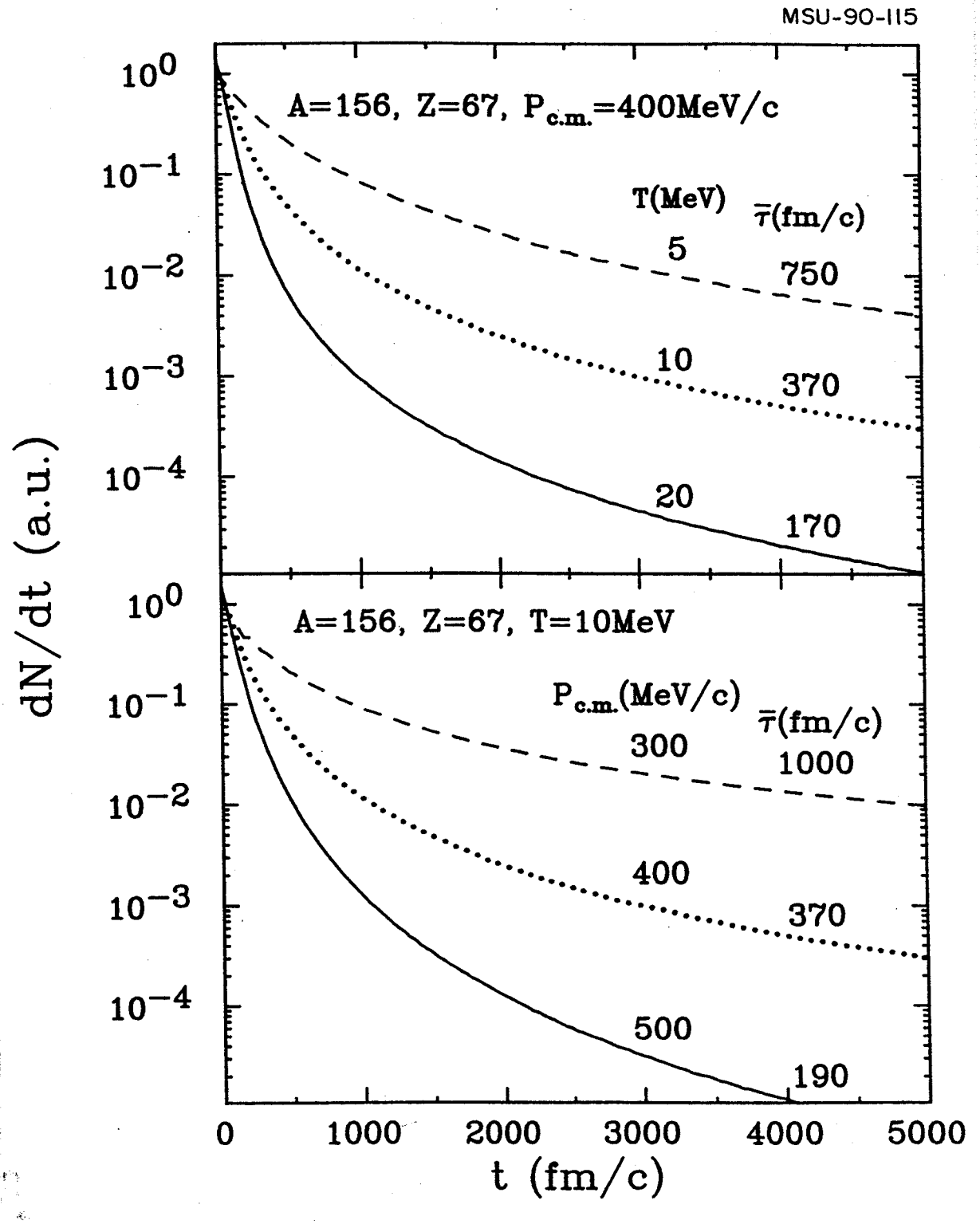

Figure 8.1: Temporal evolution of particle emission from equilibrated ^{156}Ho nuclei of different initial temperatures, T (top panel), and for different total momenta, $P_{c.m.}$ (bottom panel), of the emitted two-proton pairs.

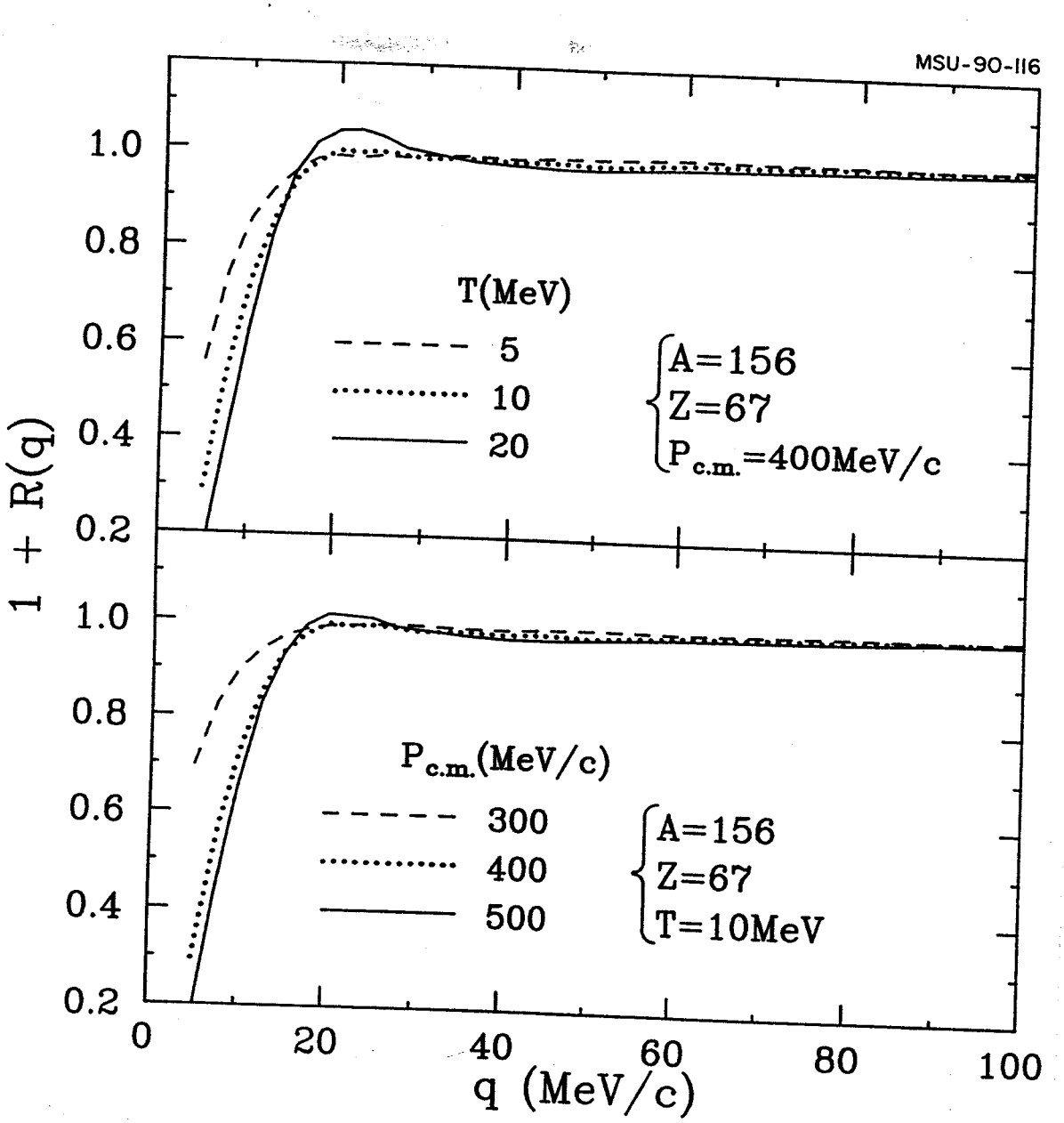

Figure 8.2: Dependence of two-proton correlation function on the total momentum, $P_{c.m.}$ (bottom panel), and on the initial temperature, T (top panel), of emitted proton pairs calculated for the decay of equilibrated ^{156}Ho nuclei.

time-scales than particles of lower energy. As a consequence, the two-proton correlation functions reflect smaller apparent source dimensions for the emission of particles of increasing energy. At lower temperatures, qualitatively similar dependences exist, but their effects on the two-proton correlation functions are less visible due to the larger emission times.

For fixed excitation energy, E^*, the decay rate of a compound nucleus depends on the relation between excitation energy and temperature since higher temperatures lead to higher emission rates and, therefore, to smaller apparent source dimensions. Figure 8.3 illustrates the sensitivity of the calculated two-proton correlation functions to the assumed relation between excitation energy and temperature for the decay of ^{156}Ho compound nuclei of fixed initial excitation energy, E^*/A=6.0 MeV. In these calculations, the level density was taken as that of an ideal Fermi-gas of the indicated density ρ. For an ideal Fermi gas, the relation between excitation energy and temperature is given to first order by:

$$T^2 = E^*/a . \tag{8.4}$$

The level density parameter, a, depends on the Fermi energy, ε_F:

$$a = \frac{\pi^2 A}{4\,\varepsilon_F} \approx 0.065A\,(\rho_0/\rho)^{2/3}\ \mathrm{MeV}^{-1}. \tag{8.5}$$

In Equation (8.5), we have used the relation $\varepsilon_F \approx 38(\rho/\rho_0)^{2/3}$ MeV, where $\rho_0 \approx$ 0.17 fm^{-3} denotes the density of normal nuclear matter. For reference, the level density parameters are also indicated in Figure 8.3. The calculations indicate only a moderate sensitivity to the level density parameter. As expected, higher temperatures produce shorter emission times and, hence, more pronounced correlations.

Particle emission rates depend largely upon the temperature of the

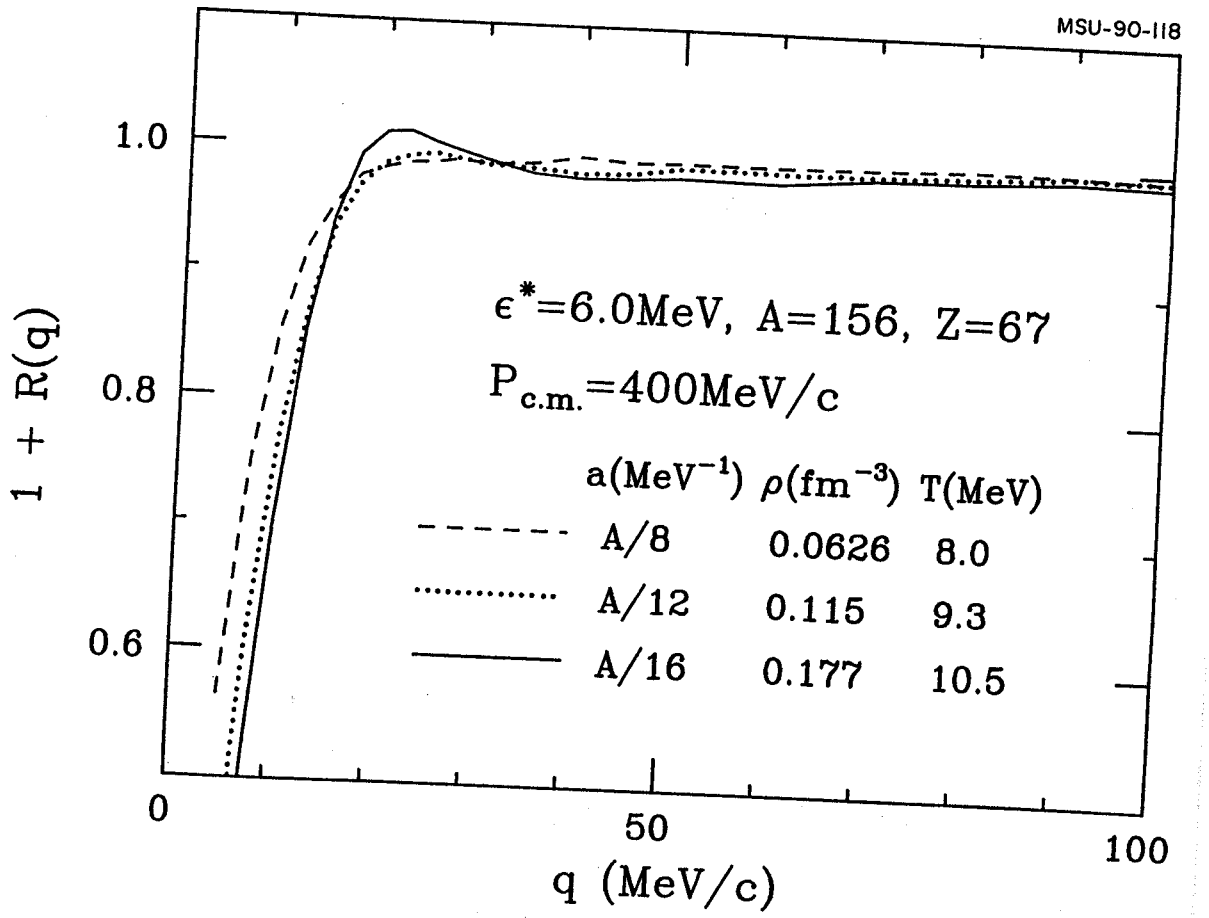

Figure 8.3: Sensitivity of calculated two-proton correlation functions to different assumptions on the level density parameter, $a=E^*/AT^2$, for the decay of ^{156}Ho compound nuclei of initial excitation energy E^*/A=6 MeV.

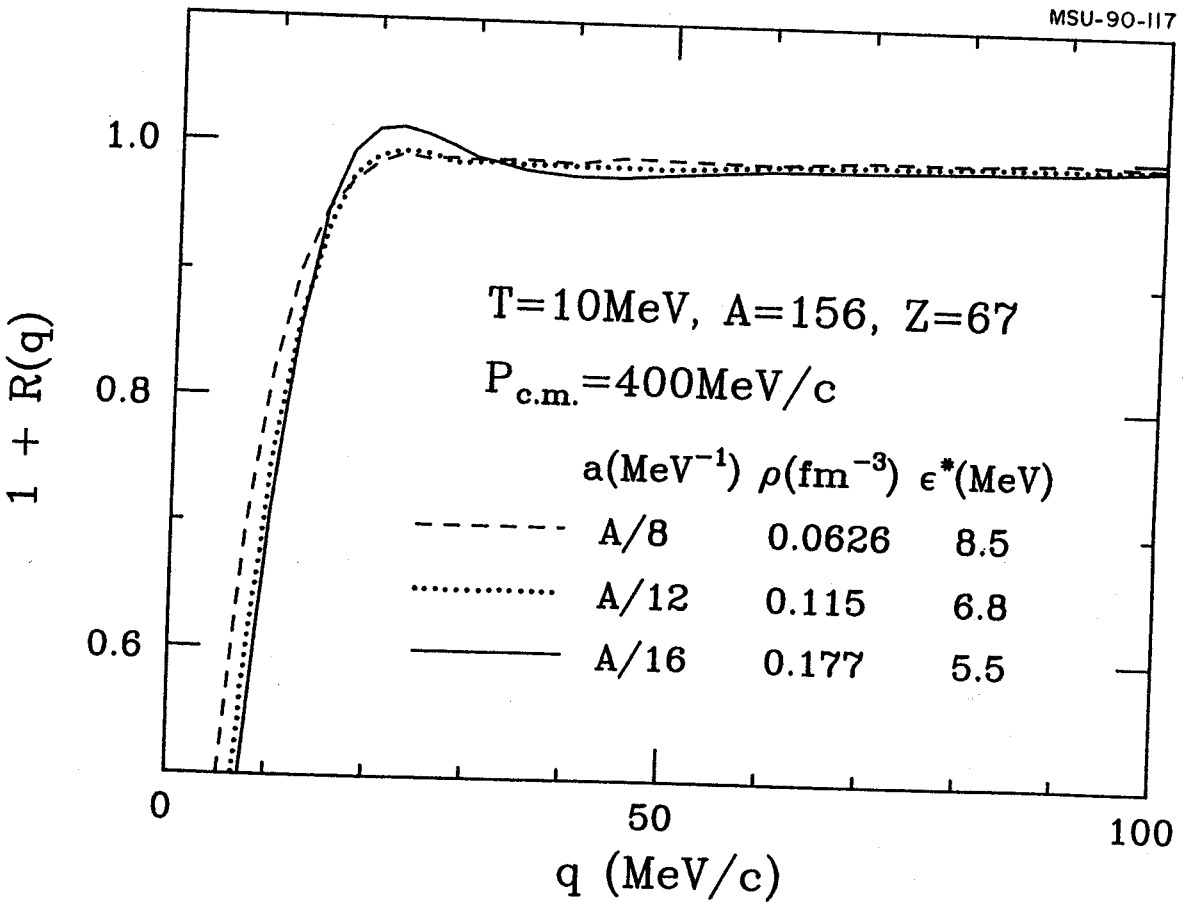

Figure 8.4: Sensitivity of calculated two-proton correlation functions to different assumptions on the level density parameter, $a=E^*/AT^2$, for the decay of ^{156}Ho compound nuclei of initial temperature T=10 MeV.

compound nucleus. Yet, the initial temperature does not specify the decay characteristics unambiguously, because different level density parameters represent different heat capacities of the decaying nuclear system. Figure 8.4 shows the sensitivity of the calculated two-proton correlation functions to the level density parameter for ^{156}Ho compound nuclei of fixed initial temperature, T = 10 MeV. The predicted correlations are slightly more attenuated for larger level density parameters, i.e. for increasing values of the heat capacity of the compound nucleus. However, the sensitivity is not very pronounced; it is even less significant at lower temperatures.

Since the predicted emission times depend strongly on the momenta of the emitted particles, the differences between longitudinal and transverse correlation functions can be expected to be momentum-dependent. Low energy particles may be emitted on such long time-scales that sensitivity to anti-symmetrization effects is lost. As emission time scales decrease for more energetic emissions, differences between longitudinal and transverse correlation functions may become more significant for particle pairs of higher total momenta. These qualitative expectations are corroborated by the calculations shown in Figure 8.5. The solid and dashed curves show longitudinal and transverse correlation functions predicted for narrow gates on the total momentum, $P_{c.m.}$ = 300, 400, 500 MeV/c, of the particle pair with respect to the center-of-mass frame of reference (i.e. the rest frame of the compound nucleus). Significant differences between longitudinal and transverse correlation functions are predicted for large momenta, P=500 MeV/c (top panel). These differences are reduced for smaller momenta, $P_{c.m.}$=400 MeV/c (center panel). For even smaller momenta, $P_{c.m.}$=300 MeV/c, longitudinal and transverse correlation functions differ only in the detailed shape of the minimum at q≈0 MeV/c (bottom panel) which is more pronounced for the longitudinal than for the transverse correlation function.

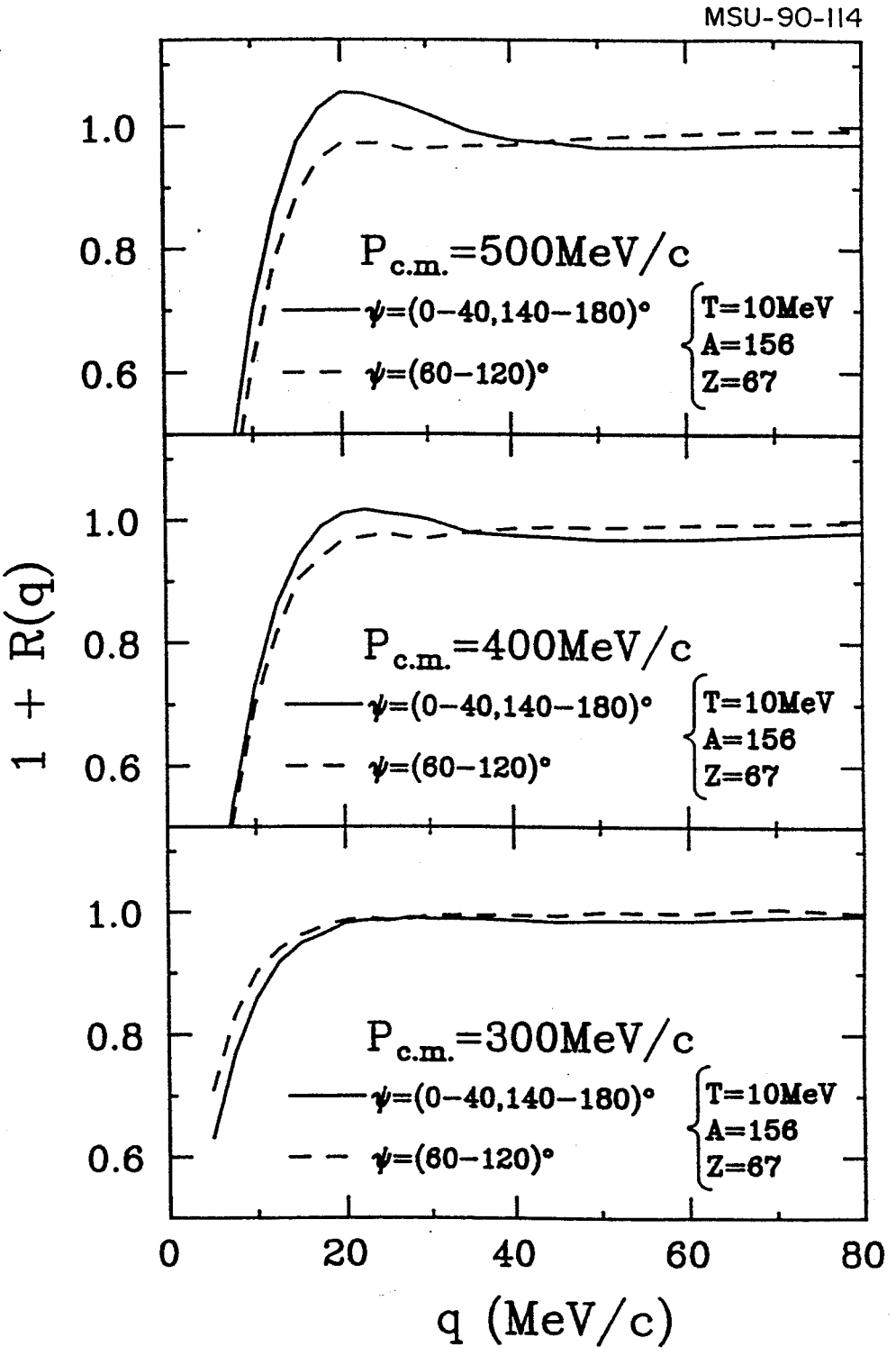

Figure 8.5: Longitudinal and transverse correlation functions predicted for evaporative emission from ^{156}Ho compound nuclei of initial temperature, T=10 MeV. Different panels show predictions for different total momenta, $P_{c.m.}$, of the emitted proton pairs: $P_{c.m.}$ =500 MeV/c (top panel), $P_{c.m.}$ =400 MeV/c (center panel), $P_{c.m.}$ = 300 MeV/c (bottom panel).

8.3 Angle-integrated Correlation Functions

Figure 8.6 shows two-proton correlations measured for the reaction $^{129}Xe + ^{27}Al$ at E/A = 31 MeV (part a) and for the reaction $^{129}Xe + ^{122}Sn$ at E/A = 31 MeV (part b,c). The gates placed on the total momenta are indicated in the figure. In Section 8.2, model calculations assuming evaporation from compound nuclei have exhibited sensitivity to total momenta of the two-proton pair, the initial temperature of the compund nucleus, and the level density parameters. The shapes of two-proton correlation functions at $q \leq 30$ MeV/c are largely determined by the average emission time scales. However, those calculations were performed in the rest frame of the emitting source.

In order to compare the calculations to our data, we have transformed the single-proton phase-space distributions from the source rest frame to the laboratory frame. The calculations were folded with the resolution of the experimental apparatus and averaged over the appropriate momentum bins using the experimental proton yields as relative weights.

Since the inclusive cross sections are consistent with substantial contributions from evaporative emission from excited projectile residues, we calculate correlation functions for two extreme cases, (i) emission from a source at rest in the compound nucleus rest frame and (ii) emission from a source at rest in the projectile rest frame.

Firstly, we used the compound nucleus values for the mass, A, and charge, Z, but treated the temperature as a free parameter to illustrate the sensitivity of the calculated emission rates to the initial temperature of the emitting system. The level density parameter is chosen to be a=A/16, corresponding to a Fermi gas of density of 0.145 fm^{-3}. In Figure 8.6, the curves represent calculations for three initial temperatures. Good agreement between calculations and data is obtained for initial temperatures of about 7-10 MeV. For complete fusion of $^{129}Xe + ^{27}Al$ and $^{129}Xe + ^{122}Sn$, initial temperatures of 8.2 and 10.3 MeV, respectively,

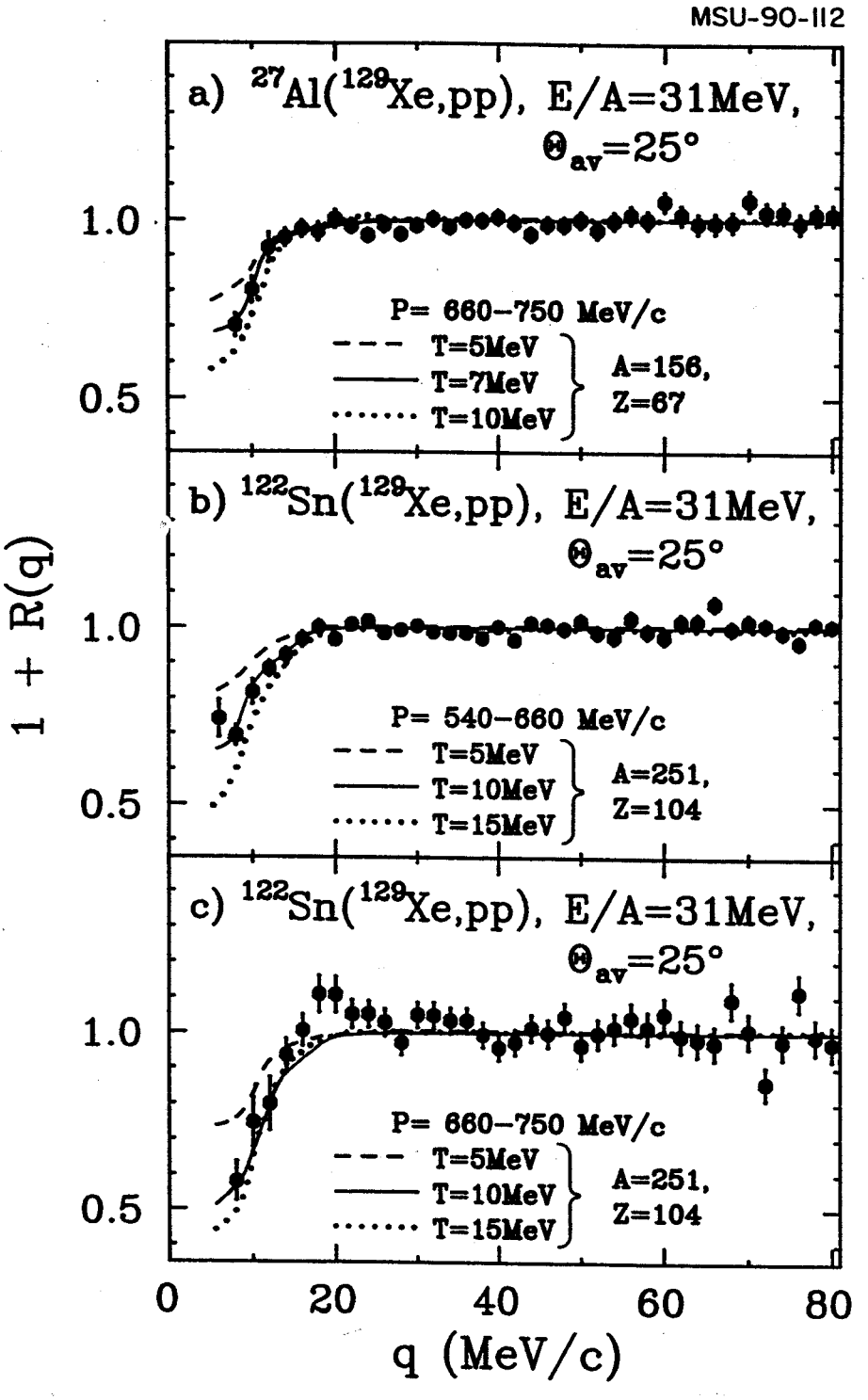

Figure 8.6: Two-proton correlation functions measured for the ^{129}Xe+^{27}Al (part a) and ^{129}Xe+^{122}Sn (parts b,c) reactions at E/A=31 MeV for the indicated gates on the total momenta, P, of the two-proton pairs. The curves represent calculations for evaporative sources at rest in the center-of-mass frame of reference; the parameters are indicated on the figure.

are calculated if one assumes the level density of an ideal Fermi gas of normal nuclear matter density; the more common relation, $T^2=(8\ \mathrm{MeV})\bullet E^*/A$, gives values of 5.8 and 7.3 MeV. However, the equilibrated emitting systems should have temperatures which are somewhat lower than those calculated for compound nuclei formed in complete fusion reactions [Poch 87, Wada 89, Jian 89, Xu 89] since some energy is carried away by pre-equilibrium emission.

In the second case, we choose the equilibrated projectile to be the proton emitting source moving at the initial beam velocity. We used the projectile values for the mass, A, and charge, Z, and treated the temperature as a free parameter. In Figure 8.7, we compare our data with calculations at T=5,10,15 MeV. For projectile decays, the lower momentum bin, P=540-660 MeV/c, largely corresponds to subbarrier emission. Therefore, we only present calculations for the higher momentum bin, P=660-750 MeV/c. Reasonable agreement with the data is obtained for temperatures of about 10-15 MeV.

Fits to the correlation functions require higher temperatures when one assumes emission from projectile-like sources rather than emission from fusion-like sources. This is related to the fact that average emission times become shorter for increasing temperature and for increasing emission energy with respect to the rest frame of the decaying nucleus [Frie 83]. In our detection geometry and for our laboratory-momentum gates, the emitted particles have lower kinetic energies in the projectile rest frame than in the compound nucleus rest frame. For fixed temperature, the correlations are therefore attenuated if one assumes emission from the rest frame of the projectile as compared to emission from the rest frame of the compound nucleus. To reproduce the experimental correlation function, one must choose a higher temperature for the projectile-like source than for the fusion-like source.

Temperatures which provide the best description of the experimental

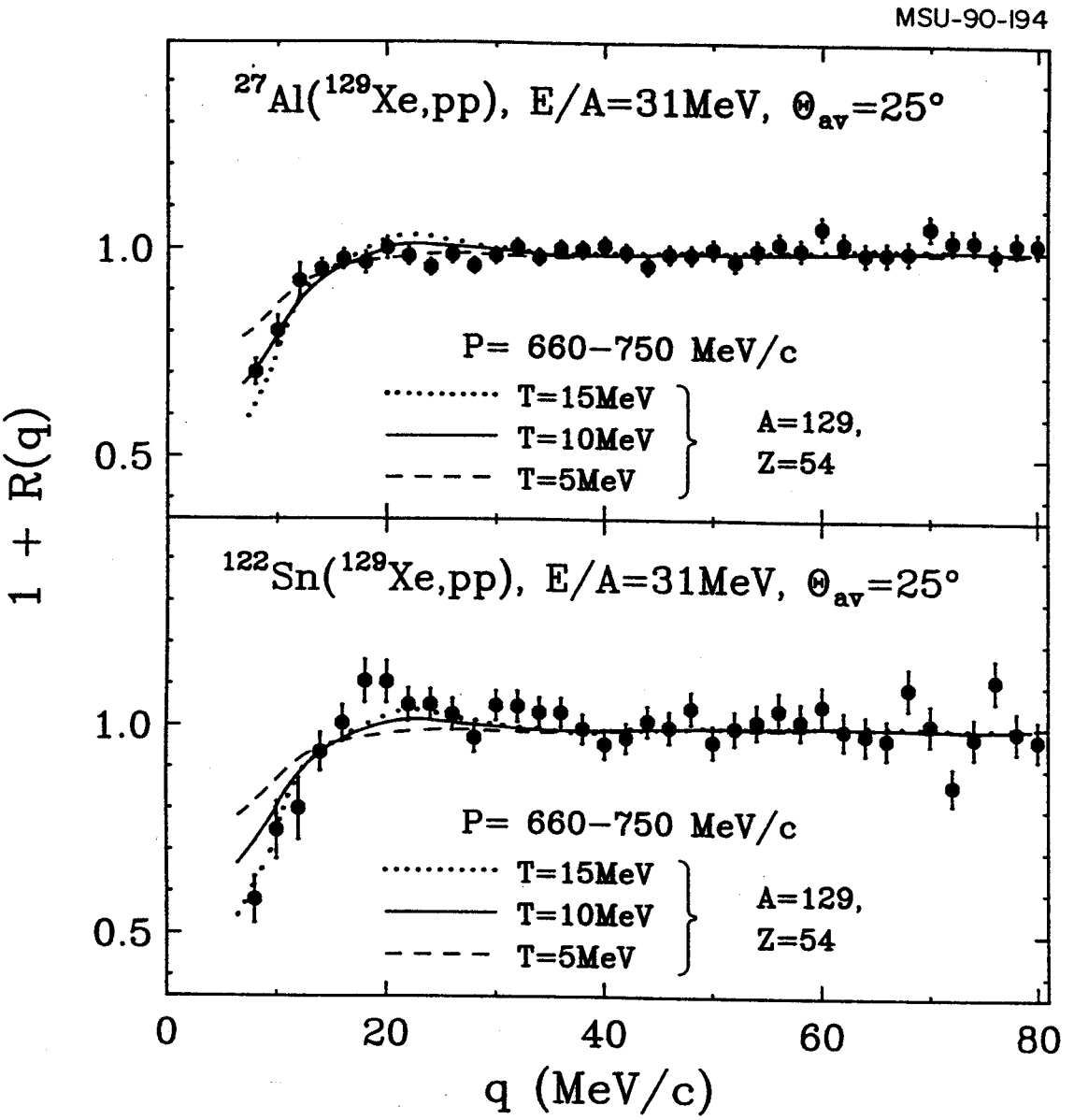

Figure 8.7: Two-proton correlation functions measured for the ^{129}Xe+^{27}Al (part a) and ^{129}Xe+^{122}Sn (part b) reactions at E/A=31 MeV for the indicated gates on the total momenta, P, of the two-proton pairs. The curves represent calculations for evaporative sources at rest in the projectile frame of reference; the parameters are indicated on the figure.

correlation functions (see Figures 8.6 and 8.7) may be unrealistically high. However, it may also be unrealistic to assume pure equilibrium emission. Some contributions from pre-equilibrium emission would decrease the average lifetime of the emitting system and produce stronger correlations. Within the present equilibrium model, stronger correlations can be produced by raising the temperature of the source (see Figure 8.2). Clearly, some quantitative uncertainties about the exact nature of the emitting system remain. In order to have a better understanding of those uncertainties, it is desirable to employ a more sophisticated statistical model of compound nucleus. However, the qualitative interpretation of the measured two-proton correlation functions as predominantly caused by slow evaporative emission is not affected by our incomplete knowledge of the mass, temperature, and velocity of the decaying nucleus or by small contributions from pre-equilibrium emission processes.

8.4 Longitudinal v.s. Transverse Correlation Functions

We have explored the dependence of the two-particle correlation function on the angle, $\Psi = \cos^{-1}(\vec{P} \bullet \vec{q}/Pq)$, between the relative and total momentum vectors of the proton pairs to search for clues on the source lifetime and shape [Koon 77, Prat 87, Awes 88, Ardo 89]. As was illustrated in Figure 1.2 and discussed in References [Prat 87, Awes 88, Bert 89, Gong 91a], emission from a long-lived system produces phase-space distributions elongated in the longitudinal direction. Because of the reduced Pauli anti-correlation in this direction, the longitudinal correlation function ($\Psi \approx 0°$ or $180°$) of a long-lived source may be enhanced compared to the transverse correlation function ($\Psi \approx 90°$), unless the average particle separations become so large that sensitivity to anti-symmetrization effects is lost.

Figure 8.8 shows longitudinal and transverse two-proton correlation functions measured for the reactions $^{129}Xe + ^{27}Al$ (top panel) and the $^{129}Xe + ^{122}Sn$ (bottom panel). The longitudinal correlation functions, shown by solid points, were evaluated for the gate $|\cos\Psi_{\ell}| \geq 0.77$ (corresponding to the

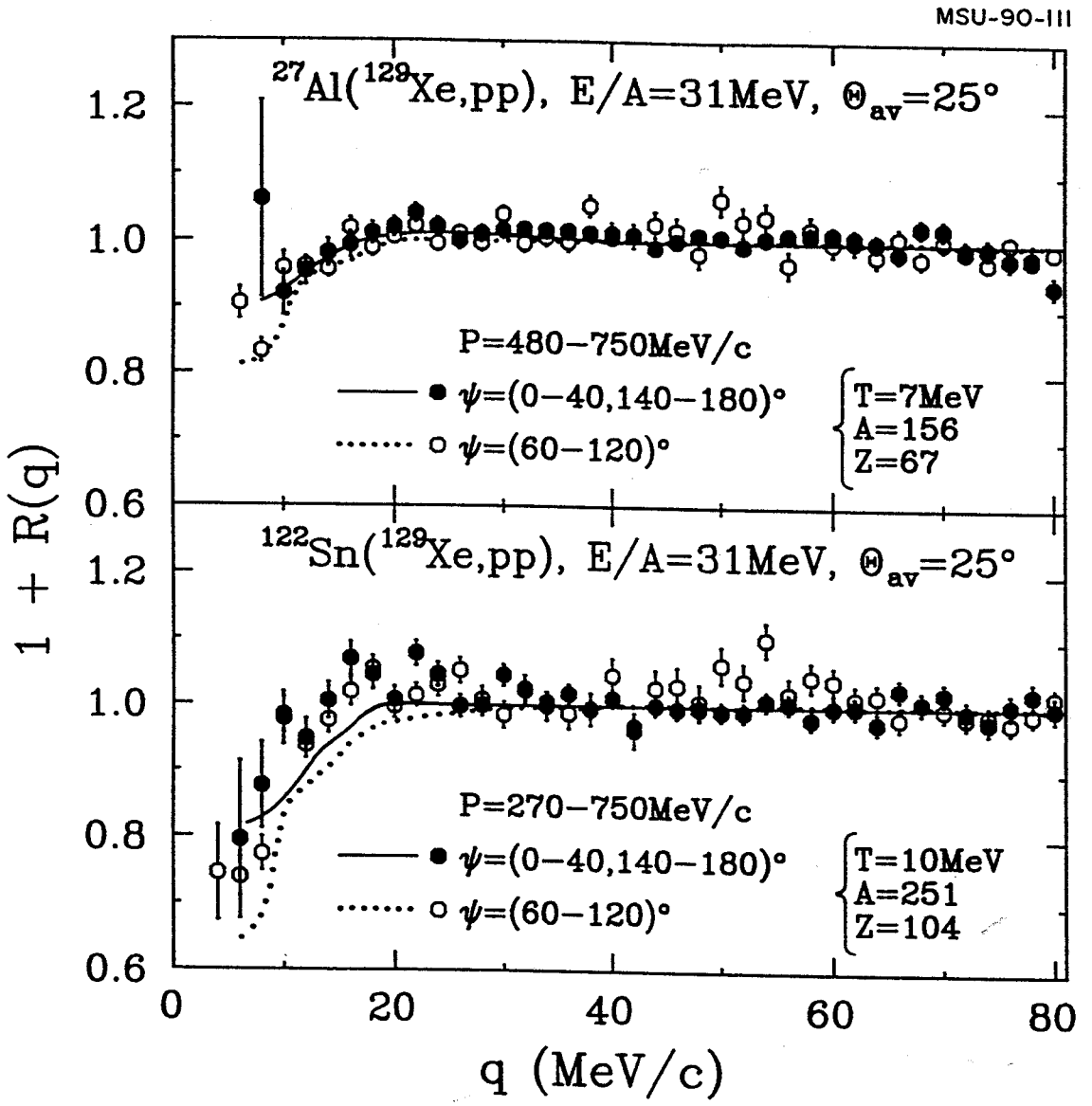

Figure 8.8: Longitudinal (Ψ=0°-40° or Ψ=140°-180°) and transverse (Ψ=60°-120°) two-proton correlation functions measured for the reaction ^{129}Xe+^{27}Al (top panel) and ^{129}Xe+^{122}Sn (bottom panel) at E/A=31 MeV.

angular cuts of Ψ_ℓ =0°-40° or 140°-180°). The transverse correlation functions, shown by open points, were evaluated for the gate $|\cos\Psi_t| \leq 0.5$ (corresponding to the angular cut of Ψ_t=60°-120°). For improved statistical accuracy, the gates on the total momenta of the proton pairs were made wider than in Figure 8.6; the values are indicated in the figure. No statistically significant difference between longitudinal and transverse correlation functions is visible. However, this result does not contradict theoretical expectations for evaporation from long-lived compound nuclei. The solid and dotted curves in Figure 8.8 show longitudinal and transverse correlation functions calculated for evaporative emission using the parameters indicated in the figure. The calculations were averaged over the appropriate momentum bins and folded with the resolution of the experimental apparatus. The predicted differences between transverse and longitudinal correlation functions are of the order of a few percent and, therefore, below the statistical sensitivity of the present experiment.

It was shown in Figure 8.5 that differences in the shapes of longitudinal and transverse correlation functions exhibit a strong dependence on the total momenta of the proton pairs. For emission from equilibrated ^{165}Ho compound nuclei, significant differences between longitudinal and transverse correlation functions are mainly predicted for large momenta, but not for small momenta corresponding to emission close to the barrier. Since evaporative cross sections decrease exponentially as a function of increasing kinetic energy of the emitted particles, integrals over wide momentum gates have predominant contributions from lower momenta for which the differences between longitudinal and transverse correlation functions are predicted to be small and difficult to detect. Unfortunately, the statistical accuracy of our experiment was insufficient for a more detailed exploration of longitudinal and transverse correlation functions at higher total momenta of the emitted proton pairs.

CHAPTER 9. TWO-PROTON CORRELATION FOR NON-EQUILIBRIUM EMISSION

For intermediate energy nucleus-nucleus collisions, particle emission already sets in at the early, non-equilibrated stages of the reaction for which purely statistical treatments are clearly inappropriate. These early stages of the reaction can be treated in terms of semi-classical models based upon the Boltzmann-Uehling-Uhlenbeck equation [Bert 84, Bert 88] which describes the space-time evolution of the one-body phase-space distribution function. The theory incorporates mean-field effects, nucleon-nucleon collisions, and the Pauli-exclusion principle in the semiclassical approximation; Coulomb effects are included. Within the Wigner-function formalism, knowledge of the one-body phase-space distribution function is sufficient for the characterization of the size and lifetime of the reaction zone formed in the nuclear collision and for the calculation of the two-proton correlation function at small relative momenta.

9.1 BUU Transport Equation for Collision Dynamics

In this section, we briefly review the derivation of the BUU transport equation which provides the basis for microscopic calculations for nonequilibrium particle emission in intermediate energy nucleus-nucleus collisions. We start with the Schrödinger equation of the N-particle system,

$$i\,\partial_t \Psi = H\Psi . \qquad (9.1)$$

Here, H is the N-particle Hamiltonian and Ψ is the N-particle wave-function.

From Ψ, one constructs the N-particle density,

$$\rho^{(N)} = \Psi\Psi^{*}, \tag{9.2}$$

which leads to the von-Neumann equation of motion:

$$i\partial_t \rho^{(N)} = [H,\rho^{(N)}]\,. \tag{9.3}$$

We introduce the reduced density matrices via

$$\rho^{(n)}(\vec{r}_1,\ldots,\vec{r}_n;\vec{r}'_1,\ldots,\vec{r}'_n) =$$

$$\frac{1}{(N-n)!}\int d^3r_{n+1}\ldots d^3r_N d^3r'_{n+1}\ldots d^3r'_N \rho^{(N)}(\vec{r}_1,\ldots,\vec{r}_N;\vec{r}'_1,\ldots,\vec{r}'_N). \tag{9.4}$$

Inserting Equation (9.4) into Equation (9.3), leads to the Bogoliubov-Born-Green-Kirkwood-Yvon (BBGKY) hierarchy of the reduced density matrices. This hierarchy links the time derivative of $\rho^{(n)}$ to $\rho^{(n+1)}$. The lowest two member's of the BBGKY hierarchy are:

$$i\partial_t \rho^{(1)}(\vec{r}_1,\vec{r}'_1) = -\frac{1}{2m}(\nabla^2_{r_1} - \nabla^2_{r'_1})\rho^{(1)}(\vec{r}_1;\vec{r}'_1)$$

$$+ \int d^3r_2\,(v(\vec{r}_1,\vec{r}_2) - v(\vec{r}'_1,\vec{r}_2))\,\rho^{(2)}(\vec{r}_1,\vec{r}_2;\vec{r}'_1,\vec{r}_2) \tag{9.5}$$

and

$$i\partial_t \rho^{(2)}(\vec{r}_1,\vec{r}_2;\vec{r}'_1,\vec{r}'_2) = -\frac{1}{2m}\sum_{i=1}^{2}(\nabla^2_{r_i} - \nabla^2_{r'_i})\rho^{(2)}(\vec{r}_1,\vec{r}_2;\vec{r}'_1,\vec{r}'_2)$$

$$+ \left(v(\vec{r}_1,\vec{r}_2)-v(\vec{r}',_1,\vec{r}',_2)\right)\rho^{(2)}(\vec{r}_1,\vec{r}_2;\vec{r}',_1,\vec{r}',_2)$$

$$+\sum_{i=1}^{2}\int d^3r_3\left(v(\vec{r}_i,\vec{r}_3)-v(\vec{r}',_i,\vec{r}_3)\right)\rho^{(3)}(\vec{r}_1,\vec{r}_2,\vec{r}_3;\vec{r}',_1,\vec{r}_2,\vec{r}_3)\ . \qquad (9.6)$$

A closed solution of the equations of this hierarchy is only possible, if one truncates at a level n and with it neglects (n+1)-body correlations. Truncating at n=1, neglecting two-body correlations, and approximating $\rho^{(2)}$ as an antisymmetrized product of one-body densities, one obtains the TDHF equations:

$$i\partial_t\rho^{(1)} = [h,\rho^{(1)}]\ , \qquad (9.7)$$

where h is the single particle Hamiltonian,

$$h(\vec{r},\vec{r}') = -\delta^3(\vec{r}-\vec{r}')\frac{1}{2m}\nabla_r^2 + \delta^3(\vec{r}-\vec{r}')\int d^3r_2\rho^{(1)}(\vec{r},\vec{r}_2)v(\vec{r},\vec{r}_2)$$

$$- \rho^{(1)}(\vec{r},\vec{r}')v(\vec{r},\vec{r}')\ . \qquad (9.8)$$

Performing a Wigner-transformation gives the Vlasov equation:

$$\partial_t f(\vec{p},\vec{r},t) + \frac{\vec{p}}{m}\bullet\vec{\nabla}_r f(\vec{p},\vec{r},t) - \vec{\nabla}_r U(\vec{r})\bullet\vec{\nabla}_p f(\vec{p},\vec{r},t) = 0\ . \qquad (9.9)$$

In Equation (9.9), $U(\vec{r})$ is the mean field or Hartree potential,

$$U(\vec{r}) = \int d^3r_2 v(\vec{r},\vec{r}_2)\rho(\vec{r},\vec{r}_2), \tag{9.10}$$

and $f(\vec{p},\vec{r},t)$ is the Wigner-transform of the single-particle density matrix,

$$f(\vec{p},\vec{r},t) = \int d^3s\, \rho^{(1)}(\vec{r}-\frac{\vec{s}}{2},\vec{r}+\frac{\vec{s}}{2})e^{i\vec{p}\bullet\vec{s}}. \tag{9.11}$$

In the derivation of Equation (9.9), the semiclassical approximation has been used. This approximation is valid since typical wavelengths ($\lambda \approx 2.5$ fm for p=500 MeV/c) are shorter than the size of the regions with the mean field (typically of the order of 8 fm diameter). The TDHF and Vlasov approximations to the many-body problem are pure one-body theories in mean field approximation in which all multi-particle correlations are neglected.

A truncation of the BBGKY hierarchy which includes two-body correlations, but neglects three- and higher-particle correlations leads to the Boltzmann-Uehling-Uhlenbeck (BUU) equation:

$$\partial_t f(\vec{p},\vec{r},t) + \frac{\vec{p}}{m}\bullet\vec{\nabla}_r f(\vec{p},\vec{r},t) - \vec{\nabla}_r U(\vec{r})\bullet\vec{\nabla}_p f(\vec{p},\vec{r},t) =$$

$$\frac{1}{2\pi^3 m^2}\int d^3q_1' d^3q_2 d^3q_2' \delta\left(\frac{1}{2m}(p^2+q_2^2-q_1'^2-q_2'^2)\right)\delta^3(\vec{p}+\vec{q}_2-\vec{q}_1'-\vec{q}_2')\frac{d\sigma}{d\Omega}$$

$$\times\{\hat{f}(\vec{q}_1',\vec{r},t)\hat{f}(\vec{q}_2',\vec{r},t)(1-\hat{f}(\vec{p},\vec{r},t))(1-\hat{f}(\vec{q}_2,\vec{r},t))$$

$$-\hat{f}(\vec{p},\vec{r},t)\hat{f}(\vec{q}_2,\vec{r},t)(1-\hat{f}(\vec{q}_1',\vec{r},t))(1-\hat{f}(\vec{q}_2',\vec{r},t))\}. \tag{9.12}$$

In Equation (9.12), $\hat{f}(\vec{p},\vec{r},t)$ is the phase-space density averaged over one phase-space cell. The left-hand side of the equation is the Vlasov term describing the temporal change of the one-body Wigner-function, $f(\vec{p},\vec{r},t)$, due to the interaction of the nucleons with the mean field. The right-hand side is the collision integral which represents the effects of the correlations due to two-body collisions on the one-body Wigner-function. Equation (9.12) was first obtained by Nordheim [Nord 28] as a quantum mechanical extension of the Boltzmann equation which incorporates Fermion statistics.

Equation (9.12) is solved by using the pseudo-particle method [Wong 82]. In this method one compares the left-hand side of the equation to the complete differential of $f(\vec{p},\vec{r},t)$:

$$\frac{d}{dt} f(\vec{p},\vec{r},t) = \frac{\partial}{\partial t} f(\vec{p},\vec{r},t) + \frac{d\vec{r}}{dt} \bullet \vec{\nabla}_r f(\vec{p},\vec{r},t) + \frac{d\vec{p}}{dt} \bullet \vec{\nabla}_p f(\vec{p},\vec{r},t) . \qquad (9.13)$$

From Equations (9.12) and (9.13), one obtains a set of six coupled first-order equations for every occupied phase-space point:

$$\frac{dr_i}{dt} = \frac{p_i}{m}, \qquad (9.14)$$

$$\frac{dp_i}{dt} = I_i(\vec{p}) - \frac{\partial}{\partial r_i} U(\vec{r}) . \qquad (9.15)$$

Here, $I_i(\vec{p})$ is the change in momentum p_i due to nucleon-nucleon collisions (i=1,2,3). The differential equations can be interpreted as the classical Hamiltonian

equations of motion for a pseudo-particle. Since the total occupied phase space is proportional to the number of nucleons, it is convenient to specify the total number of phase space points per nucleon as a measure for the numerical precision with which Equation (9.12) is solved. In the present calculations, we have used up to 700 pseudo-particles per nucleon, resulting in a total of up to 172,200 coupled first-order differential equations which were solved simultaneously. The average phase-space occupancies used to determine the effects of the Pauli principle in the collision integral were determined from the coordinates and momenta of the pseudo-particles. The cell size for averaging was chosen to be $\frac{1}{4}(h/2\pi)^3$.

We solve the BUU equation by numerical methods which are similar to the ones introduced by Reference [Bert 84], see also Reference [Bert 88]. The major new numerical technique used in our present calculations is the treatment of the Pauli exclusion principle. By explicitly storing $\hat{f}(\vec{p},\vec{r},t)$ on a six-dimensional lattice in every time-step, we were able to greatly speed up the computer program without relaxing the accuracy of the treatment of the Pauli-exclusion principle [Baue 90].

It seems at first sight surprising that it could be used to calculate two-particle correlation functions since BUU is basically a theory describing the time evolution of the one-body phase-space distribution function. However, within the Wigner-function formalism outlined in Chapter 6, the knowledge of the one-body phase-space distribution function is sufficient for the calculation of the two-proton correlation function at small relative momenta and the characterization of the size and lifetime of the reaction zone formed in the nuclear collision.

Correlations between coincident particles do not only arise from quantum statistics and/or final state interactions, but also from a number of dynamical and kinematical effects. Previously, it was shown [Knol 80, Lync 82, Lync 83, Tsan 84a, Tsan 84b, Chit 86a, Baue 87, Baue 88, Tsan 90, Ardo 90] that the main features of

two-proton coincidences at large angles are explained by the effects due to total momentum conservation, finite particle number, and/or collective motion in the reaction plane without requiring the detailed information about two-particle correlations. For example, the detection of a single particle will shift the total momentum of all remaining particles; for small systems this effect can lead to significant correlations at large relative momenta. If the single-particle distribution is azimuthally anisotropic, the detection of one particle can filter out a non-isotropic distribution of reaction-plane orientations [Tsan 84a, Tsan 84b, Chit 86a, Tsan 90, Wils 90, Ardo 90] causing non-isotropic azimuthal correlation functions.

In the next Section, we will explain in detail the procedure for averaging over impact parameters and point out the approximations used for calculating two-proton correlation functions at small relative momenta.

9.2 Impact Parameter Averaging

For semi-classical reaction models, the impact-parameter averaged correlation function, consistent with Equation (7.1), can be written in the form:

$$C(\vec{P},\vec{q}) = N(\vec{P}) \frac{\int b\,db\,d\phi \{\Pi(b,\phi,\frac{1}{2}\vec{P}+\vec{q})\,\Pi(b,\phi,\frac{1}{2}\vec{P}-\vec{q}) C^{f}(b,\phi,\vec{P},\vec{q})\}}{\int db\,d\phi \{\Pi(b,\phi\ \frac{1}{2}\vec{P}+\vec{q})\ \} \int db\,d\phi \{\Pi(b,\phi,\frac{1}{2}\vec{P}-\vec{q})\}} . \quad (9.16)$$

Here, b denotes the impact parameter; ϕ denotes the azimuthal orientation of the reaction plane; $\Pi(b,\phi,\vec{p})$ is the probability of emitting a particle with momentum $\vec{p}$ for events characterized by b and ϕ; $C^{f}(b,\phi,\vec{P},\vec{q})$ is the correlation function due to final state interactions and/or quantum statistics for given b and ϕ; $N(\vec{P})$ is a suitably chosen normalization constant which makes the normalization at large relative momenta consistent with the experimental data. We can write this expression in the form:

$$C(\vec{P},\vec{q}) = N(\vec{P}) \cdot C^{f}(\vec{P},\vec{q}) \cdot C^{d}(\vec{P},\vec{q}) \{ \frac{\int bdbd\phi \{\Pi(b,\phi,\frac{1}{2}\vec{P}+\vec{q})\Pi(b,\phi,\frac{1}{2}\vec{P}-\vec{q})C^{f}(b,\phi,\vec{P},\vec{q})\}}{\int bdbd\phi \{\Pi(b,\phi,\frac{1}{2}\vec{P})\Pi(b,\phi,\frac{1}{2}\vec{P})C^{f}(b,\phi,\vec{P},\vec{q})\}}$$

$$\times \frac{\int bdbd\phi \{\Pi(b,\phi,\frac{1}{2}\vec{P})\Pi(b,\phi,\frac{1}{2}\vec{P})\}}{\int bdbd\phi \{\Pi(b,\phi,\frac{1}{2}\vec{P}+\vec{q})\Pi(b,\phi,\frac{1}{2}\vec{P}-\vec{q})\}} \}, \qquad (9.17)$$

with

$$C^{f}(\vec{P},\vec{q}) = \frac{\int bdbd\phi \{\Pi(b,\phi,\frac{1}{2}\vec{P})\,\Pi(b,\phi,\frac{1}{2}\vec{P})\,C^{f}(b,\phi,\vec{P},\vec{q})\}}{\int bdbd\phi \{\Pi(b,\phi,\frac{1}{2}\vec{P})\Pi(b,\phi,\frac{1}{2}\vec{P})\}}, \qquad (9.18)$$

$$C^{d}(\vec{P},\vec{q}) = \frac{\int bdbd\phi \{\Pi(b,\phi,\frac{1}{2}\vec{P}+\vec{q})\,\Pi(b,\phi,\frac{1}{2}\vec{P}-\vec{q})\}}{\int bdbd\phi \{\Pi(b,\phi,\frac{1}{2}\vec{P}+\vec{q})\} \int bdbd\phi \{\Pi(b,\phi,\frac{1}{2}\vec{P}-\vec{q})\}}. \qquad (9.19)$$

Here, $C^{f}(\vec{P},\vec{q})$ is the correlation function due to final state interactions and/or quantum statistics, renormalized to unity for large relative momenta for which $C^{f}(b,\phi,\vec{P},\vec{q}) = 1$, and $C^{d}(\vec{P},\vec{q})$ is the "dynamical correlation function" which describes correlations caused by averaging over b and ϕ.

In Equation (9.17), the terms in curly brackets can be neglected to a good approximation. (If the correlation function $C^{f}(b,\phi,\vec{P},\vec{q})$ is independent of b and ϕ, the terms in the curly brackets cancel exactly.) For two-proton correlation functions, the correlation function $C^{f}(b,\phi,\vec{P},\vec{q})$ is non-trivial only for small relative momenta, $q \lesssim 30$ MeV/c, for which one may approximate $\Pi^{2}(b,\phi,\vec{P}/2) \approx \Pi(b,\phi,\vec{P}/2+\vec{q}) \cdot \Pi(b,\phi,\vec{P}/2-\vec{q})$. This approximation reduces the two factors in the curly brackets to unity. At larger relative momenta, $C^{f}(b,\phi,\vec{P},\vec{q}) \approx 1$ and the denominators and enumerators of the two terms in the curly brackets cancel cross-wise. It should, therefore, be reasonable to use the approximation:

$$C(\vec{P},\vec{q}) = N(\vec{P}) \bullet C^{f}(\vec{P},\vec{q}) \bullet C^{d}(\vec{P},\vec{q}) . \qquad (9.20)$$

With Equation (9.20), one can incorporate dynamical correlations in a fairly straightforward fashion. (Note, however, that other physical processes, not considered in our calculations, may also affect the correlations at small total momenta, e.g. distortions in the Coulomb field of the heavy reaction residue or feeding from the decay of particle unbound states.)

In our measurements, distortions due to dynamical correlations may be present in some of the correlation functions extracted for low total momenta. For example, there is evidence for shape distortions in the correlation function for the $^{14}N + ^{197}Au$ reaction at small total momenta, see Figure 7.4. More significant are the difficulties encountered in the normalization of transverse and longitudinal correlation functions for the ^{14}N-induced reactions at low total momenta discussed below (see Figures 9.8 and 9.9). However, the present BUU calculations do not provide an accurate description of the cross sections for such low-energy emissions, see Figure 5.4. Furthermore, dynamical correlations test different aspects of the model than correlations due to final state interactions. Therefore, we have decided to neglect them in our calculations and used Equation (9.18) for the calculation of the impact parameter averaged correlation functions. For comparisons with experimental data, the calculated correlation functions were renormalized at larger relative momenta, $q \approx 60$ - 100 MeV/c, to make them consistent with the normalization conventions adopted in our data analysis.

9.3 Predicted Two-proton Correlation Functions

In our standard BUU calculations, we used a stiff equation of state and energy-dependent free nucleon-nucleon cross sections. (For the present reactions, the calculations exhibit little sensitivity to the stiffness of the equation of state.) For the reactions $^{14}N + ^{27}Al$ and $^{14}N + ^{197}Au$, the correlation functions were calculated from the phase-space points obtained from a total

of 5250 and 4500 computational events, respectively, with impact parameters distributed according to their geometrical weights.

The Wigner functions of emitted particles were constructed from nucleons emitted during a time interval of Δt_e=140 fm/c following initial contact of the colliding nuclei; the time $t_>$ was taken at the end of the time interval Δt_e. Nucleons were considered as emitted when, during this time interval, the surrounding density fell below $\rho_e = \rho_0/8$ and when subsequent interaction with the mean field did not cause recapture into regions of higher density. This test for recapture was continued over a time interval of Δt = 180 fm/c after contact. The finite size of our lattice did not allow us to explore much larger emission times. However, the consideration of much larger emission times would not necessarily lead to more reliable results since, in our present approximation, the nuclei are not stable over long time scales and the BUU calculations become inaccurate due to spurious decays.

In our calculations of the correlation functions, appropriate averages over impact parameter, orientation of the reaction plane, and the indicated gates on the total momentum and the angle, Ψ, between the relative and total momentum of the two protons were taken into account.

While our particular choice of the parameters Δt_e and ρ_e is reasonable, it involves a certain degree of arbitrariness. The sensitivity of the calculations to different choices of the emission time interval, Δt_e, and the freeze-out density, ρ_e, is illustrated in Figure 9.1. Larger emission time intervals reduce the height of the maximum of the correlation function at $q \approx 20$ MeV/c due to an increase of the average emission time. On the other hand, smaller freeze-out densities lead to a slight increase in the height of the maximum of the correlation function. This can be understood as follows: lower emission densities select subsets of particles

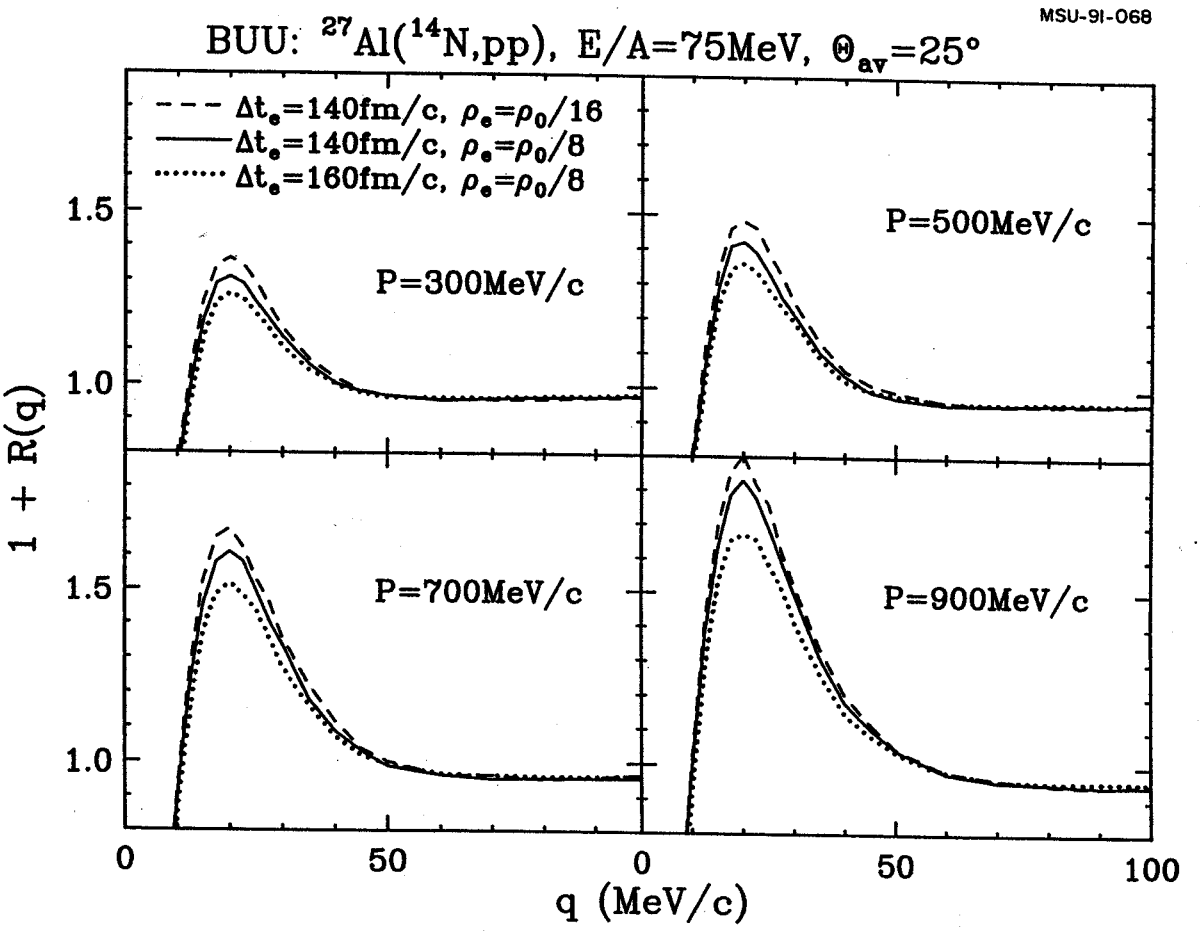

Figure 9.1 : Dependence of correlation functions predicted by BUU calculations on the emission time intervals, Δt_e, and the emission densities, ρ_e. The values of individual parameter choices and selected total momenta of the proton pairs are given in the figure. In these calculations, the in-medium cross section was approximated by the experimental free nucleon-nucleon cross section, and the stiff equation of state was used.

considered as emitted for higher freeze-out densities by eliminating late emissions (i.e. particles which have not yet reached the lower densities) and thus selecting particles which had left the higher density regime at earlier times. The corresponding reduction of the average temporal separation between emitted particles leads to enhanced correlations. Typically, different reasonable choices of Δt_e and ρ_e introduce uncertainties of the order of 5-10% into the magnitude of the predicted correlation functions. However, in some instances these uncertainties can be larger.

9.4 Dependence on Total Momentum

Two-proton correlation functions measured for the $^{14}N + ^{27}Al$ and $^{14}N + ^{197}Au$ reactions at E/A = 75 MeV are compared in Figures 9.2 and 9.4 to calculations using density distributions predicted by the BUU equation. We made cuts on the total laboratory momenta, P, and no selection on the angle, Ψ, between the total and relative momentum vectors for the emitted proton pairs. By means of extracting Gaussian radius parameters, $r_0(P)$, we present a more detailed comparison between measured and calculated two-proton correlation functions for $^{14}N + ^{27}Al$ at E/A = 75 MeV in Figure 9.3. The errors represent estimates of accuracy in extracting the radius parameters from correlation functions.

Overall, two-proton correlation functions predicted by the BUU theory (solid curves in Figures 9.2 and 9.4, open points in Figure 9.3) are in rather good agreement with the measured correlation functions (points in Figures 9.2 and 9.4, solid points in Figure 9.3). It is particularly gratifying that the calculations can qualitatively reproduce the observed strong dependence of the correlation functions on the total momentum of the emitted proton pairs. For the low-momentum gate of the $^{14}N + ^{197}Au$ reaction, the maximum of the calculated correlation function is larger than that of the experimental correlation function,

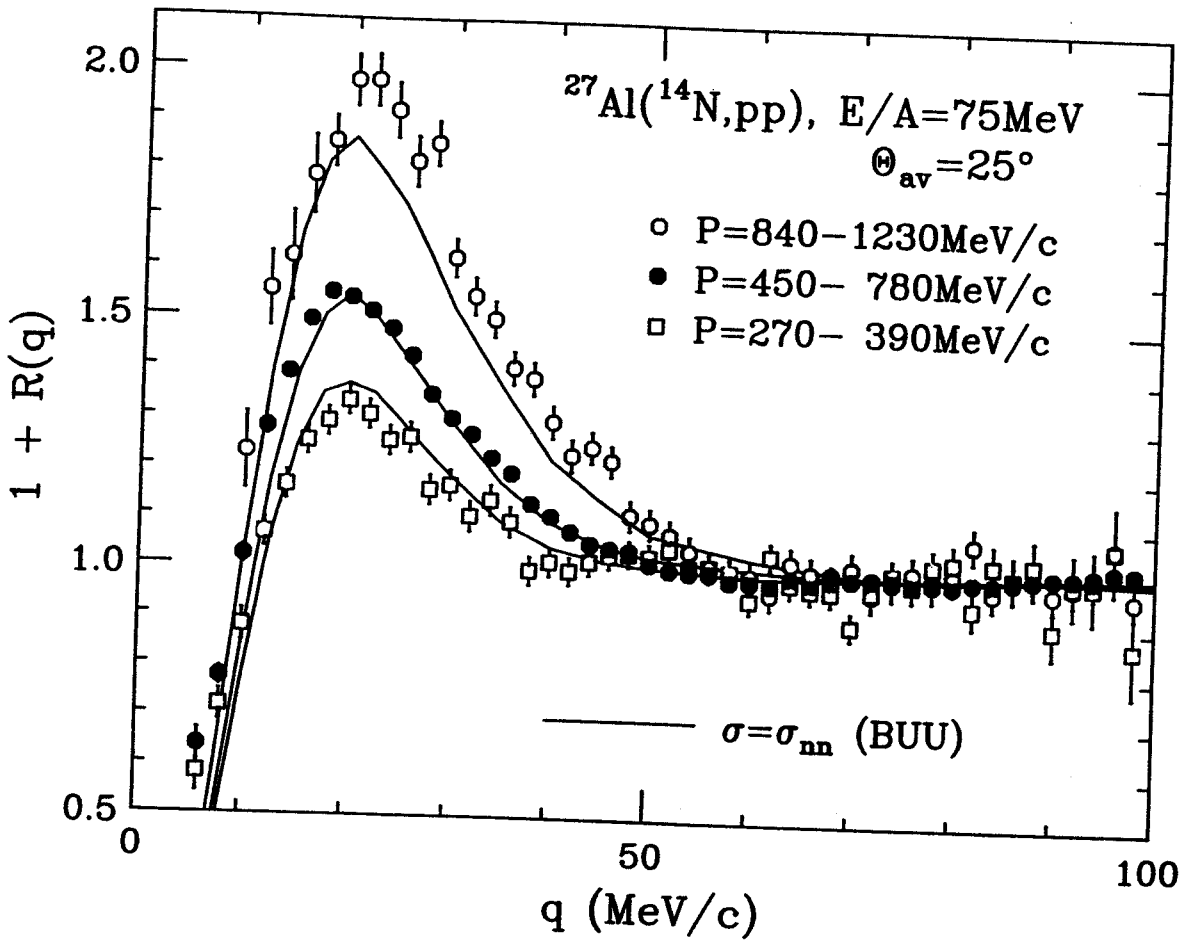

Figure 9.2 : Two-proton correlation functions, measured for the reaction ^{14}N+^{27}Al at E/A=75 MeV, are compared with correlation functions predicted with the BUU theory. The gates placed on the total momenta, P, of the coincident proton pair are indicated.

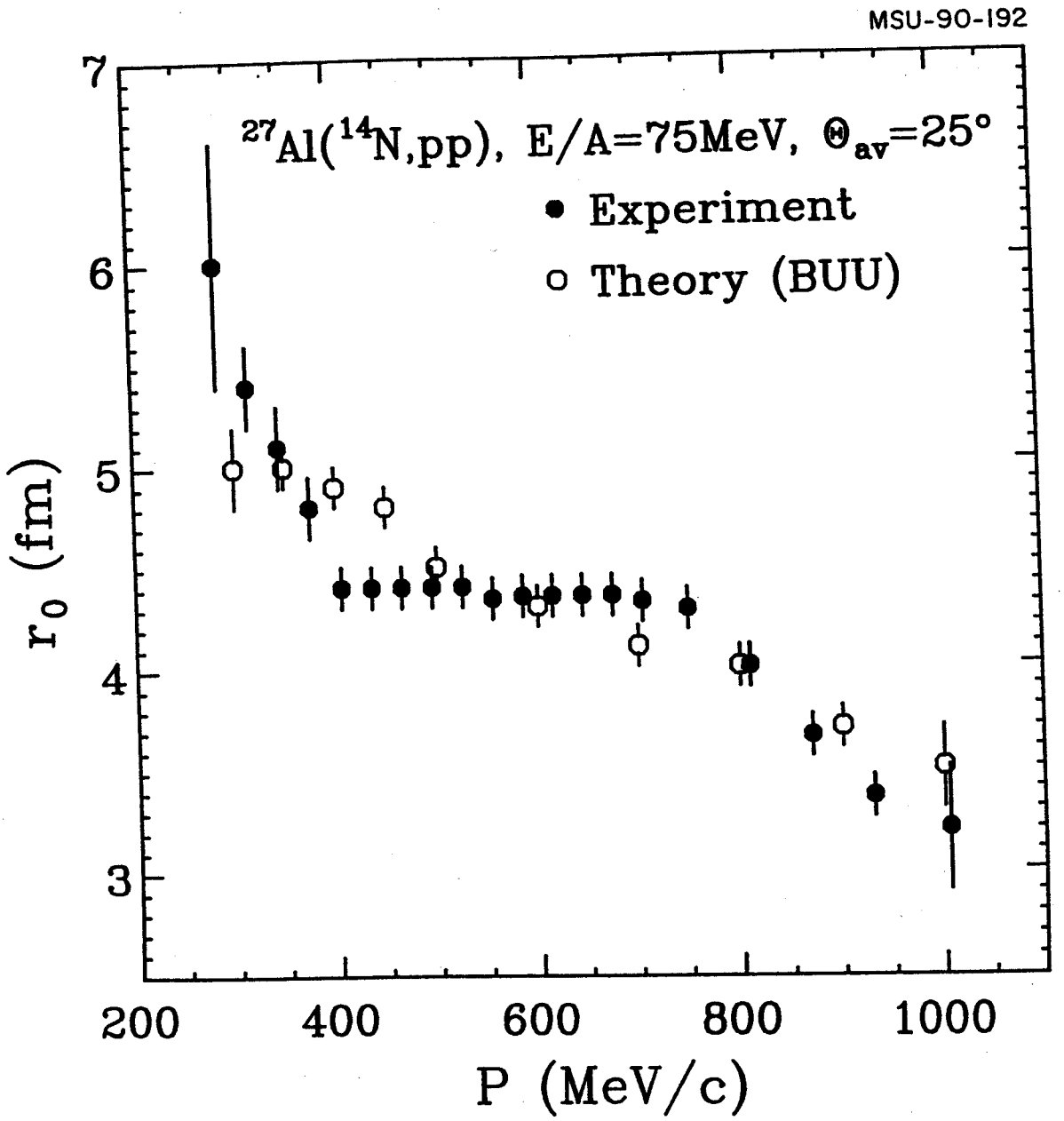

Figure 9.3 : Radius parameters $r_0(P)$ for Gaussian sources of negligible lifetime extracted from two-proton correlation functions gated by different total momenta P. Solid and open circles represent experimental and theoretical correlation functions, respectively.

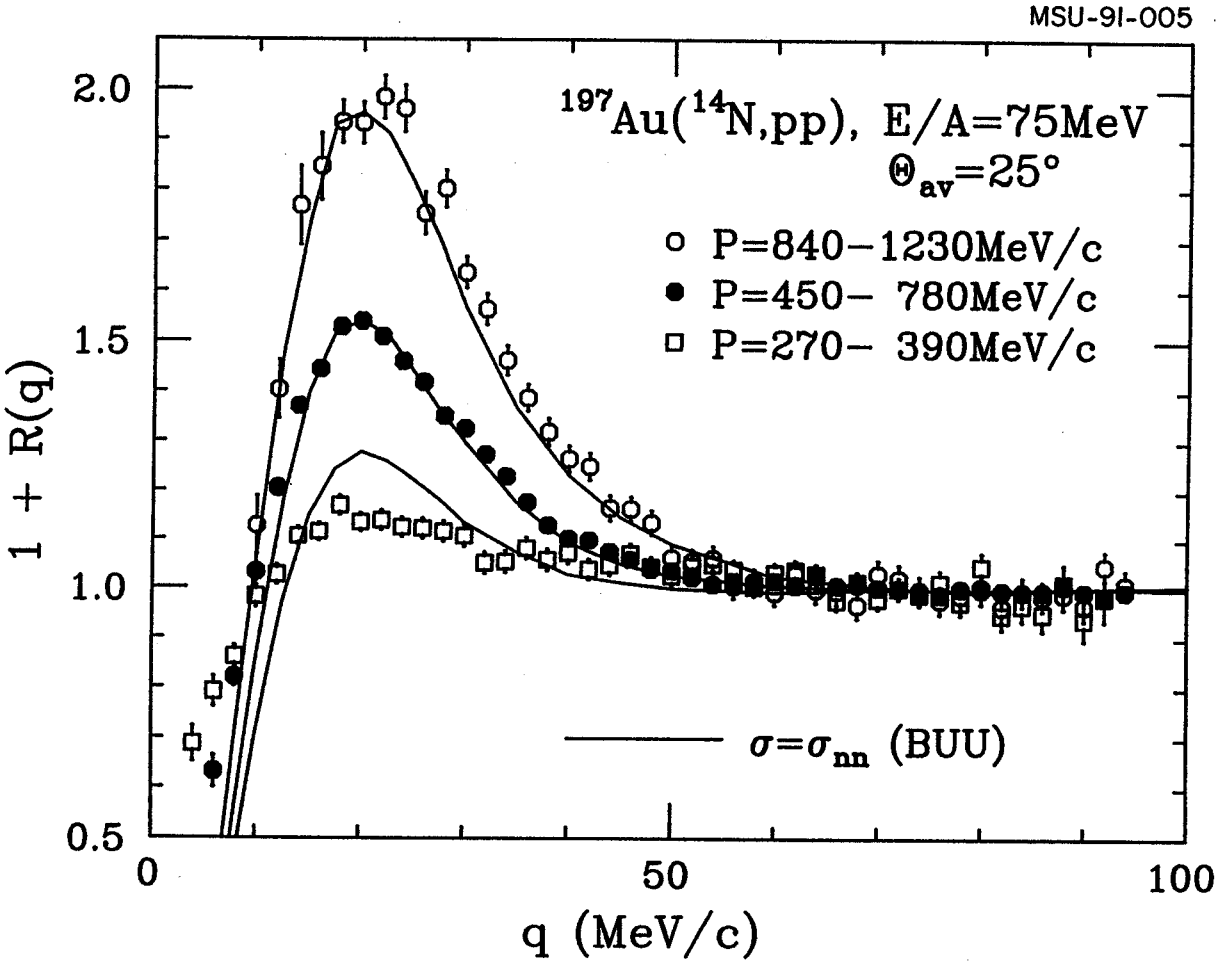

Figure 9.4 : Two-proton correlation functions, measured for the reaction ^{14}N+^{197}Au at E/A=75 MeV, are compared with correlation functions predicted with the BUU theory. The gates placed on the total momenta, P, of the coincident proton pair are indicated.

see Figure 9.4. This discrepancy is not surprising since the emission of low-energy protons is expected to have significant contributions from slow evaporative processes which are not incorporated into our calculations. In fact, the existence of a strong evaporative component in the low-energy portion of the proton spectrum for the $^{14}N + ^{197}Au$ reaction was already inferred from the shape of the minimum of the correlation function at $q \lesssim 15$ MeV/c (see Figure 7.4) as well as from the shape of the single proton spectra (see Section 5.2). The inclusion of evaporative processes would lead to more extended Wigner functions and, hence, to more attenuated correlation functions.

A close comparison of Figures 7.3 and 7.4 with Figures 9.2 and 9.4 reveals that correlations functions calculated from the BUU theory provide an improved description of the shape of the experimental correlation functions in the region of $q \approx 30$-40 MeV/c as compared to those calculated for spherical Gaussian sources.

Figure 9.5 compares the detailed shapes of two-proton correlation functions predicted for different space-time geometries. The solid points show correlation functions predicted from the BUU equation, averaged over the indicated range of total momenta, P, of the proton pairs. These calculations are in excellent agreement with data (see figure 9.2). The solid curve shows results obtained for instantaneous emission from a Gaussian source, Equation (7.1), with radius parameter $r_0 = 4.5$ fm. The two-proton correlation function calculated for the Gaussian source, exhibits a narrower maximum than that calculated for the more realistic density distribution obtained by means of the BUU equation. This difference in shape can be attributed to the fact that sources predicted by the BUU equation are non-spherical. To illustrate the sensitivity of the shape of two-proton correlation functions to the source geometry, we show the correlation function predicted for emission from a source consisting of two sharp spheres of negligible lifetime. Both spheres were assumed to have radii of $R_s = 5$ fm, and the centers

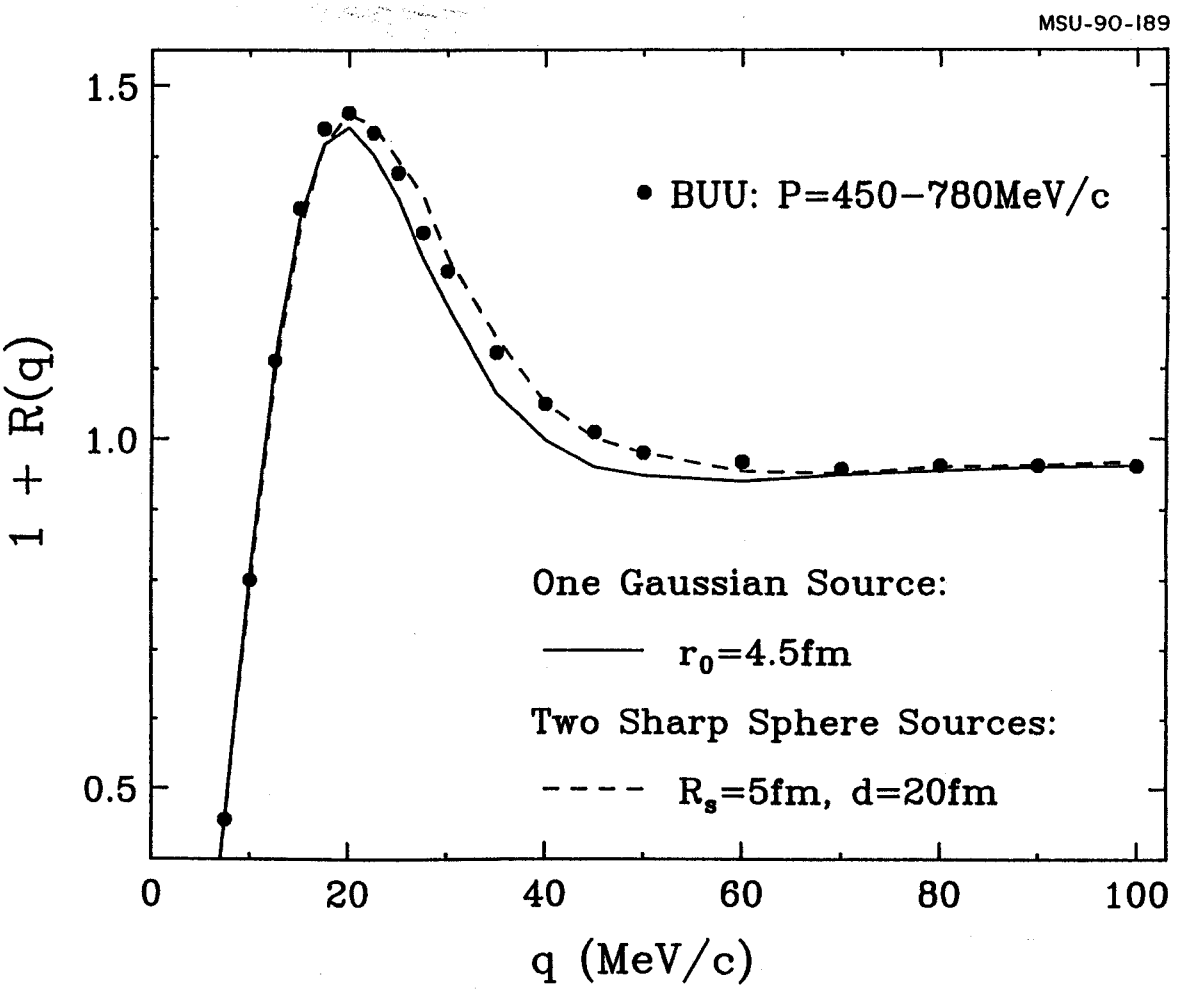

Figure 9.5 : Comparison of two-proton correlation functions predicted for different source geometries: the solid points represent the results of BUU calculations averaged over the momentum range P=450-780 MeV/c. The curves show emission from sources of negligible lifetime: the solid and dashed curves are obtained, respectively, for a spherical Gaussian source of radius parameter, r_0=4.5 fm, and a source consisting of two sharp spheres of radius, R_s=5 fm, and separated by the distance, d=20 fm.

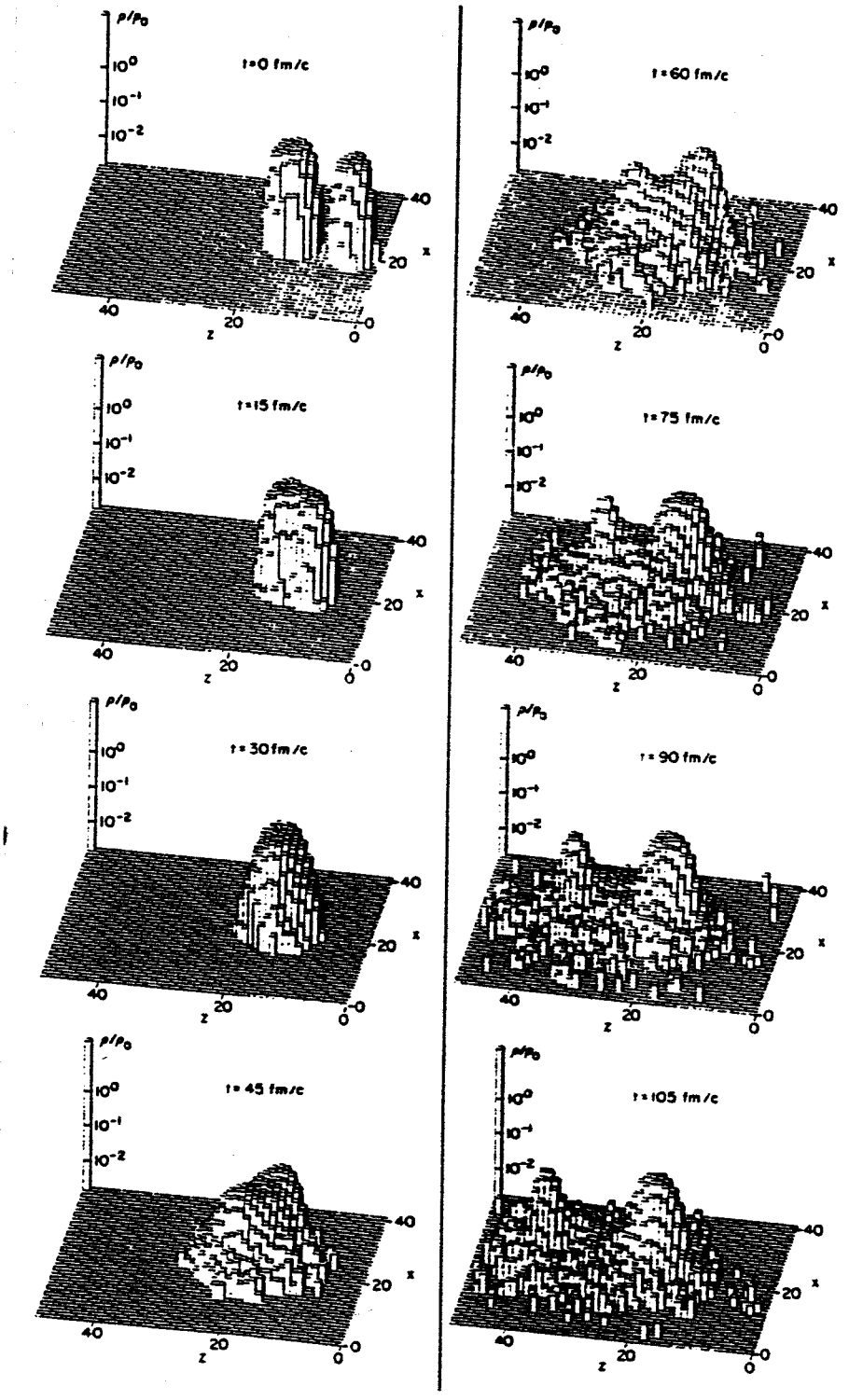

Figure 9.6 : Nucleon density distributions in the reaction plane calculated from the BUU equation for $^{14}N+^{27}Al$ collisions at E/A=75 MeV and for an impact parameter of b=2 fm. Different panels depict the distributions at different times, t.

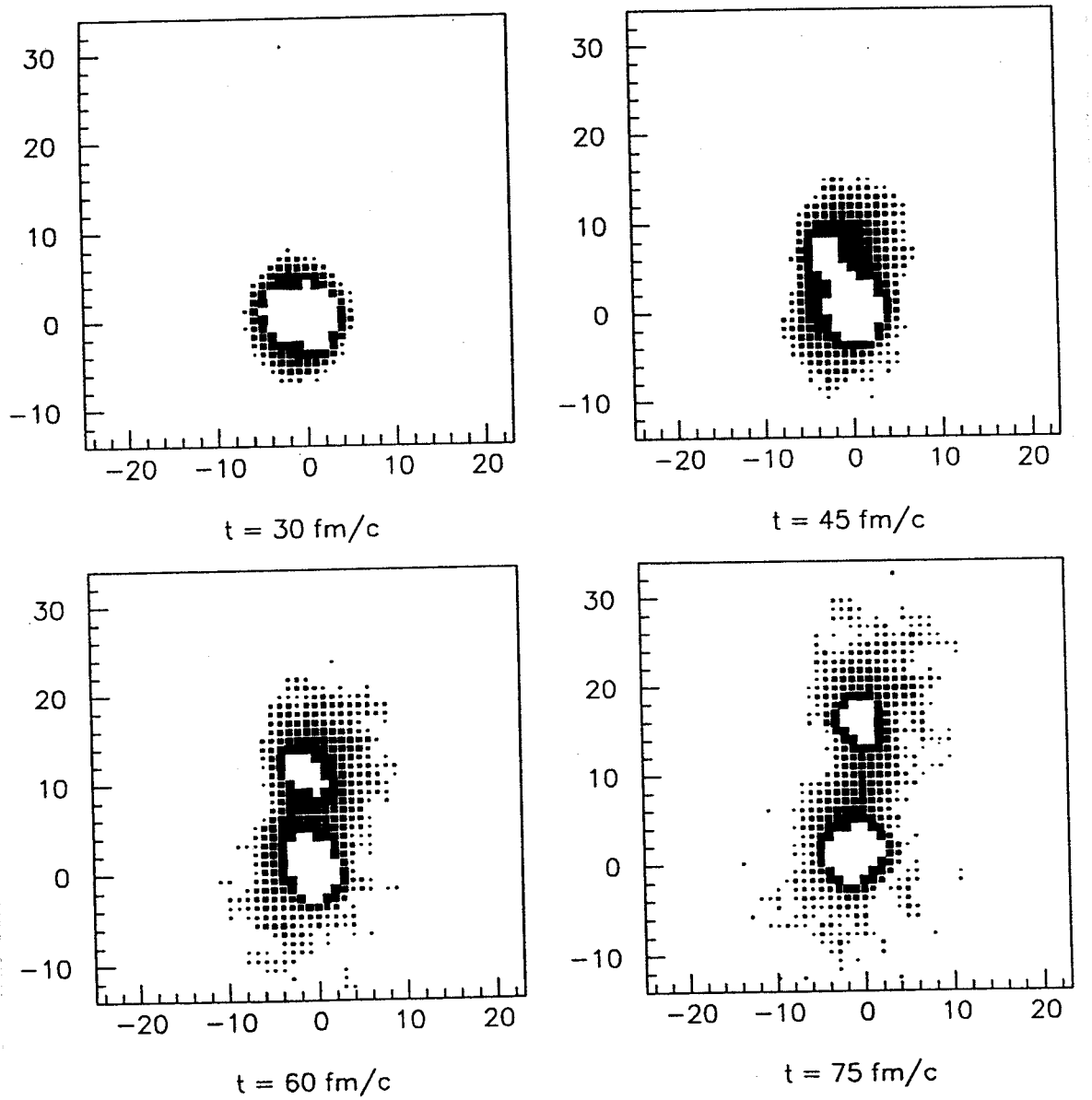

Figure 9.7 : Spatial distributions of emitted nucleons in the reaction plane calculated from the BUU equation for $^{14}N+^{27}Al$ collisions at E/A=75 MeV and for an impact parameter of b=2 fm. Different panels depict the distributions at different times, t.

of the two spheres were assumed to be separated by a distance of d=20 fm and aligned along the beam direction. The correlation function for this two-source distribution is depicted by the dashed curve in Figure 9.5; it has a wider maximum than the single Gaussian source distribution and is rather similar in shape to that predicted from the BUU calculations. (Remember: two-proton correlation functions obtained for single spherical sources of sharp sphere and Gaussian density profiles are virtually indistinguishable in shape; see also the discussion of Figures 6.3 and 6.4.)

Figures 9.6 and 9.7 depict the space-time evolution of the collision process as predicted by the BUU equation. Figure 9.6 shows the time evolution of the nucleon density in the reaction plane for a $^{14}N + ^{27}Al$ collision at E/A=75 MeV and an impact parameter of 2 fm. Different panels of the figure represent snapshots taken at the indicated times after contact of the colliding nuclei. The calculations predict that the two colliding nuclei essentially survive the collision and separate into two hot nuclear objects which may then decay on longer time scales for which BUU calculations cannot make accurate predictions. More relevant for the calculations of two-proton correlation functions is the density distribution of the emitted nucleons in the reaction plane, shown in Figure 9.7 for selected times after the initial contact of the colliding partners. The distribution of emitted nucleons clearly undergoes an evolution from a near-spherical source at early times to a two-source distribution at larger times. This two-source distribution at larger times may explain the similarity of the correlation functions obtained for a two-sphere distribution with that predicted by the BUU calculations.

9.5 Longitudinal vs. Transverse Correlation Functions

To explore the shape of the emission sources in ^{14}N induced reactions, we have compared longitudinal and transverse correlation functions following similar discussions in Section 8.4. Figures 9.8 and 9.9 show longitudinal and transverse

correlation functions measured for the $^{14}N + ^{27}Al$ and $^{14}N + ^{197}Au$ reactions at E/A = 75 MeV, respectively. As before, $\Psi = \cos^{-1}(\vec{P}\bullet\vec{q}/Pq)$, longitudinal (solid points) and transverse (open points) correlation functions were evaluated for the gates $|\cos\Psi_\ell| \geq 0.77$ and $|\cos\Psi_t| \leq 0.5$, respectively. The upper and lower panels of the figures show data for different gates on the total momenta of the emitted particle pairs, P=270-420 MeV/c and P= 420-780 MeV/c for the $^{14}N + ^{27}Al$ reaction, and P= 270-450 MeV/c and P= 450-780 MeV/c for the $^{14}N + ^{197}Au$ reaction. For each gate, left and right hand panels show results obtained with different normalization conventions. The right hand panels depict longitudinal and transverse correlation functions normalized with a single normalization constant, C_{12}, which was determined, for each gate on P, by normalizing the angle integrated correlation function, $R_0(q)$, by the condition,

$$\int_{\Delta q} dq\ R_0(q) = 0\,, \tag{9.21}$$

where Δq = 60-100 MeV/c. With this normalization, longitudinal and transverse correlation functions gated by low total momenta (P=270-420 and 270-450 MeV/c, top right-hand panels of Figures 9.8 and 9.9) attain distinctly different values for larger relative momenta, $q \gtrsim 40$ MeV/c. For higher total momenta (P=420-780 and 450-780 MeV/c, bottom right-hand panels of Figures 9.8 and 9.9) differences at large relative momenta are less significant.

At small relative momenta, residual dynamical correlations are expected to be small and the use of a single normalization constant should be justified. With this presumption, we do not find statistically significant differences between longitudinal and transverse correlation functions at small relative momenta, $q \lesssim 30$ MeV/c. This experimental result is in agreement with that of Reference [Awes 88]

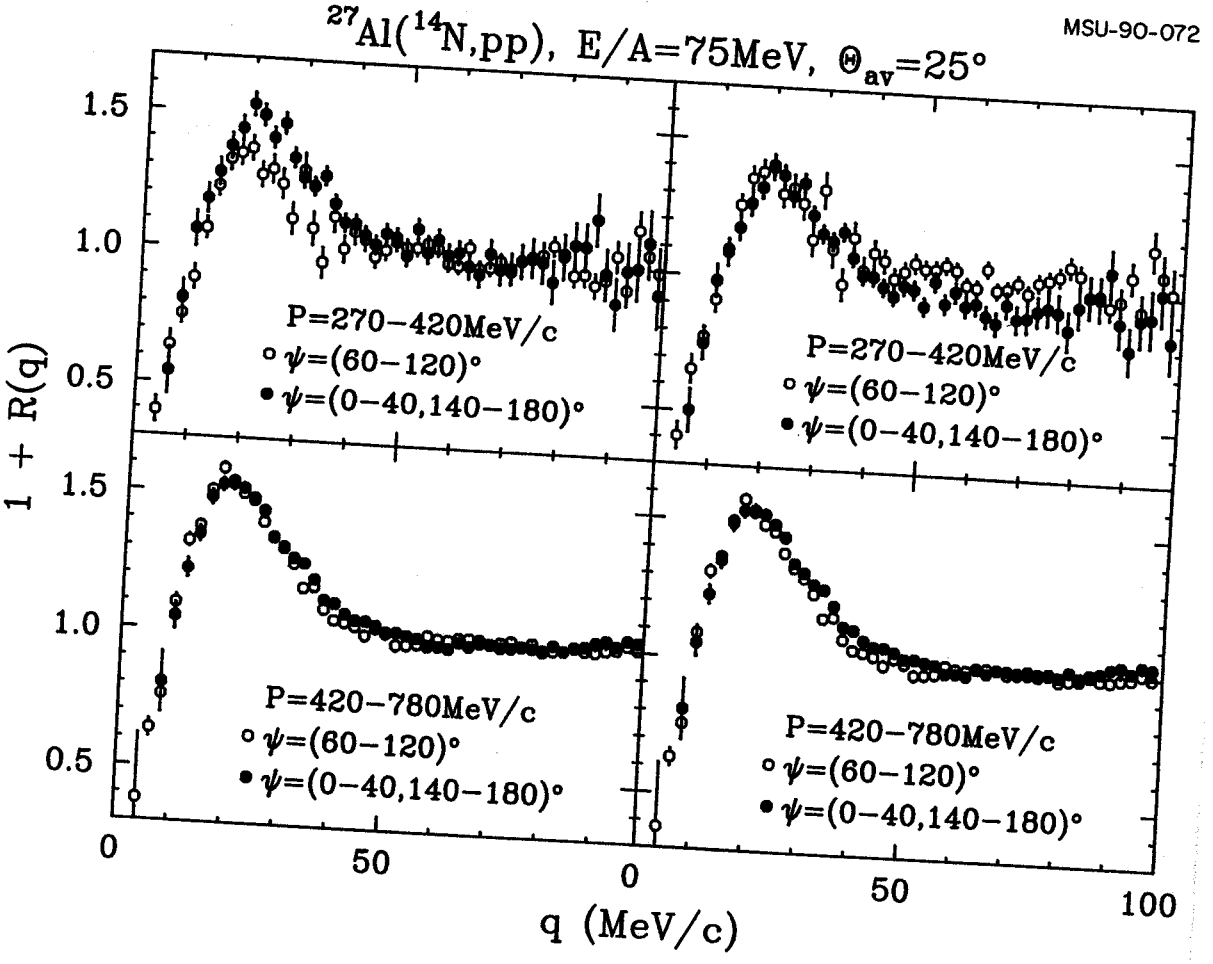

Figure 9.8 : Longitudinal (Ψ=0°-40° or Ψ=140°-180°) and transverse (Ψ=60°-120°) two-proton correlation functions measured for the ^{14}N+^{27}Al reaction at E/A=75 MeV. In the left hand panels, longitudinal and transverse correlation functions were normalized independently; in the right hand panels, the normalizations were determined from the Ψ-integrated data.

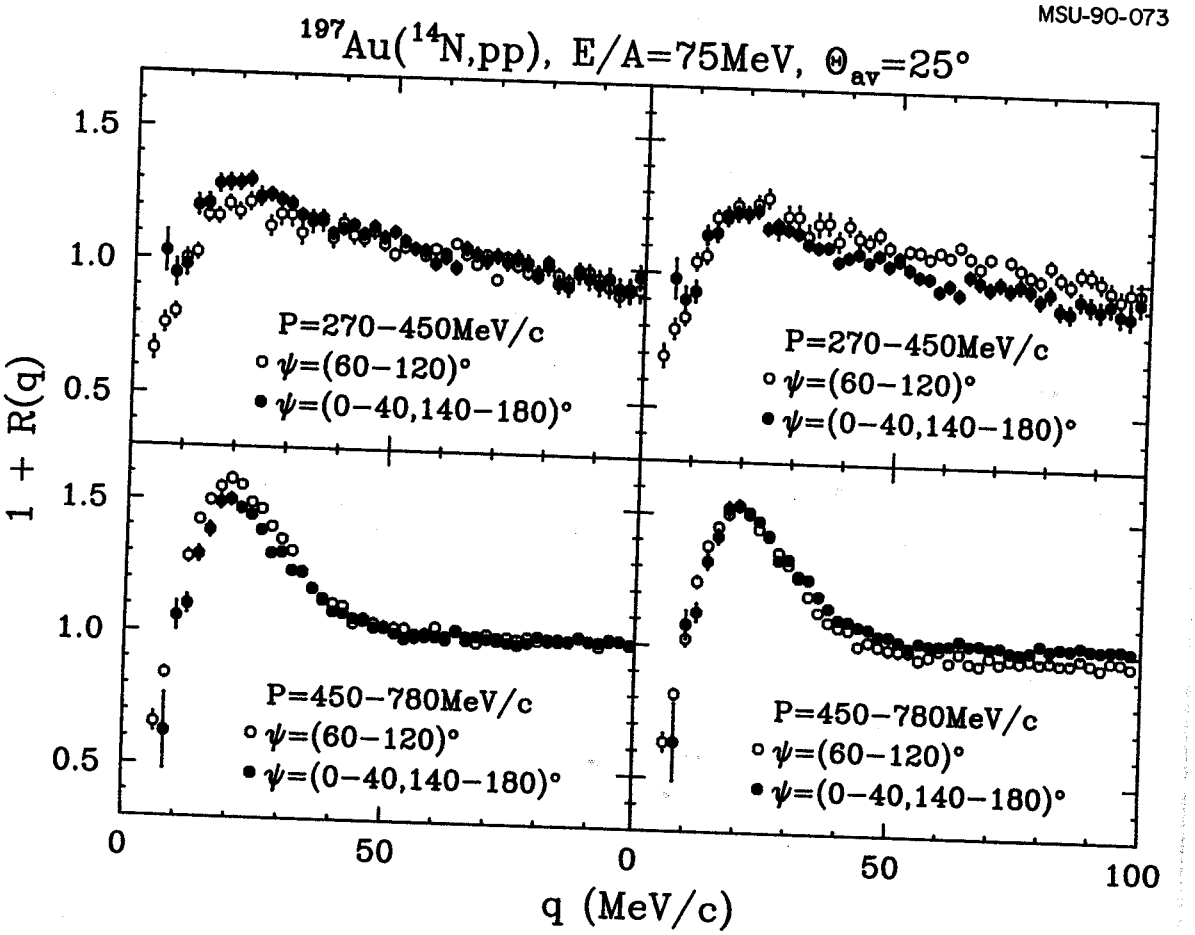

Figure 9.9 : Longitudinal (Ψ=0°-40° or Ψ=140°-180°) and transverse (Ψ=60°-120°) two-proton correlation functions measured for the $^{14}N+^{197}Au$ reaction at E/A=75 MeV. In the left hand panels, longitudinal and transverse correlation functions were normalized independently; in the right hand panels, the normalizations were determined from the Ψ-integrated data.

for which the same (angle independent) normalization convention had been adopted.

We have checked by Monte-Carlo calculations that the different asymptotic values assumed by longitudinal and transverse correlation functions are not due to trivial effects of detector acceptance or resolution. These differences cannot be understood in terms of the present model for intensity interferometry. They might, however, be related to dynamical correlations caused by impact parameter averaging effects when the single-particle distributions exhibit significant azimuthal asymmetries. It is possible that some dynamical correlations are caused by impact-parameter averaging (see Section 9.2). However, we feel that the present BUU calculations may not model such effects to a sufficient degree of accuracy since the theory does not reproduce the low-energy portion of the energy spectrum (see Figure 5.4). One should, therefore, not expect to reproduce dynamical correlations at the required level of accuracy of a few percent.

The left hand panels in Figures 9.8 and 9.9 show longitudinal and transverse correlation functions normalized independently over the relative-momentum interval, Δq = 60-100 MeV/c, by separately enforcing the conditions,

$$\int_{\Delta q} dq\ R_{L,T}(q) = 0\,, \tag{9.22}$$

for the longitudinal and transverse correlation functions $R_L(q)$ and $R_T(q)$. With this renormalization, the longitudinal correlation functions gated by the low total momentum cuts (P = 270-420 and 270-450 MeV/c, top left-hand panels of Figures 9.8 and 9.9) exhibit larger maxima than the transverse correlation functions, qualitatively consistent with an elongated source or a source of finite lifetime. For the $^{14}N + ^{27}Al$ reaction, this difference disappears for higher total momenta (P = 420-780 MeV/c, bottom left-hand panel of Figure 9.8). For the $^{14}N + ^{197}Au$ reaction, the transverse correlation function for the higher momentum gate (P =

450-780 MeV/c, bottom left-hand panel of Figure 9.9) exhibits a larger maximum than the longitudinal correlation function, consistent with an oblate source.

We should caution, that independent normalizations of longitudinal and transverse correlation functions cannot be justified a priori. Therefore, the correlation functions shown in the left hand panels of Figures 9.8 and 9.9 should not be misconstrued as experimental evidence for deformed source shapes. The different normalizations adopted for the construction of the correlation functions shown in the right and left hand panels of the two figures are only used to illustrate the uncertainties within which differences and similarities between longitudinal and transverse correlations are established experimentally.

Figure 9.10 shows theoretical predictions for longitudinal and transverse correlation functions for the $^{14}N + ^{27}Al$ and $^{14}N + ^{197}Au$ reactions. These calculations employed the same cuts on P and Ψ which were used in the data analysis. Differences predicted for longitudinal and transverse correlation functions are small. They are of the order of the statistical uncertainty of our measurements, but considerably smaller than the systematic normalization uncertainties illustrated in Figures 9.8 and 9.9.

In order to present the detailed sensitivities to various cuts on P and Ψ, Figure 9.11 shows longitudinal and transverse correlation functions predicted by BUU calculations . We have adopted the angular cuts, $\Psi_l = 0°\text{-}40°$ and $\Psi_t = 60°\text{-}90°$, for the calculation of longitudinal and transverse correlation functions, respectively. For the transverse correlation functions, we define the in-plane and out-of-plane directions by constraints on the azimuthal angle, ϕ, of the relative momentum vector, $\vec{q}$, in a coordinate system with z-axis parallel to the total momentum vector, $\vec{P}$, of the proton pair. Defining $\phi=0°$ as the plane spanned

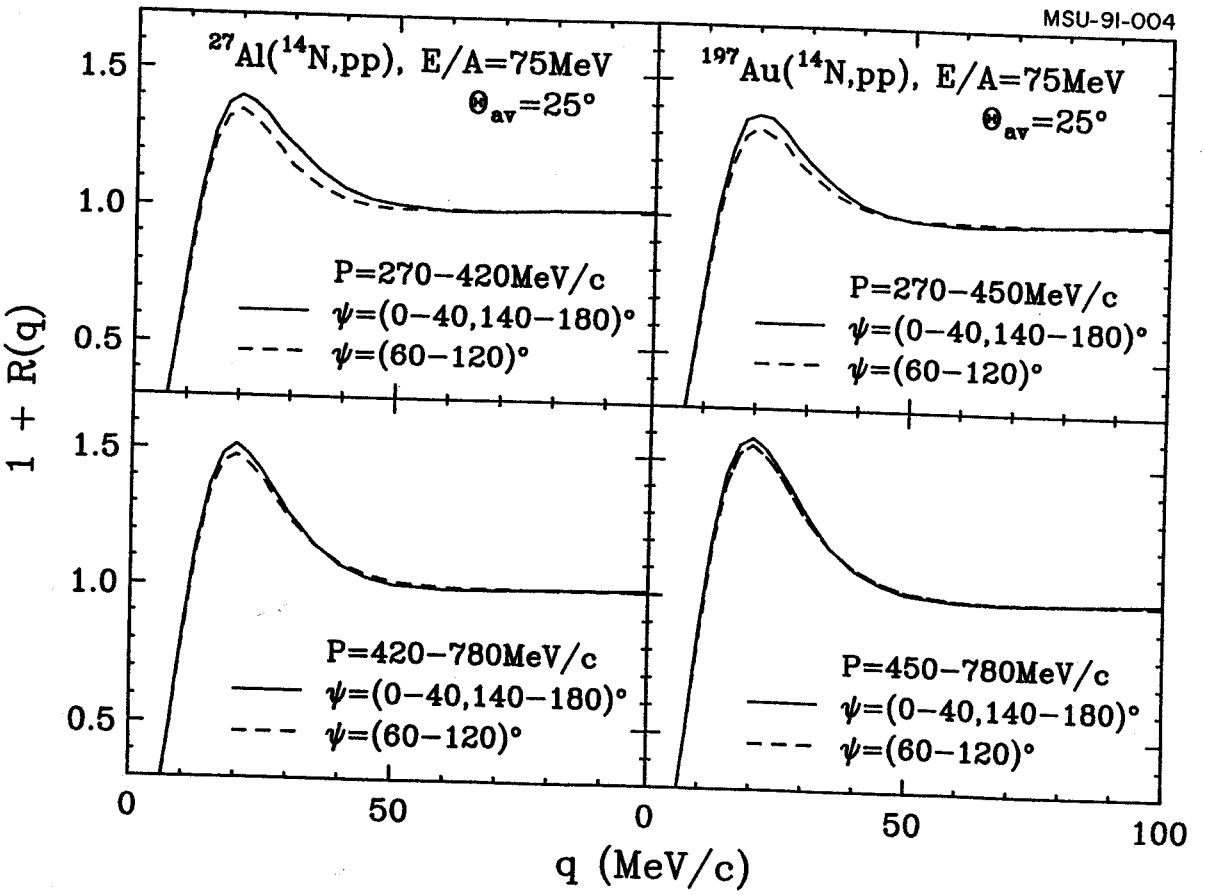

Figure 9.10: Longitudinal (Ψ=0°-40° or Ψ=140°-180°) and transverse (Ψ=60°-120°) two-proton correlation functions predicted by BUU calculations. The left and right hand panels show calculations for the reactions ^{14}N+^{27}Al and ^{14}N+^{197}Au, respectively. The momentum cuts are indicated in the individual panels.

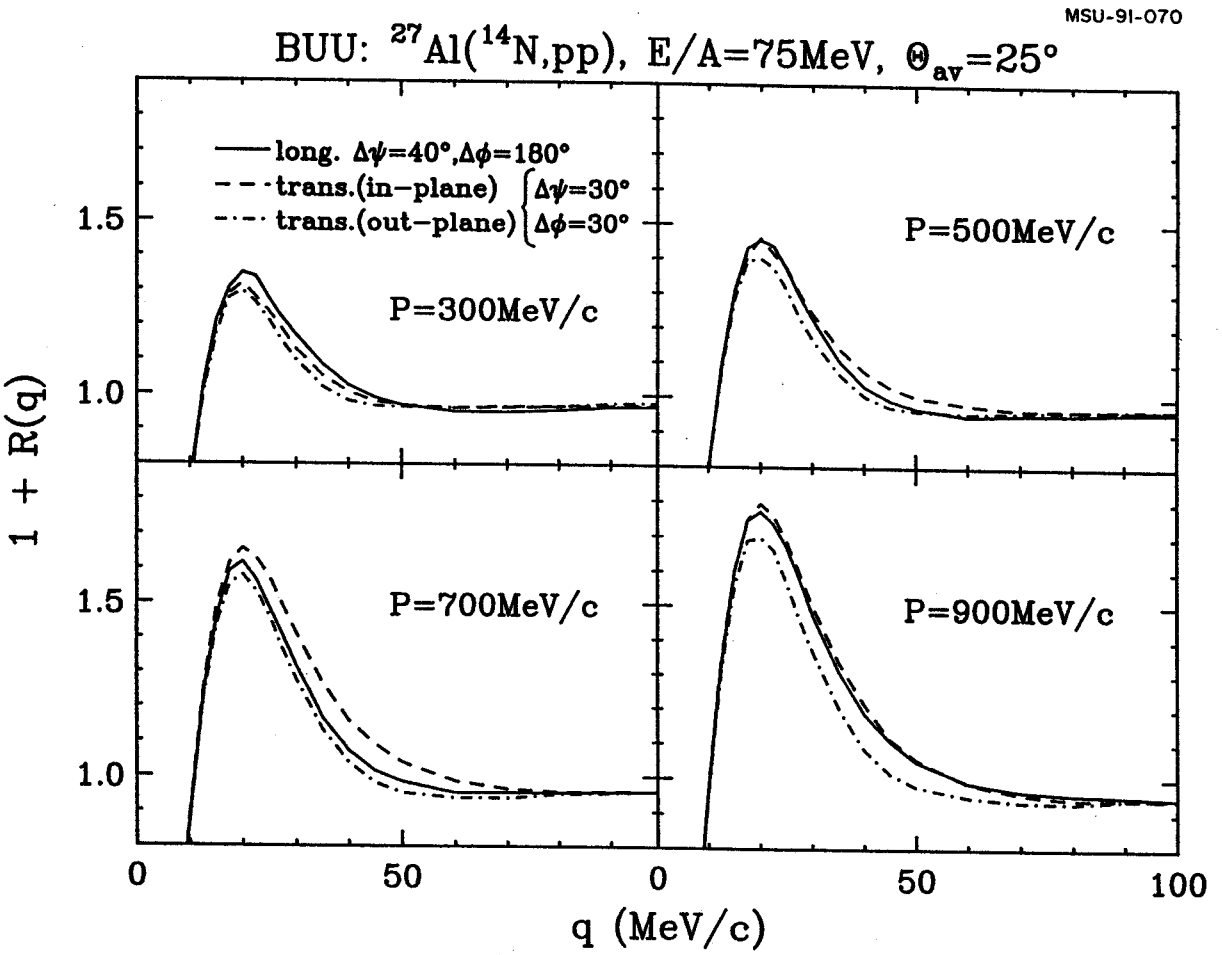

Figure 9.11: Longitudinal, and transverse correlation functions predicted by BUU calculations for ^{14}N+^{27}Al collisions at E/A=75 MeV for proton pairs for the indicated total momenta, P.

by the beam direction and $\vec{P}$, the in-plane transverse correlation function corresponds to the cut $|\phi - n\pi| \leq 30°$ (n=0,1,2); the out-of-plane transverse correlation function corresponds to the cut $|\phi - (2n+1)\pi/2| \leq 30°$ (n=0,1). Different panels of the figure show the results for the indicated cuts on the total momenta of the proton pairs. In general, the out-of-plane transverse correlation functions are smaller than the in-plane transverse correlation functions since they are less affected by finite lifetime effects and collective velocity components. At low momenta, the longitudinal correlation function is more pronounced than the transverse correlation functions, possibly due to slow emission times; at higher momenta, longitudinal and in-plane transverse correlation functions are comparable in magnitude.

Overall, correlation functions are insensitive to various cuts on angles. Without an accurate understanding of the distortions caused by dynamical correlations it appears futile to extract information on the shape of the phase - space distributions of emitted protons from differences between longitudinal and transverse correlation functions.

9.6 Dependence on the Nuclear Equation of State and in-Medium Nucleon-Nucleon Cross Section

The two major ingredients entering into Equation (9.12) are the mean field potential, $U(\vec{r})$, and the nucleon-nucleon cross section, $d\sigma/d\Omega$. In principle, one should be able to derive both from a fundamental nucleon-nucleon interaction, as has been done in some G-matrix calculations. In this paper, however, we proceed differently and use the conventional density-dependent Skyrme-type parametrization,

$$U(\rho) = A(\rho/\rho_0) + B(\rho/\rho_0)^{\sigma}, \tag{9.23}$$

where the parameters A and B are determined by the nuclear matter binding energy and the saturation density of nuclear matter at $\rho=\rho_0$ ($0.17fm^{-3}$). A choice of $\sigma=2$ results in A=-124 MeV and B=70.5 MeV and a nuclear compressibility of K = 380 MeV. This set of parameters is referred to as the "stiff" equation of state. The "soft" equation of state, with K=200 MeV, corresponds to the parameter set, $\sigma=7/6$, A=-356 MeV, and B=303 MeV. The simple parametrization, Equation (9.23), is only chosen to investigate the possible sensitivity of our calculations to the value of the nuclear compressibility.

We approximate the in-medium nucleon-nucleon cross section, $d\sigma/d\Omega$, by the energy-dependent free nucleon-nucleon cross section, $d\sigma_{NN}/d\Omega$, parametrized from experimental data. Since the exact value of the in-medium nucleon- nucleon cross section has attracted some recent attention, we also vary this input by multiplying the experimental $d\sigma_{NN}/d\Omega$ by different factors ranging from 0 to 1.

For our numerical example, we calculate two-proton correlation functions for protons emitted at the laboratory angles $\theta_{lab} \approx 25° \pm 9°$ for $^{14}N + ^{27}Al$ collisions at E/A = 75 MeV. Unless stated differently, we will use the stiff equation of state and in-medium cross sections equal to the experimental free nucleon-nucleon cross sections.

Figure 9.12 shows correlation functions calculated from the Wigner functions predicted by the BUU equation using various assumptions on the in-medium nucleon-nucleon cross section and the stiffness of the equation of state. Individual panels of the figure show correlation functions calculated for different values of the total laboratory momenta, P, of the proton pairs.

The solid and dotted curves show correlation functions predicted for the stiff and soft equations of state, using $d\sigma/d\Omega = d\sigma_{NN}/d\Omega$. These two calculations are very similar, indicating little sensitivity of the two-proton correlation functions to the stiffness of the equation of state. The lack of sensitivity of the present calculations to the stiffness of the equation of state may be due to the small size of

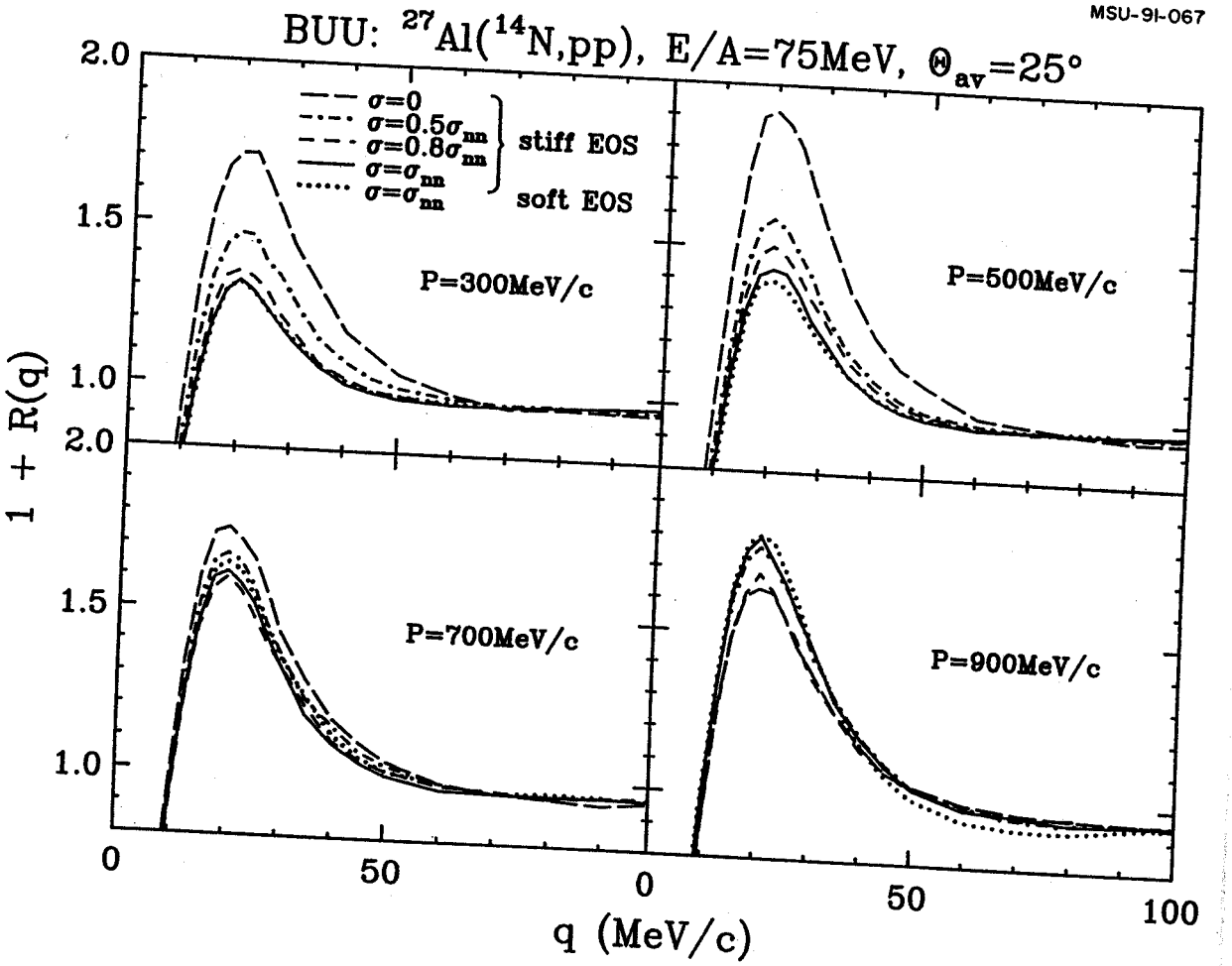

Figure 9.12: Sensitivity of two-proton correlation functions to the nuclear equation of state (EOS) and the in-medium nucleon-nucleon cross section. Different panels show results calculated for different total momenta, P, of the proton pairs.

projectile and target and the relatively moderate bombarding energy. One can try to explore it at higher energy for heavier system.

The solid, dashed, dot-dashed, and dot-dot-dashed curves represent calculations with the stiff equation of state performed with the assumption that the in-medium nucleon-nucleon cross-section is equal to 1.0, 0.8, 0.5, and 0.0 times the free nucleon-nucleon cross section. For $P \lesssim 700$ MeV/c, the predicted correlation functions become more pronounced for decreasing values of $d\sigma/d\Omega$ indicating that increased nucleon-nucleon sacttering leads to slower emission time scales and the space-time characteristics of the emitting system is more sensitive to the magnitude of the in-medium nucleon-nucleon cross section than to the stiffness of the equation of state.

To see how strongly the sensitivity to in-medium nucleon-nucleon cross section is constrainted by our measurement, we have compared data to calculations assuming one-half of the free nucleon-nucleon cross sections (see dotted curves in Figure 9.13) as the in-medium nucleon-nucleon cross sections. For the low and intermediate momentum gates, the calculated correlation functions exhibit enhanced maxima when the in-medium nucleon-nucleon cross sections are reduced. For the high momentum gate, the sensitivity is lost. The agreement with the data is significantly worse for the calculations using the reduced in-medium nucleon-nucleon cross sections.

For the $^{14}N + ^{197}Au$ reaction, dependences on the stiffness of the equation of state and the magnitude of the in-medium nucleon-nucleon cross sections were not explored because calculations for this heavier system would have required large additional amounts of computer time.

Future work should also study the effects of a momentum-dependent mean field [Gale 87, Aich 87, Welk 88, Grei 90]. Such effects are expected to be important at higher beam energies ($E/A \approx 1$ GeV). At these energies, it has been shown [Grei 90] that the effects of the momentum-dependence of the mean field on the

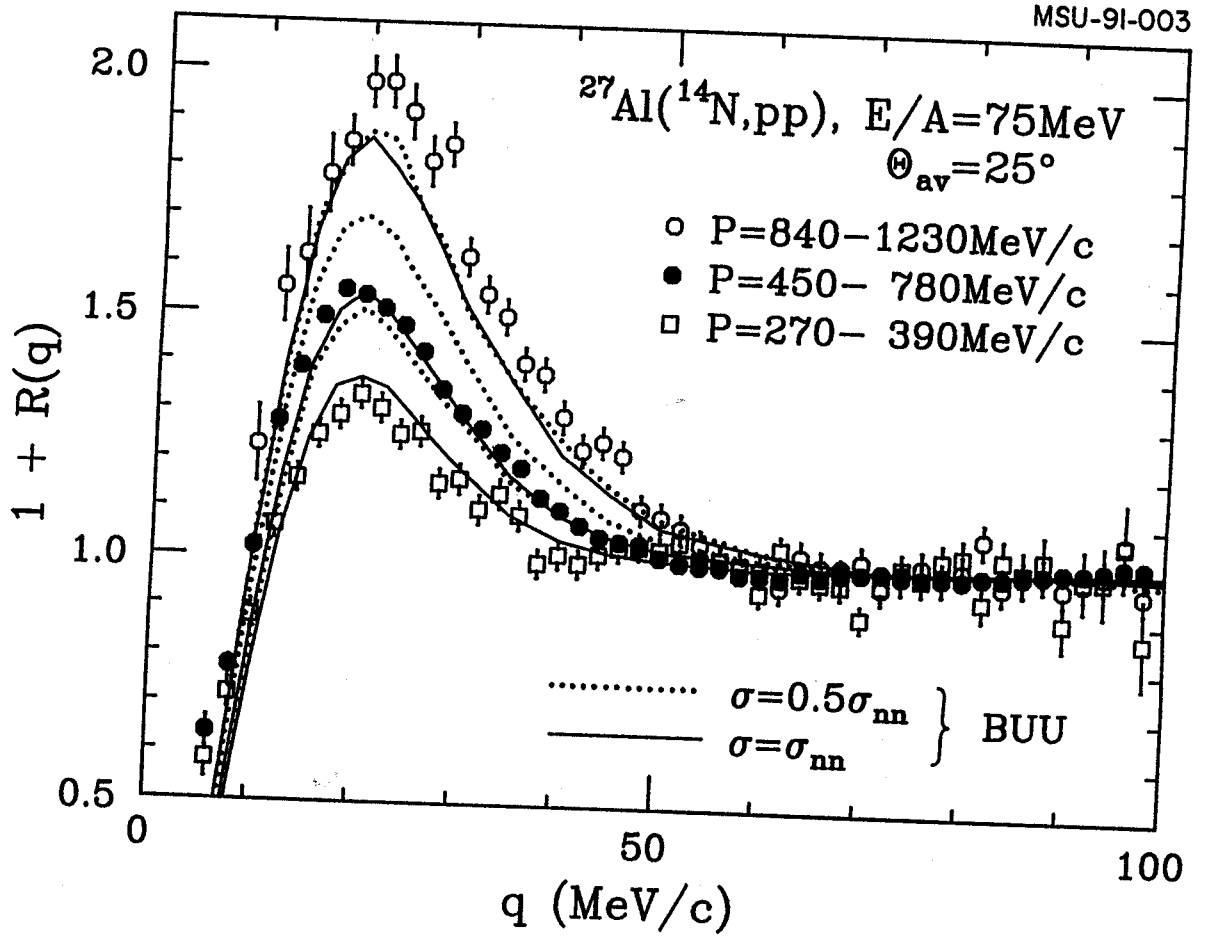

Figure 9.13: Two-proton correlation functions, measured for the reaction ^{14}N+^{27}Al at E/A=75 MeV, are compared with correlation functions predicted with the BUU theory assuming two different values of the in-medium nucleon-nucleon cross section. The total mometum gates are indicated.

collective nuclear matter flow can be approximated by a momentum-independent mean field with a suitably changed compressibility. The same effect has been found at intermediate beam energies (E/A = 50-150 MeV) where it was found that the disappearance of nuclear collective flow could be reproduced by using a momentum-dependent mean field with a compressibility of 210 MeV [Krof 89] or, alternatively, a momentum-independent mean field with a slighly higher compressibility of 240 MeV [Ogil 90]. The investigations of Reference [Ogil 90] corroborate our present finding that fast particle emission in intermediate energy nucleus-nucleus collisions (E/A $\approx$ 50-150 MeV) depends sensitively on the magnitude of the in-medium nucleon-nucleon cross sections, but only very little on the nuclear compressibility.

9.7 Dependence on Impact Parameter

Details of the Wigner function must depend on the impact parameter of the collision. The predicted dependence is illustrated in Figure 9.14; the various cuts on the total momentum of the proton pairs are indicated for the individual panels of the figure. In order to summarize the predicted trends, Figure 9.15 shows the heights of the maxima of the calculated correlation functions as a function of P for different ranges of impact parameters. For orientation, the equivalent Gaussian source radii are labeled on the right side of the figure.

For small impact parameters, b=0.5-2.5 fm, the predicted correlation functions increase in magnitude as a function of increasing total momentum of the emitted protons, consistent with shorter time scales for the emission of more energetic protons.

For peripheral collisions, b=5-7 fm, the calculated correlation functions are weakest for proton pairs with very high, P$\approx$800 MeV/c, or very low momenta, P$\lesssim$300 MeV/c; they are largest at intermediate momenta, P$\approx$500 MeV. This correlation pattern may be understood in terms of emission from fairly well defined projectile and target-like sources. Proton pairs of low and high momenta

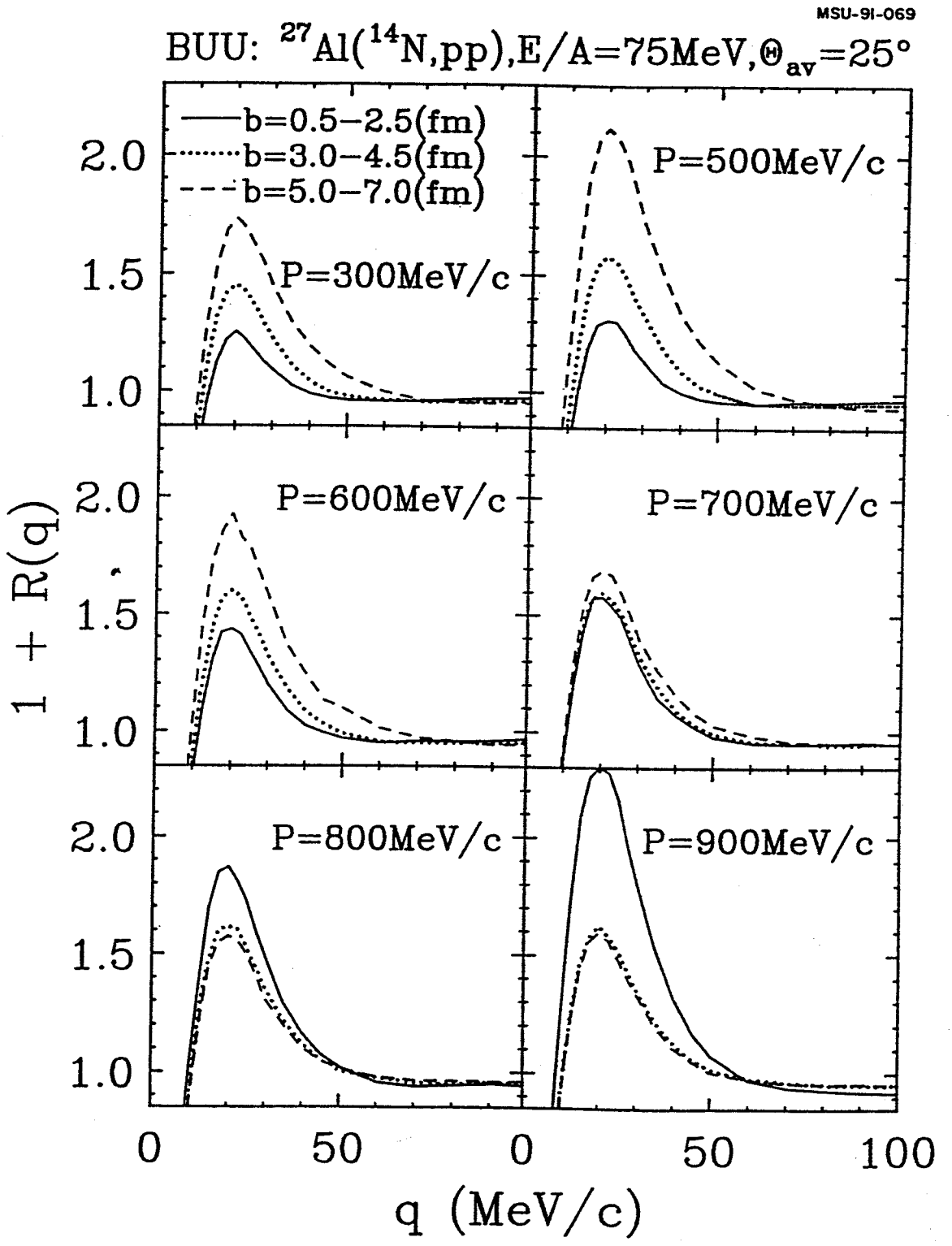

Figure 9.14: Two-proton correlation functions predicted by BUU calculations for ^{14}N+^{27}Al collisions at E/A=75 MeV for the indicated impact parameters and total momenta of the emitted proton pairs.

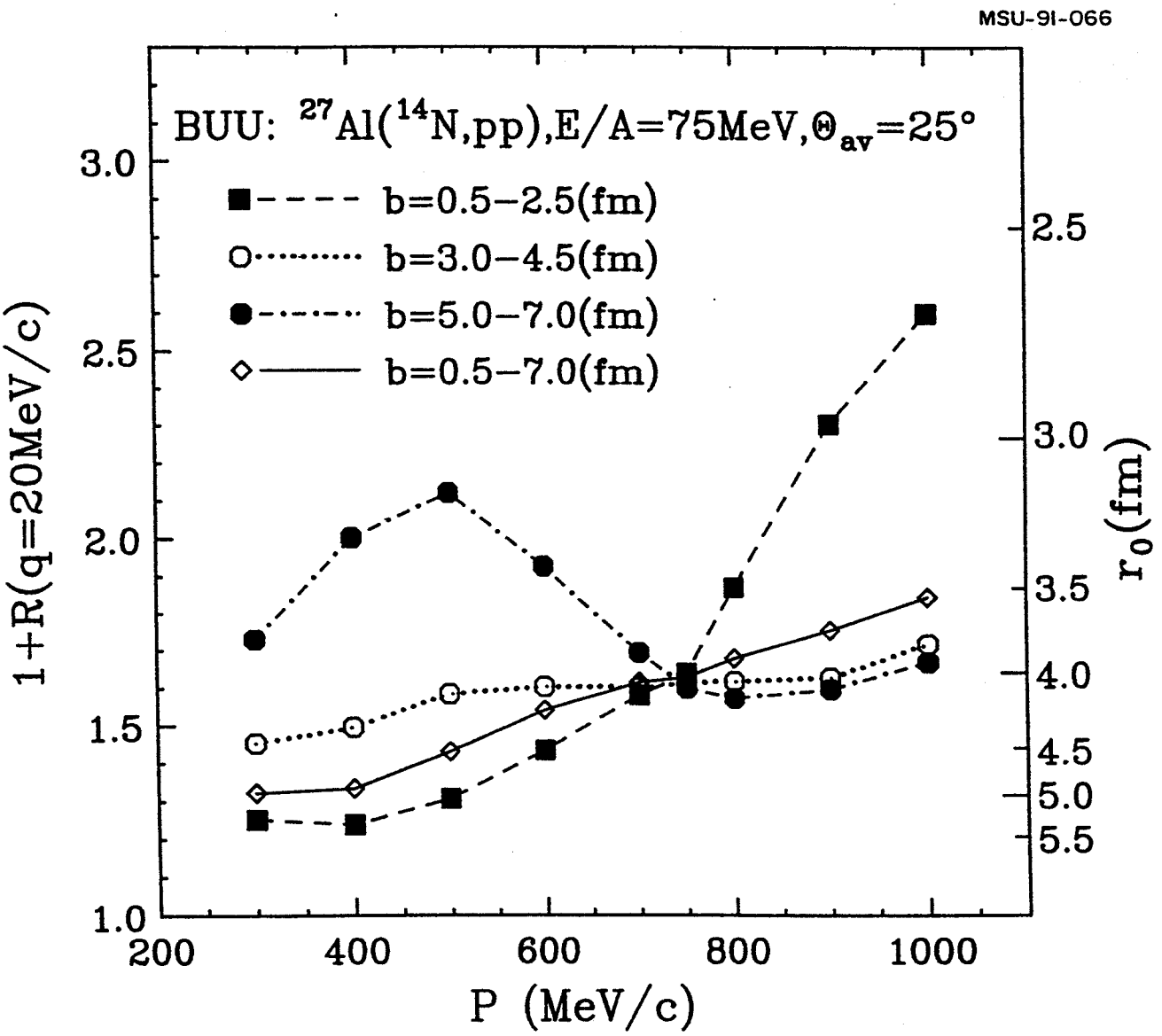

Figure 9.15: Momentum dependence of the heights of the maxima of two-proton correlation functions predicted by BUU calculations for ^{14}N+^{27}Al collisions at different impact parameters. Lines connect points corresponding to a given impact parameter to guide the eye.

correspond to low-energy emissions in the rest frames of target and projectile-like sources, respectively. More energetic emissions from these sources are selected by intermediate momenta. For these emissions the correlation functions are expected to be enhanced because of the reduced size of the participant zone and/or because of shorter emission time scales. However, nucleon-nucleon collisions appear to play only a minor role since the the maximum of the correlation function at P≈500 MeV/c remains when the in-medium nucleon-nucleon cross section is set to zero.

For intermediate impact parameters, b≈3-4.5 fm, the predicted momentum dependence is weak, most likely because of overlapping contributions from participant and spectator regions.

For total momenta, $P \lesssim 700$ MeV/c, more pronounced correlations are observed for peripheral than for central collisions - in accordance with a simple geometric interpretation of the size of the reaction zone. However, for protons emitted with velocities higher than the beam velocity, $P > 2p_{beam} \approx 760$ MeV/c, the maxima of the predicted correlation functions are larger for central than for peripheral collisions. Apparently, high energy protons from central collisions are emitted on a very fast time scale. It may be speculated that such fast emission processes are related to Fermi-jets [Bond 80], i.e. nucleons accelerated by the action of the mean field and emitted without significant nucleon-nucleon collisions. However, because of the semi-classical nucleonic momentum distribution used in our calculations, the predicted correlations may not be reliable for the highest momenta, P>1000 MeV/c, and should be viewed with caution. In any case, the calculations clearly indicate that one should be able to extract a wealth of information about the space-time evolution of the reaction zone by detailed investigations of the momentum and impact parameter dependence of two-proton correlation functions. Previous measurements of two-particle correlation functions did not determine the simultaneous dependence on impact parameter and momentum of the emitted particle pair and thus averaged over valuable

information. New measurements capable of determining such dependences are clearly desirable. The experimental effort to explore these effects is currently getting under way.

In summary, the measurement of two-proton correlation functions have provided a new sensitive observable to test the space-time geometries of nuclear collisions. With the technique of two-proton intensity interferometry, one can hope to gain more insight into nuclear reaction dynamics.

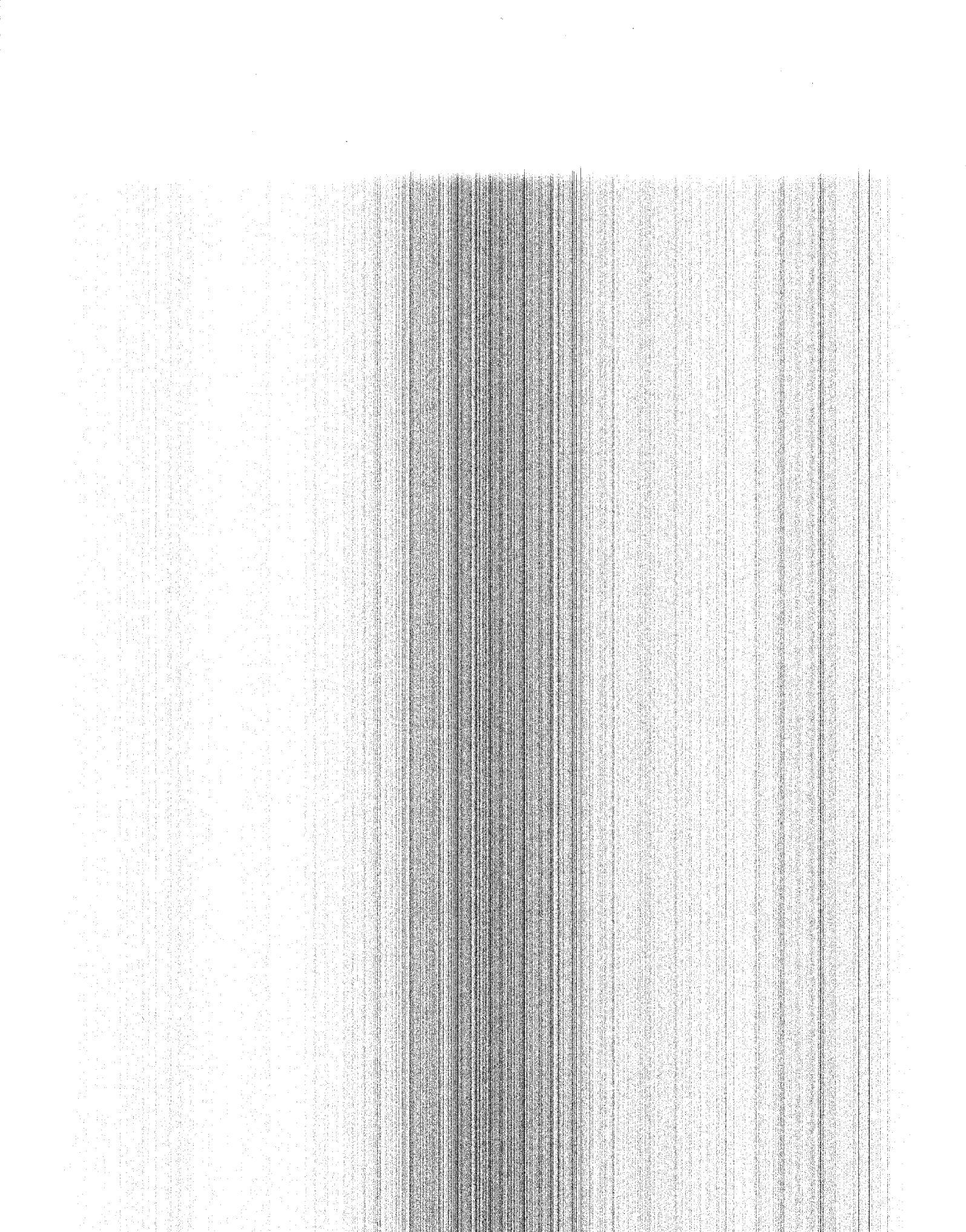

CHAPTER 10. SUMMARY AND CONCLUSIONS

Heavy-ion collisions at intermediate energy provide an unique opportunity to study the nuclear collision dynamics and thermodynamical properties of highly excited nuclei. In this thesis, we have used the technique of two-proton intensity interferometry to probe the space-time evolution of nuclear collisions.

Considerable efforts were made to develop CsI(Tl) detectors read out by PIN diodes. The detector resolution is limited by local non-uniformities of the CsI(Tl) scintillator. After selecting CsI(Tl) scintillators of good uniformity based upon a γ-ray scanning technique, we built a 56 element multi-detector array using Si ΔE-detectors and CsI(Tl) E-detectors. The detectors show high gain stability and good energy resolution for the detection of light charged particles.

We have measured two-proton correlation functions for emission processes governed by different emission time scales. Slow evaporative processes were studied at E/A = 31 MeV for the near-symmetric reaction $^{129}Xe + ^{122}Sn$ and for the "inverse kinematics" reaction $^{129}Xe + ^{27}Al$. Fast non-equilibrium processes were investigated, in "forward kinematics", for ^{14}N induced reactions on ^{27}Al and ^{197}Au at E/A = 75 MeV. Two-proton correlation functions measured for these qualitatively different reaction mechanisms exhibit significant differences in shape. These differences are well understood in terms of the different emission time scales governing equilibrium and non-equilibrium processes.

We have used the Wigner-function formalism which allows the calculation of two-proton correlation functions for any reaction model capable of predicting the one-body phase-space distribution of the emitted particles. We demonstrated the sensitivity of two-proton correlation functions to the space-time geometry of the emitting system via calculations for schematic emission sources. Results obtained with the Wigner-function formalism were compared with classical trajectory calculations for long-lived evaporative sources.

Two-proton correlation functions measured for evaporative processes in ^{129}Xe induced reactions at E/A = 31 MeV do not exhibit maxima at q ≈ 20 MeV/c, but only minima at q ≈ 0 MeV/c. Particle emission from equilibrated compound nuclei typically proceeds on such long time scales that anti-symmetrization and nuclear interaction between the two emitted particles play a relatively minor role. The correlation functions are dominated by final state Coulomb interactions. The measured correlation functions can be rather well understood by applying the Wigner-function formalism to one-body phase-space distributions predicted by statistical model calculations based on the Weisskopf formula. For these reactions, rather small emission rates lead to large spatial separations between emitted particles and a loss of memory of the size of the emitting nucleus. The predicted correlation functions exhibit only moderate sensitivity to detailed properties of the decaying nucleus.

Two-proton correlation functions measured for non-equilibrium emission in ^{14}N induced reactions at E/A = 75 MeV exhibit pronounced maxima at relative momenta q ≈ 20 MeV/c and minima at q ≈ 0 MeV/c. The maximum at q ≈ 20 MeV/c is caused by the attractive singlet S-wave interaction between the two emitted protons. The minimum at q≈0 MeV/c reflects the combined effects of the Coulomb repulsion and the exclusion due to Pauli principle. For these reactions, the emission time scales are sufficiently short that the final phase-space distributions of the emitted particles are of nuclear or smaller dimensions. Once

emission times are of the order of a few hundred fm/c or less, anti-symmetrization effects, nuclear and Coulomb interactions must all be incorporated into the calculations. The measured correlation functions can be rather well understood by applying the Wigner function formalism to one-body phase-space distributions predicted by the Boltzmann-Uehling-Uhlenbeck transport equation. It is particularly gratifying that the theory can reproduce the observed strong dependence of the experimental correlation functions on the total momentum of the coincident proton pairs.

For all cases investigated, longitudinal and transverse correlation functions were found to be very similar. Our data could not provide definitive evidence for elongated source shapes expected from simple lifetime arguments. The experimental observations are, however, consistent with more detailed calculations for which the predicted differences between longitudinal and transverse correlation functions were too small to be detected by the present experiment.

The calculated two-proton correlation functions predicted by the BUU model for the reaction $^{14}N + ^{27}Al$ at E/A = 75MeV exhibit significant sensitivity to details of the space-time evolution of the reaction zone. They indicate large sensitivity to the magnitude of the in-medium nucleon-nucleon cross sections used in the BUU calculations. Considerable sensitivity is predicted for measurements which explore the dependence of the two-proton correlation function on the collision impact parameter and on the total momenta of the emitted proton pairs. However, there is very little sensitivity to the compressibility of nuclear matter.

Exclusive measurements of two-proton correlation functions with selection on impact parameters can be pursued by combining the 56-element hodoscope with the 4π detector array. Better characterization of the collision geometry will enable us to make more stringent tests on the dynamical models for heavy-ion

collisions. It is desirable to extend future studies of two-proton intensity interferometry to higher beam energies (E/A $\approx$ 1 GeV) and to heavier projectile-target combinations. Such studies may provide additional insight into the collision dynamics and compressibility of nuclear matter, which could not be gained in an unambiguous fashion from observables tested so far.

LIST OF REFERENCES

LIST OF REFERENCES

[Aich 85] J. Aichelin and G. Bertsch, Phys. Rev. C31, 1730 (1985).

[Aich 87] J. Aichelin, A. Rosenhauer, G. Peilert, H. Stöcker, and W. Greiner, Phys. Rev. Lett. 58, 1926 (1987).

[Alar 86] J. Alarja, A. Dauchy, A. Giorni, C. Morand, E. Pollaco, P. Stassi, B. Billerey, B. Chambon, B. Cheynis, D. Drain, and C. Pastor, Nucl. Instr. and Meth. A242, 352 (1986).

[Ardo 89] D. Ardouin, F. Guilbault, C. Lebrun, D. Ardouin, S. Pratt, P. Lautridou, R. Boisgard, J. Québert, and A. Péghaire, University of Nantes, Internal Report LPN-89-02.

[Ardo 90] D. Ardouin, Z. Basrak, P. Schuck, A. Péghaire, F. Saint-Laurent, H. Delagrange, H. Doubre, C. Grégoire, A. Kyanowski, W. Mittig, J. Péter, Y.P. Viyogi, J. Québert, C.K. Gelbke, W.G. Lynch, M. Maier, J. Pochodzalla, G. Bizard, F. Lefèbvres, B. Tamain, B. Remaud, and F. Sébille, Nucl. Phys. A514, 564 (1990).

[Awes 88] T.C. Awes, R.L. Ferguson, F.E. Obenshain, F. Plasil, G.R. Young, S. Pratt, Z. Chen, C.K. Gelbke, W.G. Lynch, J. Pochodzalla, and H.M. Xu, Phys. Rev. Lett. 61, 2665 (1988).

[Bart 86] J. Bartke, Phys. Lett. B174, 32 (1986).

[Baue 87] W. Bauer, Nucl. Phys. A471, 604 (1987).

[Baue 88] W. Bauer, G.D. Westfall, D. Fox, and D. Cebra, Phys. Rev. C37, 664 (1988).

[Baue 90] W. Bauer, Michigan State University Report No. MSUCL-699, 1990 (unpublished), for an account of the numerical detailes.

[Bert 84] G.F. Bertsch, H. Kruse, and S. Das Gupta, Phys. Rev. C29, 673 (1984).

[Bert 88] G.F. Bertsch and S. Das Gupta, Phys. Rep. 160, 189 (1988).

[Bert 89] G.F. Bertsch, Nucl. Phys. A498, 173c (1989).

[Bigg 61] J.A. Biggerstaff, R.L. Becker, and M.T. McEllistrem, Nucl. Instr. and Meth. 10, 327 (1961).

[Birk 64] J.B. Birks, "The Theory and Practice of Scintillation Counting", Pergamon Press, 1964.

[Birk 83] J.R. Birkelund and J.R. Huizenga, Annu. Rev. Nucl. Sci. 33, 265 (1983).

[Bluc 86] E. Blucher, B. Gittelman, B.K. Heltsley, J. Kandaswamy, R. Kowalewski, Y. Kubota, N. Mistry, S. Stone, and A. Bean, Nucl. Instr. and Meth. A249, 201 (1986).

[Boal 86a] D.H. Boal and H. DeGuise, Phys. Rev. Lett. 57, 2901 (1986).

[Boal 86b] D.H. Boal and J.C. Shillcock, Phys. Rev. C33, 549 (1986).

[Boal 90] D.H. Boal, C.K. Gelbke, and B.K. Jennings, Rev. Mod. Phys. 62, 553 (1990).

[Bond 80] J.P. Bondorf, J.N. De, G. Faì, A.O.T. Karvinen, B. Jacobsson, and J. Randrup, Nucl. Phys. A333, 285 (1980).

[Bord 90] B. Borderie, M.F. Rivet, and L. Tassan-Got, Ann. Phys. Fr. 15, 287 (1990).

[Bowm 91] D.R. Bowman, G.F. Peaslee, R.T. de Souza, N. Carlin, C.K. Gelbke, W.G. Gong, Y.D. Kim, M.A. Lisa, W.G. Lynch, L. Phair, M.B. Tsang, C. Williams, N. Colonna, K. Hanold, M.A. McMahan, G.J. Wozniak, L.G. Moretto, and W.A. Friedman, Phys. Rev. Lett. 67, 1527 (1991).

[Brow 84] B.A. Brown, C.R. Bronk, and P.E. Hodgson, J. Phys. G10, 1683 (1984).

[Burn 70] D.C. Burnham and D.L. Weinberg, Phys. Rev. Lett. 25, 84 (1970).

[Cass 88] W. Cassing, Z. Phys. A329, 471 (1988).

[Cebr 89] D.A. Cebra, W. Benenson, Y. Chen, E. Kashy, A. Pradhan, A. Vander Molen, G.D. Westfall, W.K. Wilson, D.J. Morrissey, R.S. Tickle, R. Korteling, and R.L. Helmer, Phys. Lett. B227, 336 (1989).

[Chac 91] A.D. Chacon, J.A. Bistirlich, R.R. Bossingham, H. Bossy, H.R. Bowman, C.W. Clawson, K.M. Crowe, T.J. Humanic, M. Justice, P. Kammel, J.M. Kurck, S. Ljung-felt, C.A. Meyer, C. Petitjean, J.O. Rasmussen, M.A. Stoyer, O. Hashimoto, W.C. McHarris, J.P. Sullivan, K.L. Wolf, W.A. Zajc, Phys. Rev. C43, 2670 (1991).

[Chen 87a] Z. Chen, C.K. Gelbke, J. Pochodzalla, C.B. Chitwood, D.J. Fields, W.G. Lynch and M.B. Tsang, Phys. Lett. B186, 280 (1987).

[Chen 87b] Z. Chen, C.K. Gelbke, W.G. Gong, Y.D. Kim, W.G. Lynch, M.R. Maier, J. Pochodzalla, M.B. Tsang, F. Saint-Laurent, D. Ardouin, H. Delagrange, H. Doubre, J. Kasagi, A. Kyanowski, A. Péghaire, J. Peter, E. Rosato, G. Bizard, F. Lefèbvres, B. Tamain, J. Québert, and Y.P. Viyogi, Phys. Rev. C36, 2297 (1987).

[Chen 88] Z. Chen, Ph.D. thesis, Michigan State University, 1988.

[Chit 85] C.B. Chitwood, J. Aichelin, D.H. Boal, G. Bertsch, D.J. Fields, C.K. Gelbke, W.G. Lynch, M.B. Tsang, J.C. Shillcock, T.C. Awes, R.L. Ferguson, F.E. Obenshain, F. Plasil, R.L. Robinson, and G.R. Young, Phys. Rev. Lett. 54, 302 (1985).

[Chit 86a] C.B. Chitwood, C.K. Gelbke, J. Pochodzalla, Z. Chen, D.J. Fields, W.G. Lynch, R. Morse, M.B. Tsang, D.H. Boal, and J.C. Shillcock, Phys. Lett. 172B, 27 (1986).

[Chit 86b] C.B. Chitwood, D.J. Fields, C.K. Gelbke, D.R. Klesch, W.G.Lynch, M.B. Tsang, T.C. Awes, R.L. Ferguson, F.E. Obenshain, F. Plasil, R.L. Robinson, and G.R. Young, Phys. Rev. C34, 858 (1986).

[Cocc 74] G. Cocconi, Phys. Lett. 49B, 459 (1974).

[Cser 86] L.P. Csernai and J. Kapusta, Phys. Rep. 131, 223 (1986).

[DasG 81] S. Das Gupta and A.Z. Mekjian, Phys. Rep. 72, 131 (1981).

[DeSo 91] R.T. de Souza, L. Phair, D.R. Bowman, N. Carlin, C.K. Gelbke, W.G. Gong, Y.D. Kim, M.A. Lisa, W.G. Lynch, G.F. Peaslee, M.B. Tsang, H.M. Xu, F. Zhu, and W.A. Friedman, Phys. Lett. B, (1991) (in press).

[DeYo 89] P.A. DeYoung, M.S. Gordon, Xiu qin Lu, R.L. McGrath, J.M. Alexander, D.M. de Castro Rizzo, and L.C. Vaz, Phys. Rev. C39, 128 (1989).

[DeYo 90] P.A. DeYoung, C.J. Gelderloos, D. Kortering, J. Sarafa, K. Vienert, M.S. Gordon, B.J. Fineman, G.P. Gilfoyle, X. Lu, R.L. McGrath, D.M. de Castro Rizzo, J.M. Alexander, G. Auger, S. Kox, L.C. Vaz, C. Beck, D.J. Henderson, D.G. Kovar, and M.F. Vineyard, Phys. Rev. C41, R1885 (1990).

[Elma 91] A. Elmaani, N.N. Ajitanand, J.M. Alexander, R. Lacey, S. Kox, E. Liatard, F. Merchez, T. Motobayashi, B. Noren, C. Perrin, D. Rebreyend, Tsan Ung Chan, G. Auger, and S. Goult, Phys. Rev. C43, R2474 (1991).

[Fiel 86] D.J. Fields, W.G. Lynch, T.K. Nayak, M.B. Tsang, C.B. Chitwood, C.K. Gelbke, R. Morse, J. Wilczynski, T.C. Awes, R.L. Ferguson, F. Plasil, F.E. Obenshain, and G.R. Young, Phys. Rev. C34, 536 (1986).

[Fox 88] D. Fox, D.A. Cebra, J. Karn, C. Parks, A. Pradhan, A. Vander Molen, J. van der Plicht, G.D. Westfall, W.K. Wilson, and R.S. Tickle, Phys. Rev. C38, 146 (1988).

[Fran 89] J.D. Franson, Phys. Rev. Lett. 62, 2205 (1989).

[Frib 85] S. Friberg, C.K. Hong, and L. Mandel, Phys. Rev. Lett. 54, 2011 (1985).

[Frie 83] W.A. Friedman and W.G. Lynch, Phys. Rev. C28, 16 (1983).

[Gale 87] C. Gale, G.F. Bertsch, and S. Das Gupta, Phys. Rev. C35, 1666 (1987).

[Gelb 87] C.K. Gelbke and D.H. Boal, Prog. Part. Nucl. Phys. 19, 33 (1987).

[Gold 59] G. Goldhaber, W.B. Fowler, S. Goldhaber, T.F. Hoang, T.E. Kalogeropolous, and W.M. Powell, Phys. Rev. Lett. 3, 181 (1959).

[Gold 60] G. Goldhaber, S. Goldhaber, W. Lee, and A. Pais, Phys. Rev. 120, 300 (1960).

[Gong 88] W.G. Gong, Y.D. Kim, G. Poggi, Z. Chen, C.K. Gelbke, W.G. Lynch, M.R. Maier, T. Murakami, M.B. Tsang, H.M. Xu and K. Kwiatkowski, Nucl. Instr. and Meth. A268, 190 (1988).

[Gong 90a] W.G. Gong, N. Carlin, C.K. Gelbke, and R. Dayton, Nucl. Instr. and Meth. A287, 639 (1990).

[Gong 90b] W.G. Gong, C.K. Gelbke, N. Carlin, R.T. de Souza, Y.D. Kim, W.G. Lynch, T. Murakami, G. Poggi, D. Sanderson, M.B. Tsang, H.M. Xu, D.E. Fields, K. Kwiatkowski, R. Planeta, V.E. Viola, Jr., S.J. Yennello, and S. Pratt, Phys. Lett. B246, 21 (1990).

[Gong 90c] W.G. Gong, W. Bauer, C.K. Gelbke, N. Carlin, R.T. de Souza, Y.D. Kim, W.G. Lynch, T. Murakami, G. Poggi, D.P. Sanderson, M.B. Tsang, H.M. Xu, S. Pratt, D.E. Fields, K. Kwiatkowski, R. Planeta, V.E. Viola, Jr., and S.J. Yennello, Phys. Rev. Lett. 65, 2114 (1990).

[Gong 91a] W.G. Gong, W. Bauer, C.K. Gelbke, and S. Pratt, Phys. Rev. C43, 781 (1991)

[Gong 91b] W.G. Gong, C.K. Gelbke, W. Bauer, N. Carlin, R.T. de Souza, Y.D. Kim, W.G. Lynch, T. Murakami, G. Poggi, D.P. Sanderson, M.B. Tsang, H.M. Xu, S. Pratt, D.E. Fields, K. Kwiatkowski, R. Planeta, V.E. Viola, Jr., and S.J. Yennello, Phys. Rev. C43, 1804 (1991).

[Gong 91c] W.G. Gong, Y.D. Kim, and C.K. Gelbke, Phys. Rev. C, (1991) (in press).

[Goul 75] F.S. Goulding and B.G. Harvey, Ann. Rev. Nucl. Sci. 25, 167 (1975).

[Gras 85a] H. Grassmann, E. Lorenz, and H.-G. Moser, Nucl. Instr. and Meth. 228, 323 (1985).

[Gras 85b] H. Grassmann, H.G. Moser, H. Dietl, G. Eigen, V. Fonseca, E. Lorenz, and G. Mageras, Nucl. Instr. and Meth. 234, 122 (1985).

[Greg 86] C. Gregoire and B. Tamain, Ann. Phys. Fr. 11, 323 (1986).

[Grei 90] W. Greiner and H. Stocker, "The Nuclear Equation of State", NATO ASI Series B: Physics, Vol. 216A (1990).

[Gust 84] H.A. Gustafsson, H.H. Gutbrod, B. Kolb, H. Löhner, B. Ludewigt, A.M. Poskanzer, T. Renner, H. Riedesel, H.G. Ritter, A. Warwick, F. Weik, and H. Wieman, Phys. Rev. Lett. 53, 544 (1984).

[Gyul 79] M. Gyulassy, S.K. Kaufmann, and L.W. Wilson, Phys. Rev. C20, 2267 (1979).

[Hanb 54] R. Hanbury Brown and R.Q. Twiss, Phil. Mag. 45, 663 (1954).

[Hanb 74] R. Hanbury Brown, "The Intensity Interferometer --- its Application to Astronomy", Taylor & Francis Ltd London and Halsted Press New York, 1974

[Hari 85] P. Hariharan, "Optical Interferometry", Academic Press Australia, 1985.

[Hong 87] C.K. Hong, Z.Y. Ou, and L. Mandel, Phys. Rev. Lett. 59, 2044 (1987).

[Horn 89] M.A. Horne, A. Shimony, A. Zeilinger, Phys. Rev. Lett. 62, 2209 (1989)

[Hube 90] F. Hubert, R. Bimbot, and H. Gauvin, Atomic Data and Nuclear Data Tables 46, 1 (1990).

[Jenn 86] B.K. Jennings, D.H. Boal, and J.C. Shillcock, Phys. Rev. C33, 1303 (1986).

[Jian 89] D.X. Jiang, H. Doubre, J. Galin, D. Guerreau, E. Piasecki, J. Pouthas, A. Sokolov, B. Cramer, G. Ingold, U. Jahnke, E. Schwinn, J.L. Charvet, F. Frehaut, B. Lott, C. Magnago, M. Morjean, Y. Patin, Y. Pranal, J.L. Uzureau, B. Gatty, and D. Jacquet, Nucl. Phys. A503, 560 (1989).

[Kim 89] Y.D. Kim, M.B. Tsang, C.K. Gelbke, W.G. Lynch, N. Carlin, Z. Chen, R. Fox, W.G. Gong, T. Murakami, T. Nayak, R.M. Ronningen, H.M. Xu, F. Zhu, W. Bauer, L.G. Sobotka, D.W. Stracener, D.G. Sarantites, Z. Majka, V. Abenante, and H. Griffin, Phys. Rev. Lett. 63, 494 (1989).

[Kim 91a] Y.D. Kim, R.T. de Souza, D.R. Bowman, N. Carlin, C.K. Gelbke, W.G. Gong, W.G. Lynch, L. Phair, M.B. Tsang, F. Zhu, and S. Pratt, Phys. Rev. Lett. 67, 14 (1991).

[Kim 91b] Y.D. Kim, R.T. de Souza, C.K. Gelbke, W.G. Gong, and S. Pratt, Michigan State University Preprint MSUCL-782, 1991.

[Knol 80] J. Knoll, Nucl. Phys. A343, 511 (1980).

[Knol 89] G.F. Knoll, "Radiation Detection and Measurement", 2nd ed., John Wiley & Sons, Inc., 1989.

[Koon 77] S.E. Koonin, Phys. Lett. 70B, 43 (1977).

[Koon 89] S.E. Koonin, W. Bauer, and A. Schafer, Phys. Rev. Lett. 62, 1247 (1989).

[Kopy 72] G.I. Kopylov and M.I. Podgoretskii, Sov. J. Nucl. Phys. 15, 219 (1972).

[Kopy 74] G.I. Kopylov, Phys. Lett. 50B, 472 (1974).

[Kox 87] S. Kox, A. Gamp, C. Perrin, J. Arvieux, R. Bertholet, J.F. Bruandet, M. Buenerd, R. Cherkaoui, A.J. Colde, Y. El-Masri, N. Longequeue, J. Menet, F. Merchez, and J.B. Viano, Phys. Rev. C35, 1678 (1987)

[Kreu 87] P. Kreutz, A. Kuelmichel, C. Pinkenburg, J. Pochodzalla, Z.Y. Guo, U. Lynen, H. Sann, W. Trautmann, and R. Trockel, Nucl. Instr. and Meth. A260, 120 (1987).

[Krof 89] D. Krofcheck, W. Bauer, G.M. Crawley, C. Djalali, S. Howden, C.A. Ogilvie, A. Vander Molen, G.D. Westfall, W.K. Wilson, R.S. Tickle, and C. Gale, Phys. Rev. Lett. 63, 2028 (1989).

[Ledn 83] R. Lednicky, V.L. Lyuboshits, and M.I. Podgoretskii, Sov. J. Nucl. Phys. 38, 147 (1983).

[Lync 82] W.G. Lynch, L.W. Richardson, M.B. Tsang, R.E. Ellis, C.K. Gelbke, and R.E. Warner, Phys. Lett. 108B, 274 (1982).

[Lync 83] W.G. Lynch, C.B. Chitwood, M.B. Tsang, D.J. Fields, D.R. Klesch, C.K. Gelbke, G.R. Young, T.C. Awes, R.L. Ferguson, F.E. Obenshain, F. Plasil, R.L. Robinson and A.D. Panagiotou, Phys. Rev. Lett. 51, 1850 (1983).

[Meij 87] R.J. Meijer, A. Van den Brink, E.A. Bakkum, P. Decowski, K.A. Griffioen, and K.A. Kamermans, Nucl. Instr. and Meth. A256, 521 (1987).

[Mess 76] A. Messiah, "Quantum Mechanics", Vol. 1, North Holland Publishing Company, Amsterdam, 1976.

[Mich 03] A.A. Michelson, "Light waves and their uses", The University of Chicago Press, 1903.

[Mich 27] A.A. Michelson, "Studies in Optics", The University of Chicago Press, 1927.

[Nord 28] L.W. Nordheim, Proc. Roy. Soc. A119, 689 (1928).

[Ogil 90] C.A. Ogilvie, W. Bauer, D.A. Cebra, J. Clayton, S. Howden, J. Karn, A. Nadasen, A. Vander Molen, G.D. Westfall, W.K. Wilson, and J.S. Winfield, Phys. Rev. C42, R10 (1990).

[Ou 89] Z.Y. Ou and L. Mandel, Phys. Rev. Lett. 62, 2941 (1989).

[Ou 90] Z.Y. Ou, X.Y. Zou, L.J. Wang, and L. Mandel, Phys. Rev. Lett. 62, 2941 (1990).

[Paul 86] H. Paul, Rev. Mod. Phys. 58, 209 (1986).

[Pias 91] E. Piasecki, et al., Phys. Rev. Lett. 66, 1291 (1991).

[Pink 89] C.H. Pinkenburg, Diplomarbeit, Johann Wolfgang Goethe-Universitat, 1989.

[Poch 86] J. Pochodzalla, C.B. Chitwood, D.J. Fields, C.K. Gelbke, W.G. Lynch, M.B. Tsang, D.H. Boal, and J.C. Shillcock, Phys. Lett. B174, 36 (1986).

[Poch 87] J. Pochodzalla, C.K. Gelbke, W.G. Lynch, M. Maier, D. Ardouin, H. Delagrange, H. Doubre, C. Grégoire, A. Kyanowski, W. Mittig, A. Péghaire, J. Péter, F.Saint-Laurent, B. Zwieglinski, G. Bizard, F. Lefebvres, B. Tamain, and J. Québert, Y.P. Viyogi, W.A. Friedman, and D.H. Boal, Phys. Rev. C35, 1695 (1987).

[Prat 84] S. Pratt, Phys. Rev. Lett. 53, 1219 (1984).

[Prat 87] S. Pratt and M.B. Tsang, Phys. Rev. C36, 2390 (1987).

[Queb 89] J. Quebert, R. Boisgard, P. Lautridou, D. Ardouin, D. Durand, D. Goujdami, F. Guilbault, C. Lebrun, R. Tamisier, A. Péghaire, and F. Saint-Laurent, Proceedings of the Symposium on Nuclear Dynamics and Nuclear Disassembly, held at Dallas, April 1989, edited by J.B. Natowitz, World Scientific, Singapore 1989, p. 337.

[Rebr 90] D. Rebreyend, Serge Kox, J.C. Gondrand, B. Khelfaoui, F. Merchez, B. Noren, C. Perrin, Corinne 90, Proc. of Intl. Workshop on Particle Correlations and Interferometry in Nuclear Collisions, Nantes, France, 1990.

[Reid 68] R.V. Reid, Jr., Ann. Phys. (N.Y.) 50, 411 (1968).

[Shim 79] T. Shimoda, M. Ishihara, K. Nagatani, Nucl. Instr. and Meth. 165, 261 (1979).

[Sobo 91] L.G. Sobotka, L. Gallamore, A. Chbihi, D.G. Saratites, D.W. Stracener, W. Bauer, D.R. Bowman, N. Carlin, R.T. de Souza, C.K. Gelbke, W.G. Gong, S. Hannuschke, Y.D. Kim, W.G. Lynch, R. Ronningen, M.B. Tsang, F. Zhu, J.R. Beene, M.L. Halbert, and M. Thoennessen, Phys. Rev. C, (1991).

[Shur 73] E.V. Shuryak, Phys. Lett. 44B, 387 (1973).

[Stor 58] R.S. Storey, W. Jack, and A. Ward, Proceedings of the Phys. Society 72, 1 (1958).

[Stoc 86] R. Stock, Phys. Rep. 135, 259 (1986).

[Stöc 86] H. Stöcker and W. Greiner, Phys. Rep. 137, 277 (1986).

[Swen 87] Loyd S. Swenson, Jr., Physics Today 40, 24 (May,1987).

[Town 88] L.W. Townsend and J.W. Wilson, Phys. Rev. C37, 892 (1988).

[Tsan 84a] M.B. Tsang, C.B. Chitwood, D.J. Fields, C.K. Gelbke, D.R. Klesch, W.G. Lynch, K. Kwiatkowski and V.E. Viola, Jr., Phys. Rev. Lett. 52, 1967 (1984).

[Tsan 84b] M.B. Tsang, W.G. Lynch, C.B. Chitwood, D.J. Fields, D.R. Klesch, C.K. Gelbke, G.R. Young, T.C. Awes, R.L. Ferguson, F. E.

Obenshain, F. Plasil, and R.L. Robinson, Phys. Lett. 148B, 265 (1984).

[Tsan 89] M.B. Tsang, Y.D. Kim, N. Carlin, Z. Chen, C.K. Gelbke, W.G. Gong, W.G. Lynch, T. Murakami, T. Nayak, R.M. Ronningen, H.M. Xu, F. Zhu, L.G. Sobotka, D.W. Stracener, D.G. Sarantites, Z. Majka, V. Abenante, and H. Griffin, Phys. Lett. B220, 492 (1989).

[Tsan 90] M.B. Tsang, Y.D. Kim, N. Carlin, Z. Chen, C.K. Gelbke, W.G. Gong, W.G. Lynch, T. Murakami, T. Nayak, R.M. Ronningen, H.M. Xu, F. Zhu, L.G. Sobotka, D.W. Stracener, D.G. Sarantites, Z. Majka, and V. Abenante, Phys. Rev. C42, R15 (1990).

[Vies 86] G. Viesti, G. Prete, D. Fabris, K. Hagel, G. Nebbia, and A. Menchaca-Rocha, Nucl. Instr. and Meth. A252, 75 (1986).

[Wada 89] R. Wada, D. Fabris, K. Hagel, G. Nebbia, Y. Lou, M. Gonin, J.B. Natowitz, R. Billerey, B. Cheynis, A. Demeyer, D. Drain, D. Guinet, C. Pastor, L. Vagneron, K. Zaid, J. Alarja, A. Giorni, D. Heuer, C. Morand, B. Viano, C. Mazur, C. Ngô, S. Leray, R. Lucas, M. Ribrag, and E. Tomasi, Phys. Rev. C39, 497 (1989).

[Welk 88] G. Welke, M. Prakash, T.T.S. Kuo, S. Das Gupta, and C. Gale, Phys. Rev. C38, 2101 (1988).

[Wils 90] W.K. Wilson, W. Benenson, D.A. Cebra, J. Clayton, S. Howden, J. Karn, T. Li, C.A. Ogilvie, A. Vander Molen, G.D. Westfall, J.S. Winfield, B. Young, and A. Nadasen, Phys. Rev. C41, R1881 (1990).

[Wong 82] C.Y. Wong, Phys. Rev. C25, 1460 (1982).

[Xu 89] H.M. Xu, W.G. Lynch, C.K. Gelbke, M.B. Tsang, D.J. Fields, M.R. Maier, D.J. Morrissey, T.K. Nayak, J. Pochodzalla, D.G. Sarantites, L.G. Sobotka, M.L. Halbert, and D.C. Hensley, Phys. Rev. C40, 186 (1989).

[Yano 78] F.B. Yano and S.E. Koonin, Phys. Lett. 78B, 556 (1978).

[Zarb 81] F. Zarbakhsh, A.L. Sagle, F. Brochard, T.A. Mulera, V. Perez-Mendez, R. Talaga, I. Tanihata, J.B. Carroll, K.S. Ganezer, G. Igo, J. Oostens, D. Woodard, and R. Sutter, Phys. Rev. Lett. 46, 1268 (1981).

[Zhu 91] F. Zhu, W.G. Lynch, T.Murakami, C.K. Gelbke, Y.D. Kim, T.K. Nayak, R. Pelak, M.B. Tsang, H.M. Xu, W.G. Gong, W. Bauer, K. Kwiatkowski, R. Planeta, S. Rose, V.E. Viola,Jr., L.W. Woo, S. Yennello, J. Zhang, Phys. Rev. C44, R582 (1991).

[Zieg 77] J.F. Ziegler, "Hydrogen(Helium) -- Stopping Powers and Ranges in All Elemental Matter", Vol 3(4), Pergamon Press, 1977.

[Zieg 85] J.F. Ziegler, J.P Biersack, U. Littmark, "The Stopping and Range of Ions in Solids", Vol. 1 of "The Stopping and Range of Ions in Matter", Edited by J.F. Ziegler, Pergamon Press, 1985.